



DISSERTATION

Advancing Continuous Biomanufacturing: Quality Control and Process Intensification Strategies for Perfusion Cell Culture

ausgeführt zum Zwecke der Erlangung des akademischen Grades eines Doktors der technischen Wissenschaften eingereicht an der Technischen Universität Wien,
Fakultät für Technische Chemie

von

Patrick Romann, MSc

Matrikelnummer 12130537

unter der Anleitung von

Prof. Dipl.-Ing. Dr.nat.techn. Oliver Spadiut

Institut für Verfahrenstechnik, Umwelttechnik und technische Biowissenschaften
Forschungsbereich Integrated Bioprocess Development
Technische Universität Wien,
Getreidemarkt 9/166-4, A-1060 Wien

11.09.2023

Wien, am

A black rectangular box redacting the signature of the author.

eigenhändige Unterschrift

I hereby declare that I am the sole author of this work. No assistance other than which is permitted has been used. Ideas and quotes taken directly or indirectly from other sources are identified as such. This written work has not yet been submitted in any part.

Patrick Romann

Abstract

Emerging product classes, like fusion proteins, antibody-drug conjugates (ADCs), and bispecifics, are reshaping the landscape of biologics. Biosimilars have also entered the market in recent years. As competition grows and product pipelines expand, continuous manufacturing of biologics has gained momentum due to its potential for process intensification. A number of manufacturers are evolving or adapting their production platform to use perfusion cell culture and continuous downstream purification principles to benefit from more productive and faster production and purification capabilities.

The present work aims at providing a product quality control framework for intensified steady-state perfusion processes, with the objective to build a time-independent integrated continuous biomanufacturing platform for biologics in Chinese hamster ovary (CHO) cells. A prerequisite for such a continuous manufacturing platform is a steady-state perfusion cell culture yielding consistent product quality over time. This is especially challenging for highly intensified processes, almost indispensably requiring real-time process control to detect process excursions and initiate preventive actions to avoid product quality drifts. Process analytical technologies (PAT) such as multivariate spectroscopic sensors are promising tools to enable real-time process monitoring and control, yet direct measurement of critical quality attributes such as glycosylation remains extremely challenging due to relatively low concentrations and complex process matrices. Leveraging the understanding of the relationship between critical process parameters (CPPs) and critical quality attributes (CQAs), according to the Quality by Design (QbD) principle, appears to be a more tangible approach. This strategy involves estimating CQAs based on real-time PAT measurements of CPPs. However, spectroscopic sensor calibration remains a challenging and time-consuming task, especially for perfusion processes with inherently low process variability.

The first step towards incorporating spectroscopic PAT tools into the manufacturing platform involved therefore the creation of a novel PAT sensor calibration method designed specifically for steady-state perfusion. This approach enables the

development of exceptionally precise and robust prediction models within a matter of days, as opposed to the traditional duration of several months. With this method in place, a real-time Raman spectroscopy feedback control strategy was established, reducing ammonium accumulation 3-fold, which in turn stabilized CQAs of the bispecific antibody product. Various critical glycoforms, such as high mannose glycans and fucosylation, were stabilized to yield standard deviations below 0.2% over the course of a 40-day perfusion process, qualifying the operation as time-independent manufacturing process. Additionally, promising glycosylation modulators to fine-tune antibody-dependent cell-mediated cytotoxicity (ADCC) were successfully screened and evaluated for applicability in continuous manufacturing, representing a particularly interesting tool to match reference product quality in the biosimilars field.

This work further investigated potential process intensification strategies to boost productivity with a particular focus on their impact on product quality. Technologies for innovative bleed recycling applications were evaluated and scaled to manufacturing scale, with the intent to selectively concentrate the biomass and recycle the liquid fraction containing the product, which would otherwise be wasted. In conjunction with extended culture durations enabled through product quality stabilization by real-time control, a novel operating mode for frequently applied hollow fiber-based tangential flow filtration (TFF) was proposed. Additional harvest volumes gained through process intensification can be handled, thereby alleviating extensive product retention or premature filter clogging as experienced for standard TFF operation.

In summary, the implementation of the developed quality control framework represents a significant contribution to the field of continuous biomanufacturing, as exemplified by an intensified CHO perfusion process producing a glycosylated bispecific antibody. QbD principles in combination with Raman spectroscopy as PAT technology ensure time-independent product quality profiles under highly intensified manufacturing conditions, thereby qualify the perfusion upstream process for seamless incorporation into the integrated continuous biopharmaceutical manufacturing platform.

Zusammenfassung

Aufstrebende Produktklassen wie Fusionproteine, Antikörper-Wirkstoff-Konjugate (ADCs) und Bispezifika revolutionieren das Feld der Biologika, während Biosimilars in jüngerer Vergangenheit Marktzutritt erlangt haben. Mit wachsendem Wettbewerb und der Erweiterung der Produktpipelines erhält die kontinuierliche Produktion von Biologika durch ihr Potenzial zur Prozessintensivierung immer mehr Auftrieb. Eine Reihe von Herstellern entwickelt ihre Produktionsplattform weiter oder passt sie an, um die Prinzipien der Perfusionszellkultur und der kontinuierlichen nachgeschalteten Aufreinigung zu nutzen und so von produktiveren und schnelleren Produktions- und Aufreinigungsmöglichkeiten zu profitieren.

Ziel dieser Arbeit ist es, einen Rahmen zur Qualitätskontrolle für intensivierete Steady-state-Perfusionsprozesse zu entwickeln, um eine zeitunabhängige integrierte kontinuierliche Produktionsplattform für Biologika in Chinesischen Hamster Ovarialzellen (CHO) zu etablieren. Voraussetzung für eine solche kontinuierliche Produktionsplattform ist eine Steady-state-Perfusionskultur, die über die Zeit hinweg eine gleichbleibende Produktqualität liefert. Dies ist insbesondere für hochintensivierte Prozesse eine Herausforderung, die eine Echtzeit-Prozesskontrolle nahezu unabdingbar macht, um Prozessabweichungen frühzeitig zu erkennen und vorbeugende Maßnahmen zur Vermeidung von Qualitätsabweichungen einzuleiten. Obwohl Prozessanalysetechnologien (PAT), wie multivariate spektroskopische Sensoren, großes Potenzial zur Ermöglichung von Echtzeit-Prozessüberwachung und -steuerung bieten, bleibt die direkte Messung kritischer Qualitätsmerkmale wie der Glykosylierung aufgrund relativ niedriger Konzentrationen und komplexer Prozessmatrizen extrem anspruchsvoll. Ein vielversprechender Ansatz scheint hierbei das Verständnis der Beziehung zwischen kritischen Prozessparametern (CPPs) und kritischen Qualitätsattributen (CQAs) gemäß dem Quality by Design (QbD) Prinzip zu nutzen. Diese Strategie beinhaltet die Abschätzung der CQAs basierend auf Echtzeit-PAT-Messungen der CPPs. Die Kalibrierung von spektroskopischen Sensoren bleibt allerdings eine herausfordernde und zeitaufwendige Aufgabe, insbesondere für Perfusionsprozesse mit intrinsisch niedriger Prozessvariabilität.

Der erste Schritt zur Integration spektroskopischer PAT-Sensorik in die Produktionsplattform bestand daher in der Entwicklung einer neuartigen Kalibrierungsmethode für PAT-Sensoren, die speziell für Steady-state-Perfusion ausgelegt ist. Dieser Ansatz ermöglicht die Entwicklung von äußerst präzisen und robusten Vorhersagemodellen innerhalb weniger Tage, im Gegensatz zu der herkömmlichen Dauer von mehreren Monaten. Mit dieser Methode wurde eine Echtzeit-Raman-Spektroskopie-Kontrollstrategie etabliert, die die Anreicherung von Ammonium auf ein Drittel reduzierte und somit die CQAs des bispezifischen Antikörperprodukts stabilisierte. Verschiedene kritische Glykolysierungsformen, wie hohe Mannose und Fucosylierung, wurden so stabilisiert, dass die Standardabweichungen über den Verlauf eines 40-tägigen Perfusionprozesses unter 0.2% lagen, was das Verfahren als zeitunabhängigen Produktionsprozess qualifizierte. Darüber hinaus wurden vielversprechende Glykosylierungsmodulatoren zur Feinabstimmung der antikörperabhängigen zellvermittelten Zytotoxizität (ADCC) erfolgreich gescreent und auf ihre Anwendbarkeit in der kontinuierlichen Herstellung hin untersucht, was ein besonders interessantes Instrument zur Anpassung der Qualität von Referenzprodukten im Bereich der Biosimilars darstellt.

Diese Arbeit untersuchte weiterhin mögliche Prozessintensivierungsstrategien zur Steigerung der volumetrischen Produktivität mit besonderem Fokus auf ihre Auswirkungen auf die Produktqualität. Technologien für innovative Bleed-Recycling-Anwendungen wurden evaluiert und auf Produktionsgröße skaliert, mit der Absicht, die Biomasse im Bleed selektiv zu konzentrieren und den Flüssigkeitsanteil, der das Produkt enthält und sonst verschwendet würde, zum Bioreaktor zurückzuführen. In Kombination mit verlängerter Kultivierungsdauer, die durch die Stabilisierung der Produktqualität durch Echtzeitkontrolle ermöglicht wird, wurde ein neuartiger Betriebsmodus für häufig angewandte hohlfaserbasierte Tangentialflussfiltration (TFF) vorgeschlagen. Auf diese Weise können zusätzliche Erntevolumina, die durch die Prozessintensivierung gewonnen werden, gehandhabt werden, wodurch eine umfangreiche Produktretention oder ein vorzeitiges Verstopfen des Filters, wie es bei der Standard-TFF der Fall sein kann, vermieden wird.

Zusammenfassend lässt sich sagen, dass die Implementierung des entwickelten Qualitätskontrollrahmens einen bedeutenden Beitrag zum Bereich der kontinuierlichen Produktion von Biologika darstellt, wie am Beispiel eines intensivierten CHO-Perfusionsprozesses zur Herstellung eines glykosylierten bispezifischen Antikörpers gezeigt wurde. QbD-Prinzipien in Kombination mit Raman-Spektroskopie als PAT-Technologie gewährleisteten zeitunabhängige Produktqualitätsprofile unter intensivierten Herstellungsbedingungen und qualifizieren den Perfusionprozess für die

nahtlose Integration in eine vollkontinuierliche Produktionsplattform.

Partnership Acknowledgements

This work represents a collaboration between:

University of Applied Sciences and Arts Northwestern Switzerland

Muttenz, Switzerland

Institute of Pharmatechnology

Supervisor: Prof. Dr. Thomas K. Villiger

Merck Serono SA (an affiliate of Merck KGaA)

Vevey, Switzerland

Biotech Process Sciences

Supervisor: Dr. Jean-Marc Bielser

TU Wien

Vienna, Austria

Institute of Chemical Environmental and Bioscience Engineering

Supervisor: Prof. Dr. Oliver Spadiut

Acknowledgements

I would like to express my deepest gratitude to the following people who have made this journey possible and enriched my doctoral experience in their own significant ways.

Firstly, my heartfelt thanks go to Prof. Thomas K. Villiger for guidance, trust, and faith in my work over the past years as part of his research group at FHNW. In no less extent I would like to thank Jean-Marc Bielser for the unwavering support and the invaluable opportunity to be a part of his technology innovation team at Merck Serono. My appreciation extends to Prof. Christoph Herwig, who guided me during my initial three years at TU Wien and whose astute inputs were vital to my work, and to Prof. Oliver Spadiut, for his dedication and expert guidance during the final stages of my doctoral work. Equally, I must express my gratitude to Prof. Jarka Glassey and Prof. Ralf Pörtner as for their work as co-examiners on the evaluation of this thesis.

The foundation of any successful collaboration, especially those bridging the worlds of academia and industry, lies in the dedicated efforts of its contributors. At FHNW, I owe my sincerest thanks to the Villiger group, particularly Sherin Panikulam, Daniela Tobler, Maïke Otto and Damian von Blarer, whose support and collaboration were invaluable. I also extend my gratitude to all my students – Francesco Lipari, Jakub Kolář, Silvia Pavone, Philip Giller, and Sebastian Schneider – whose relentless commitment and diligent work on various elements of this project greatly amplified its success. A special thanks goes to the workshop team with Pavel Dagorov, Theo Walser and Georg Hasler. Their exceptional skills and unyielding resolve, whether in designing and constructing prototypes or tackling various technical challenges, were truly unparalleled. I further wish to acknowledge Christof Jeiziner and Andreas Seelig for infrastructure support, Theodor Bühler for spectroscopy advice, François Vogel and the procurement team for the endless orderings that have been made, and Prof. Georgios Imanidis for the support in establishing a mammalian bioprocess laboratory at FHNW.

At Merck Serono, I am grateful to the entire biopharma technology and inno-

vation (BTI) group, especially to Stefania Caso, Matthieu Aeby, Stéphane Ugo, Thomas Vuillemin, and Alexandre Chatelin for their guidance and support from the very beginning of this journey. Many thanks to Jonathan Souquet and Arnaud Perilleux for sponsoring this project and their valuable input from an industrial perspective. A special thank goes to Loïc Chappuis for his hospitality during my stays in Vevey, the shared enthusiasm about technology and the many enjoyable moments together in the laboratory. Additionally, I wish to express my appreciation to Martin Jordan, whose profound expertise and meticulous attention to detail have always been a source of admiration and inspiration to me.

I would also like to extend my gratitude to external collaborators, Antony Sibia from Levitronix and Prof. Andrew L. Zydney from Pennsylvania State University for their significant contribution to advance tangential flow filtration, Prof. Miroslav Šoóš from UCT Prague for his expert advice on gravity settler design, and to Evgueni Voronkov, Matthew McRae, and Roystein Bulman from Nova Biomedical for their collaboration on cell culture sampling.

Auf persönlicher Ebene möchte ich meinen Freunden von den Zurzigansters, dem HC Hopfenperle und dem Mittwuchsklübli für die notwendige Ablenkung und Balance danken. Ein besonderes Dankeschön geht an meine engsten Freunde Lucki, Luk, Joel, Marco & Sara für ihre Kameradschaft, ihren Rückhalt und die gemeinsam geteilten Erlebnisse. Mein tiefster Dank geht an Laura, für ihre unermüdliche Unterstützung, ihr Verständnis während der langen Arbeitstage und die wunderbaren gemeinsamen Momente, die wir in den letzten Jahren erleben durften. Abschließend möchte ich meine tiefste Wertschätzung für meine Eltern zum Ausdruck bringen, die mich kontinuierlich bei der Verwirklichung meiner Träume unterstützen und immer für mich da sind.

Contents

Abstract	I
Zusammenfassung	III
Partnership Acknowledgements	VII
Acknowledgements	IX
List of Figures	XIV
List of Tables	XXIX
Abbreviations	XXXIII
1 Introduction	1
1.1 Background on biopharmaceutical manufacturing	1
1.2 Monoclonal antibodies and advanced antibody therapeutics	2
1.3 Regulatory framework for commercialization of biotherapeutics	5
1.4 Critical quality attributes of biotherapeutic proteins	6
1.4.1 Contaminants	6
1.4.2 Process-related impurities	6
1.4.3 Product-related impurities	7
1.5 N-glycosylation of therapeutic proteins	9
1.5.1 N-glycosylation machinery	9
1.5.2 Different types of N-glycosylation and their impact on product characteristics	10
1.6 Levers to modulate N-glycosylation of biotherapeutics in mammalian cell culture	12
1.6.1 Selection of the host cell line and cell line engineering	12
1.6.2 Media components and supplements with their impact on N- glycosylation	13

1.6.3	Process parameters influencing N-glycosylation	15
1.7	Modern manufacturing of biotherapeutics: From batch to continuous	16
1.7.1	Manufacturing unit operations in upstream and downstream processing	16
1.7.2	State-of-the-art manufacturing of biologics and future trends .	18
1.8	Steady-state perfusion: A key unit operation for continuous manufacturing of biologics	22
1.8.1	Steady-state perfusion process setup	23
1.8.2	Stable operation by bleeding: Bleed control strategy	24
1.8.3	Cell retention devices for high density perfusion processes . . .	25
1.8.4	Advanced PAT for perfusion cell culture: Raman spectroscopy	26
1.8.5	Current challenges for continuous perfusion processes	27
1.8.6	Process intensification in steady-state perfusion	30
2	Scope of the Thesis	33
3	Results and Discussion	37
3.1	Product quality control: Attaining consistent product quality in intensified perfusion processes	37
3.1.1	Section I - Advancing Raman model calibration for perfusion bioprocesses using spiked harvest libraries	38
3.1.2	Section II - Raman-controlled pyruvate feeding to control metabolic activity and product quality in continuous biomanufacturing .	43
3.1.3	Section III - Maduramycin, a novel glycosylation modulator for mammalian fed-batch and steady-state perfusion processes	48
3.2	Productivity increase: Investigation of process intensification strategies and their impact on product quality	52
3.2.1	Section IV - Maximizing yield of perfusion cell culture processes: Evaluation and scale-up of continuous bleed recycling .	53
3.2.2	Section V - Co-current filtrate flow in TFF perfusion processes: Decoupling transmembrane pressure from crossflow to improve product sieving	58
4	Concluding Remark	63
	References	66
A	Scientific Publications	99
A.1	Scientific Publication Section I	101

A.2 Scientific Publication Section II	131
A.3 Scientific Publication Section III	165
A.4 Scientific Publication Section IV	201
A.5 Scientific Publication Section V	235

B Curriculum Vitae	265
---------------------------	------------

Die approbierte gedruckte Originalversion dieser Dissertation ist an der TU Wien Bibliothek verfügbar.
The approved original version of this doctoral thesis is available in print at TU Wien Bibliothek.

List of Figures

1.1	Schematic representation of different Ig isotypes, with heavy chain (blue) and light chain (purple). N-glycosylation sites are shown with complex (red) and oligomannose (green). O-glycosylation is represented as yellow. Disulfide bridges are represented by black lines. Figure reprinted from literature [11].	3
1.2	Schematic N-glycosylation pathway in the ER and GA reprinted from the literature [79].	10
1.3	Exemplary continuous manufacturing scenario at 2,000L scale taken from literature [192]. Continuously collected harvest is processed on a daily basis by a continuous downstream processing (cDSP) sequence composed of six cycles of capture, two cycles of VI-F, AEX, and MM. A pool of four daily cDSP sequences is then further processed in NAF and UF/DF, prior to further pooling into DS. Two diversion points are present that enable to divert process stream that do not meet product quality requirements – one in the perfusion bioreactor harvest stream and a second if the post-cDSP stream does not qualify for further processing. Time-independent product quality is required in this scenario in order to allow diversion without impacting the product quality of the final DS pool.	22
1.4	Schematic representation of a steady-state perfusion setup. Fresh media and feeds are entering the bioreactor. Sensor technology is mounted to the bioreactor for real-time control of CPPs. Bleed is controlled by a capacitance sensor monitoring VCV. A CRD generates cell-free product harvest that is either collected in a tank or directly processed in cDSP.	23

3.1	Schematic representation of the harvest library calibration approach. Harvest library samples are thawed and spiked with analytes of interest (A). Spectra for spiked harvest samples are collected in an off-line setup (B) followed by chemometric modeling to create prediction models (C). Subsequently, the flow cell is connected to the bioreactor harvest stream and in-line model verification by adding analytes or other matrix components into the bioreactor is performed to assess model performance (D).	39
3.2	Raman spectra for glucose (A), raffinose (B), galactose (C), mannose (D), and fructose (E) in perfusion process harvest. All spectra were pretreated with a Savitzky–Golay filter (derivative 1, polynomial = 2, window size = 31) followed by standard normal variate (SNV). Background bands represent the min-max normalized regression coefficient for the respective wavenumber for the individual models. Blue colors show the negative contribution of the wavenumber to the predicted value, red colors indicate a positive contribution. The more intense the coloring, the more important the wavenumber for the respective model.	40
3.3	Raman predictions of the model verification run comparing the simple calibration model consisting solely of raffinose spikes (A) with the comprehensive DoE model incorporating raffinose as well as glucose spiked (B). RA1 and RA2 represent raffinose additions of 10.9 g L ⁻¹ and 11.1 g L ⁻¹ to the bioreactor, whereas GA1 is a glucose addition of 11.8 g L ⁻¹ and GA2 a glucose addition of 5.6 g L ⁻¹ . Raw predictions without moving average are shown and aligned with reference values for glucose (circles) and raffinose (squares). GA, glucose addition; RA, raffinose addition.	41
3.4	Raman controlled pyruvate feeding strategy. Schematic setup of a perfusion bioreactor with Raman flow cell after cell retention device (CRD) in harvest stream predicting lactate concentration and controlling pyruvate feed addition (A). Simplified metabolic scheme of feeding strategy (B).	44

3.5	Cell culture parameter, nutrient and metabolite trends for steady-state perfusion cultivations. VCV and viability (A), product titer (B), lactate (C), pyruvate (D), ammonium (E) and pyruvate feed rate (F). The vertical black lines represent the start of Raman controlled pyruvate feeding and the blue and red vertical line represent the end of pyruvate feeding of the respective runs. Blue horizontal lines represent a phase of ammonium addition of 5 mmol L ⁻¹ to the perfusion media in the perfusion run with 0.3 g L ⁻¹ lactate setpoint.	45
3.6	Product glycosylation profiles for steady-state perfusion cultivations. High mannose (A), fucosylation (B), G0 (C), G1 (D), G2 (E), a-sialylation (F), mono-sialylation (G) and di-sialylation (H). The vertical black lines represent the start of Raman controlled pyruvate feeding and the blue and red vertical line represent the end of pyruvate feeding of the respective runs. Blue horizontal lines represent a phase of ammonium addition of 5 mmol L ⁻¹ to the perfusion media in the perfusion run with 0.3 g L ⁻¹ lactate setpoint.	46
3.7	Steady-state perfusion process data at 2 L bioreactor scale for control run, kifunensine and maduramycin run producing a bispecific antibody. VCV and viability (A), process titer (B), feeding strategy and calculated modulator concentration in the bioreactor for kifunensine run (C) and for maduramycin run (D), with respective absolute HM levels for kifunensine run (E) and maduramycin (F). Steady-state HM glycoforms averaged over last 3 days before media change for kifunensine run (G) and for maduramycin run (H).	49
3.8	N-glycosylation data of steady-state perfusion process at 2 L bioreactor scale for continuous 50 nM maduramycin run and control run producing a bispecific antibody. Absolute HM (A), a-fucosylated species (B), galactosylated species (C) and a-sialylated species (D). The dashed lines represent the change from modulator free media to 50 nM maduramycin media on day 11.	50
3.9	Schematic representation of the bleed recycling setup (A), lab-scale acoustic settler (B), lab-scale inclined gravity settler (C), and large-scale inclined gravity settler (D).	54

3.10 Bleed recycling efficiency data and performance calculations. VCV contour plot showing the relationship of VCD and average cell diameter for VCV (A). Experimental data to evaluate optimal recycle rates by accumulating and non-accumulating settler experiments (B). The straight line represents an expected accumulation limit based on linear regression of all data points. Process yield increase contour plot relating process bleed rate to settler recycle rate (C) or process VCV setpoint (D) assuming optimal settler recycle rate as evaluated by the regression line in (B). The points in (A), (C) and (D) serve as an example for a process bleed of approximately 20% with the specified VCV of roughly 12%. Acoustic settler (AS), Inclined Gravity Settler (IS).	55
3.11 Process data of lab-scale 2 L perfusion settler run compared with a standard control run without bleed recycling for a bispecific mAb product. VCV and viability (A), process harvest rate (B), ammonia and pH profile (C), harvest titer and debris trend (D), high-mannose (D) and fucosylation (E). Grey areas represent process phases where bleed recycling was performed, whereas bleed recycling was turned off during white process phases.	56
3.12 Schematic representation for TFF (A), HPTFF (B) and scTFF (C) systems with centrifugal pumps based on pressure characterization. Relative pressure curves along the filter length for each system are given and arrows indicate filtrate flux, longer arrows represent larger fluxes. Additionally, a zoom into a fiber at the beginning, middle and at the end of the filter is provided and colored from red (high pressure) to blue (low pressure). As scTFF consists of two phases, the situation for reduced (scTFF Phase 1) and enhanced co-current filtrate flow (scTFF Phase 2) and are depicted.	59

3.13	Detailed schematic representation of the experimental setup for the pressure characterization in water (A). Pressure transmitters (PT), flow sensors (FS), centrifugal pumps (CD) and peristaltic pumps (PP) are specified with subscripted letters according to their position (R: Retentate; F: Filtrate; A: Additional sensors on filtrate side; H: Harvest). Minimally required setup for HPTFF or scTFF operation used for cell culture runs are further shown (B). Pressure measurements according to their position along the filter length are provided for HPTFF (C) and scTFF (D) at 650 mL min ⁻¹ crossflow, grey areas represent absolute fiber length.	60
3.14	Perfusion cell culture runs with TFF (black), rTFF (blue), HPTFF or scTFF (red) as cell retention devices. VCV and viability (A), cell diameter (B), harvest titer (C) and product sieving (D).	61
4.1	Schematic overview where the different Section integrate into the steady-state perfusion platform. Section I: Novel offline calibration method for PAT tools. Section II: Raman-based pyruvate feeding strategy to ensure consistent product quality. Section III: Medium supplementation with modulators to fine-tune N-glycosylation. Section IV: Bleed recycling to reduce process waste and increase productivity. Section V: Improved TFF by applying co-current filtrate flow to alleviate product retention.	64
A.1	Spiking chart for the spiking-based Raman calibration workflow. The workflow consists of three phases. Initial screening phase: identification if calibration of a certain analyte is possible. Model calibration phase: actual model calibration using the harvest library. Model verification phase: final stage to verify calibration models with independent bioreactor runs.	108
A.2	Schematic of the harvest library spiking approach. Fresh harvest samples of two reactors (A) and harvest samples of three reactors (B) which were frozen and stored in a harvest library (C) were used for model calibration. Harvests were spiked with glucose and/or raffinose and pumped through a Raman flow cell (D) to generate Raman calibration data. The flow cell was then connected directly to the bioreactor run (E) for model verification.	110

A.3 PCA plot colored by the spiked compounds are depicted in (A) and the corresponding theoretical concentrations in (B). Single raffinose spikes are colored in red, single glucose spikes in blue and mixed spikes in green. CS1 is composed of red samples, CS2 of red and blue samples, CS3 of red, blue, and green samples. PCA plots of the individual sugar concentrations are depicted for glucose in (C) and raffinose concentration in (D). CS, calibration set; PCA, principal component analysis. 111

A.4 Principal component analysis (PCA) plots for the initial screening phase for raffinose, galactose, mannose, and fructose with increasing color intensity according to their concentration (A) and glucose (B). Originating from a common center point, all sugars populate in a distinct direction. The higher the concentration, the further away from the center, demonstrating that the Raman spectra can distinguish the various sugars in a concentration-dependent manner. 112

A.5 Raman spectra for glucose (A), raffinose (B), galactose (C), mannose (D), and fructose (E) in perfusion process harvest. All spectra were pretreated with a Savitzky–Golay filter (derivative 1, polynomial = 2, window size = 31) followed by standard normal variate (SNV). Background bands represent the min-max normalized regression coefficient for the respective wavenumber for the individual models. Blue colors show the negative contribution of the wavenumber to the predicted value, whereas red colors indicate a positive contribution. The more intense the coloring, the more important the wavenumber for the respective model. 115

A.6 Raman predictions of the verification run using models based on calibration set CS1 (A), CS2 (B), and CS3 (C). RA1 and RA2 represent raffinose additions of 10.9 and 11.1 g L⁻¹ to the bioreactor, whereas GA1 is a glucose addition of 11.8 g L⁻¹ and GA2 a glucose addition of 5.6 g L⁻¹. Raw predictions without moving average are shown and aligned with reference values for glucose (circles) and raffinose (squares). CS, calibration set; GA, glucose addition; RA, raffinose addition. 118

A.7 Regression coefficients for glucose models (A) and raffinose models (B). 120

A.8	Illustration of the Raman flow cell using a diagonal cut to show the flow chamber with the inlet (lower left side, close to Raman probe) and outlet (upper right side, further away from Raman sensor) (A). This design enabled efficient bubble removing ensuring stable operation. Picture of Raman flow cell setup connected to a perfusion harvest stream (B).	123
A.9	Detailed drawing of the Raman flow cell, dimensions given in mm. . .	124
A.10	PCA plot for glucose and raffinose model calibration using the harvest library colored according to the base harvest origin.	125
A.11	RMSEP for glucose models (A) and raffinose models (B) according to the number of latent variables (LVs) used for PLS regression. . . .	125
A.12	Spike validation of Raman models during steady-state perfusion. Glucose model (A), lactate model (B), ammonium model (C) and pyruvate model (D) were evaluated by addition of spiked compounds (Table A.6). Vertical dashed lines represent the time of the respective spike addition.	141
A.13	Raman controlled feeding strategy. Schematic setup of perfusion bioreactor with Raman flow cell after cell retention device (CRD) in harvest stream predicting lactate concentration and controlling pyruvate feed addition (A). Simplified metabolic scheme of feeding strategy (B). Real-time Raman predictions and corresponding at-line reference measurements for a perfusion run with 0.7 g L^{-1} lactate setpoint (C) and a perfusion run with a lower lactate setpoint of 0.3 g L^{-1} (D).	142
A.14	Cell culture parameter, nutrient and metabolite trends for steady-state perfusion cultivations. VCV and viability (A), product titer (B), lactate (C), pyruvate (D), ammonium (E), pyruvate feed rate (F), culture pH (G), glucose and osmolality (H). The vertical black lines represent the start of Raman controlled pyruvate feeding and the blue and red vertical line represent the end of pyruvate feeding of the respective runs. Blue horizontal lines represent a phase of ammonium addition of 5 mmol L^{-1} to the perfusion media in the perfusion run with 0.3 g L^{-1} lactate setpoint.	144

A.15	Product glycosylation profiles for steady-state perfusion cultivations. High mannose (A), fucosylation (B), G0 (C), G1 (D), G2 (E), a-sialylation (F), mono-sialylation (G) and di-sialylation (H). The vertical black lines represent the start of Raman controlled pyruvate feeding and the blue and red vertical line represent the end of pyruvate feeding of the respective runs. Blue horizontal lines represent a phase of ammonium addition of 5 mmol L ⁻¹ to the perfusion media in the perfusion run with 0.3 g L ⁻¹ lactate setpoint.	146
A.16	Amino acid profiles during steady-state perfusion cultivation. Alanine (A), glycine (B), glutamine (C), glutamate (D), asparagine (E) and aspartate (F). The vertical black lines represent the start of Raman controlled pyruvate feeding and the blue and red vertical line represent the end of pyruvate feeding of the respective runs.	150
A.17	Consumption rate of nutrients, metabolites and amino acids during steady-state perfusion cell culture. Steady-state data was used to calculate consumption rates, three control runs were combined for the calculation of control data. Consumption rates of net consumed amino acids (A) and nutrients (B), consumption rates of net produced amino acids (C) and nutrients and metabolites (D). The Welch's test was applied to determine statistical significance (* $P < 0.05$, ** $P < 0.01$, *** $P < 0.001$, n.s. not significant). Simplified schematic representation of cellular metabolism without pyruvate feed (E) and with Raman controlled pyruvate feeding (F).	151
A.18	RMSE, RMSECV and RMSEP versus the amount of latent variables. Glucose prediction model (A), lactate (B), ammonium (C) and pyruvate (D).	155
A.19	Amino acid profiles during steady-state perfusion cultivation for all measured amino acids.	156
A.20	HM modulator screening for cell line A in ST. Maduramycin, narasin and salinomycin, abbreviated with M, N and S were used at nM concentrations supplemented to the cell culture. VCD (A), viability (B) and total HM (C) for a fed-batch process. Conditions with error bars were performed in duplicates (n=2).	176

A.21 HM modulator comparison in ambr15 fed-batch process for cell line A (first column), cell line B (second column) and cell line C (third column). Kifunensine and maduramycin, abbreviated with K, respectively M, were investigated at nM concentrations supplemented to the cell culture. VCD and viability (A, B, C), total HM (D, E, F), HM distribution (G, H, I) and product titer (J, K, L). Conditions with error bars were performed in duplicates (n=2). 178

A.22 Feeding strategy evaluation in ambr250 high-seed fed-batch process for cell line B. VCD (A), cell viability (B), total HM (C) and process titer (D). The green arrow represents the seconds Maduramycin addition for the condition M 40+40 nM. Conditions were performed in duplicates and pooled for titer and glycosylation analysis (n=2). . . . 179

A.23 Semi-continuous perfusion ST experiment evaluating reversibility of maduramycin and kifunensine effects on cell line D. VCV and viability (A) and HM glycoforms (C) for kifunensine cultures at 1 μ M. VCV and cell viability (B) and HM glycoforms (D) for maduramycin cultures at 200 nM. Dashed lines indicate the switch from modulator media to modulator-free perfusion media. HM glycoforms for kifunensine (E) and maduramycin (F) screening in ST stopped after 3 days. Conditions with error bars were performed in duplicates (n=2). 181

A.24 HM fine-tuning experimental data of cell line D in semi-continuous ST by supplementing maduramycin, kifunensine or a combination of both compounds. Response surface plots for enzyme conversion efficiency are shown in the top row in (A), the relative HM distributions for the specific HM forms in the lower row. Total HM response surface is shown in (B), the red rectangle highlights data used for the total HM and the HM distribution plot in (C), the blue rectangle for the total HM and the HM distribution plot in (D). Black dots on the response surface correspond to experimental data points used for modelling. 183

A.25 Steady-state perfusion process data at 2 L bioreactor scale for control run, kifunensine and maduramycin run using cell line D. VCV and viability (A), process titer (B), feeding strategy and calculated modulator concentration in the bioreactor for kifunensine run (C) and for maduramycin run (D), with respective absolute HM levels for kifunensine run (E) and maduramycin (F). Steady-state HM glycoforms averaged over last 3 days before media change for kifunensine run (G) and for maduramycin run (H). 187

A.26	Glycosylation data of steady-state perfusion process at 2 L bioreactor scale for continuous 50 nM maduramycin run and control run using cell line D. Absolute HM (A), HM glycoforms for maduramycin run (B), a-sialylated species (C), afucosylated species (D), A1 form (E), A2 and A2G1 forms (F), galactosylated species (G), FA1 and FA2 forms (H), FA2G1 and FA2G2 forms (I). The dashed lines represent the change to 50 nM maduramycin media on day 11.	189
A.27	Polyether ionophore screening in ST bioreactors for cell line A (first column), and in ambr15 fed-batch process for cell line B (second column) and cell line C (third column). Narasin, salinomycin and maduramycin with the respective abbreviation N, S and M were evaluated. VCD (A, B, C), viability (D, E, F), total HM (G, H, I) and product titer (J, K, L). Conditions with error bars were performed in duplicates (n=2).	192
A.28	VCV and cell viability (A) and process titer (B) of continuous 50 nM maduramycin feeding during steady-state perfusion process and a control run. The dashed line represents the start of the continuous maduramycin feeding.	193
A.29	Predicted vs. actual plots for the MLR plots of the HM fine-tuning experiment of cell line D in semi-continuous ST bioreactors. Predicted vs. actual plots for the enzyme conversion efficiency plots are provided in the upper row of (A), for the relative HM distributions in the lower row of (B) and for the total HM in (B).	194
A.30	Schematic representation of the bleed recycling setup (A), lab-scale acoustic settler (B), lab-scale inclined gravity settler (C) and large-scale inclined gravity settler (D).	208
A.31	Difference in glucose (A), lactate (B), ammonia (C) and pH (D) of the inlet stream into the settler (dashed zero line) compared the respective recycle and waste stream for acoustic separator (AS) and inclined gravity settler (IS) (n = 8).	212
A.32	Glycan forms of antibodies in the recycle stream of the acoustic settler (AS) and inclined gravity settler (IS) compared to the inlet stream for the offline experiment (n = 14).	213

A.33 Offline debris investigation of recycle streams using the UV-Vis spectrometer (A) and the fluid imaging device FlowCam (B). Layered histogram of intensified debris experiment showing the debris size distribution for the lab-scale inclined gravity settler (C) and the lab-scale acoustic settler (D), particle removal rate for specific debris size (E) and the calculated effectively returned particle amount considering a recycle rate of 80% irrelevantly of their size (F). Acoustic settler (AS), Inclined Gravity Settler (IS). 214

A.34 Bleed recycling efficiency data and performance calculations. VCV contour plot showing the relationship of VCD and average cell diameter for VCV (A). Experimental data to evaluate optimal recycle rates by accumulating and non-accumulating settler experiments (B). The straight line represents an expected accumulation limit based on linear regression of all data points. Process yield increase contour plot relating process bleed rate to settler recycle rate (C) or process VCV setpoint (D) assuming optimal settler recycle rate as evaluated by the regression line in (B). The points in (A), (C) and (D) serve as an example for a process bleed of approximately 20% with the specified VCV of roughly 12%. Acoustic settler (AS), Inclined Gravity Settler (IS). 216

A.35 Process data of lab-scale 2 L perfusion settler run compared with a standard control run without bleed recycling for mAb1. VCV and viability (A), glucose and lactate concentration (B), theoretical recycle rate setpoint (C), ammonia and pH profile (D), process harvest rate (E), harvest titer and debris trend (F), cumulative harvest volume (G) and cumulative process yield (H). Grey areas represent process phases where bleed recycling was performed, whereas bleed recycling was turned off during white process phases. 219

A.36 CQA trends of lab-scale 2 L perfusion settler run compared with a standard control run without bleed recycling for mAb1. Galactosylation G0 (A), galactosylation G1 (B), galactosylation G2 (C), high-mannose (D), fucosylation (E), a-sialylation (F), mono-sialylation (G), and di-sialylation (H). Grey areas represent process phases where bleed recycling was performed, whereas bleed recycling was turned off during white process phases. 221

A.37 Offline large-scale 2,000 L perfusion process settler evaluation for various process bleed rates and recycle rates showing VCV of inlet and recycle streams (A), separation efficiency (B), cell viabilities (C) and process yield increase (D). Inline, real-time data of flow rates of inclined gravity settler connected to the 2,000 L perfusion run (E). 223

A.38 Detailed drawing of the lab-scale inclined gravity settler, dimensions given in mm. 227

A.39 Detailed drawing of the large-scale inclined gravity settler, dimensions given in mm. 228

A.40 Experimental offline setup of Inclined Settler (IS) and acoustic separator (AS). Both bleed recycling devices are fed from a common stirred vessel (Inlet). The return pump of the acoustic separator is turned on and off synchronously with the on and off times of the ultrasound input. The outlet streams (Bleed and Return) for both devices are collected in separate vessels for further analyses 228

A.41 Detailed schematic representation of the experimental setup for the pressure characterization in water (A). Pressure transmitters (PT), flow sensors (FS), centrifugal pumps (CD) and peristaltic pumps (PP) are specified with subscripted letters according to their position (R: Retentate; F: Filtrate; A: Additional sensors on filtrate side; H: Harvest). Minimal required setups for TFF (B), rTFF (C) and HPTFF or scTFF (D) operation used for cell culture runs are further shown. . 241

A.42 Pressure characterization results for TFF, rTFF and HPTFF operation. Crossflow ramping in TFF and rTFF operation (A) and crossflow ramping with delta pressure control in HPTFF operation (B). Dashed lines represent the standard operating region of $1,470 \text{ s}^{-1}$ shear resulting in approximately 650 mL min^{-1} crossflow. Pressure measurements according to their position along the filter length are provided for TFF and the forward crossflow phase of rTFF (C), and for HPTFF (D), grey areas represent absolute fiber length. Pressure distributions at 650 mL min^{-1} crossflow versus time are shown for TFF and rTFF (E), where the forward crossflow phase corresponds to TFF operation, and rTFF is defined by alternation between forward and reverse crossflow. HPTFF pressure distribution versus time upon co-current filtrate flow activation was further measured at 650 mL min^{-1} crossflow (F). 245

- A.43 Schematic representation for TFF (A), rTFF (B) and HPTFF (C) systems with centrifugal pumps based on pressure characterization. Pressure curves along the filter length for each system are given and arrows indicate filtrate flux, longer arrows represent larger fluxes. Additionally, a zoom into a fiber at the beginning, middle and at the end of the filter is provided and colored from red (high pressure) to blue (low pressure). As rTFF consist of two phases, the situation for forward crossflow and reverse crossflow are depicted. 247
- A.44 Concept of stepping co-current TFF (scTFF) by schematic representation of pressure gradient along filter length (A). Co-current flow ramping at 650 mL min^{-1} crossflow (B). Vertical dashed lines represent operating conditions for HPTFF (black), scTFF phase 1 with -10 mbar pressure difference (blue) and scTFF phase 2 with +10 mbar pressure difference (red) on filter inlet. Pressure measurements according to their position along the filter length are provided for all three dashed lines (C), grey areas represent absolute fiber length. Operation of scTFF with two alternating phases (± 10 mbar pressure difference) is demonstrated by time resolved pressure distribution plots (D). Alternative operating mode of HPTFF with alternating membrane sweeps by scPTFF phases of ± 10 mbar in between HPTFF phases (E). Red areas represent flux of filtrate back into the retentate, blue areas represent flux from retentate to filtrate. 249
- A.45 Perfusion cell culture runs with TFF (black), rTFF (blue), HPTFF or scTFF (red) as cell retention devices. VCV and viability (A), cell diameter (B), pH (C), cell culture debris (D), harvest titer (E) and product sieving (F). 250
- A.46 Membrane sweep in HPTFF operation upon crossflow stop. Inlet pressure of the retentate (PT_{R1}) and inlet pressure on filtrate side (PT_{F1}) were recorded upon a 3 s stop of the levitated centrifugal pump (CD_{R1}) to release air bubbles (A). The delta pressure ($PT_{R1} - PT_{F1}$) was calculated and the blue area represents a negative delta pressure during which a backflush is happening in the first half of the filter, whereas the red area represents a positive delta pressure resulting in a backflush at the second half of the filter (B). 252

A.47 Large-scale pressure characterization results. Schematic representation of the experimental setup for the large-scale pressure characterization in water (A). Pressure transmitters (PT), flow sensors (FS), centrifugal pumps (CD) and peristaltic pumps (PP) are specified with subscripted letters according to their position (R: Retentate; F: Filtrate; A and AB: Additional sensors on filtrate side; H: Harvest). Picture of experimental setup (B). Large-scale crossflow ramping in TFF operation (C) and crossflow ramping with delta pressure control in HPTFF operation (D). Pressure measurements according to their position along the filter length are provided for TFF (E) and for HPTFF (F) at standard operation of $1,470 \text{ s}^{-1}$ shear, grey areas represent absolute fiber length. 253

A.48 Required co-current filtrate flow to generate HPTFF operation at respective crossflows for lab-scale filter (A) and large-scale filter (B). . 260

A.49 Pressure characterization for scTFF operation with large-scale filter. Co-current flow ramping at 14.5 L min^{-1} crossflow (A). Vertical dashed lines represent operating conditions for scTFF phase 1 (blue) and scTFF phase 2 (red). Pressure measurements according to their position along the filter length are provided for scTFF phase 1 (B) and scTFF phase 2 (C), grey areas represent absolute fiber length. Membrane sweeping could further be demonstrated upon crossflow stop keeping the co-current filtrate flow control active (D). The delta pressure ($PT_{R1} - PT_{F1}$) leads to a backflush in the first half of the filter (blue area), whereas the red area represents a positive delta pressure resulting in a backflush at the second half of the filter. 260

List of Tables

A.1	PLS models were generated for the five different sugars within the specified concentration ranges. The calibration data set consisted of 200 samples, and the test data set of 28 samples. A five-fold cross-validation was performed. LV, latent variables; R^2 , coefficients of determination calibration; R^2CV , coefficients of determination cross validation; RMSE, root mean square error; RMSECV, root mean square error cross validation; RMSEP, root mean square error prediction; R^2P , coefficients of determination prediction.	112
A.2	Perfusion harvest composition for model calibration. Overview of nutrient compositions, metabolite concentrations, and cell parameters of the five runs (harvest library) used for Raman model calibration and of 12 reference runs. Ranges from the harvest library, mean and SD represent inter-process statistics for the respective data origin. SD, standard deviation; VCD, viable cell density.	114
A.3	Modeling results for final glucose and raffinose models. Models based on calibration sets CS1, CS2, and CS3 for glucose (G) and raffinose (R) were evaluated on their prediction performance in the verification run. Spectra with aligned reference analytics for glucose and raffinose served as a prediction set. RMSEP versus LVs plots for all models can be found in the Supporting Information section (Supporting Information Figure A.11). LV, latent variables; R^2 , coefficients of determination calibration; R^2CV , coefficients of determination cross validation; RMSE, root mean square error; RMSECV, root mean square error cross validation; RMSEP, root mean square error prediction; R^2P , coefficients of determination prediction. ^a 3 LVs were used for the sake of comparison. RMSEP as a function of LVs are provided in the Supporting Information (Figure A.11).	114

A.4	Modeling results of leave-one-out validation for glucose and raffinose. Based on calibration set CS3, glucose and raffinose models were built by leaving out data from a specific run, which was then used as prediction set. The removed data was used as a test set. All-R1 means that data from all runs except Run 1 are included to build the model, and the data from Run 1 was used as a test set in this particular case. For the models names “All”, all data from all five runs was included and an independent test set of the validation run was used.	124
A.5	PLS models were generated for lactate, glucose, pyruvate and ammonium within the specified concentration ranges. The calibration data set consisted of 286 spiked samples and 71 in-process samples, the spike validation (Figure A.12) served as test set. 5-fold cross-validation was performed.	137
A.6	Spiked compounds as well as stock solution, effectively increase of compound concentration in bioreactor (spike addition) and added spike volume. Spike solutions were prepared in perfusion harvest. . .	138
A.7	Process stabilization metrics for control runs and Raman controlled perfusion runs. Minimal and maximal fraction of glycoforms (Min, Max), the difference of lowest and highest measured fraction of glycoforms during the same perfusion run (Delta), Mean and standard deviation (SD) are provided for the respective glycoforms.	149
A.8	Process stabilization metrics for control runs and Raman controlled perfusion runs. Minimal and maximal fraction of glycoforms (min, max), the difference of lowest and highest measured fraction of glycoforms during the same perfusion run (Delta), mean and standard deviation (SD) are provided for the respective glycoforms.	157
A.9	Description of cell lines, products and glycosylation sites.	169
A.10	Experimental conditions for polyether ionophore compound screening.	170
A.11	Experimental conditions for maduramycin vs. kifunensine comparison in ambr15 fed-batch processes.	173
A.12	Overview of 2L steady-state STR perfusion cell culture media compositions.	174
A.13	Cell culture parameters for combined utilization of maduramycin and kifunensine in ST bioreactors.	193
A.14	Response surface model equations for the HM fine-tuning experimental data of cell line D in semi-continuous ST bioreactors.	193

A.15 Separator and settler specifications used to concentrate the bleed stream. *Residence time was calculated using inlet flow rates of 0.5 L day⁻¹ for lab-scale operation and 500 L day⁻¹ for large-scale operation. 208

A.16 Absolute CQA changes for offline large-scale settler evaluation. Absolute CQA changes were calculated by subtracting the recycle CQA from the inlet CQA. The tested mAb2 contained 3 different glycosylation sites, which were all analyzed for their glycosylation changes. . 229

A.17 Absolute CQA changes for inline large-scale settler evaluation. Absolute CQA changes for mAb1 were calculated by subtracting the recycle CQA from the inlet CQA. 229

Abbreviations

ADC	Antibody drug conjugate
ADCC	Antibody-dependent cell-mediated cytotoxicity
AEX	Anion exchange chromatography
AIDS	Acquired immune deficiency syndrome
ALL	Acute lymphoblastic leukemia
AML	Acute myeloid leukemia
AS	Acoustic settler
ATF	Alternating tangential flow filtration
BiTEs	Bispecific T-cell engagers
BLA	Biologics license application
bsAb	Bispecific antibodies
CD	Centrifugal discharge
CDC	Complement-dependent cytotoxicity
cDSP	Continuous downstream processing
CEX	Cation exchange chromatography
C _H	Constant domain of heavy chain
CHO Cells	Chinese hamster ovary cells
CIP	Cleaning in place
C _L	Constant domain of light chain
CMC	Chemistry, manufacturing, and control
COGs	Cost of goods
CPP	Critical process parameter
CQA	Critical quality attribute
CRISPR	Clustered regularly interspaced short palindromic repeats
CSPR	Cell-specific perfusion rate
DNA	Deoxyribonucleic acid
DO	Dissolved oxygen
DoE	Design of experiment

DS	Drug substance
DSP	Downstream processing
ER	Endoplasmic reticulum
ERAD	ER-associated degradation pathway
Fc	Crystallizable fragment
FDA	U.S. food and drug administration
FS	Flow sensor
FUT8	Fucosyl transferase gene 8
GA	Golgi apparatus
GA1-2	Glucose addition 1-2
Glc	Glucose
GlcNAc	N-acetylglucosamine
GS	Gravity settler
hcDNA	Host-cell DNA
HCP	Host cell protein
HL	Harvest library
HM	High mannose
HPTFF	High-Performance TFF
Ig	Immunoglobulin
M5-M9	High mannose-type N-glycans 5 to 9
mAb	Monoclonal antibody
Man	Mannose
MIR	Mid-infrared
NIR	Near-infrared
NSD	Nucleotide sugar donor
OKT3	Murine mAb muromonab-CD3
OST	Oligosaccharyltransferase
PAT	Process analytical technology
PCC	Periodic counter current chromatography
PLS	Partial least squares
PP	Peristaltic pump
PT	Pressure transmitter
PTM	Posttranslational modification
QbD	Quality by design
QTPP	Quality target product profile
RA1-2	Raffinose addition 1-2
RMSECV	Root mean square error of cross-validation

RMSEP	Root mean square error of prediction
RNA	Ribonucleic acid
rTFF	Reverse TFF
RTRT	Real-time release testing
scFv	Single-chain variable fragments
scTFF	Stepping-co-current TFF
SIP	Sterilization in place
SMB	Simulated moving bed chromatography
SUT	Single-use technology
TALEN	Transcription activator like effector nuclease
TFF	Tangential flow filtration
TMP	Transmembrane pressure
TNFR	Tumor necrosis factor receptor
UF/DF	Ultrafiltration and diafiltration
USP	Upstream processing
VCV	Viable cell volume
V _H	Variable domain of heavy chain
VI	Viral inactivation
V _L	Variable domain of light chain
ZFN	Zinc finger nuclease

1 Introduction

1.1 Background on biopharmaceutical manufacturing

The field of biopharmaceutical manufacturing began its journey with the identification of several macromolecular molecules with promising characteristics to treat diseases. As such, insulin was found to effectively treat diabetes in 1921 and was extracted from the pancreas of pork [1]. Similarly, other macromolecules such as Factor VIII, a vital blood clotting protein to treat hemophilia A, were obtained from human blood plasma. However, these extraction methods from animal or human sources had their limitations and were bearing risk for patients. Non-human derived products often resulted in severe immunologic responses, whereas human-derived products were prone to transmit other diseases such as acquired immune deficiency syndrome (AIDS) from donor to patient [2].

The advent of genetic engineering in the 1970s revolutionized biopharmaceutical manufacturing and allowed to insert genetic sequences into bacteria or other cell lines coding for the product of interest. Many biopharmaceuticals no longer had to be extracted from animal or human sources but could instead be recombinantly manufactured in a much safer and better controlled bioreactor environment. Recombinant insulin was the first approved recombinant protein by the U.S. Food and Drug Administration (FDA) in 1982 and produced in bacteria [3], whereas factor VIII due to its complex post-translational modification was produced in CHO cells, which was approved in 1992 [2].

Parallel to these developments, the first monoclonal antibody (mAb) was created using hybridoma technology in 1975 [4]. In 1986, the first murine mAb muromonab-CD3 (OKT3) to prevent transplant rejection was approved. Monoclonal antibodies have since experienced unprecedented success in treating cancer, auto immune and inflammatory diseases and infectious diseases [5]. With over 162 approved therapies worldwide and an ever-increasing demand, mAbs constitute the largest and fastest

growing class of biologics [6–8]. At the same time, more complex protein formats such as antibody-drug conjugates (ADCs), bispecific antibodies or fusion proteins are being developed with the aim to achieve advanced therapeutic applications [9]. As the biologics landscape undergoes rapid evolution, manufacturing complexity is on the rise, necessitating a shift from the relatively standard monoclonal antibody (mAb) platform processes that have been extensively developed over the past decades to more advanced manufacturing strategies [10]. Advancements in biomanufacturing that offer enhanced flexibility and intensified manufacturing capabilities are therefore crucial to address the demands of these complex protein formats.

1.2 Monoclonal antibodies and advanced antibody therapeutics

Antibodies, complex glycoproteins of the adaptive immune system, are generated by B-lymphocytes within the human body and provide a fast yet effective response to foreign immunogens [11, 12]. The structure of an antibody, also immunoglobulins (Ig), is composed of four polypeptide chains – two identical heavy chains (γ , α , μ , δ or ϵ isotype, 50 – 77 kDa) and two identical light chains (κ or λ isotype, 25 kDa) covalently bound by disulfide bridges at conserved cysteine residues. The heavy chains of the Ig are composed of one variable domain (V_H) and three to four constant domains (C_{H1-4}). Variability in the constant region of the heavy chain determines the isotype of the antibody (IgG, IgA, IgM, IgD, and IgE), graphically illustrated in Figure 1.1. The light chains consist of one variable domain (V_L) and one constant domain (C_L). Antibody specificity is generated by the Fab region, the composition of the entire light chain and the V_H combined with the adjacent constant domain of the heavy chain (C_{H1}), located at both tips of the Y-shaped molecule. The remaining heavy chain domains build the crystallizable fragment (Fc domain), enabling cell-mediated immune responses, such as antibody-dependent cellular cytotoxicity (ADCC), as well as complement-based immune responses, notably complement-dependent cytotoxicity (CDC). Additionally, the Fc domain plays a significant role in promoting phagocytosis and the clearance of pathogens [13–15]. Glycosylation, both O-linked and N-linked, contribute to roughly 3% of the molecular weight of the IgG isotype, but can increase up to 14% for highly glycosylated isotypes such as IgM, IgE and IgD and is mainly located in the constant domains of the heavy chain [11].

Even though five different Ig isotypes exist, marketed antibody products mainly represent the IgG isotype for multiple reasons. Firstly, IgG isotypes are with around

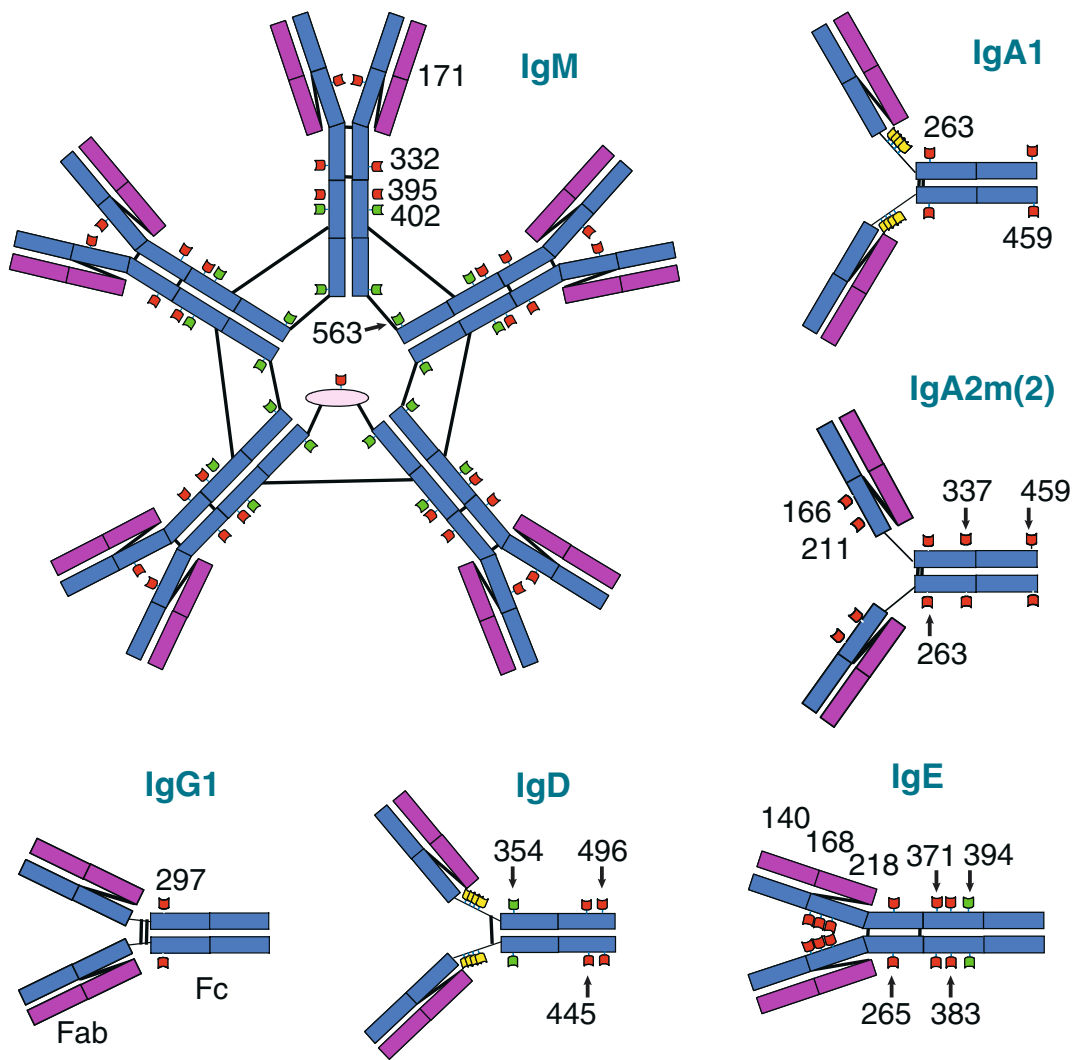


Figure 1.1: Schematic representation of different Ig isotypes, with heavy chain (blue) and light chain (purple). N-glycosylation sites are shown with complex (red) and oligomannose (green). O-glycosylation is represented as yellow. Disulfide bridges are represented by black lines. Figure reprinted from literature [11].

80% the most abundant isotype in human blood serum, reflecting their importance in the immune system [14, 15]. Secondly, they both efficiently trigger ADCC and CDC, being pivotal for the potency and therapeutic success of these antibodies as drug candidates. Moreover, IgG exhibit a notably extended serum half-life, prolonging their presence and efficacy within the patient and thereby allowing for less frequent dosing while maintaining robust therapeutic efficacy, which enhances patient compliance and treatment outcomes [15]. To guarantee a high degree of specificity in biotherapeutics, commercially available antibodies are produced as monoclonal antibodies (mAb). Unlike human serum with a diverse mixture of antibodies, mAb products were produced using a monoclonal manufacturing cell line ensuring the

presence of only one particular type of antibody [16, 17]. The majority of mAbs have a conserved N-glycosylation site (Asn297) in the Fc-domain which is critical for molecular stability, effector function and pharmacokinetics.

Despite the tremendous success story of mAbs over recent decades, the biopharmaceutical landscape is evolving to get more diverse [18]. An increasing number of complex therapeutic formats do not only make their way into clinical trials, but also achieve regulatory approval [19–22]. Advanced genetic engineering approaches paired with better understanding of protein structures, intercellular signaling mechanisms, and disease pathophysiology have enabled the combination of various proteins, protein domains or even small molecules to achieve multi-specific molecules with more sophisticated effector functions [9, 23–25]. As such, the first fusion protein etanercept composed of two proteins subunits with different effector functions was approved in 1998. This dimeric fusion protein consists of a tumor necrosis factor receptor (TNFR) and a Fc domain of an IgG to prolong serum half-life, designed to capture and neutralize tumor necrosis factor (TNF) molecules, which plays a crucial role in driving inflammation in several auto-immune diseases [26, 27]. ADCs are another entity consisting of three main components – an mAb to target specific antigens present on cancer cells, a cytotoxic drug to kill targeted cells, and a linker responsible for release and thereby activating the cytotoxic drug upon entry into the target cell. Gemtuzumab ozogamicin was the first approved ADC in 2000 to treat acute myeloid leukemia (AML) consisting of a mAb targeting the AML cells by the CD33 antigen and the cytotoxic drug component calicheamicin being released upon entering AML cells to exhibit its cytotoxic effect. Compared to traditional chemotherapy indiscriminately targeting all rapidly dividing cells within the patient’s body, ADCs offer targeted therapeutic approach and thereby reduce the side effects significantly [20, 28, 29]. A third way to generate multi-specific biotherapeutics are bispecific antibodies (bsAb). Bispecific antibodies are engineered to have two different antigen-binding sites, yet various designs of bispecific antibodies exist. Some retain the basic Y shape but have different variable regions at each of the two tips and feature a common Fc domain to retain Fc related effector functions whilst increasing serum half-life. Alternatively, formats with identical antigen binding sites at the tips exist but introduce an additional antigen binding site at the Fc domain. Other bsAb designs include single-chain variable fragments (scFv) designs, bispecific T-cell engagers (BiTEs) and dual-affinity retargeting (DART) molecules [9, 19, 25]. Blinatumomab notably was the first approved bsAb by the FDA in 2014 and belongs to the T-cell engagers (BiTE) to treat acute lymphoblastic leukemia (ALL) [21, 30]. The vast variety of bsAbs designs reflect the immense flexibility and

adaptability in targeting diverse diseases through recombination protein domains. Depending on the type and structure of these multi-specific molecules, several glycosylation sites can be present on the molecule. Additional challenges can therefore occur during the manufacturing process to ensure consistent product quality of these more sophisticated molecules.

1.3 Regulatory framework for commercialization of biotherapeutics

Commercialization of a biopharmaceutical drug involves several key steps that are well defined by regulatory organs to ensure an effective, safe, and high-quality product for patients. Assuming a drug candidate has successfully passed development, pre-clinical and clinical trials, the next step is compiling all data into the Biologics License Application (BLA). The BLA is a submission that a company makes to the regulators such as the FDA to seek approval to market a biological product. It contains extensive data from pre-clinical and clinical trials demonstrating the safety and efficacy of the drug candidate, detailed information about the product chemistry, manufacturing process and control (CMC), but also labeling and packaging suggestions and information about manufacturing facilities.

The CMC is one of the most critical sections in a BLA and gives regulators the information to assess whether a company is capable of consistently producing a high-quality biotherapeutic. Manufacturing information, such as description of all process steps, equipment used, raw materials, and PAT, but also control strategies including process controls, finished product controls or stability controls must be defined. Additionally, the chemistry section providing detailed information about the chemical composition, properties and structure of the drug candidate must be described.

Whereas in the traditional reactive model, end product testing to assess if all CQAs fulfill the requirements was the norm, the FDA launched an initiative to facilitate the manufacturing process of pharmaceuticals in 2002. This led to the concept of QbD to encourage a more systematic and science-based risk assessment approach to pharmaceutical development described in the International Conference on Harmonization guidelines (ICH) Q8 – 11 [31–34], later described in detail in ICH Q8(R2) [35]. Overall, the QbD approach attempts to engineer product quality into the manufacturing process to obtain a more proactive process potentially reducing or even avoiding end product testing. The first step in the QbD approach consists in defining a quality target product profile (QTPP) and CQAs of the product. As

such, CQAs, product quality attributes that have an impact on clinical efficacy and patient safety, must be identified. Subsequently, statistical methods such as Design of Experiment are essential tools in the QbD workflow to establish the relationship between CPPs and CQAs. Understanding the relationship between CPPs and CQAs enables the definition of a so-called design space, a multidimensional area of operating conditions of CPPs, where the CQAs are highly likely to fall within the predefined acceptable ranges, as long as the process was operated correctly within the design space [35].

1.4 Critical quality attributes of biotherapeutic proteins

Quality attributes of biotherapeutic drugs manufactured in mammalian expression systems can in general be subdivided into three categories: Contaminants, process-related impurities and product-related impurities [36].

1.4.1 Contaminants

Living organisms such as bacteria, fungi, mycoplasma or viruses including their potential byproducts, such as endotoxins, classify as contaminants. Equipment damage, contamination originating from raw materials or aseptic operating conditions can be reasons for their presence in the drug product and pose serious safety concerns for patients such as inflammation or sepsis [37]. Additionally, care should be taken to sufficiently remove endogenous retroviruses from the manufacturing cell line during purification activities [38–40].

1.4.2 Process-related impurities

Impurities coming from the raw material or from the manufacturing cell line such as host-cell DNA (HCDNA) or host cell proteins (HCP) that are secreted or released upon cell death are labelled process-related impurities. Even though HCDNA poses potential risk of oncogenic material being transferred to the patient, injections of highly dosed injections into primates did not cause any tumors [41]. HCPs from non-human manufacturing cell lines are expected to be detected by the immune system and cause side effects. These side effects were more frequently observed during earlier studies with relatively impure drug products [42, 43]. Today's efforts to optimize purification processes to minimize not only the presence of HCPs but also HCDNA has largely alleviated these safety concerns with mammalian expression

systems [43]. Raw material related impurities can either stem from media components, purification buffers as well as excipient for drug product formulation, or being released from manufacturing equipment such as leachables of single use components, chromatography resins, filtration membranes or other process equipment in contact with the drug substance or product. A thorough risk assessment is crucial to evaluate the potential impact of these impurities on patient safety [36].

1.4.3 Product-related impurities

Proteins, as macromolecules, are known to undergo a wide spectrum of posttranslational modifications (PTMs), some of which can induce undesirable side effects in patients. Not only can PTMs intentionally be added to proteins by the host cell line's complex protein processing machinery, they can also alter during the manufacturing process or storage due to chemical or physical influences. These PTMs can alter protein structure and function, leading to therapeutic proteins that may not perform as expected or might cause adverse reactions. Despite the myriad of possible PTMs, only a restricted subset has been linked with recombinant biotherapeutics [36].

Deamidation and oxidation products: Whereas asparagine and glutamine are mainly susceptible to deamination, methionine and tryptophan and common residues known for oxidation reactions [44–47]. In both cases, the amino acids properties are altered impacting protein stability, loss of function and can trigger potential immunogenic reactors [36, 48].

Glycation: The posttranslational chemical addition of a reducing monosaccharide to lysine residues such as glucose, fructose or galactose is called glycation and mainly happens in the cell culture due to the presence of glucose in the media [49]. Although glycan was reported not to appear substantially affecting mAb activity, loss of activity was reported in some cases and keeping the glycation level close to human plasma protein levels is advisable [50, 51].

C- and N-terminal modifications: C-terminal lysine cleavage, C-terminal carboxylamidation or N-terminal glutamate cyclization are frequently observed modifications of mAbs and also found in the native proteins [45, 52, 53]. Negligible impact on biological activity and no adverse effects regarding drug safety or efficiency are reported so far [36, 54].

Disulfide bond modifications: The mAb structure heavily depends on disulfide bonding between cysteine residues of the HC and LC. Dissociation, incorrect pairing between cysteine residues, or even trisulfide bonds can therefore heavily impact the protein structure and function [45, 55]. Similarly, unbound cysteine residues

(free thiols) can result in reduced potency, even though they are rather uncommon in mAbs [56].

Charge variants: A change in the overall charge of the protein can result in different charge variants as a consequence of various PTMs such as deamidation, oxidation, glycosylation, and other previously mentioned PTMs. These charge variants have gained considerable attention due to their ability to influence protein stability and biological activity [57, 58].

Glycosylation: Glycosylation consists of covalently attached glycan moieties to the protein which can significantly influence their solubility, stability, and biological function. With almost 70% of all human proteins being glycosylated, glycosylation is one of the most common PTMs in proteins [59]. Due to the significant impact of glycosylation on product stability, pharmacokinetics, but also effector functions such as ADCC or CDC, glycosylation has become one of the most vital CQA for the biopharmaceutical industry [60–62]. Hence, a comprehensive understanding of the glycosylation machinery and the development of efficient tools to control glycosylation during manufacturing processes remains a significant focus of ongoing research. Although various types of glycosylation exist, O-glycosylation and N-glycosylation are the most common ones also represented in antibodies [63]. Whereas O-glycosylation involves the attachment of a sugar moiety to the oxygen atom of serin or threonine without the requirement of a consensus sequence, N-glycosylation happens at a asparagine residue within a well-defined consensus sequence (Asn-X-Ser/Thr) [64, 65]. N-glycosylation is more common than O-glycosylation and the sugar moieties tend to be larger and more heterogeneous and described in more detail in section 1.5.

Next to PTMs, aggregation of proteins or fragmentation represent further CQAs that can impact effector functions. **Aggregation:** Protein aggregation is defined as the process whereby a minimum of two proteins associate to form dimers, with the potential to escalate into the formation of visibly detectable particulates comprised of a multitude of proteins. The factors that contribute to protein aggregation are multifaceted and include temperature, pH, protein concentration, ionic strength, as well as the type of buffer in the formulation. Physical stresses such as stirring, shaking, freezing, thawing, shearing, and interactions at surfaces can also initiate aggregation [66]. Aggregates have been associated with impaired biological activity and efficacy, but also with provoking immune responses [67–69].

Fragmentation: Enzymatic cleavage or chemical disruption of the peptide bond can result in fragmentation of the biotherapeutic with the effect of reduced or completely lost efficacy, reduced serum half-life and potential immunogenicity issues [70].

Enzymatic cleavage can be caused by proteases present in the cell culture process or drug product or by chemical disruption mainly described for solvent-exposed amino acid side chains under acidic or basic conditions and should be avoided by proper formulation and storage conditions [71–74].

1.5 N-glycosylation of therapeutic proteins

IgGs, and therefore also most marketed mAbs - if not engineered otherwise - are N-glycosylated at a conserved asparagine residue (Asn297) in the C_{H2} domain of the Fc region. Additionally, about 15 – 20% of the IgGs contain a second N-glycosylation site Fab region [36]. More complex biotherapeutic formats such as fusion proteins, ADCs and bsAb also often contain glycosylation sites, but their number and location can vary widely depending on their construct. For fusion proteins, the presence of glycosylation sites depends on the different proteins being fused, but also on accessibility of these sites within the fusion protein. ADCs mostly retain their glycosylation site as they are usually based on an IgG antibody with inherent glycosylation sites. BsAb when still containing the Fc domain can retain the glycosylation site but constructs with either no or additional glycosylation sites are no exception.

1.5.1 N-glycosylation machinery

N-glycosylation is a complex process involving hundreds of enzymes and is initiated on the cytosolic face of the endoplasmic reticulum (ER) of the eukaryotic expression cell. An oligosaccharide precursor bound to a membrane linked dolichol phosphate anchor is synthesized consisting of 14 carbohydrate residues ($\text{Glc}_3\text{Man}_9\text{GlcNAc}_2$): two N-acetylglucosamine (GlcNAc), nine mannose (Man) and three glucose (Glc) units. During the assembly, the dolichol-oligosaccharide precursor is translocated to the lumen side of the ER where it is subsequently transferred to the asparagine in the consensus sequence catalysed by an oligosaccharyltransferase (OST) [75, 76]. The oligosaccharide undergoes a series of modifications as it passes through the secretory pathway (ER and cis-Golgi). This includes trimming by glycosidases and mannosidases resulting in range of high mannose-type N-glycans (HM), reaching from HM glycans with 9 mannose residues (M9) to mostly 5 mannose residues (M5). Glycosylase trimming removing the three Glucose residues constitutes a key regulatory mechanism for correct protein folding and subsequent transfer to the Golgi Apparatus (GA) for further trimming, or, if incorrectly folded degradation initiation by the ubiquitin-proteasome referred as ER-associated degradation pathway (ERAD) [77,

78]. Enzymes in the medial Golgi can further modify the HM glycan structure, leading to the formation of complex glycans, followed by further branching and capping reactions in the trans-golgi and trans-golgi network [79, 80], summarized in Figure 1.2. The addition of sugar by glycosyltransferases and the cleavage by glycosidases is a complex process which is highly influenced by the cellular environment, availability of specific enzymes within cells and varying processing times in the GA, ultimately resulting in a heterogeneous mixture of complex-, hybrid- and HM-type N-glycans [81–83].

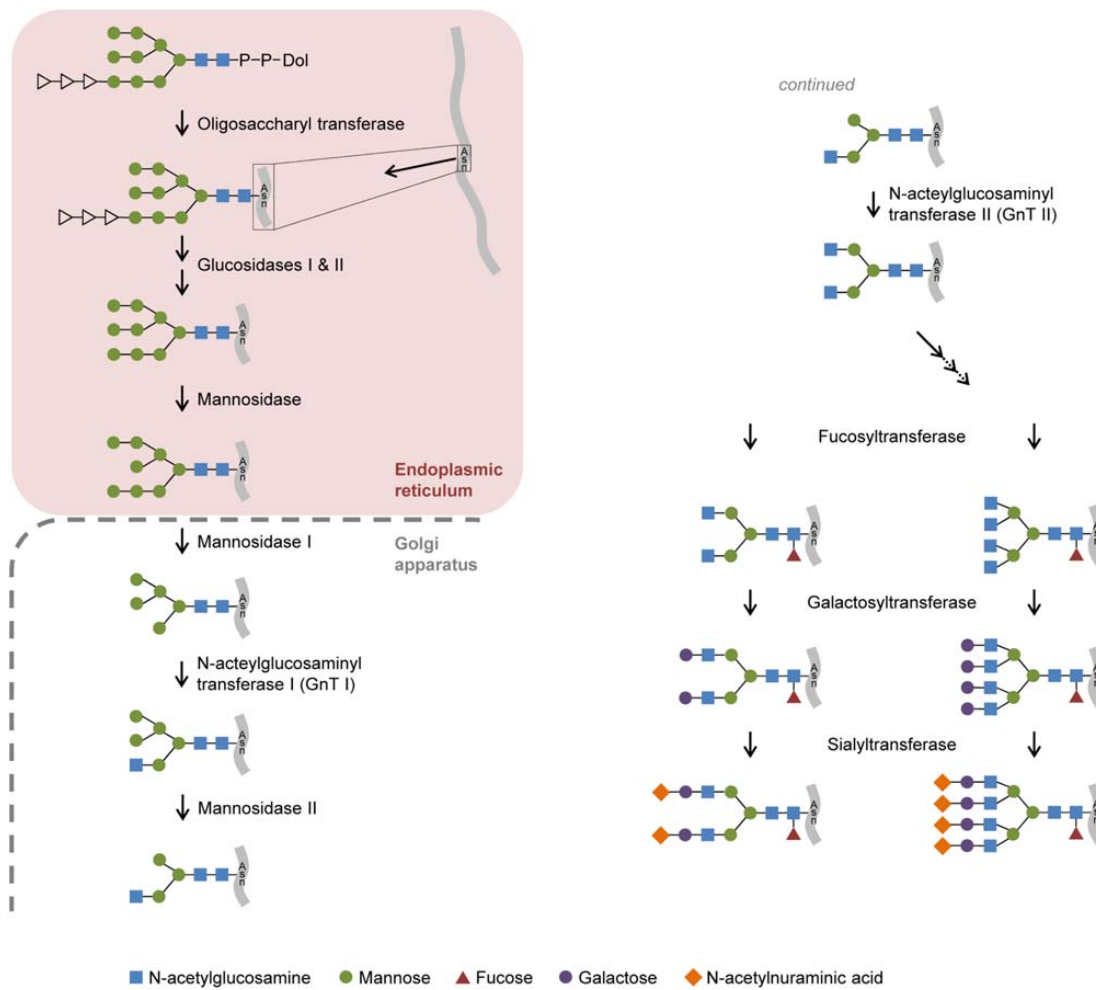


Figure 1.2: Schematic N-glycosylation pathway in the ER and GA reprinted from the literature [79].

1.5.2 Different types of N-glycosylation and their impact on product characteristics

Complex glycan forms of mAbs are based on a $\text{GlcNAc}_2\text{Man}_3$ base structure with additional sugars attached to both branches, such as N-acetylglucosamine, galactose,

fructose and sialic acid. Compared to HM or hybrid glycoforms, complex glycans undergo more extensive processing and are typically found in proteins that have transited through both the ER and GA.

Fucosylation: Core fucosylation of mAbs has been demonstrated to significantly impact biological activity of the biotherapeutic. Whereas recombinantly produced mAbs, similar to their native counterparts in human serum, consist of predominantly biantennary fucosylated glycosylation species, reduced core-fucosylation of IgGs was reported to enhance ADCC activity without changing CDC activity [84–88]. Accordingly, increasing the afucosylated glycan species in a biotherapeutic represents an interesting target for engineering strategies to increase ADCC activity of mAbs [85, 89, 90].

Galactosylation: It is common to observe that over 50% of the glycan species in a monoclonal antibody consist of terminal galactose [45]. Despite increased binding to the Fc γ RIII receptor, no major increase in ADCC is reported for increasing terminal Galactosylation in mAb products [84, 91, 92]. The effect of galactosylation on CDC activity appears to be unique to each antibody, with various studies reporting both increases and decreases in CDC activity due to galactosylation [93, 94]. No change in pharmacokinetics was observed for variable terminal galactosylation [92, 94, 95].

Sialylation: Sialic acid constitutes the final sugar in N-glycosylation with an abundance of about 10% in human serum mAbs, however, much lower levels are usually present in recombinantly produced mAbs [85]. Either decreased or similar ADCC activity was reported for sialylated antibodies compared to the asialylated form [96–98]. Whereas most studies reported no change in serum half-life with increasing sialylation, others demonstrated increased serum half-life at elevated sialic acid levels [92, 96, 99, 100].

Bisecting N-acetylglucosamine: Compared to the standard core structure of two N-acetylglucosamine branches, a third one can be attached to the core mannose via a β (1-4) glycosidic bond. This bisecting N-acetylglucosamine creates a third branch and is present in human serum mAbs with about 9 – 15%. In contrast, bisecting N-acetylglucosamine is not commonly observed in recombinantly produced mAbs with common mammalian expression systems such as CHO cells [101, 102]. Due to their presence in human serum mAbs they are not considered to cause immunogenic reactions [103].

Hybrid glycans: While HM glycans are solely composed of core N-acetylglucosamine and terminal mannose sugar residues, complex glycans are fully branched structures with two antennae composed of various additional sugar types. On the other hand,

hybrid glycoforms represent an intermediate structure where one antenna mirrors that of complex glycans, while the second antenna retains terminal mannose residues characteristic of HM glycans. Despite lower CDC, no difference in ADCC activity and serum half-life was observed compared to complex glycoforms [82, 103]. Their abundance is rather low with up to 2% in human serum mAbs and is negligible in recombinantly produced therapeutic products [36, 101].

HM glycoforms: Premature termination of the glycosylation process can result in incomplete glycoforms consisting solely of core N-acetylglucosamine and five to nine terminal mannose residues. These HM glycan species are almost inexistant in endogenous IgGs but can be significantly higher in marketed antibody therapeutics where they can constitute as much as 10% of the total glycan fraction [101, 104]. HM glycans are of particular importance given their impact on pharmacokinetics and effector function. In general, higher ADCC [82, 105–108], reduced CDC [82, 109], and reduced serum half-time are reported for HM-type mAbs [50, 107, 110, 111]. Increased ADCC is however thought to be a secondary effect related to the concomitantly reduced core fucosylation, rather than being a direct consequence of the increased HM glycan fraction [85].

1.6 Levers to modulate N-glycosylation of bio-therapeutics in mammalian cell culture

Strategies to ensure high-quality biotherapeutic production involve the choice of a proper host cell line, but also cell line engineering, careful selection of media composition and optimization of process conditions can be crucial when targeting a specific set of CQAs in a biotherapeutic product [79, 112]. Considering the high importance of N-glycosylation as CQA in biotherapeutics and its particular relevance for this Thesis, the following parts will primarily focus on the aspects related to N-glycosylation.

1.6.1 Selection of the host cell line and cell line engineering

The selection of the host cell line is a crucial decision with a strong influence on product quality attributes, given that each cell line possesses a cell line specific glycosylation fingerprint. CHO cell lines are by far the most dominantly used cell line in biotherapeutic production due to their human-like, non-immunogenic glycosylation [18, 112, 113]. While other cell lines, such as NS0 and Sp2/0 likewise, produce human-like glycosylation, their use in manufacturing is less frequent. This

is primarily due to the presence of immunogenic epitopes such as the Gal α (1–3)Gal epitope and high contents of NeuGc sialic acid, constituting risks for product safety if not properly controlled [114, 115].

The access to genomic sequences in combination with genome editing tools such as zinc finger nucleases (ZFNs), transcription activator like effector nucleases (TALENs) and clustered regularly interspaced short palindromic repeats (CRISPR) systems has enabled cell line engineering at an unprecedented precision. Knock down, knock out and over expression of glycosylation enzymes or nucleotide sugar donor transporters are common strategies to alter glycosylation patterns [115–118]. The primary focus of mAb glycoengineering has so far relied on increasing afucosylation with the potential to increase ADCC up to 100-fold. This was either tackled by gene knock-out of the fucosyl transferase gene (FUT8) or by genetic inactivation of FUT8 by RNA interference [89, 90, 119–121]. Other engineering approaches aiming to increase serum half-life and improve anti-inflammatory properties of mAbs targeted enhanced protein sialylation. Overexpression of sialyl transferases (ST3- and ST6GALTs) or increased precursor availability by boosting CMP-NeuAc synthesis and transport to the GA represent interesting genetic engineering targets [122, 123]. More recently, protein backbone engineering in combination with cell line engineering has gained attention. Protein backbone engineering alters the accessibility of the glycosylation site by glycan remodelling enzymes and thereby generates some control or limitations on the glycosylation profile [124–126]. Further backbone modifications include removal or addition of glycosylation sites and the formation of fusion constructs or scaffolds for multimerization. Despite achievements in the field of cell line engineering, the process of getting an approved new cell line remains challenging, expensive and not always successful [127].

1.6.2 Media components and supplements with their impact on N-glycosylation

Since the introduction of the first cell culture media with the necessity to supplement bovine serum, or later hydrolysates, both with significant batch-to-batch variability, the industry has been moving towards completely chemically defined culture media [112, 128]. Better control of media components and reduced batch-to-batch variability had also significant impact on more consistent product quality. Ever since, knowledge about the relationship between certain media components and resulting product quality attributes has been collected and summarized in many reviews [79, 112, 127]. It must be mentioned that results are often ambiguous and depend heav-

ily on the different cell lines, processes but also product characteristics, rendering thorough case-by-case process characterization absolute indispensable.

As such, media component concentration, such as glucose or amino acids, have shown impact on the glycosylation profile. While glucose deprivation through a secondary effect of reduced oligosaccharide precursors led to a higher fraction of non-glycosylated proteins [129, 130], fine-tuning amino acids compositions can largely affect ammonium concentrations as ammonium is a byproduct of anaplerotic reactions to replenish the tricarboxylic acid (TCA) cycle [131–134]. Ammonium in turn is well known to interfere with the glycosylation machinery by altering nucleotide sugar synthesis and transport [135–137], changing protein expression [138], misslocalizing glycosyltransferases or changing pH in the Golgi apparatus impacting enzymatic activity [139, 140], consequently shifting glycosylation to less complex glycoforms. Media supplementation with TCA cycle intermediates or precursors such as lactate or pyruvate have effectively reduced ammonia with a beneficial effect on product quality [141, 142]. Especially the addition of pyruvate to the cell culture reduced HM species, expanding the very limited levers for HM reduction [143].

Nucleotide and monosaccharide supplementation have been reported to increase the level of nucleotide activated sugars, representing important precursors in the N-glycosylation pathway [144]. The addition of pyrimidine nucleosides, glucosamine [145], N-acetylmannosamine [146], galactose [147–149], mannose [150, 151], fucose [151], and fructose [149, 151] has consequently led to more processed glycan patterns. The trisaccharide raffinose on the other hand increased HM species when supplemented to the cell culture media [152].

Cofactors for glycosylation remodelling enzymes are another critical media component highly affecting product glycosylation. Manganese, a cofactor of involved enzymes, has been demonstrated to influence various glycoforms, such as high mannose, galactosylation, fucosylation and sialylation [147, 153]. In general, the presence of manganese led to a shift towards more complex glycoforms, with the most pronounced effects observed in combination with additional supplements to ensure sufficient oligosaccharide precursors [154, 155]. Even though also calcium, iron copper and other divalent ions are relevant enzymatic cofactors in cell culture media, their roles are less well understood [127, 156].

Altering enzymatic activity of glycosylation remodelling enzymes by the addition specific enzyme inhibitors such as kifunensine, swainsonin or deoxymannojirimycin comprises a very effective way to change glycosylation patterns [157–159]. Kifunensine, the most popular α -mannosidase I inhibitor in the ER, has extensively been used in mammalian cell culture to drastically increase HM glycans and thereby

modulating ADCC [105, 107, 108, 158]. Whereas kifunensine and most of these inhibitors predominantly increase M8/M9 structures, M5 type glycans could be selectively increased using monensin [160]. Monensin belongs to the polyether ionophore compound family and is a sodium-hydrogen ionophore inhibiting glycan processing by increasing the pH in the Golgi. This pH change alters enzymatic activity of Golgi resident enzymes due to their dependency on pH [161, 162].

1.6.3 Process parameters influencing N-glycosylation

Advanced sensor technology has enabled to accurately monitor a large set of process parameters in real-time and realize feedback control loops to keep target setpoint throughout fermentation processes. Manipulating process parameters is a relatively cheap and fast approach to fine-tune product quality attributes compared to cell line engineering or media reformulation. This requires however thorough understanding of the relationship between CPPs and CQAs, which in most cases is highly cell line and product dependent. Design of Experiment (DoE) approaches executed in high-throughput miniature bioreactor systems are a valid tool for gaining process understanding. Despite case-by-case differences, a general overview of the most important process parameters can be given.

Temperature reductions during the manufacturing process are a widely accepted strategy to reduce cell growth, keep high viabilities and boost product titer. Nevertheless, mild hypothermia can influence product glycosylation by reduced intracellular nucleotide sugar donor (NSD) availability, reduced expression of glycosyltransferases and reduced NSD transportation activity [163, 164]. In general, a trend of less processed glycans was observed in both fed-batch but also perfusion cultivations upon temperature reduction [163, 165, 166].

Efficiency of the glycosylation machinery can be influenced by both low and high pH excursion during the manufacturing process due to the delicate pH gradients between different cellular compartments [104]. Reduced pH has been associated with enhanced galactosylation and sialylation but decreased specific productivity [167, 168], whereas others described a sialylation maximum at pH 7.0 and reduction at higher or lower pH [165]. Based on the extent of pH reduction, ER-Golgi trafficking and even disassembling of the GA can constitute reasons for reduced productivity and glycan processing [169]. Elevated pH on the other hand can perturbate the functionality of glycosyltransferases which are active in the external GA at lower pH, resulting in less processes glycosylation patterns [140, 170].

Hyperosmolality can be a result of progression bioreactor run time, extensive nutrient feeding or acid and base addition to control pH. Next to decreased cell

growth, reduced viability and lower product titer, osmolality also impacts product glycosylation [171]. Reduced galactosylation [172], decreased levels of core fucosylation [173] and increased HM glycan were observed at elevated osmolality [171, 174]. These effects might be explained by reduced activity of the glycosylation machinery due to hyperosmolality.

Dissolved oxygen (DO) is a critical process parameter and should be chosen carefully to ensure sufficient oxygen for cellular respiration in aerobic fermentation processes. DO was assigned less critical role to influence glycosylation, only marginal differences when operating at reduced or elevated DO were reported in the literature [175, 176]. Even though changes in galactosylation and sialylation were observed, these were mainly attributed to secondary effects caused by reduced mAb production rates due to oxygen limitations [177].

Cell density is a key parameter to boost process productivity and significant effort is made in order to reach as high cell densities as possible. At the same time, high cell densities can impact product quality such as N-glycosylation. Increasing HM fraction were observed with increasing cell densities, concomitantly reducing the fraction of complex glycoforms [143, 178–180]. This observation might be explained by increasing ammonia concentration at elevated cell densities, media limitations resulting in suboptimal glycan processing or altered cellular metabolism under high-density conditions. Balancing productivity and product quality remains therefore a critical task in bioprocess development.

1.7 Modern manufacturing of biotherapeutics: From batch to continuous

1.7.1 Manufacturing unit operations in upstream and downstream processing

The manufacturing of biologics can be divided into two main steps - upstream processing (USP) and the downstream processing (DSP). Unit operations related to cell culture and the expression of the recombinant protein group into the USP section, whereas purification activities and formulation to a final drug product fall into the DSP.

The main cultivation strategies applied in the USP with suspension cell lines are batch, fed-batch, chemostat or perfusion. The simplest bioreactor operation mode, the batch bioreactor, consists in growing the cells until media is depleted, and cell density starts to decline. Low maximal cell densities and productivities

achieved in the batch cultivation can be mitigated in fed-batch processes by feed additions at predefined culture times. Feeds are highly concentrated nutrient stock solutions that enable significantly higher maximal cell densities of above 30×10^6 cells mL^{-1} [10, 141], high cell viabilities and increased product titer. Despite the fresh nutrient addition, waste products of the cellular metabolism accumulate with progressing cultivation time in fed-batch as well as in batch processes and can impact culture viability as well as product quality [181]. In contrast to batch cultivations, continuous cultivations do not only benefit from continuously added fresh nutrients, at the same time waste products are removed from the cell culture resulting in much more stable cultivation environment. In a chemostat, there is a constant introduction of fresh culture medium, while an equivalent volume, including the manufacturing cells, is removed for further downstream processing. Even though maximal cell densities of around 30×10^6 cells mL^{-1} were achieved in chemostats, much higher cell densities can be achieved in perfusion mode with the integration of a cell retention device (CRD) [181, 182]. The CRD selectively retains cells within the bioreactor while only cell free harvest containing the secreted product is passed to the downstream processing. Cell densities of above 200×10^6 cells mL^{-1} were achieved in perfusion operation, demonstrating the enormous potential for recombinant protein manufacturing [181, 183, 184]. Recombinant proteins produced secreted to the liquid fraction of the cell culture have subsequently to be separated from cell material prior to chromatographic purification. This unit operation is called clarification and involves flocculation, precipitation, centrifugation and depth filtration technologies for batch and fed-batch processes [185, 186]. Perfusion cell culture with an integrated cell retention device does not require additional filtration steps prior to DSP as long as the chosen CRD meets the filtration requirements for further steps.

In general, the DSP consists of a capture step, several polishing steps, viral inactivation and a set of filtrations such as sterile filtration and crossflow filtration. The capture step is frequently an affinity chromatography, usually protein A for mAbs, with a high affinity for the product of interest. Viral inactivation (VI) is another critical unit operation to inactivate and remove potentially harmful viruses from the drug substance. Remaining impurities are then removed in a sequence of polishing steps such as anion exchange chromatography (AEX) or cation exchange chromatography (CEX). Sterile filtration steps are commonly performed between various chromatography steps to reduce the bioburden. Ultrafiltration and diafiltration (UF/DF) to concentrate the product and exchange the buffer for stable formulation prior to fill and finish operation finalize the downstream processing. The chosen purification steps and their sequence might vary depending on the molecular

properties of the molecule and the specific manufacturing process, pursue however all the same goal of a highly pure and safe final drug product free from any impurities [185, 187, 188]. As for USP, batch mode purification or continuous purification strategies exist. Whereas batch mode purification consists mainly of large multiuse chromatography columns that are considered as independent unit operations enabled by intermediate hold tanks, continuous downstream operations have greatly advanced in recent years [188]. Dual or multicolumn chromatography equipment that can be operated in several modes such as simulated moving bed (SMB) or periodic counter current (PCC) chromatography have entered the market and enable continuous harvest purification [189–191]. Additionally, process designs away from binding and elute towards flow-through operations more compatible with continuous manufacturing platforms are on the rise [192, 193].

1.7.2 State-of-the-art manufacturing of biologics and future trends

Batch processing has dominated the biopharmaceutical industries since the beginnings in the 1980s, defined as separated unit operations that are incrementally processed before being transferred to the subsequent independent unit operation. Since then, batch processing has been the prevailing processing mode in upstream as well as downstream processing. The standard manufacturing processes today for mAbs and most other recombinantly expressed proteins in mammalian expression systems consists of large fed-batch bioreactors with working volumes up to 20,000 L [183, 194]. After completed fermentation, the entire bioreactor is emptied, and culture broth is clarified for further processing in the downstream purification and formulation. Large hold tanks enable product storage and transfer in between different unit operations. This classical batch processing in biopharmaceutical manufacturing contrasts with more continuous methods used by other industries such as the chemical, petroleum food and other high-tech sectors [195, 196]. Continuous manufacturing involves the uninterrupted flow of raw materials through interconnected unit operations, yielding a constant output of the final product. Unlike batch manufacturing, continuous manufacturing tailors all unit operations for continuous processing, eliminating the need for holding or pause steps. Consequently, the shift towards more continuous processing in these industries is frequently a sign of their maturation, requiring a higher degree of process understanding, more sophisticated equipment and mature technologies for advanced process control. Therefore, continuous manufacturing is often seen as the natural progression following batch processing with

the potential to eventually replace it.

Continuous manufacturing is not particularly new to the biopharmaceutical industry. A series of different commercial molecules were launched using perfusion processes in the 1990s. The decision to produce these molecules in perfusion mode, such as recombinant follicle stimulating hormone, interferon β -1a, and factor VIII, was mainly driven by the molecular instability [183, 197]. Additionally, adherent cells attached to microcarriers changed particle properties allowing to use cell retention technologies such as spin filters, fixed bed or gravity settler to attain efficient cell retention [198, 199]. Perfusion operation for suspension cells was not ready back then, expression yields were too low, media was not competitive and technologies for cell retention and integration with seamless downstream operations was not mature enough, resulting in a lack of process reproducibility and robustness [195]. At the same time, tremendous advances in batch processing were achieved by improved expression systems, optimized media and feed formulation as well as facilitated process development through enabler technologies such as screening platforms and scale-down models [200, 201]. With titers having doubled every 5 years in batch manufacturing, the industry largely moved away from perfusion and continuous manufacturing to focus on today's fed-batch platforms with titers above 10 g L⁻¹ [10, 141, 195, 202].

Currently, the biopharmaceutical industry is facing a new set of business realities and uncertainties challenging the well-established batch manufacturing approach. Rapidly evolving product portfolios with emerging complex product classes like fusion proteins, ADCs, and bispecifics call for more flexible manufacturing capabilities and more stringent product quality control. Uncertainties related to clinical trial failure, demand variability, and overall product success are contributing to these challenging market conditions [197, 203–206]. Moreover, the entry of biosimilars into the market fosters a competitive manufacturing environment that necessitates more cost-effective manufacturing [207, 208]. An end-to-end integrated continuous manufacturing scenario in a single use facility constitutes an interesting solution to respond to the dynamic market situation for several reasons:

Economic benefits: Continuous manufacturing has well-reviewed cost advantages for clinical and commercial manufacturing scenarios [196, 198, 203, 209, 210]. Significant intensification of the volumetric bioreactor productivity allows to build much smaller manufacturing plants with similar productivity output. Cost estimations for an integrated continuous manufacturing facility with a product output of 8 tons of product per year are estimated to \$100 – 150 M [211], whereas a similarly sized fed-batch facility accounts for \$500 – 1,000 M [206]. Despite higher cost

for single use consumables in upstream processing, significant saving due to better downstream resin utilization such as protein A contribute to the reduction of cost of goods (COGs) [210–212].

Ecological benefits: The ecological impact of continuous manufacturing has been studied by numerous organizations. However, its assessment varies considerably based on the underlying assumptions and specific process characteristics. Single use technology (SUT) eliminates the need for cleaning in place (CIP) and sterilization in place (SIP), thereby decreasing both chemical and energy consumption [213–215]. While continuous processes typically consume more water than fed-batch processes, the immense potential of continuous perfusion processes for process intensification and higher process titers can considerably mitigate this ecological impact [216, 217]. In fact, when optimized, continuous manufacturing could even surpass the ecological efficiency of fed-batch processes.

Manufacturing flexibility: Single use facilities, while offering reduced capital expenditure, can be built in as little as 1 year, whereas large-scale stainless-steel facilities require 5 years or more for design and construction [211]. This acceleration in facility readiness empowers manufacturers to respond much more agile to changing market situations and can give competitive advantages. Multiproduct manufacturing scenarios given the increasing product pipelines can further better be accommodated within a single use facility as downtime due to extensive cleaning procedures can be reduced to a minimum [197]. Continuous manufacturing also decreases the cost associated with process failures by more flexible failure handling. While failures in a batch scenario result in complete batch abortion, product in continuous manufacturing collected prior and after the process excursion can meet regulatory requirements [192].

Product quality considerations: Labile proteins have traditionally benefited from continuous manufacturing as residence times in the respective unit operations are significantly shorter compared to batch processing [218]. Upstream perfusion culture aims to achieve a steady-state, a condition where all key process parameters remain constant over time, leading to a similarly time-independent product quality profile. The more complex molecular formats entering the market renew accordingly the interest in a more stable manufacturing environment, demonstrated by many case examples in the literature. As such, reduced protein clipping of fusion proteins, significantly improved and stabilized N-glycosylation profiles, and reduced impurities such as HCPs were observed by continuous manufacturing of biologics [179, 219, 220].

The biopharmaceutical industry seems matured enough to seriously challenge

batch processing by continuous manufacturing. In contrast to earlier days, technological advances support this undertaking as device manufacturers redesigned previous batch unit operations to provide integrated continuous solutions. Companies are gradually adopting the new continuous unit operations, both in upstream as well as in downstream processing. This leads to a dizzying array of reported options for integrated continuous biomanufacturing, depending on the companies' requirements, experience but also existing manufacturing facility designs. Whereas some manufacturers with existing large-scale fed-batch facilities attempt to intensify their existing fed-batch facilities by perfused N-1 bioreactors or by subsequent continuous capture chromatography to increase resin utilization [189, 221], others envision the continuous integrated manufacturing approach by building novel single use facilities with 2,000 L single use perfusion bioreactors and continuous DSP (cDSP) capabilities. While direct adoption of continuous biomanufacturing remains a significant challenge, a more feasible approach is to implement continuous unit operations in a stepwise manner and subsequently connect them once each operation is ready. Several small-scale studies have demonstrated feasibility of continuous integrated biomanufacturing [180, 190, 222, 223] and first successful pilot scale and GMP productions were reported [192, 224]. Even though real-time release, meaning the ability to release products based on in-process monitoring and analysis without the need for end product testing, would be the vision for the future, end product testing is still the norm. Defining manufacturing batches is an essential step in this process. While defining batches is relatively straightforward for fed-batch manufacturing, steady-state perfusion operations offer different possibilities to define a manufacturing batch. Depending on the downstream strategy, either stable process intermediates have been generated and pooled at the end of a manufacturing run to define a batch [192], or several lots were created from one bioreactor run, treated as individual drug substance (DS) batches for end-product testing [224]. Storing stable process intermediates at manufacturing scale can compensate for product quality drifts over time as they are pooled to one large manufacturing batch, assuming that the same drift occurs in all manufacturing batches as known for fed-batch processes [155]. This final pooling strategy can however require large storage capacities exceeding 20,000 L and requires in-process hold studies to demonstrate product stability [211]. Splitting the perfusion harvest of one long-term run into multiple DS batches offers various advantages in terms of storage capacity reduction, reduced residence time for labile proteins and flexibility with respect to the process duration and excursion handling even at manufacturing scale (Figure 1.3). In this case however, as well as for the ultimately aspired real-time release scenario, consistent

product quality is required at any time during the continuous manufacturing process and each DS batch must fulfil the quality expectations.

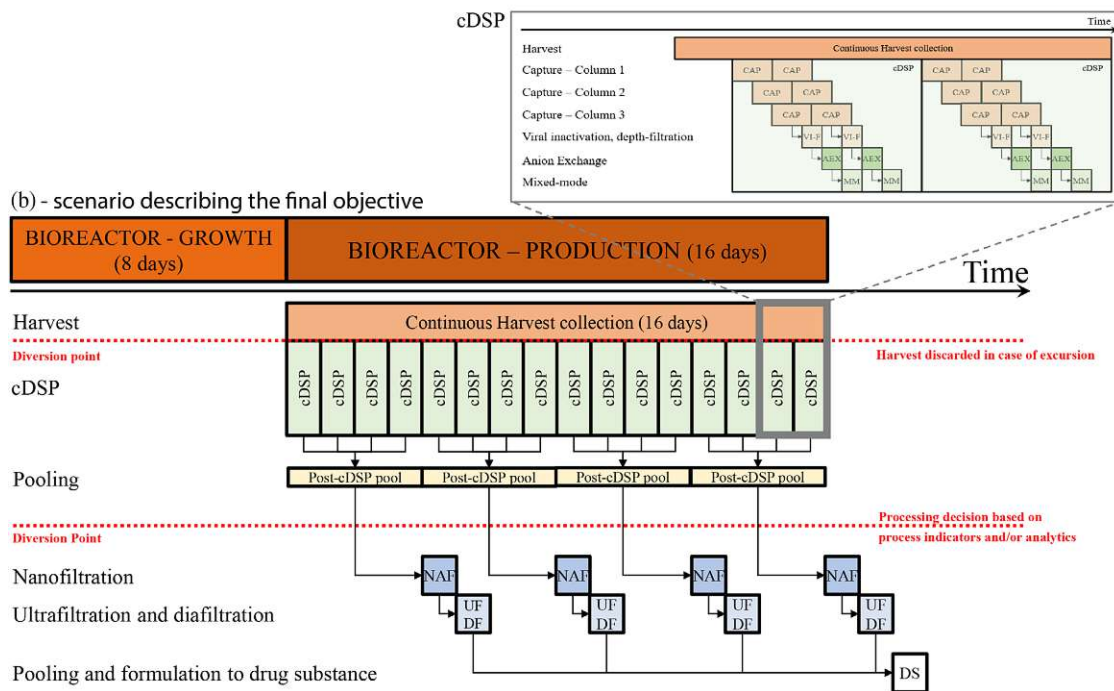


Figure 1.3: Exemplary continuous manufacturing scenario at 2,000L scale taken from literature [192]. Continuously collected harvest is processed on a daily basis by a continuous downstream processing (cDSP) sequence composed of six cycles of capture, two cycles of VI-F, AEX, and MM. A pool of four daily cDSP sequences is then further processed in NAF and UF/DF, prior to further pooling into DS. Two diversion points are present that enable to divert process stream that do not meet product quality requirements – one in the perfusion bioreactor harvest stream and a second if the post-cDSP stream does not qualify for further processing. Time-independent product quality is required in this scenario in order to allow diversion without impacting the product quality of the final DS pool.

1.8 Steady-state perfusion: A key unit operation for continuous manufacturing of biologics

Steady-state perfusion cell culture, the stage for protein expressed and primary hotspot for post translational modifications, plays a central role in attaining the time independent quality profile. The highest product quality must be achieved in this step as modification and corrective actions are limited in subsequent purification and formulation steps.

1.8.1 Steady-state perfusion process setup

Steady-state perfusion involves a sophisticated interplay of various devices, along with the incorporation of sensor technology. This technology plays a key role in assessing process states and facilitating communication between devices, ultimately resulting in a robust and efficient operational system (Figure 1.4).

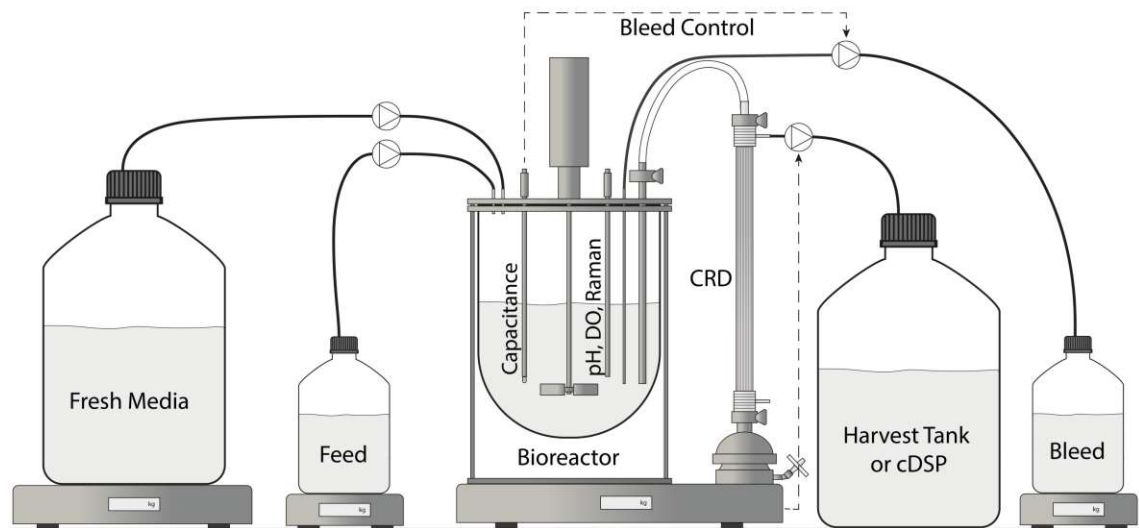


Figure 1.4: Schematic representation of a steady-state perfusion setup. Fresh media and feeds are entering the bioreactor. Sensor technology is mounted to the bioreactor for real-time control of CPPs. Bleed is controlled by a capacitance sensor monitoring VCV. A CRD generates cell-free product harvest that is either collected in a tank or directly processed in cDSP.

The bioreactor is the heart of each perfusion system and ensures an optimal growth and production environment for manufacturing cell lines. No different to fed-batch bioreactors, minimal sensor requirement to measure temperature, pH and DO are essential for tight control of culture environment. Mixing and gas sparging setups should be designed to support highest cell densities achieved in perfusion bioreactors [197, 225]. Bioreactor types in manufacturing are most commonly single use vessels and cover a wide range from 50, 200, 500, 1,000 up to 2,000 L. Due to the higher cell density and consequently higher volumetric productivity, these are significantly smaller compared to their fed-batch counterparts of up to 20,000 L. Small-scale perfusion bioreactors reach down to 2 mL vessel volume [226], whereas identical sensor technology as in manufacturing scale can usually be incorporated into 2 L vessels or larger.

Next to acid, base, antifoam or feed addition pumps, perfusion systems require additional liquid transfer capabilities for continuous fresh media addition, continuous harvesting as well as removal of excess biomass called bleed removal. Large media

tanks, frequently much larger than the bioreactor itself, allow media preparation in batch mode and supply for continuous bioreactor perfusion. Continuous media preparation stations are under development and might replace large hold tanks in the future to further reduce the facility footprint. If not yet processed by an integrated continuous capture step, large harvest tanks are necessary to collect cell free product harvest until further processing. Process bleed is considered waste and is further collected in storage tanks, smaller vessels than for media and harvest are sufficient due to the lower relative bleed stream.

All liquid streams must be controlled by sensor technology ensuring that the correct flow rates for entering liquids, but also exiting liquid streams are applied. Bolus additions of acid and base are triggered by the pH sensor readings. Antifoam is frequently added on demand by operator intervention unless foam sensors are available. Media and feed are continuously added and require a feed rate calculation to control liquid flow per unit time. Feeding rates are frequently calculated based on balance reading at smaller scale, whereas flow sensors readings become more feasible at large scale. As cell division rates can fluctuate with proceeding run time, sensor readings for cell density or viable cell volume (VCV) are required to control continuous bleed removal [227]. This feedback control strategy is described in more detail in section 1.8.2. Given the sum of entering and existing liquids defined by flow rates or sensor feedback control loops, the harvest flow rate can be gravimetrically controlled to keep a constant vessel volume. The CRDs, additionally required to provide a cell free harvest stream, are described in section 1.8.3. Less frequently, the harvest rate is defined and counterbalanced by a variable media addition rate to keep the bioreactor level constant.

1.8.2 Stable operation by bleeding: Bleed control strategy

Accurate continuous bleeding is a prerequisite for a stable perfusion process. Even though daily bleed adjustments based on low-frequency at-line measurement are reported, the industry has moved towards real-time PAT sensors. Next to acoustic resonance densitometry, conductivity, optical sensors and real-time imaging, capacitance probes are the currently most utilized sensors for online biomass monitoring [228–230]. The capacitance sensors measure permittivity on the principle of dielectric spectroscopy, the ability to transmit an electric field. Viable cells, non-conductive entities surrounded by a conductive field, distort this electric field. As dead cells lack an intact membrane, they are not influencing the measurement [231]. The degree of distortion can then be correlated to the viable cell volume (VCV), a measure for the viable biomass in cell culture. These real-time VCV measurements

can then be integrated into a feedback control loop actuating a bleed pump to keep VCV on target setpoint.

1.8.3 Cell retention devices for high density perfusion processes

Recent advances in the development of CRDs are one of the key enablers for continuous manufacturing. As density-based separation technologies such as gravity settler, acoustic separators cyclones or centrifuges require additional filtration steps prior to chromatography, hollow fiber-based tangential flow filtration delivers readily filtered harvest that can directly be integrated to continuous downstream operations [199]. Additionally, higher cell densities can be reached compared to density-based separators, increasing the volumetric productivity of the bioreactor. Thus, hollow fiber-based tangential flow filtration has emerged to the dominant cell retention technology for mammalian perfusion processes [183, 211, 232]. Two main operating modes of tangential flow filtration are common in the biopharmaceutical industry – the unidirectional tangential flow filtration (TFF) mostly driven by a low-shear centrifugal pump, and the alternating tangential flow filtration (ATF) driven by a diaphragm pump [233–235]. The alternating flow in the ATF systems has been shown superiority in terms of product sieving in lab-scale studies compared to unidirectional TFF operation [236–238]. Consequently, ATF was proposed as more suitable technology for long-term perfusion cultivations with a desire to maximize product passage. However, scalability of ATF system is not trivial leading to simultaneous operation of several parallel systems at 2,000 L manufacturing scale [211]. Additionally, ATF systems driven by diaphragm pumps were associated with operational instability at manufacturing scale [211, 239–241]. Thus, TFF systems were claimed the preferred choice at manufacturing scale due to smaller facility footprint and higher robustness, whereas ATF systems showed improved product sieving and reduced development time for lab-scale and pilot-scale operations [211]. As cultivation durations extend and cell densities increase, the loads on the filter modules are expected to rise, in turn challenging the filtration modules even more. Filter clogging and product retention remain major challenges that risk run abortion and must be solved moving towards robust continuous manufacturing processes. Low-shear levitated centrifugal pumps or diaphragm pumps support higher cell culture viabilities and consequently reduce the amount of fouling provoking particles on the filter membrane, but alone are not enough to mitigate filtration limitations [236, 238, 242, 243]. Better understanding of the underlying mechanism driving further

innovations to enhance filtration capacity must be realized in the future.

1.8.4 Advanced PAT for perfusion cell culture: Raman spectroscopy

On top of the minimally required setup to achieve a stable operation in perfusion cell culture, further PAT tools have found their place in biopharmaceutical manufacturing for simultaneous monitoring of multiple process parameters. The vision to continuously monitor CQAs driving the industry towards real-time release testing (RTRT) is another key driver for PAT implementation [244–246]. Spectroscopic techniques gained particular interest due to their measurement speed, non-invasiveness and relatively low impact material being analyzed [247]. Vibrational spectroscopy analyses such as near-infrared (NIR), mid-infrared (MIR) and Raman spectroscopy are powerful tools, of which Raman spectroscopy is arguably the most versatile for upstream processing due to the inherently low water inference [183, 248–250].

Raman spectroscopy works of the principle of Raman scattering, where incident laser light is scattered by a molecule and experiences a change of its vibrational energy. A small fraction of the incident light is inelastically scattered (Stokes and anti-Stokes), resulting in photons being released with a different energy. Raman devices usually focus on the Stokes scattering due to higher photon intensity compared to anti-Stokes scattering. This change in energy (Raman shift) is detected by the system and provides specific information about the chemical composition of the molecules present in the culture represented as specific peaks in the resulting Raman spectrum [251]. Knowledge about culture composition by at-line or off-line analytics at various process stages in combination with simultaneously acquired Raman spectra can be leveraged to create quantification models. This process called chemometric modelling uses spectral pre-processing algorithms to remove spectral noise prior to regression analysis such as partial least squares regression (PLS) to establish the correlation between reference measurements and acquired Raman spectra. Special care should be taken to ensure that these chemometric models are truly based on the fingerprint of the analyte of interest, rather than just being a correlation to unknown other effects concomitantly changing in the process matrix with run evolution [252]. Resulting predictions models can then be used to monitor culture components of interest in real-time and establish control strategies based on the prediction outputs.

Even though some groups have reported real-time CQA monitoring, such as gly-

cosylation, by Raman spectroscopy in cell culture processes, the measurement of CPPs such as glucose lactate or amino acids seems a more feasible at sufficiently high accuracy and robustness with current Raman analysers [178, 248, 253–257]. Detection limits provided by device manufacturers of modern Raman analysers in cell culture processes lie around $0.1 - 0.2 \text{ g L}^{-1}$ and root mean square errors in the same range or higher depending on the analyte are reported in the literature. In the case of mAb glycosylation, glycosylation represents approximately 3% of the molecular weight of a mAb molecule [11]. Given mAb titers in the lower gram range for state-of-the-art cell culture processes, the glycosylation seems to constitute a very small fraction of the complex cultivation matrix. Manyfold higher concentrated nutrients, metabolites or cell components are therefore likely to cover the glycosylation signal. Understanding the relationship between higher concentrated nutrient or metabolites (CPPs) and the resulting product CQAs according to the QbD concept, and monitoring or even controlling the levels of the CPPs by real-time Raman measurements seems a more approachable solution unless further technology advancements are introduced. Based on this concept, a glucose feedback control strategy was implemented for a fed-batch process maintaining a stable glucose setpoint throughout the culture time and thereby reducing product glycation [258].

The use of Raman spectroscopy in perfusion cell culture has so far been limited to nutrient and metabolite monitoring activities [178, 259–261], even though real-time prediction of CPPs and feedback control could represent a gamechanger in achieving the much-desired time-independent quality profiles for continuous manufacturing [183, 262]. In contrast to fed-batch processes where culture composition changes with proceeding runtime, perfusion cell culture has inherently a much lower component variability. In terms of chemometrics, reduced analyte variability can negatively impact sensor calibration activities due to restricted calibration ranges. Integrating sufficient analyte variability remains therefore one of the biggest challenges for Raman implementation in perfusion processes. As previously accomplished for fed-batch processes, analyte spiking or the execution of DoE strategies with miniaturized bioreactor systems to increase variability in the calibration data set might be the next steps towards reliable and robust Raman calibration for perfusion applications [252, 263–268].

1.8.5 Current challenges for continuous perfusion processes

While it is fairly simple to get a stable perfusion process with consistent product quality over time at low cell densities, high media perfusion rates and oversized equipment to avoid any potential limitations endangering the run progression, such

best-case scenarios are not economically profitable. From a manufacturer's point of view, the process should be pushed to the limits in terms of production in order to reduce the COGs of the final drug product. This can be achieved by maximizing cell density, minimized media utilization, and optimally designed or operated manufacturing equipment to support these extreme conditions. The major challenge of pushing productivity boundaries lies in maintaining consistent product quality attributed. Consistent CQAs are of highest priority in continuous manufacturing scenarios and ultimately contribute to patient safety of the biological drug. A lack of process understanding, insufficient process development and unexpected effects during process scale-up are the main reasons for undesired product quality drifts. As such, next to other CQAs, drifting glycosylation profiles were reported in steady-state perfusion cell culture. A general tendency towards less processed glycoforms such as HM was observed with progression run time [143, 178–180]. Despite stable cell density setpoint, reduced cell division rates and consequently reduced process bleed rates were observed at the same time. Accordingly changing nutrient and metabolite levels, such as increasing ammonia levels and changing amino acid consumption rates, further indicate alterations in cellular metabolism of these perfusion cultures [143]. Altogether, these are clear signs that despite stable operation at a predefined cell density setpoint, no metabolic steady-state was achieved resulting in drifting product quality profiles, highlighting the current challenges in perfusion cell culture.

Process development for fed-batch processes has significantly benefited from streamlined development activities in recent years. Robotic platforms and miniaturized bioreactor systems have been developed and tailored to support optimization of fed-batch processes [10, 183]. These high-throughput tools in combination with decade-long experience ensure smooth scale-up from lab-scale to manufacturing scale of current fed-batch processes delivering predictable process yield and product quality. Perfusion processes in contrast to fed-batch processes require a more complex bioreactor configuration and processing times tend to be significantly longer, complicating perfusion process development. With commonly reported steady-state duration 20 – 30 days, compared to 12 – 16 days of fed-batch process duration, and a persisting trend to further prolong perfusion operating times, requirements for a manufacturing cell line are changing [211]. Whereas robust growth kinetics and high productivity were the major hallmarks for fed-batch cell lines, perfusion cell lines must additionally provide higher stability to ensure constant product secretion with consistent product quality over prolonged process duration [269, 270]. Reduced growth in steady-state operation while maintaining productivity and product qual-

ity is a further positive perfusion cell line attribute to improve overall process yield by reduced bleed stream [166, 183]. In addition to cell line engineering, environmental factors can influence the performance of a particular manufacturing cell line and were summarized in section 1.6.2. As such, media development is central for perfusion process optimization due to its direct impact on culture viability and productivity. At the same time, media cost is one of the main drivers of manufacturing cost, generating a trade-off between high perfusion rates to ensure optimal cell culture conditions and cost considerations with endeavors to minimize media utilization [203, 210, 271]. Significant media optimization to make perfusion processes more robust, economically viable, but also more sustainable, represents a major milestone for continuous biomanufacturing. Most cell culture media were developed for fed-batch processes and are expected not to be ideal for perfusion process requirements [183]. Media reformulation from fed-batch to perfusion culture suitability, development of higher concentrated media formulations to reduce perfusion rates and media rebalancing to optimize nutrient utilization in steady-state operation are topics of ongoing development activities [221, 272–274].

The maximization of the process output for a steady-state perfusion process requires a holistic approach - only the combination of a high producing cell line, an optimized media formulation and the appropriate set of process parameters will enable manufacturers to fully take advantage of continuous manufacturing. To solve these multivariate process optimization challenges, high-throughput capabilities such as available for fed-batch process development are necessary and must be adapted to perfusion development requirements. Even though semi-continuous workflows in shake tube or miniaturized bioreactor systems were evaluated for perfusion processes development, these methodologies originally designed for fed-batch process platforms only partially mimic true perfusion [275–278]. Increasing interest in screening tools especially designed for perfusion process development has been identified by device manufacturers and novel designs as well as retrofitted fed-batch platform tools are becoming available. Scale-down of continuous media addition and harvest removal by cell retention devices, as well as continuous cell density monitoring ensuring continuous bleed removal are the main difficulties to overcome when designing such high-throughput devices. Nevertheless, first devices for highly parallelized cell line screening in nanofluidic-chips [279], fully controlled perfusion systems at 2 mL working volume [226], and miniaturized stirred tank bioreactor systems with cell retention capabilities have entered the market [280]. Integration of these high-throughput screening tools and scale-down models have the potential to decrease development timelines, increase process robustness and ensure smooth

scale-up to manufacturing scale and are expected to become important pieces of industrial perfusion platforms.

1.8.6 Process intensification in steady-state perfusion

Despite upcoming perfusion adapted process development tools, increasing time-to-market pressure continues to compress development schedules. Instead of lengthening the process development timelines to accommodate the additional challenges in continuous perfusion process development, timelines can be expected to further decrease in order to stay competitive in the fast-evolving market environment [197, 203–206]. Insufficient process development can potentially lead to suboptimal manufacturing processes, resulting in lower yields and issues with product quality. Process intensification strategies and fine-tuning of continuous processes during a later stage closer to market entry can address these challenges, given that identical product quality can be assured at intensified processes. The QbD approach was especially designed to support more flexibility in the approval process. Changes within the defined design space are not considered as a change to the manufacturing process, whereas moving out of the design space is considered a change and would initiate a post approval change process [33, 35]. This new concept gives manufacturers the possibility to evaluate innovative approaches throughout the product lifecycle and expand, reduce, or redefine the design space upon gaining additional process knowledge.

Process intensification in biopharmaceutical manufacturing refers to the strategy of making processes more efficient and effective. The goal is to enhance productivity, quality, and sustainability of the manufacturing process, while decreasing its footprint, cost, and waste production. This methodology involves a rethinking of current manufacturing practices, looking for opportunities to optimize and streamline every aspect, from raw material input to final product output [269, 281, 282]. In upstream processing, one of the main drivers for process intensification is the increase of volumetric productivity in the bioreactor. A large increase in volumetric productivity can already be achieved by switching from batch processing to continuous manufacturing. As such, an increase from $0.1\text{--}0.7\text{ g L}^{-1}\text{ day}^{-1}$ in fed-batch processes to volumetric productivities above $2\text{ g L}^{-1}\text{ day}^{-1}$ [269], even expected to increase to $4.8\text{ g L}^{-1}\text{ day}^{-1}$ in the near future [211], can be achieved. Focussing on N-stage steady-state perfusion intensification, volumetric productivities can be improved by increasing cell-specific productivity (Q_P), increasing the total amount of viable cells in the steady-state, reduce the process waste stream (bleed), or reduce bioreactor idle stages.

Cell-specific productivity can be increase by cell line engineering and media or process optimization. In contrast to cell line engineering and media optimization that require large screening capabilities, late-stage process optimization such as PAT controlled feeding strategies are more amenable for Q_P tuning [258]. Much more common and more attractive alternatives to increase volumetric bioreactor productivity in continuous perfusion cultures are increasing the cell density in the bioreactor or prolongation of the run duration [269]. A straight-forward strategy to increase cell density consists in finding the minimally required medium renewal rate per cell density to ensure stable process operation, namely the critical cell-specific perfusion rate (CSPR). Once the CSPR is determined, cell density can be increased in the bioreactor by maintaining a constant CSPR [283, 284]. Obviously, operational bioreactor constraints such as mixing and gas transfer, as well as CRD limitations due to high viscosity and high perfusion rates will limit the maximally achievable cell density. Further, prolonged run duration reduces the idle time of the bioreactor. Non-productive phases such as initial growth phase before reaching steady-state operation and bioreactor turnaround times can be reduced if runs have to be started less frequently [269]. The highly productive bioreactor steady-state phase can be extended leading to an increased number of productive days annually, ultimately enhancing the facility output. In addition, consumable utilization gets enhanced which translates to reduced COGs. Main challenges such drifting product quality attributes with proceeding process time due to cell line stability issues must be overcome as discussed in section 1.8.5. A very steady-state perfusion specific and more recent process intensification strategy consists in bleed stream reduction. Bleed is inherently required for maintaining a stable perfusion operation and is a good indicator for continuing cell division ensuring stable process operation. Simultaneously, bleeding means product loss as the liquid fraction of the bleed, containing the product of interest, gets wasted and reduces the overall productivity. Endeavours to either reduce the bleed stream by reducing cell division [166], or recycle part of the liquid fraction in the bleed have recently been reported [285], and constitute a less explored process intensification strategy for perfusion cell culture.

Altogether, a systematic investigation of possible process intensification strategies for steady-state perfusion processes is required to fully leverage the potential of continuous manufacturing. Not only their capacity and extent of pushing volumetric productivity have to be evaluated, more importantly, their impact on product quality attributes must be characterized in detail. With this in-depth understanding of process intensifications, their incorporation into the QbD framework can become achievable, facilitating the definition of appropri-

ate control strategies that ensure consistent product quality in intensified perfusion processes.

2 Scope of the Thesis

The biopharmaceutical industry is facing a new set of business realities and uncertainties which challenge the well-established batch manufacturing approach. Emerging complex product classes are reshaping the biological landscape and biosimilars have entered the biological drug market. With the broadening of product portfolios and growing competition, continuous manufacturing of biologics has gained momentum due to its potential for cost saving, higher flexibility, and product quality considerations. Responding to these industry shifts, the healthcare unit of Merck KGaA, the industrial partner of this project, aspires to adopt continuous manufacturing technologies for both USP and DSP. Merck KGaA recently invested in a center of process development and clinical manufacturing excellence called the Biotech Development Center (BDC). The laboratories and the manufacturing areas were designed to improve process development capabilities and enable the production of clinical material using continuous manufacturing technologies.

From a manufacturer's perspective, establishing a highly efficient, steady-state perfusion process is essential to fully leverage the advantages of continuous manufacturing and consequently, lower the COGs. At the same time, continuous manufacturing is at its best when time-independent product quality profiles can be achieved. This increases the operational flexibility and is clearly the target for commercial processes. The run duration could then be adapted to the product demand and some operational risks are decreased. If a contamination occurs after 10 days of production for example, some of the produced material could still be released if the segregation strategy is well defined. But in terms of process development, maintaining process stability is often leading to a delicate balance between optimizing productivity without impaction on product quality. This is a challenge that is also exacerbated by the time pressure that early-stage development programs are dealing with.

The aim of this cumulative Thesis, performed on Merck's perfusion platform, is directed towards achieving two main objectives which were addressed in five sections:

- **Product quality control: Attaining time-independent product qual-**

ity in intensified perfusion processes

In **Section I**, a novel PAT calibration approach specifically tailored for steady-state perfusion processes is introduced. This innovative approach facilitates the rapid development of exceptionally precise and robust prediction models within a few days, as opposed to the traditional timeframe of several months. Together with considerable cost savings due to reduced model calibration activities, this approach substantially alleviates the burden of implementing PAT in continuous perfusion processes, making it more accessible and practical. Building upon the established PAT calibration approach and comprehensive knowledge about the relationship between CPPs and CQAs from prior process characterization, **Section II** outlines the successful implementation of a Raman-based feedback control strategy. This QbD compliant control strategy effectively stabilizes product quality profiles during extended periods of intensified steady-state perfusion, satisfying the criteria for seamless integration into the continuous manufacturing platform. Additionally, **Section III** presents promising novel N-glycosylation modulators to fine-tune antibody effector functions such as ADCC and demonstrates their applicability in continuous feeding scenarios, which are required for continuous manufacturing processes. This expands platform capabilities from product quality control to modulation, representing a particularly interesting tool to match reference product quality in the biosimilars field.

- **Productivity increase: Investigation of process intensification strategies and their impact on product quality**

Next to extended cultivation time as process intensification strategy to boost volumetric productivity, **Section IV** explores innovative bleed recycling applications to selectively recycle the liquid fraction of the bleed stream containing the product, which would otherwise go to waste. Different bleed recycling technologies are compared at lab-scale and manufacturing scale, with a particular focus on their impact on product quality attributes.

Lastly, **Section V** elaborates on enhancements for hollow fiber-based TFF to accommodate the increased harvest volumes generated by process intensification. Co-current filtrate flow as a solution to prevent premature filter clogging and extensive product retention is discussed, thereby reducing CRD-related bottlenecks in steady-state perfusion processes.

This cumulative Thesis comprises five first-authored research articles, of which two are published (**Section I and IV**), and three are under review (**Section II,**

III and V). All publications are assembled in **Appendix A**. The author's scientific curriculum vitae is attached to **Appendix B**.

3 Results and Discussion

3.1 Product quality control: Attaining consistent product quality in intensified perfusion processes

3.1.1 Section I - Advancing Raman model calibration for perfusion bioprocesses using spiked harvest libraries

PAT plays a major role in transitioning from batch to the envisioned integrated continuous manufacturing platform to gain better process understanding and improve process control. Especially spectroscopic sensors with the ability to monitor multiple CPPs at the same time are interesting for the biopharmaceutical industry as they could enable real-time feedback control strategies to stabilize intensified perfusion processes and prevent product quality drifts [34, 35, 247]. Despite the great potential in development as well as in commercial manufacturing, implementation of PAT has been associated with tremendous hurdles. Time and resource intensive calibration efforts, insufficient analyte variability in calibration data sets and high cross-correlation of various media components resulted in unspecific prediction models with low robustness, not suitable for feedback control strategies [252]. Further, traditional calibration strategies by aligning at-line reference measurements with simultaneously acquired process spectra are challenged by steady-state perfusion processes with inherently low analyte variability compared to evolving fed-batch processes.

In order to address the urgent needs for enhanced model performance and practicability of spectroscopic PAT, as well as to establish a basis for their incorporation into development workflows and continuous manufacturing environments, a novel calibration approach was developed (Figure 3.1). This workflow harnesses the presence of the cell free harvest stream in perfusion processes to monitor analytes by inserting a specifically designed flow cell accommodating standard PAT sensor probes. This strategic repositioning of the PAT sensor into the harvest stream, instead of within the bioreactor, allows a fundamental restructuring of the calibration approach, resulting in the following workflow:

1. **Harvest library (HL) generation:** Perfusion harvest samples from multiple development bioreactor runs at different processing times are collected and frozen at $-80\text{ }^{\circ}\text{C}$ to build a harvest library, covering intra- as well as inter-process variability.
2. **Sensor calibration by HL spiking:** Once a HL is established, new calibration models can be created at any time by thawing HL samples and spiking them with analytes of interest. Alternatively, fresh harvest samples can be used instead or in addition to HL samples. Spiking enables to selectively change concentrations of particular analytes to decouple their spectral peaks

from the process matrix. Optimized DoE spiking additionally offers to spike multiple analytes at the same time to reduce calibration efforts and further increase prediction performance. All calibration activities are executed offline under non-aseptic conditions, meaning not connected to the bioreactor.

3. **Chemometric modeling:** Standard pre-processing methods commonly applied for the respective spectroscopic technology can be used, followed by regression modeling such as PLS regression.
4. **Model verification and in-line predictions:** The flow cell is connected to the bioreactor harvest stream and analyte additions into the bioreactor are performed. Model predictions are then compared to reference analytics to assess accuracy and robustness of the model. Not just analytes of interest, but also other matrix components can be added to assess the independency of the prediction models from other components.

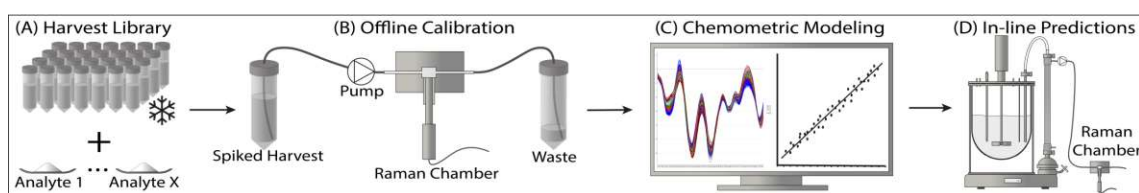


Figure 3.1: Schematic representation of the harvest library calibration approach. Harvest library samples are thawed and spiked with analytes of interest (A). Spectra for spiked harvest samples are collected in an offline setup (B) followed by chemometric modeling to create prediction models (C). Subsequently, the flow cell is connected to the bioreactor harvest stream and in-line model verification by adding analytes or other matrix components into the bioreactor is performed to assess model performance (D).

Raman spectroscopy, particularly advantageous for measuring aqueous solutions due to its minimal interference with water, was selected as the preferred platform technology to monitor perfusion cell culture [183, 249]. Various sugars such as glucose, raffinose, galactose, mannose, and fructose, were chosen as excellent test subjects for assessing this new PAT calibration approach via Raman spectroscopy, due to their relevance in cell culture by modifying the N-glycosylation of recombinantly produced proteins [144, 147, 149–152].

An initial screening to assess whether these sugars with a high degree of molecular similarity can be distinguished by Raman spectroscopy at process relevant concentration was performed using a single batch of perfusion harvest. In this ideal scenario at a fixed matrix composition, spiking of 200 samples revealed that Raman spectroscopy was indeed able to distinguish and quantify the different sugars, resulting

in root mean square error of prediction (RMSEP) between 0.2 to 0.4 g L⁻¹. More importantly, model regression coefficient patterns varied strongly between different sugars (Figure 3.2) and the most important spectral regions for prediction were in good agreement with specific vibrational bands reported in the literature [286, 287].

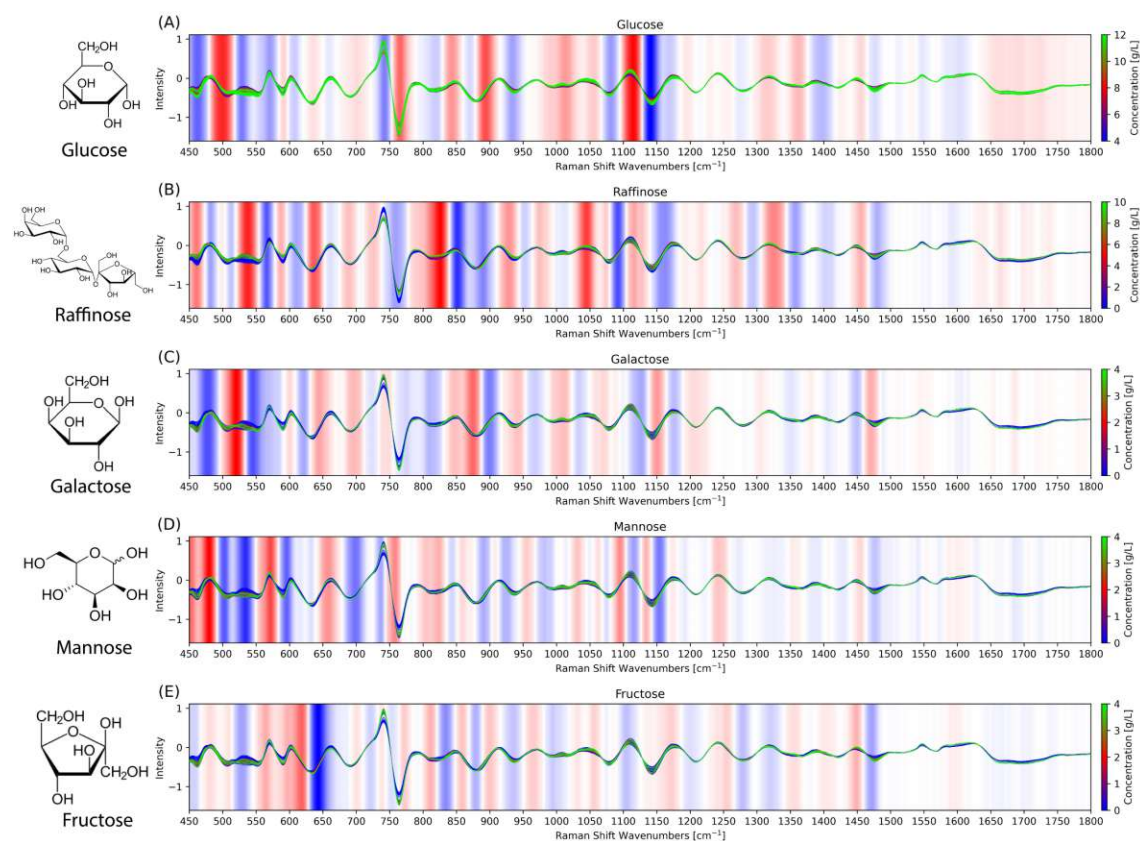


Figure 3.2: Raman spectra for glucose (A), raffinose (B), galactose (C), mannose (D), and fructose (E) in perfusion process harvest. All spectra were pretreated with a Savitzky–Golay filter (derivative 1, polynomial = 2, window size = 31) followed by standard normal variate (SNV). Background bands represent the min-max normalized regression coefficient for the respective wavenumber for the individual models. Blue colors show the negative contribution of the wavenumber to the predicted value, red colors indicate a positive contribution. The more intense the coloring, the more important the wavenumber for the respective model.

As a next step and more realistic scenario, a robust Raman prediction model for raffinose as a glycosylation modulating sugar in the presence of glucose as main energy source in cell culture media was aspired [152]. Raffinose, a trisaccharide containing even a glucose molecule, was chosen as a worst-case sugar to demonstrate the applicability of the calibration workflow for similar compounds. This time, matrix variability was incorporated by using HL samples. Different calibration models were created and compared to assess whether raffinose spiking alone is sufficient for robust model calibration, or if additional glucose spikes are required to extend the matrix variability. Although both the simple model based solely on raffinose spikes

and the comprehensive DoE model, which incorporates both raffinose and glucose spiking, demonstrated a low root mean square error of cross-validation (RMSECV) below 0.3 g L^{-1} for raffinose predictions, the deficiencies of the simpler model became evident during in-line model verification. When challenged with glucose additions to the bioreactor, simulating potential process deviations, the simpler raffinose model predicted an increase of raffinose, even though no raffinose at all was present in the culture (Figure 3.3A). The DoE model on the other hand could accurately predict raffinose at any time due to properly decoupled spectral peaks between raffinose and other matrix components such as glucose at low RMSEP of 0.35 g L^{-1} (Figure 3.3B).

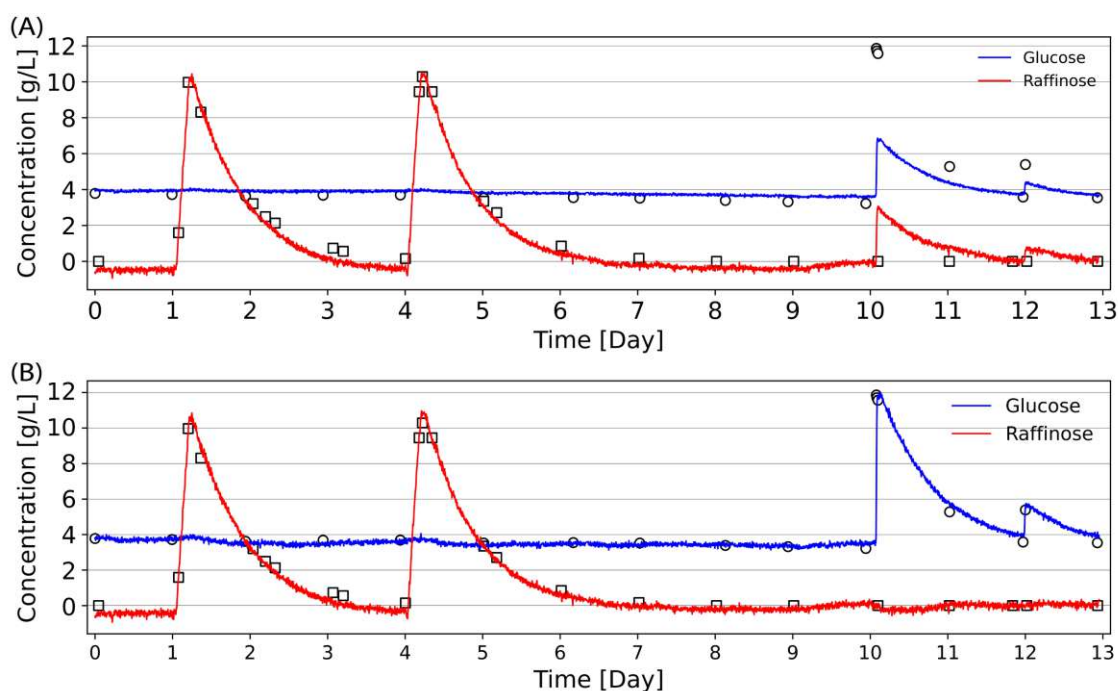


Figure 3.3: Raman predictions of the model verification run comparing the simple calibration model consisting solely of raffinose spikes (A) with the comprehensive DoE model incorporating raffinose as well as glucose spiked (B). RA1 and RA2 represent raffinose additions of 10.9 g L^{-1} and 11.1 g L^{-1} to the bioreactor, whereas GA1 is a glucose addition of 11.8 g L^{-1} and GA2 a glucose addition of 5.6 g L^{-1} . Raw predictions without moving average are shown and aligned with reference values for glucose (circles) and raffinose (squares). GA, glucose addition; RA, raffinose addition.

In summary, this innovative PAT calibration approach enables the generation of highly accurate and robust prediction models at unprecedented speed. Unlike traditional calibration procedures that take months and span a wide range of process development activities, this approach reduces the calibration timeline to days. With a well-defined HL in place, spiking calibration activities can be conducted offline without interfering with ongoing process development activities and prediction models

can be made accessible already for initial development bioreactor runs. The fact that the PAT sensor is placed in the perfusion harvest stream, contributing to a less complex background matrix due to absence of cells, cell debris and gas bubbles, might further facilitate the creation of generic platform calibration models rather than recalibrating predictions models for each new process. Considering scale-up, the same flow cell as in lab-scale can be used for commercial manufacturing when connected in a harvest by-pass, thereby alleviating scalability risks. In combination with considerable cost savings due to reduced calibration activities and better model performance by calibration range extension and proper peak decoupling, this approach substantially facilitates the burden of implementing PAT in continuous perfusion processes and paves the way for the envisioned real-time product quality control framework.

This section is based on the following publication: P. Romann, J. Kolar, D. Tobler, C. Herwig, J. Bielser, and T. K. Villiger, **Advancing Raman model calibration for perfusion bioprocesses using spiked harvest libraries**, *Biotechnology Journal*, vol. 17, no. 11, p. 2200184, Nov. 2022, DOI: 10.1002/biot.202200184.

3.1.2 Section II - Raman-controlled pyruvate feeding to control metabolic activity and product quality in continuous biomanufacturing

Despite advancements in technology ensuring stable cell culture perfusion operation at constant cell densities and fixed CSPR, maintaining a cellular steady-state metabolism throughout the extended perfusion process duration remains a considerable challenge. Metabolic drifts are especially pronounced at highly intensified processes and might be related to media limitations or other effects such as cell aging. Merck's proprietary CHO-K1 platform cell line, among other reported cell lines, revealed a lack of steady-state metabolism for various recombinantly expressed products [143, 178–180]. As run time progressed, the cultures exhibited reduced cell division rates, altering amino acid consumption rates, increasing ammonium concentrations and reduced productivity. The severity of these trends increased with higher cell densities and prolonged run duration, putting constraints on process intensification by limiting maximal cell density and run duration to prevent extensive product quality drifts towards less processed N-glycosylation species such as high mannose. Process characterizations studies revealed pyruvate, a precursor entering the TCA cycle, as an effective lever to stabilize the cellular metabolism [143]. Constant pyruvate feeding was proposed to substitute amino acid catabolism and reduce anaplerotic reactions replenishing the TCA cycle. Despite significantly lowered ammonium levels, which had a beneficial effect on product quality, the cell cultures' needs evolved with extended run duration. This altering of the pyruvate consumption rate led to a residual yet diminished drift in product quality, calling for an on-demand feeding strategy adjusting the pyruvate supplementation to the evolving needs of the cell culture.

Utilizing pyruvate as a potent glycosylation modulator and leveraging the previously described PAT calibration approach (Section I), a real-time Raman-based product quality control strategy was developed and exemplified with a steady-state perfusion process producing a bispecific antibody. Raman calibration activities incorporated a DoE spiking approach to generate prediction models for pyruvate, lactate, and ammonium. Furthermore, glucose was spiked to avoid peak interference with the analytes of interest. Raman model verification by inline analyte additions revealed that the ammonium model was entirely based on correlation to other matrix components and disqualified for feedback control. Noticing the swift conversion of pyruvate into lactate by the culture upon pyruvate addition, leading to consistently low pyruvate levels but elevated lactate levels, identified lactate as an ideal marker

for TCA saturation that can be robustly measured using Raman spectroscopy. As a result, the real-time quality control strategy comprises an on-demand pyruvate feed, regulated by adhering to a predefined lactate setpoint, which is measured in real-time using Raman spectroscopy (Figure 3.4).

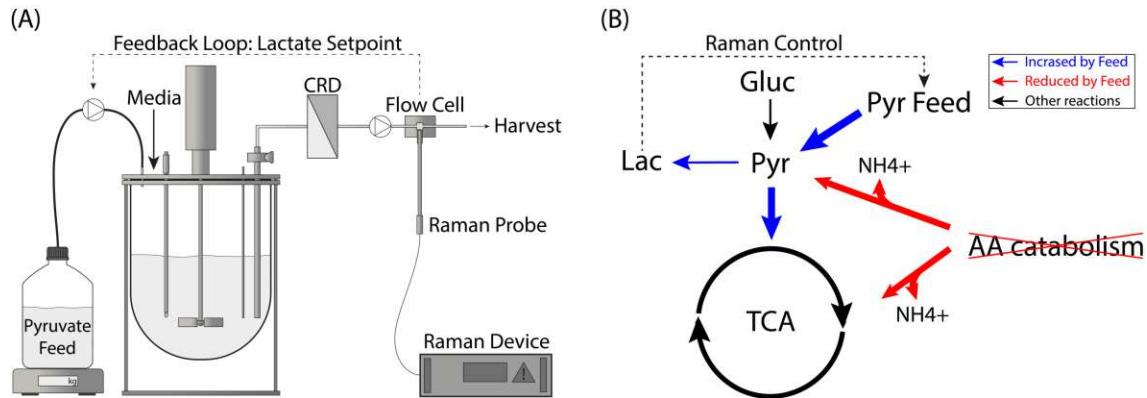


Figure 3.4: Raman controlled pyruvate feeding strategy. Schematic setup of a perfusion bioreactor with Raman flow cell after cell retention device (CRD) in harvest stream predicting lactate concentration and controlling pyruvate feed addition (A). Simplified metabolic scheme of feeding strategy (B).

Two different lactate setpoints were evaluated by pyruvate feeding, a rather low concentration of 0.3 g L^{-1} and a slightly higher concentration of 0.7 g L^{-1} . In both cases, stable VCV and high cell viabilities were achieved (Figure 3.5A). Lactate levels in contrast to depletion after an initial lactate peak in the control runs were stabilized at the respective setpoint (Figure 3.5C), but pyruvate levels remained much lower due to rapid conversion into lactate (Figure 3.5D). Pyruvate feeding profiles increased slowly with run progression and decreased again towards the end of the runs (Figure 3.5F) and higher pyruvate feeding rates were required for the higher lactate setpoint of 0.7 g L^{-1} . Ammonia was significantly stabilized and maintained below 2 mmol L^{-1} for the 0.7 g L^{-1} lactate and was only slightly higher for the lower lactate setpoint, marking an up to 3-fold ammonium reduction at peak concentrations (Figure 3.5E). On day 20 of the 0.3 g L^{-1} lactate setpoint run, external ammonium at a concentration of 5 mmol L^{-1} was supplemented to the cell culture medium to evaluate its impact on N-glycosylation. Whereas productivity was not impacted by pyruvate feeding at all, additional ammonium supplementation reduced productivity significantly (Figure 3.5B).

N-glycosylation of the bispecific mAb was stabilized resulting in a flat profile across the board and no residual drifting was remaining (Figure 3.6). The most critical glycosylation species, high mannose and fucosylation, which exhibited serious drifts in the absence of on-demand pyruvate feeding were effectively stabilized to standard deviations below 0.2% for high mannose and fucosylation throughout a

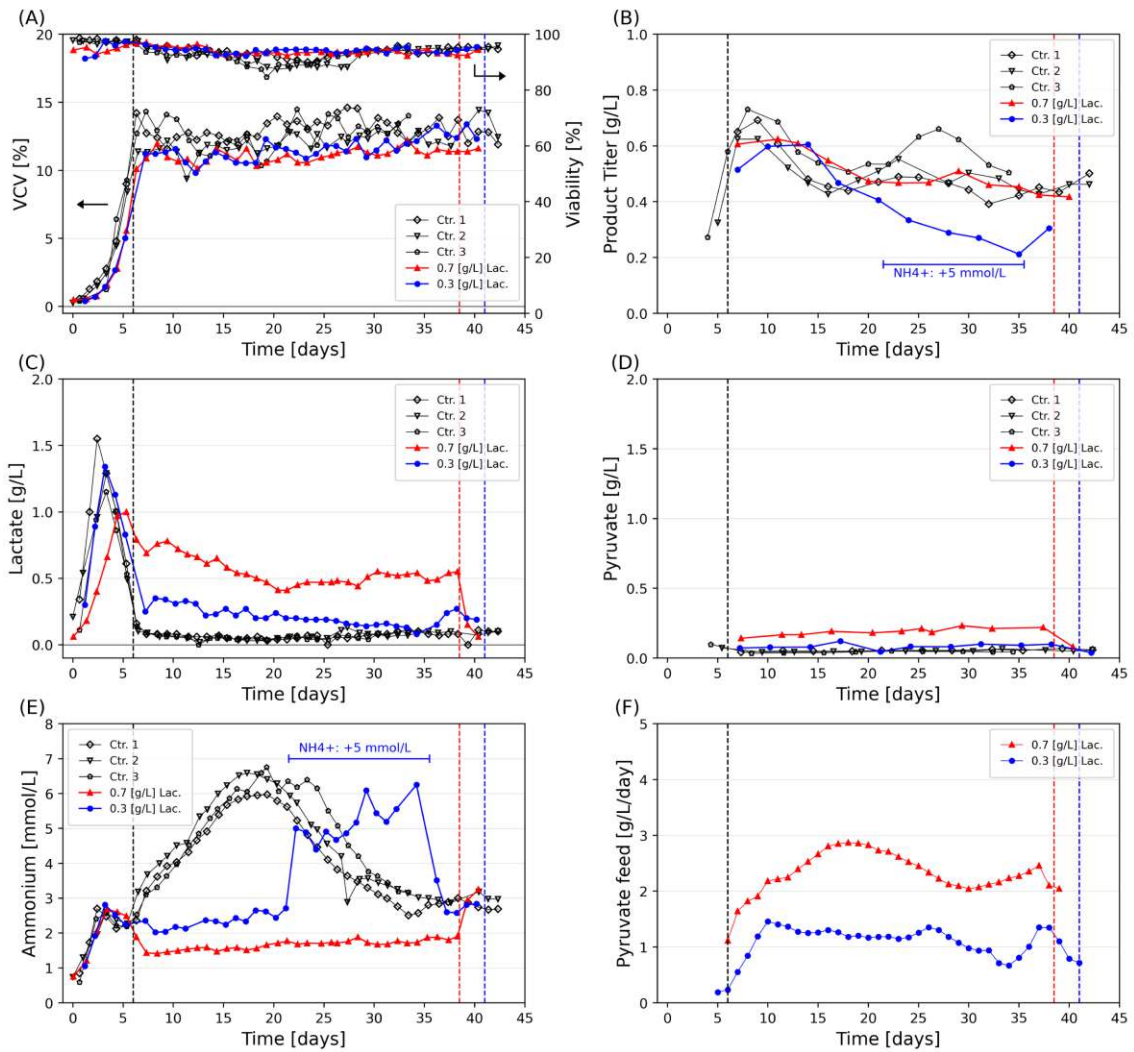


Figure 3.5: Cell culture parameter, nutrient and metabolite trends for steady-state perfusion cultivations. VCV and viability (A), product titer (B), lactate (C), pyruvate (D), ammonium (E) and pyruvate feed rate (F). The vertical black lines represent the start of Raman controlled pyruvate feeding and the blue and red vertical line represent the end of pyruvate feeding of the respective runs. Blue horizontal lines represent a phase of ammonium addition of 5 mmol L^{-1} to the perfusion media in the perfusion run with 0.3 g L^{-1} lactate setpoint.

perfusion process duration of over 40 days. While galactosylation and sialylation were stabilized in a comparable way, adjusting lactate setpoints could provide a method for moderate fine-tuning of these specific glycan forms. Unless specific preferences for galactosylation or sialylation favor higher lactate setpoints, reducing the lactate setpoint to 0.3 g L^{-1} or lower reduces the pyruvate feed consumption which translates into a more economic process. However, care should be taken that extensive lactate setpoint reduction does not compromise the TCA supplementation, as this would result in destabilization of the N-glycosylation species. Interestingly, additional ammonium supplementation did not impact the product quality at all

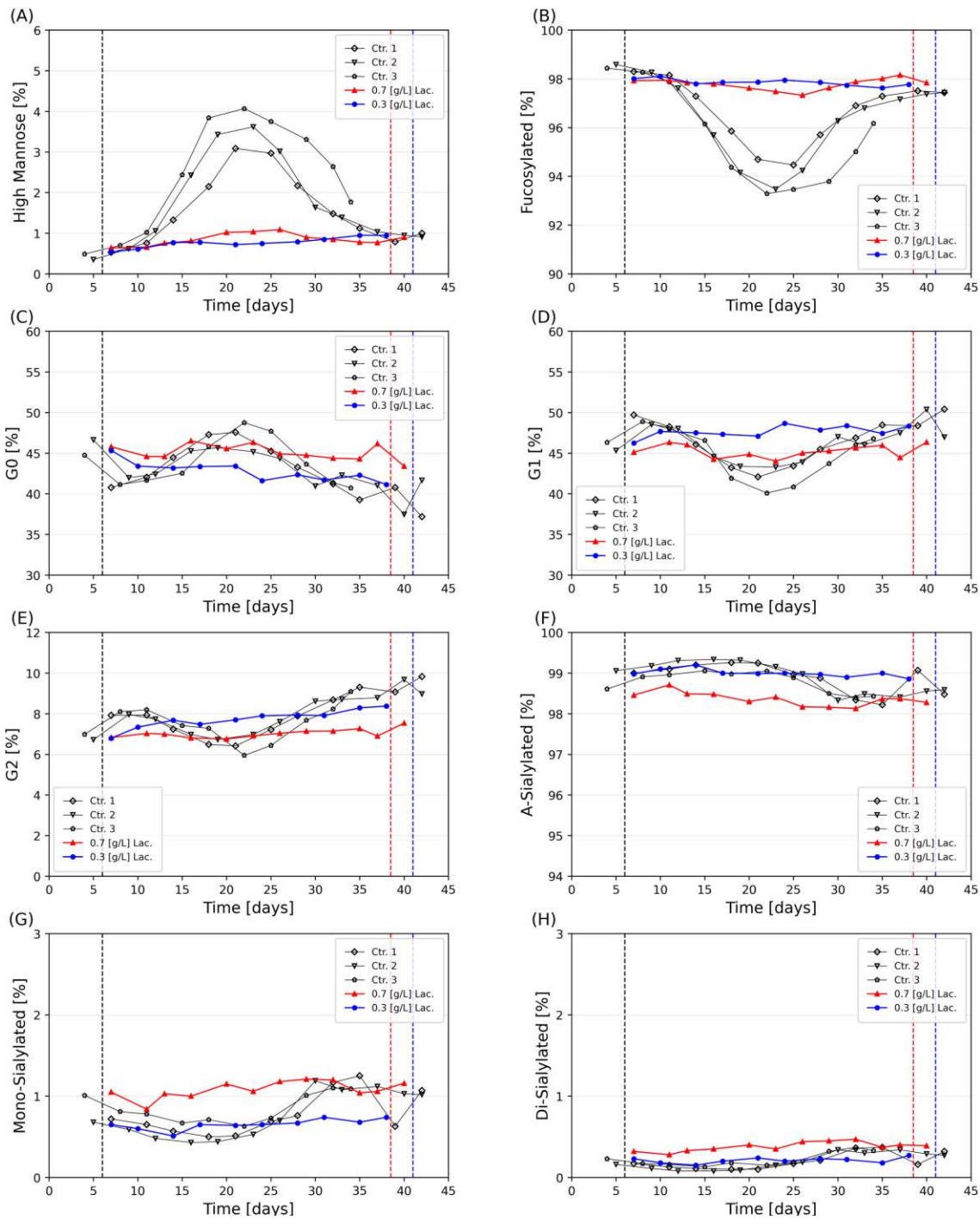


Figure 3.6: Product glycosylation profiles for steady-state perfusion cultivations. High mannose (A), fucosylation (B), G0 (C), G1 (D), G2 (E), a-sialylation (F), mono-sialylation (G) and di-sialylation (H). The vertical black lines represent the start of Raman controlled pyruvate feeding and the blue and red vertical line represent the end of pyruvate feeding of the respective runs. Blue horizontal lines represent a phase of ammonium addition of 5 mmol L^{-1} to the perfusion media in the perfusion run with 0.3 g L^{-1} lactate setpoint.

even though ammonium is well known to impact N-glycosylation [138, 139, 155]. This effect might have been masked in this study by sufficient TCA cycle saturation, thereby minimizing the impact of ammonium, but is not fully understood.

The Raman-controlled pyruvate feeding strategy represents a valuable platform tool for continuous manufacturing, effectively addressing one of the most substantial challenges in intensified perfusion processes – the need to compromise productivity for the sake of product quality. In general, all cell lines demonstrating a metabolic shift caused by insufficient TCA cycle saturation accompanied by accumulating ammonium concentration might profit from this control strategy. Rapid model calibration workflows enable early implementation into process development activities, helping to identify pyruvate feeding profiles. This allows to investigate manufacturing cell line specific pyruvate demands with ease. Should there be an altering pyruvate requirement over time, the on-demand pyruvate feeding strategy can be transferred to commercial manufacturing. If requirements remain constant, this strategy supports development in determining the optimal constant pyruvate feed rate. This exemplary application of a QbD approach, which bridges the knowledge between CPPs and CQAs, while utilizing PAT for real-time control, highlights the potential of real-time process control in a continuous manufacturing environment and shall serve as a blueprint for further process optimization efforts.

This section is based on the following publication: P. Romann, S. Schneider, D. Tobler, M. Jordan, A. Perilleux, J. Souquet, C. Herwig, J-M. Bielser, and T. K. Villiger, **Raman-controlled pyruvate feeding to control metabolic activity and product quality in continuous biomanufacturing**, 2023, Under review in *Biotechnology Journal*

3.1.3 Section III - Maduramycin, a novel glycosylation modulator for mammalian fed-batch and steady-state perfusion processes

On top of controlling product quality attributes at consistent levels throughout the manufacturing run, the ability to modulate product quality to fine-tune antibody effector functions such as ADCC, or to match reference product quality attributes in the biosimilar field, could offer substantial advantages to the biopharmaceutical industry [104]. A-fucosylation and high mannose glycan species are particular modulation targets given their role in enhancing ADCC, even though the effect of high mannose is attributed to its intrinsic a-fucosylation [83, 84, 86, 107, 108]. A practical strategy to increase ADCC involves therefore in increasing the proportion of less processed glycan species like high mannose through media supplementation of enzymatic inhibitors, arresting the glycan processing at an early stage. Kifunensine, the most popular α -mannosidase I inhibitor in the ER, has extensively been used in cell culture and mainly increases M8-M9 species [105, 107, 108, 158]. Although commercial mAbs primarily feature M5 type high mannose species, modulators that specifically increase M5 are scarce. Moreover, the use of these modulators has so far been limited to bolus additions in batch manufacturing or dynamic perfusion systems. Their suitability in continuous feeding regimes over prolonged process durations for steady-state perfusion, however, has yet to be explored [160].

Several compounds of the polyether ionophore family, molecules influencing the glycosylation machinery by increasing the pH in the Golgi [161, 162], were screened for their ability to selectively increase M5 glycans of mAb products. Maduramycin, in contrast to other promising polyether ionophores, showed the intended effect on all tested cell lines and was subsequently compared to kifunensine in continuous perfusion cultures by media supplementation. Continuous feeding of both maduramycin and kifunensine in separate perfusion runs did not disrupt stable operation at the target VCV setpoint and high viabilities were maintained throughout the duration of 35 days (Figure 3.7A). During this period, different modulator concentrations were targeted, incorporating both ascending and descending ramps, to assess the dynamics and the reversibility of the effect on glycosylation (Figure 3.7C and 3.7D). Glycosylation patterns of high mannose closely mirrored the modulator concentration trends were decreasing after reducing the modulator concentration, suggesting reversibility and no accumulation of maduramycin nor kifunensine within the cells (Figure 3.7E and 3.7F). The total high mannose proportion could be regulated in a concentration-dependent manner for both tested modulators, the effective high

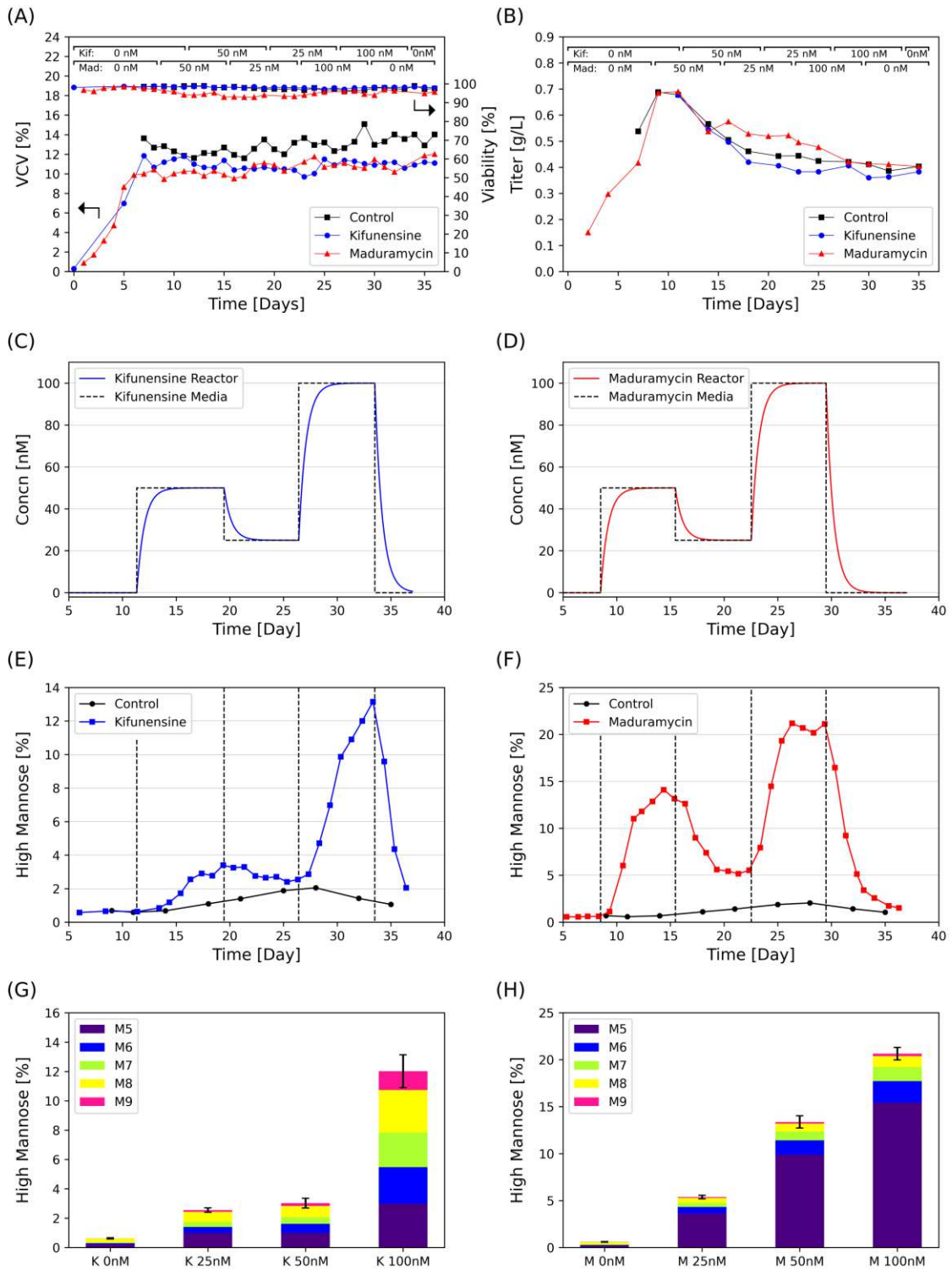


Figure 3.7: Steady-state perfusion process data at 2 L bioreactor scale for control run, kifunensine and maduramycin run producing a bispecific antibody. VCV and viability (A), process titer (B), feeding strategy and calculated modulator concentration in the bioreactor for kifunensine run (C) and for maduramycin run (D), with respective absolute HM levels for kifunensine run (E) and maduramycin (F). Steady-state HM glycoforms averaged over last 3 days before media change for kifunensine run (G) and for maduramycin run (H).

mannose distribution did however vary significantly. While kifunensine increased all high mannose type glycans, particularly M8-M9 (Figure 3.7G), maduramycin, as desired, mainly increased the M5 fraction (Figure 3.7H). Bispecific mAb titers did not decrease compared to the modulator-free control run, indicating no impact on process productivity (Figure 3.7B).

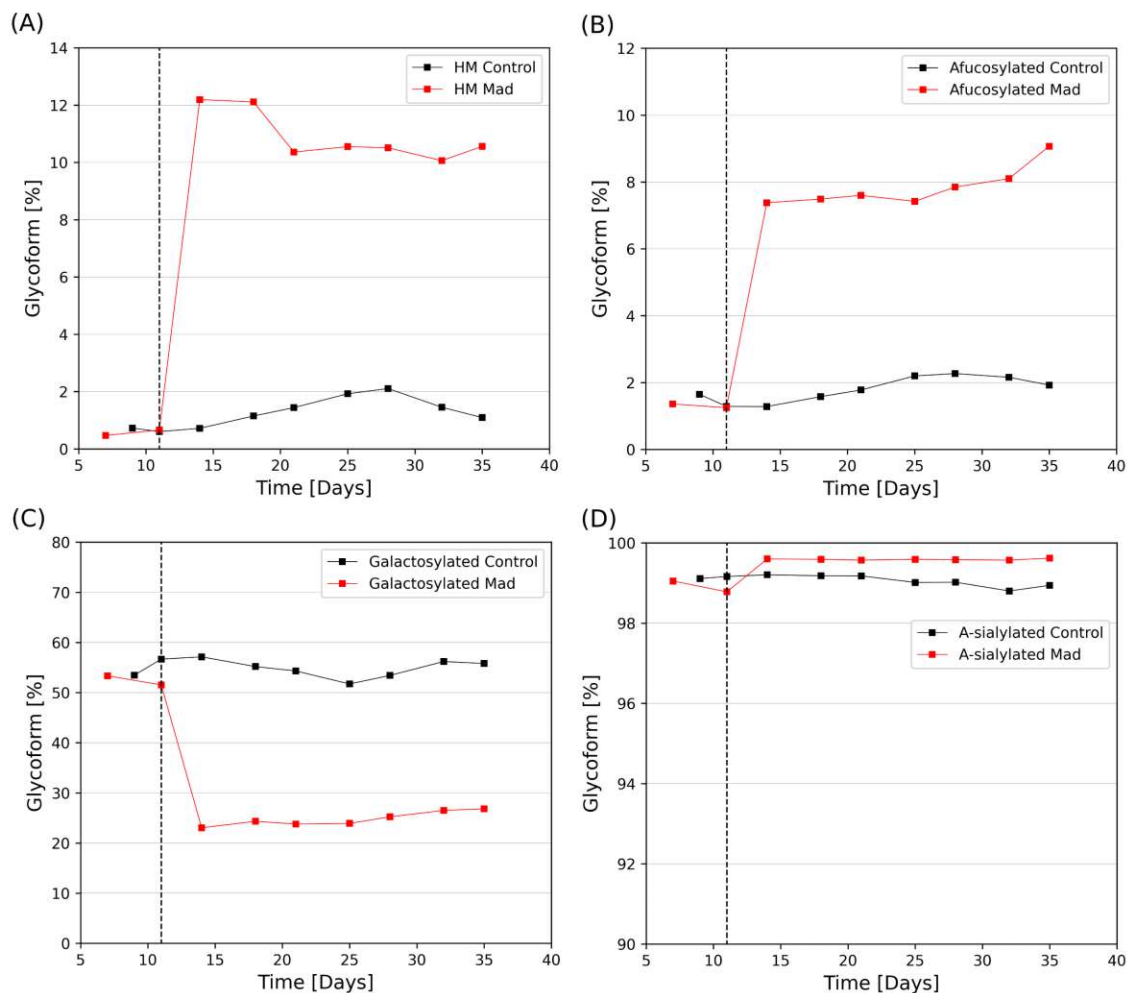


Figure 3.8: N-glycosylation data of steady-state perfusion process at 2 L bioreactor scale for continuous 50 nM maduramycin run and control run producing a bispecific antibody. Absolute HM (A), a-fucosylated species (B), galactosylated species (C) and a-sialylated species (D). The dashed lines represent the change from modulator free media to 50 nM maduramycin media on day 11.

The primary objective of this study was to develop a method to increase and control total HM glycoforms, specifically augmenting the high mannose M5 type glycan species, within a continuous steady-state perfusion process and maintain this altered glycan distribution stable over time. Constant maduramycin feeding supplemented to the cell culture media at 50 nM concentration increased HM from 0.7% to 12.2% and remained over 10% until the end of the run (Figure 3.8A). As anticipated due to their interdependency, afucosylation increased simultaneously

from approximately 2% to 8% (Figure 3.8B). At the same time, galactosylation decreased from 55% to 25% while asialylation remained rather constant around 99% (Figure 3.8C and 3.8D).

The discovered N-glycosylation modulators expand the current effector function modulating toolbox for biotherapeutics. Their applicability or extended steady-state perfusion processes without impacting culture performance make them a universal tool with regards to integrated continuous manufacturing processes. Once the relationship between the modulator concentration and its effect on N-glycosylation is understood, a straightforward continuous feeding regime, achieved by supplementing the culture media, allows to consistently modulate N-glycosylation. Given their complimentary effect on high mannose glycan distribution, and depending on the specific requirements, kifunensine, maduramycin, or a combination of both can be selected to fine-tune N-glycosylation. The demonstrated reversibility of modulation even enables real-time adjustments through concentration changes, an aspect that becomes particularly compelling once real-time glycan measurements are accessible. These modulators extend platform capabilities from product quality control to modulation, representing a particularly interesting tool to produce differently glycosylated biologics to investigate effector functions or match reference product quality in the biosimilars field.

This section is based on the following publication: P. Romann, T. Vuillemin, S. Pavone, M. Jordan, A. Perilleux, J. Souquet, J-M. Bielser, C. Herwig, and T. K. Villiger, **Maduramycin, a novel glycosylation modulator for mammalian fed-batch and steady-state perfusion processes**, 2023, Under review in *Journal of Biotechnology*

3.2 Productivity increase: Investigation of process intensification strategies and their impact on product quality

3.2.1 Section IV - Maximizing yield of perfusion cell culture processes: Evaluation and scale-up of continuous bleed recycling

Process intensification strategies to make processes more cost-efficient and sustainable are a major focus of manufacturers to stay competitive in the demanding market environment. Prolonging the cultivation period enabled by the real-time Raman-based product quality control framework was a first step towards improved process productivities of Merck's continuous manufacturing platform. Meanwhile, the bleed stream of a perfusion process, of which the liquid phase contains a substantial amount of product, represents another interesting target to further improve process productivity and reduce waste. Given that bleed rates often reach up to 30% of the perfusion rate, significant process intensification potential lies within either reducing the bleed stream or recovering the liquid fraction containing the product. While growth reduction to reduce bleed streams was associated with negative effects on process long-term stability [166], innovative bleed recycling applications have recently gained attention. Acoustic separators have been used in a proof-of-concept study to selectively concentrate the cell fraction of the perfusion bleed stream and recycling the liquid fraction back to the bioreactor ultimately increasing the perfusion harvest [285]. This resulted in significant product saving which otherwise would go to waste. As long as cells can be concentrated and separated, existing cell separation devices can be employed for such an application. However, to seriously consider incorporating bleed recycling into the continuous manufacturing platform, it is essential to gather knowledge about the advantages of various cell concentrating technologies. This includes understanding their efficiency, scalability, and the potential impact on product quality when employed in a continuous long-term bleed recycling scenario.

In this study, continuous bleed operation, which maintains uninterrupted liquid flow, was achieved by integrating the bleed recycling devices into the bleed stream. The clarified harvest stream was then recirculated back into the bioreactor. The recycle pump speed was automatically adjusted to a predefined fraction of the capacitance control process bleed pump. The difference between the inlet flow and the recirculation flow defined the effective concentrated waste stream (Figure 3.9A). For the first time, inclined gravity settlers (Figure 3.9C and D) were evaluated as bleed recycling device and compared to an acoustic separator (Figure 3.9B) with respect to bleed recycling efficiency, metabolite profiles, product quality attributes, cell debris removal, and ease of operation.

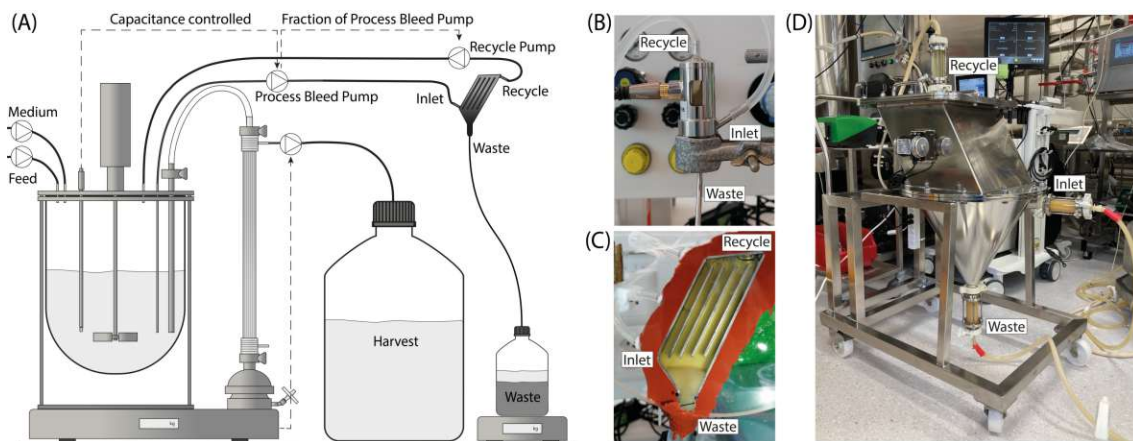


Figure 3.9: Schematic representation of the bleed recycling setup (A), lab-scale acoustic settler (B), lab-scale inclined gravity settler (C), and large-scale inclined gravity settler (D).

The evaluation of bleed recycling efficiencies revealed no observable difference between gravity settling and acoustic separation. VCV of the perfusion process, defining the VCV entering the bleed recycling device, is an important parameter that determines the settler recycle rate (Figure 3.10A). Conditions that lead to a gradual accumulation of biomass within the separation device, typically due to insufficient waste stream, were identified. These undesired conditions have provided a foundation for determining optimal recycle rates and depend heavily on the VCV in the inlet stream (Figure 3.10B). Assuming bleed recycling at optimal, non-accumulating conditions, estimates about the process yield increase can be made and provide useful information to estimate process yield increases depending on perfusion process characteristics (Figure 3.10C and D).

Except for lower debris removal, inclined gravity settling showed similar bleed recycling efficiency and no negative impact on cell viabilities, nutrient and metabolite levels and product N-glycosylation. Taking reduced system complexity and facilitated scale-up of gravity settlers into account, inclined gravity settling emerged as the favoured technology for further evaluation during a 42-day lab-scale perfusion process. The automated bleed recycling strategy (Figure 3.9A) was operated during two consecutive periods of 17 and 5 days to assess long-term effects on culture performance and product quality, could however also have been operated without interruption. No difference in culture stability concerning VCV setpoint and viability was observed (Figure 3.11A). During active bleed recycling phases in the perfusion process with a VCV setpoint of 12% and a bleed rate between 20% and 25%, the waste stream could be reduced by up to 3.5 times down to 6% effective bleed rate, resulting in a harvest rate increase of 19% (Figure 3.11B). Ammonium levels and pH were unaffected by bleed recycling operation (Figure 3.11C), solely debris levels

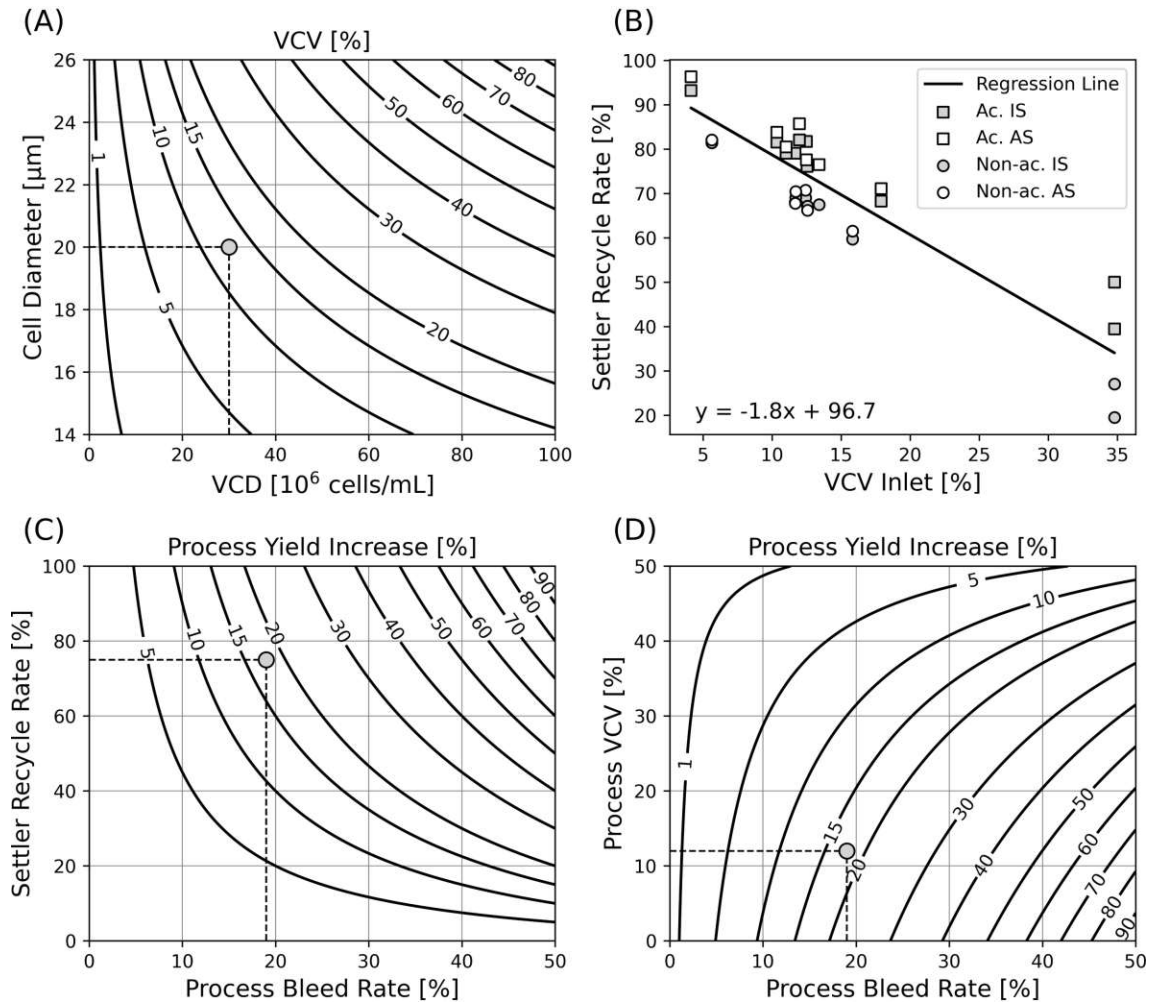


Figure 3.10: Bleed recycling efficiency data and performance calculations. VCV contour plot showing the relationship of VCD and average cell diameter for VCV (A). Experimental data to evaluate optimal recycle rates by accumulating and non-accumulating settler experiments (B). The straight line represents an expected accumulation limit based on linear regression of all data points. Process yield increase contour plot relating process bleed rate to settler recycle rate (C) or process VCV setpoint (D) assuming optimal settler recycle rate as evaluated by the regression line in (B). The points in (A), (C) and (D) serve as an example for a process bleed of approximately 20% with the specified VCV of roughly 12%. Acoustic settler (AS), Inclined Gravity Settler (IS).

slightly increased, did however not impede CRD performance as process titer remained high (Figure 3.11D). The long-term perfusion process validated that bleed recycling had no impact on product quality, such as high mannose or fucosylation (Figure 3.11E and F). Subsequent gravity settler scale-up designed to process bleed for a 2,000 L manufacturing scale perfusion bioreactor confirmed lab-scale efficiency and quality considerations.

Gravity settling has been identified bleed recycling technology with reduced complexity which is readily scalable to manufacturing scale. Significant volumetric

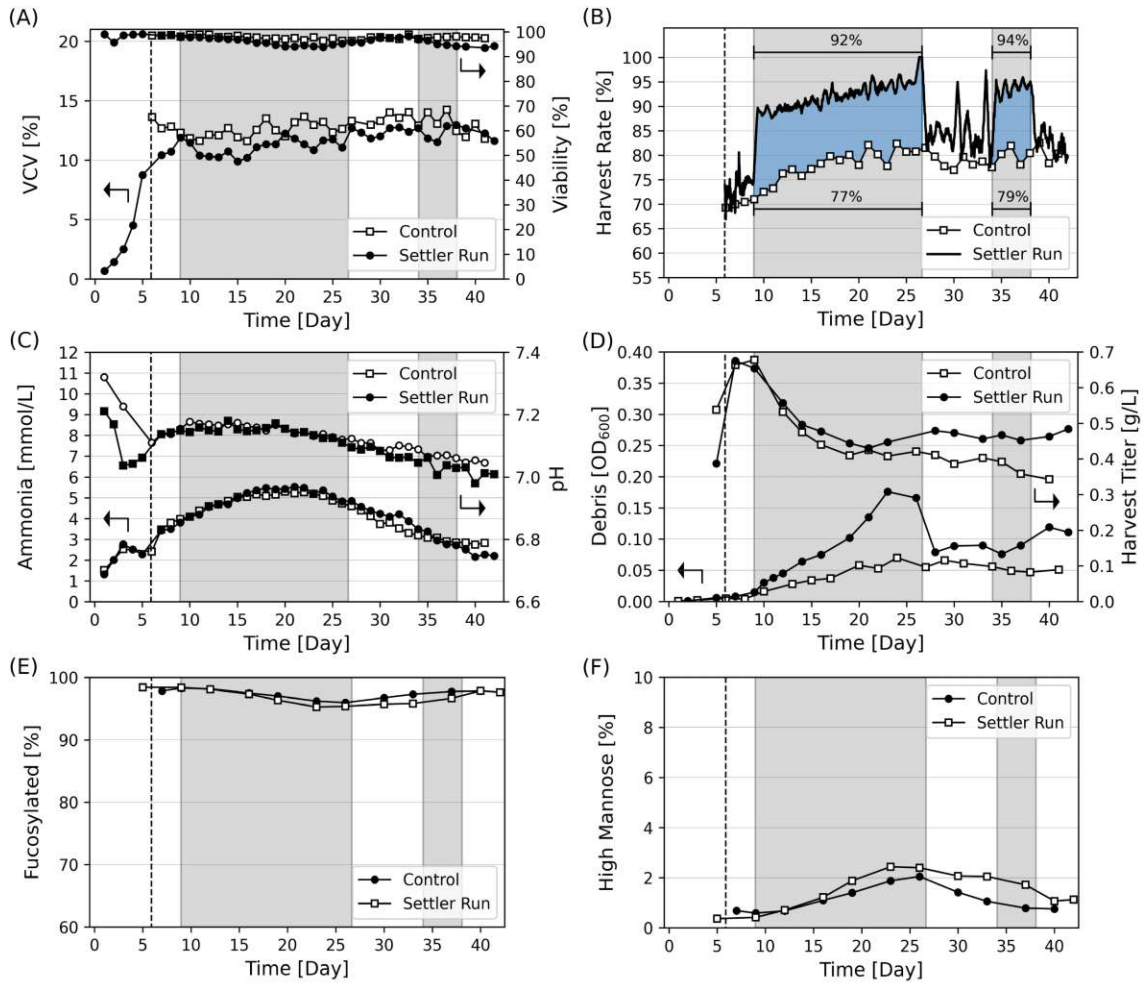


Figure 3.11: Process data of lab-scale 2 L perfusion settler run compared with a standard control run without bleed recycling for a bispecific mAb product. VCV and viability (A), process harvest rate (B), ammonia and pH profile (C), harvest titer and debris trend (D), high-mannose (D) and fucosylation (E). Grey areas represent process phases where bleed recycling was performed, whereas bleed recycling was turned off during white process phases.

productivity increases of 20% were demonstrated during long-term perfusion and waste was reduced 3-fold. This process intensification strategy can be connected to the perfusion processes without disturbing the cell culture, solely reducing the net bleed stream, and thereby increasing the harvest stream. The presented automation strategy adjusted the recirculation pump to the actual process bleed stream and required no operator interference throughout the entire perfusion run. Bleed recycling characterization across a variety of perfusion parameters supports informed decision-making regarding integration of bleed recycling into a particular perfusion process with the aim to reduce perfusion waste, increase process sustainability and boost overall process yield. Fully continuous operation enables integration into Merck's continuous manufacturing platform. With emerging technologies enabling

even higher biomass compaction, such as single use continuous centrifuges, bleed recycling efficiency might be even further improved and advanced PAT might support advanced control strategies to ensure maximal efficiency.

This section is based on the following publication: P. Romann, J. Kolar, L. Chappuis, C. Herwig, T. K. Villiger, and J.-M. Bielser, **Maximizing yield of perfusion cell culture processes: Evaluation and scale-up of continuous bleed recycling**, *Biochem. Eng. J.*, vol. 193, no. 2, p. 108873, Apr. 2023, DOI: 10.1016/j.bej.2023.108873.

3.2.2 Section V - Co-current filtrate flow in TFF perfusion processes: Decoupling transmembrane pressure from crossflow to improve product sieving

As cultivation durations extend and cell densities rise, further process intensifications such as bleed recycling continue to increase the loads on the hollow fiber-based cell retention devices. These intensified filtration conditions bear risk of premature filter clogging and severe product retention, major challenges that must be overcome while moving towards robust continuous manufacturing processes. While ATF systems showed improved product sieving [236–238], TFF systems were claimed to be better suited for manufacturing scale operations due to higher technology robustness with smaller facility footprint [211]. Irrelevantly of ATF or TFF operation, low filtrate fluxes in perfusion processes and high axial pressure drops within the filtration module generate a reverse flow of filtrate back into the fiber lumen at the filter exit, named Starling recirculation [288]. This backflush was credited with beneficial effects on product sieving by washing the membrane in ATF systems upon alternating the crossflow, whereas unidirectional TFF systems could not benefit [237, 289]. Nonetheless, this backflush must be compensated by an enhanced filtration flux at the filter inlet, which in turn puts additional stress on the filtration module. A more comprehensive understanding of the delicate balance between the advantageous effects of backflush and the added stress of Starling recirculation on filtration appears necessary. Approaches to control Starling recirculation independently of filter characteristics and the crossflow might allow to design more efficient TFF filtration systems that are ready to accommodate increased harvest volumes of intensified perfusion processes.

This study aimed at evaluating co-current filtrate flow in TFF systems to decouple transmembrane pressure from crossflow to improve product sieving in steady-state perfusion processes. In conventional TFF operation, the magnitude of the axial pressure drop within the fiber lumen is dependent on the crossflow, culture viscosity and filter characteristics. Even though a certain flexibility in filter choice and crossflow range is available, adjusting these parameters does not solve the fundamental problem of extensive Starling recirculation in TFF systems (Figure 3.12A). As an alternative strategy to diminish the axial pressure drop within the fiber lumen, efforts can also be directed towards achieving a similar axial pressure drop on the filtrate side as on the retentate side, resulting in a nearly uniform transmembrane pressure (TMP) throughout the module (Figure 3.12B). This concept, originally applied to control membrane polarization along the filter length to enable high resolution

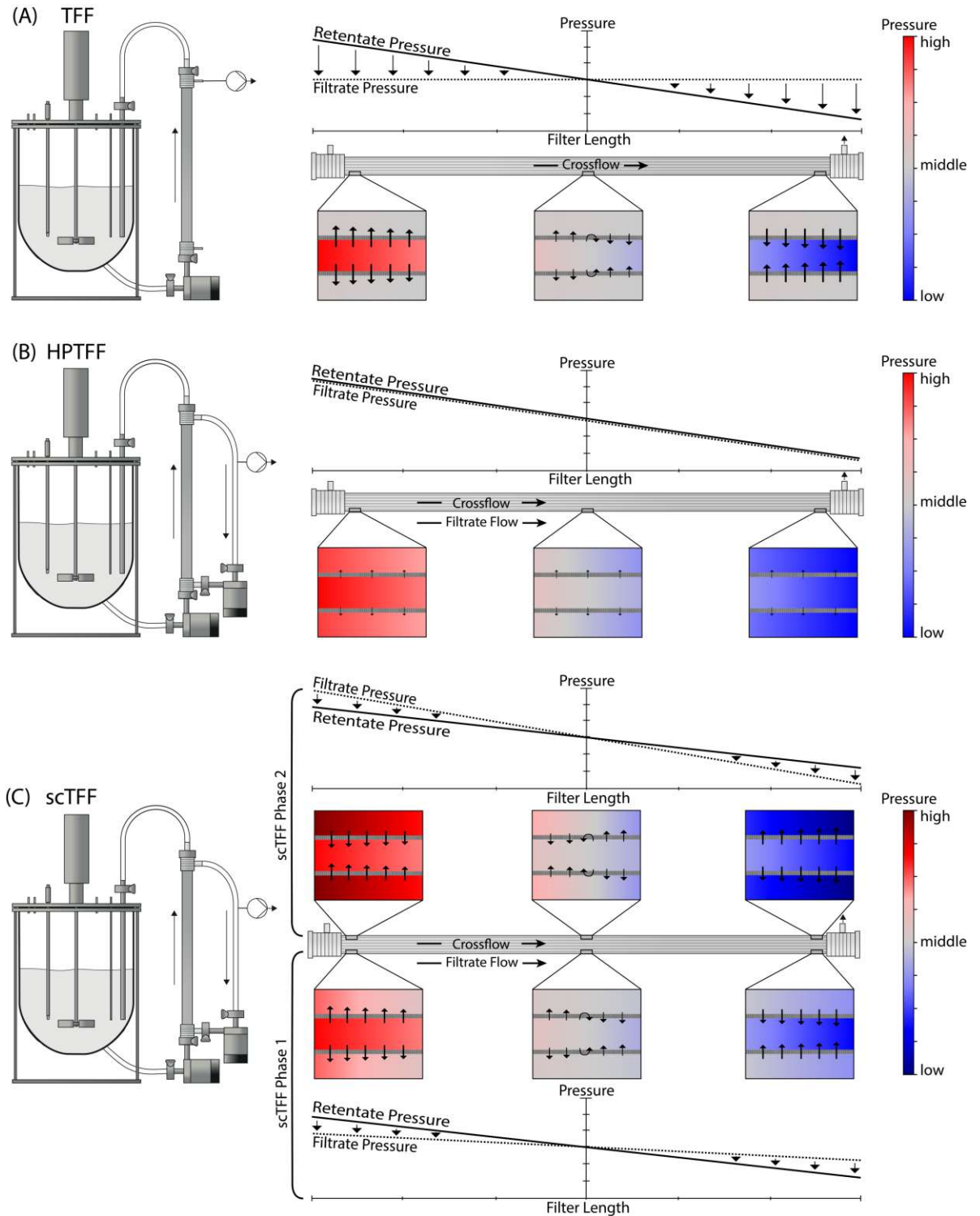


Figure 3.12: Schematic representation for TFF (A), HPTFF (B) and scTFF (C) systems with centrifugal pumps based on pressure characterization. Relative pressure curves along the filter length for each system are given and arrows indicate filtrate flux, longer arrows represent larger fluxes. Additionally, a zoom into a fiber at the beginning, middle and at the end of the filter is provided and colored from red (high pressure) to blue (low pressure). As scTFF consists of two phases, the situation for reduced (scTFF Phase 1) and enhanced co-current filtrate flow (scTFF Phase 2) and are depicted.

protein-protein separations in downstream operations, was coined High-Performance TFF (HPTFF) and was enabled by a co-current filtrate flow driven by an additional gear pump in a filtrate loop [290, 291]. In addition to translating the HPTFF concept from DSP operation to steady-state perfusion, a novel concept coined stepping co-current TFF (scTFF) was developed in this study to extend HPTFF operation with the ability to play with the Starling recirculation. Consequently, instead of generating a uniform TMP across the filtration module, the co-current filtrate flow is periodically increased or decreased to generate well-controlled membrane sweeping phases by Starling recirculation at the start or end of the filtration module (Figure 3.12C).

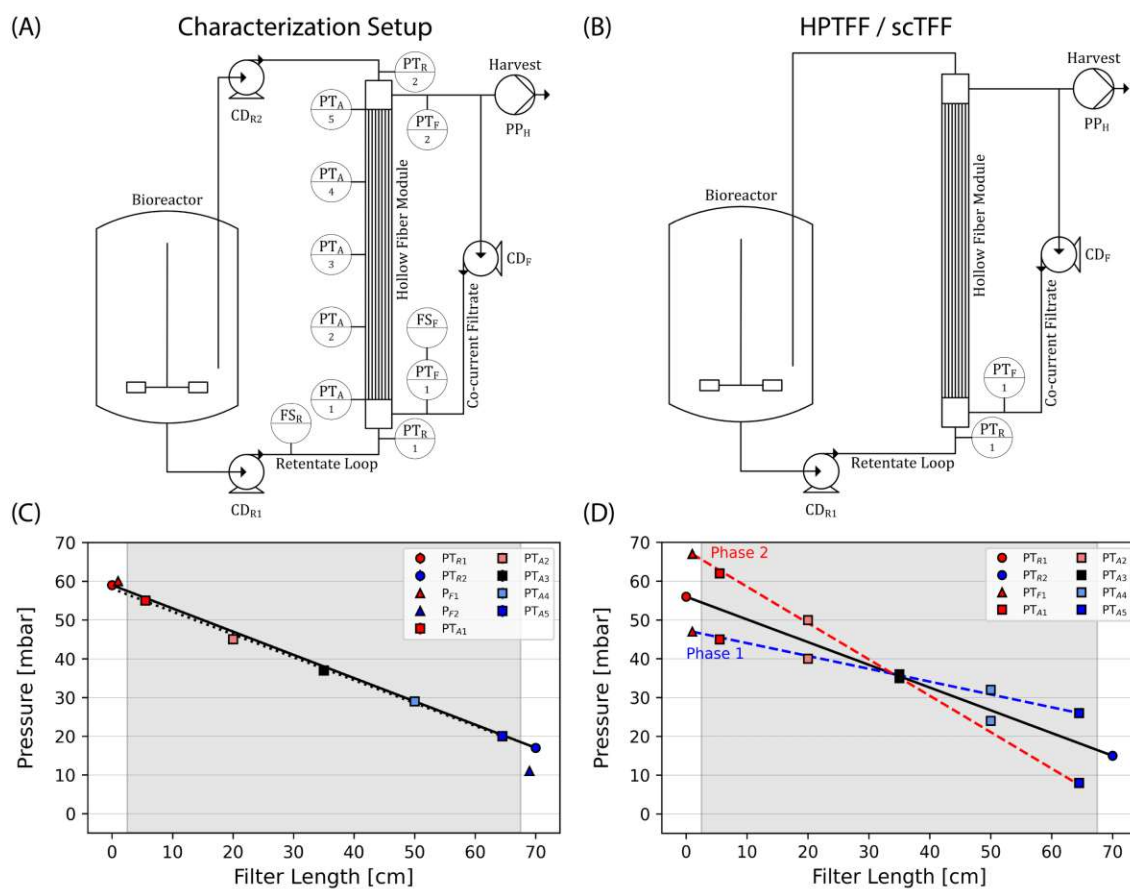


Figure 3.13: Detailed schematic representation of the experimental setup for the pressure characterization in water (A). Pressure transmitters (PT), flow sensors (FS), centrifugal pumps (CD) and peristaltic pumps (PP) are specified with subscripted letters according to their position (R: Retentate; F: Filtrate; A: Additional sensors on filtrate side; H: Harvest). Minimally required setup for HPTFF or scTFF operation used for cell culture runs are further shown (B). Pressure measurements according to their position along the filter length are provided for HPTFF (C) and scTFF (D) at 650 mL min^{-1} crossflow, grey areas represent absolute fiber length.

Co-current filtrate flow in TFF systems was achieved by inserting a second low-shear centrifugal pump (CD_F), identical to the pump in the cell loop (CD_{R1}), into

the filtrate loop directed towards the filter inlet. A pressure characterization setup with pressure sensors at both inlet and outlet of the retentate loop (PT_{R1} and PT_{R2}), and filtrate loop (PT_{F1} and PT_{F2}), and five additional pressure sensors along the filter length on the filtrate side (PT_{A1-5}) was built. Two flow sensors (FS_R and FS_F) were integrated to measure flows of the retentate and filtrate loop (Figure 3.13A). Pressure characterization studies revealed that ideal HPTFF conditions can be achieved by simply matching the filtrate loop inlet pressure (PT_{F1}) with the retentate loop inlet pressure (PT_{R1}) (Figure 3.13C). This allows a reduced design for controlling HPTFF operation in steady-state perfusion with only two pressure sensors (Figure 3.13B). The scTFF concept could further be validated by demonstrating the ability to adjust the TMP profile to achieve targeted backflush either at the filter outlet (scTFF Phase 1) or at the filter inlet (scTFF Phase 2) (Figure 3.13D). The same device setup as depicted for HPTFF in Figure 3.13B can be applied for scTFF, with the difference not to match PT_{F1} with PT_{R1} , but controlling at slightly reduced PT_{F1} (scTFF Phase 1) or elevated PT_{F1} (scTFF Phase 2). Additionally, pressure profiles revealed that HPTFF and scTFF are scalable to manufacturing scale by repeating pressure characterization using a large-scale filtration module.

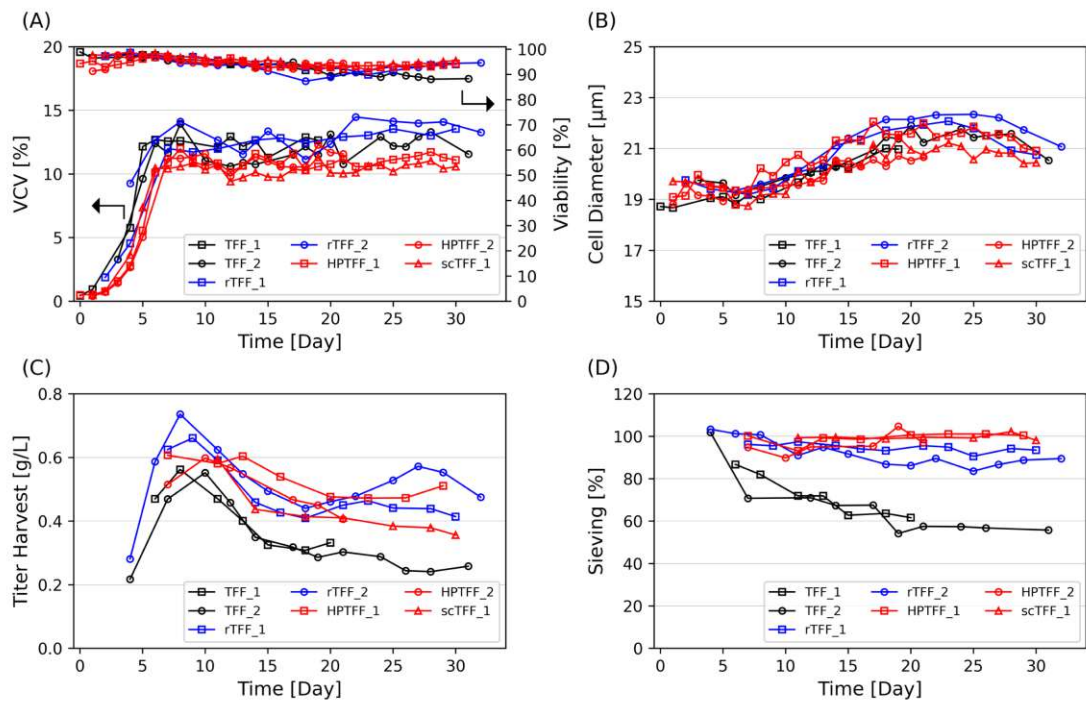


Figure 3.14: Perfusion cell culture runs with TFF (black), rTFF (blue), HPTFF or scTFF (red) as cell retention devices. VCV and viability (A), cell diameter (B), harvest titer (C) and product sieving (D).

The benefits of HPTFF operation or precise control of the direction and inten-

sity of Starling recirculation in scTFF operation was subsequently demonstrated in steady-state perfusion cell culture processes. Comparison to standard TFF reveal up to 40% higher product sieving and even outperformed reverse TFF (rTFF), a system featuring alternating crossflow driven by two inversely positioned centrifugal pumps in the cell loop (Figure 3.14D). At the same time, no impact on cell parameters was observed (Figure 3.14A and B) and product titer remain high (Figure 3.14C).

Co-current filtrate flow in unidirectional TFF systems represents an interesting and scalable extension to standard TFF or alternating TFF operation when dealing with growing volumes of harvest due to process intensification. The flexibility to adjust the duration, frequency, and extent of Starling recirculation in HPTFF or scTFF operation resulted in highest product sieving performance under intensified perfusion process conditions. Decoupling of TMP from crossflow and filter characteristics, thereby enabling control of local TMP along the filtration module, addresses common obstacles associated with filter length constraints and crossflow restrictions. This opens an entirely new playground to optimize filtration performance of unidirectional as well as of alternating TFF systems, consequently reducing CRD-related bottlenecks in intensified steady-state perfusion processes.

This section is based on the following publication: P. Romann, P. Giller, A. Sibia, C. Herwig, A. Zydney, A. Perilleux, J. Souquet, J-M. Bielser, and T. K. Villiger, **Co-current filtrate flow in TFF perfusion processes: Decoupling transmembrane pressure from crossflow to improve product sieving**, 2023, Under review in *Biotechnology and Bioengineering*.

4 Concluding Remark

Continuous manufacturing of biologics offers immense potential for process intensification, helping manufacturers maintain competitiveness in a diversifying market environment. Maximizing benefits from continuous manufacturing requires time-independent product quality profiles for highest operational flexibility. However, maintaining process stability often presents a delicate balance between optimizing productivity without compromising product quality. This Thesis tackled both aspects - intensifying processes to bolster productivity, while also introducing a framework for product quality control.

The quality control framework, developed in line with the Quality by Design (QbD) principle, comprises three primary components: a glycosylation modulator, an indirect metabolic marker (which links culture conditions to product quality if the modulator itself cannot be easily quantified), and a PAT sensor that includes a novel PAT calibration approach specifically tailored for steady-state perfusion processes. The sensor monitors the metabolic marker in real time, enabling an on-demand modulator feeding strategy to ensure consistent product quality outcomes. This novel calibration strategy accelerates the creation of robust and accurate prediction models to a matter of days, rather than months. It not only reduces costs and eases the implementation of various PAT in continuous perfusion processes but can also be translated to cDSP monitoring. Leveraging pyruvate as an effective glycosylation lever, lactate as indirect metabolic marker that estimates TCA cycle saturation and allows to detect pyruvate shortage, coupled with Raman spectroscopy enabled effective control of product quality in an intensified CHO perfusion process, demonstrating the feasibility of the proposed quality control framework. This process, producing a bispecific antibody, achieved time-independent quality profiles, qualifying for seamless integration into the envisioned integrated continuous manufacturing platform. Moreover, novel glycosylation modulators such as maduramycin were found to effectively fine-tune N-glycosylation, ultimately allowing to fine-tune ADCC. Their applicability as media supplements in continuous feeding regimes augment the toolbox for quality modulation of the continuous manufacturing platform.

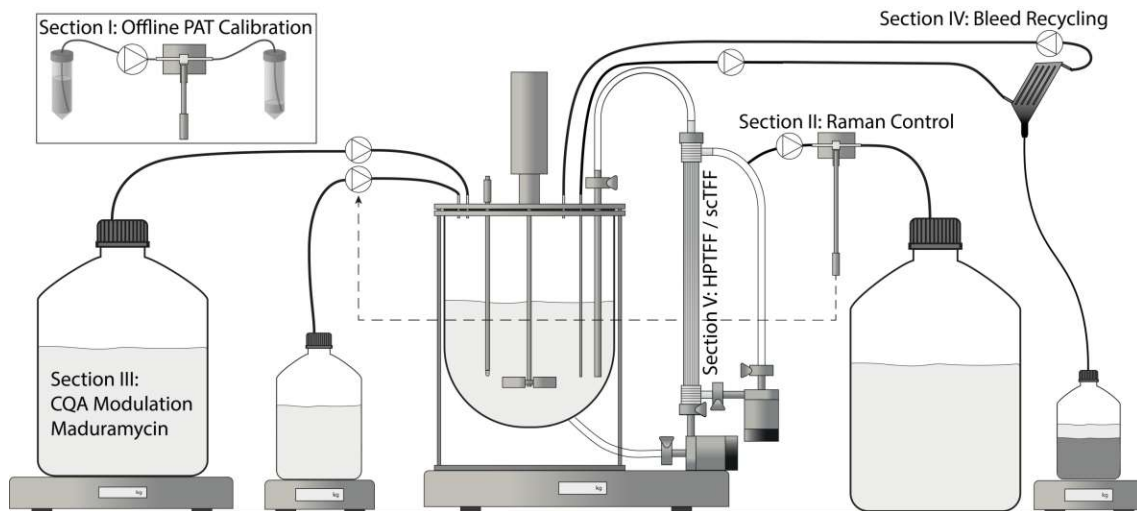


Figure 4.1: Schematic overview where the different Section integrate into the steady-state perfusion platform. **Section I:** Novel offline calibration method for PAT tools. **Section II:** Raman-based pyruvate feeding strategy to ensure consistent product quality. **Section III:** Medium supplementation with modulators to fine-tune N-glycosylation. **Section IV:** Bleed recycling to reduce process waste and increase productivity. **Section V:** Improved TFF by applying co-current filtrate flow to alleviate product retention.

Process intensification strategies to boost volumetric productivity of perfusion bioreactors is crucial for achieving cost-effective manufacturing. While the presented quality control framework resulting in time-independent product quality enabled significant prolongation of the perfusion process run time, innovative bleed recycling applications were investigated to simultaneously increase the product harvest stream. Gravity settling was identified as a scalable technology that increased the process yield by 19% by recycling the liquid fraction of the bleed stream without impacting product quality. Upcoming technologies such as continuous single-use centrifuges might further advance the recycling potential. With further process intensification expected in the future, harvest volumes and protein concentration are expected to rise, whereas higher cell densities will contribute to even more challenging filtration matrices. To address the increased filtration challenge and avoid premature filter clogging or extensive product retention, a novel TFF strategy was introduced to perfusion processing. By upgrading existing TFF systems with a co-current filtrate flow, which minimizes or eliminates Starling recirculation within the hollow fiber module, maximum product passage was achieved compared to nearly 40% retention in standard TFF operation. As a result, this strategic enhancement to the TFF system significantly reduces current CRD-related bottlenecks in steady-state perfusion processes and contributes to the overall robustness of the continuous manufacturing platform.

Regarding the scope of this work, a better understanding of process intensification and its impact on product quality was generated, while the presented quality control framework supports leveraging the intensification potential of continuous perfusion processes without compromising consistency of product quality profiles (Figure 4.1).

Bibliography

- [1] F. G Banting, M.B Best, and B.A Best. “The Internal Secretion of the Pancreas”. In: *Journal of Laboratory and Clinical Medicine* VII.5 (1922), pp. 251–266.
- [2] Gilbert C. White et al. “Use of Recombinant Antihemophilic Factor in the Treatment of Two Patients with Classic Hemophilia”. In: *The New England journal of medicine* 320.3 (1989), pp. 166–170.
- [3] Ignazio Vecchio et al. “The discovery of insulin: An important milestone in the history of medicine”. In: *Frontiers in Endocrinology* 9.October (2018), pp. 1–8. ISSN: 16642392. DOI: 10.3389/fendo.2018.00613.
- [4] G. Köhler and C. Milstein. “Continuous Cultures of Fused Cells Secreting Antibody of Predefined Specificity”. In: *Nature* 256 (1975), pp. 495–497.
- [5] Peter A. Todd and Rex N. Brogden. “Muromonab CD3: A Review of its Pharmacology and Therapeutic Potential”. In: *Drugs* 37.6 (1989), pp. 871–899. ISSN: 11791950. DOI: 10.2165/00003495-198937060-00004.
- [6] Xiaochen Lyu et al. “The global landscape of approved antibody therapies”. In: *Antibody Therapeutics* 5.4 (2022), pp. 233–257. ISSN: 2516-4236. DOI: 10.1093/abt/tbac021.
- [7] Theo Vos et al. “Global, regional, and national incidence, prevalence, and years lived with disability for 301 acute and chronic diseases and injuries in 188 countries, 1990–2013: a systematic analysis for the Global Burden of Disease Study 2013”. In: *The Lancet* 386.9995 (2015), pp. 743–800. ISSN: 01406736. DOI: 10.1016/S0140-6736(15)60692-4.
- [8] Christina Fitzmaurice et al. “Global, regional, and national cancer incidence, mortality, years of life lost, years lived with disability, and disability-adjusted life-years for 32 cancer groups, 1990 to 2015: A Systematic Analysis for the Global Burden of Disease Study Global Burden ”. In: *JAMA Oncology* 3.4 (2017), pp. 524–548. ISSN: 23742445. DOI: 10.1001/jamaoncol.2016.5688.

- [9] Mariam Elshiaty, Hannah Schindler, and Petros Christopoulos. “Principles and current clinical landscape of multispecific antibodies against cancer”. In: *International Journal of Molecular Sciences* 22.11 (2021). ISSN: 14220067. DOI: 10.3390/ijms22115632.
- [10] Abhinav A. Shukla et al. “Evolving trends in mAb production processes”. In: *Bioengineering & Translational Medicine* 2.1 (2017), pp. 58–69. ISSN: 23806761. DOI: 10.1002/btm2.10061.
- [11] James N. Arnold et al. “The Impact of Glycosylation on the Biological Function and Structure of Human Immunoglobulins”. In: *Annual Review of Immunology* 25.1 (2007), pp. 21–50. ISSN: 0732-0582. DOI: 10.1146/annurev.immunol.25.022106.141702.
- [12] Taketoshi Yoshida et al. “Memory B and memory plasma cells”. In: *Immunological Reviews* 237.1 (2010), pp. 117–139. ISSN: 01052896. DOI: 10.1111/j.1600-065X.2010.00938.x.
- [13] Leonard G. Presta. “Engineering of therapeutic antibodies to minimize immunogenicity and optimize function”. In: *Advanced Drug Delivery Reviews* 58.5-6 (2006), pp. 640–656. ISSN: 0169409X. DOI: 10.1016/j.addr.2006.01.026.
- [14] Harry W. Schroeder and Lisa Cavacini. “Structure and function of immunoglobulins”. In: *Journal of Allergy and Clinical Immunology* 125.2 (2010), S41–S52. ISSN: 00916749. DOI: 10.1016/j.jaci.2009.09.046.
- [15] Gestur Vidarsson, Gillian Dekkers, and Theo Rispens. “IgG subclasses and allotypes: From structure to effector functions”. In: *Frontiers in Immunology* 5.OCT (2014), pp. 1–17. ISSN: 16643224. DOI: 10.3389/fimmu.2014.00520.
- [16] Ruei-Min Lu et al. “Development of therapeutic antibodies for the treatment of diseases”. In: *Journal of Biomedical Science* 27.1 (2020), p. 1. ISSN: 1423-0127. DOI: 10.1186/s12929-019-0592-z.
- [17] Bharath Wootla, Aleksandar Denic, and Moses Rodriguez. “Polyclonal and Monoclonal Antibodies in Clinic”. In: *Methods in Molecular Biology*. Vol. 1060. 2014, pp. 79–110. ISBN: 9781627035859. DOI: 10.1007/978-1-62703-586-6_5.
- [18] Gary Walsh. “Biopharmaceutical benchmarks 2018”. In: *Nature Biotechnology* 36.12 (2018), pp. 1136–1145. ISSN: 1087-0156. DOI: 10.1038/nbt.4305.

- [19] Christoph Spiess, Qianting Zhai, and Paul J. Carter. “Alternative molecular formats and therapeutic applications for bispecific antibodies”. In: *Molecular Immunology* 67.2 (2015), pp. 95–106. ISSN: 18729142. DOI: 10.1016/j.molimm.2015.01.003.
- [20] Juliana T. W. Tong et al. “An Insight into FDA Approved Antibody-Drug Conjugates for Cancer Therapy”. In: *Molecules* 26.19 (2021), p. 5847. ISSN: 1420-3049. DOI: 10.3390/molecules26195847.
- [21] Asher Mullard. “FDA approves first bispecific”. In: *Nature Reviews Drug Discovery* 14.1 (2015), pp. 7–7. ISSN: 1474-1776. DOI: 10.1038/nrd4531.
- [22] Natalia Nuñez-Prado et al. “The coming of age of engineered multivalent antibodies”. In: *Drug Discovery Today* 20.5 (2015), pp. 588–594. ISSN: 13596446. DOI: 10.1016/j.drudis.2015.02.013.
- [23] S. Songsivilai and P Lachmann. “Bispecific antibody: a tool for diagnosis and treatment of disease”. In: *Clinical & Experimental Immunology* 79 (1990), pp. 315–321.
- [24] B. Vijayalakshmi Ayyar, Sushrut Arora, and Richard O’Kennedy. “Coming-of-Age of Antibodies in Cancer Therapeutics”. In: *Trends in Pharmacological Sciences* 37.12 (2016), pp. 1009–1028. ISSN: 01656147. DOI: 10.1016/j.tips.2016.09.005.
- [25] Anuradha Krishnamurthy and Antonio Jimeno. “Bispecific antibodies for cancer therapy: A review”. In: *Pharmacology & Therapeutics* 185.December 2017 (2018), pp. 122–134. ISSN: 01637258. DOI: 10.1016/j.pharmthera.2017.12.002.
- [26] Brian Hassett et al. “Manufacturing history of etanercept (Enbrel [®]): Consistency of product quality through major process revisions”. In: *mAbs* 10.1 (2018), pp. 159–165. ISSN: 1942-0862. DOI: 10.1080/19420862.2017.1388483.
- [27] Bernie Scallon et al. “Binding and Functional Comparisons of Two Types of Tumor Necrosis Factor Antagonists”. In: *Journal of Pharmacology and Experimental Therapeutics* 301.2 (2002), pp. 418–426. ISSN: 0022-3565. DOI: 10.1124/jpet.301.2.418.
- [28] K. Naito et al. “Calicheamicin-conjugated humanized anti-CD33 monoclonal antibody (gemtuzumab zogamicin, CMA-676) shows cytotoxic effect on CD33-positive leukemia cell lines, but is inactive on P-glycoprotein-expressing sub-

lines”. In: *Leukemia* 14.8 (2000), pp. 1436–1443. ISSN: 08876924. DOI: 10.1038/sj.leu.2401851.

- [29] Mahesh Swaminathan and Jorge E. Cortes. “Update on the role of gemtuzumab-ozogamicin in the treatment of acute myeloid leukemia”. In: *Therapeutic Advances in Hematology* 14 (2023), pp. 1–10. ISSN: 20406215. DOI: 10.1177/20406207231154708.
- [30] Mark Sanford. “Blinatumomab: First Global Approval”. In: *Drugs* 75.3 (2015), pp. 321–327. ISSN: 0012-6667. DOI: 10.1007/s40265-015-0356-3.
- [31] International Conference on Harmonisation of Technical Requirements for Registration of Pharmaceuticals for Human Use. *ICH Harmonised Tripartite Guideline: Pharmaceutical Development Q8*. 2005. URL: <http://www.ich.org/>.
- [32] International Conference on Harmonisation of Technical Requirements for Registration of Pharmaceuticals for Human Use. *ICH Harmonised Tripartite Guideline: Quality Risk Management Q9*. 2005. URL: <http://www.ich.org/>.
- [33] International Conference on Harmonisation of Technical Requirements for Registration of Pharmaceuticals for Human Use. *ICH Harmonised Tripartite Guideline: Pharmaceutical Quality Systems Q10*. 2008. URL: <http://www.ich.org/>.
- [34] International Conference on Harmonisation of Technical Requirements for Registration of Pharmaceuticals for Human Use. *ICH Harmonised Tripartite Guideline: Development and Manufacture of Drug Substances (Chemical Entities and Biotechnological/Biological Entities) Q11*. 2011. URL: <http://www.ich.org/>.
- [35] International Conference on Harmonisation of Technical Requirements for Registration of Pharmaceuticals for Human Use. *ICH Harmonised Tripartite Guideline: Pharmaceutical Development Q8(R2)*. 2009. URL: <http://www.ich.org/>.
- [36] “Quality attributes of recombinant therapeutic proteins: An assessment of impact on safety and efficacy as part of a quality by design development approach”. In: *Biotechnology Progress* 28.3 (2012), pp. 608–622. ISSN: 87567938. DOI: 10.1002/btpr.1548.

- [37] Klaus Buttenschoen, Peter Radermacher, and Hendrik Bracht. “Endotoxin elimination in sepsis: physiology and therapeutic application”. In: *Langenbeck’s Archives of Surgery* 395.6 (2010), pp. 597–605. ISSN: 1435-2443. DOI: 10.1007/s00423-010-0658-6.
- [38] A.J Shepherd, N.J Wilson, and K.T Smith. “Characterisation of endogenous retrovirus in rodent cell lines used for production of biologicals”. In: *Biologicals* 31.4 (2003), pp. 251–260. ISSN: 10451056. DOI: 10.1016/S1045-1056(03)00065-4.
- [39] Pierre Olivier Duroy et al. “Characterization and mutagenesis of Chinese hamster ovary cells endogenous retroviruses to inactivate viral particle release”. In: *Biotechnology and Bioengineering* 117.2 (2020), pp. 466–485. ISSN: 10970290. DOI: 10.1002/bit.27200.
- [40] International Conference on Harmonisation of Technical Requirements for Registration of Pharmaceuticals for Human Use. *ICH Harmonised Tripartite Guideline: Viral Safety Evaluation of Biotechnology Products Derived from Cell Lines of Human or Animal Origin, Q5A(R1)*. 1999. URL: <http://www.ich.org/>.
- [41] D.E. Wierenga, J. Cogan, and J.C. Petricciani. “Administration of Tumor Cell Chromatin to Immunosuppressed and Non-immunosuppressed Non-human Primates”. In: *Biologicals* 23.3 (1995), pp. 221–224. ISSN: 10451056. DOI: 10.1006/biol.1995.0036.
- [42] G Scherthaner. “Immunogenicity and Allergenic Potential of Animal and Human Insulins”. In: *Diabetes Care* 16 (1993), pp. 155–165.
- [43] Basant Sharma. “Immunogenicity of therapeutic proteins. Part 3: Impact of manufacturing changes”. In: *Biotechnology Advances* 25.3 (2007), pp. 325–331. ISSN: 07349750. DOI: 10.1016/j.biotechadv.2007.01.007.
- [44] Daniel J. Kroon, Alysia Baldwin-Ferro, and Praful Lalan. “Identification of Sites of Degradation in a Therapeutic Monoclonal Antibody by Peptide Mapping”. In: *Pharmaceutical Research* 9.11 (1992), pp. 1386–1393.
- [45] Hongcheng Liu et al. “Heterogeneity of Monoclonal Antibodies”. In: *Journal of Pharmaceutical Sciences* 97.7 (2008), pp. 2426–2447. ISSN: 00223549. DOI: 10.1002/jps.21180.

- [46] Andrea Bertolotti-Ciarlet et al. “Impact of methionine oxidation on the binding of human IgG1 to FcRn and Fc γ receptors”. In: *Molecular Immunology* 46.8-9 (2009), pp. 1878–1882. ISSN: 01615890. DOI: 10.1016/j.molimm.2009.02.002.
- [47] Satoshi Ohtake, Shaoxin Feng, and Evgenyi Shalaev. “Effect of Water on the Chemical Stability of Amorphous Pharmaceuticals: 2. Deamidation of Peptides and Proteins”. In: *Journal of Pharmaceutical Sciences* 107.1 (2018), pp. 42–56. ISSN: 00223549. DOI: 10.1016/j.xphs.2017.09.003.
- [48] Weirong Wang et al. “Impact of methionine oxidation in human IgG1 Fc on serum half-life of monoclonal antibodies”. In: *Molecular Immunology* 48.6-7 (2011), pp. 860–866. ISSN: 01615890. DOI: 10.1016/j.molimm.2010.12.009.
- [49] Bingchuan Wei et al. “Glycation of antibodies: Modification, methods and potential effects on biological functions”. In: *mAbs* 9.4 (2017), pp. 586–594. ISSN: 1942-0862. DOI: 10.1080/19420862.2017.1300214.
- [50] Andrew M. Goetze et al. “Rates and impact of human antibody glycation in vivo”. In: *Glycobiology* 22.2 (2012), pp. 221–234. ISSN: 0959-6658. DOI: 10.1093/glycob/cwr141.
- [51] Cynthia Quan et al. “A study in glycation of a therapeutic recombinant humanized monoclonal antibody: Where it is, how it got there, and how it affects charge-based behavior”. In: *Analytical Biochemistry* 373.2 (2008), pp. 179–191. ISSN: 00032697. DOI: 10.1016/j.ab.2007.09.027.
- [52] Keith A. Johnson et al. “Cation exchange–HPLC and mass spectrometry reveal C-terminal amidation of an IgG1 heavy chain”. In: *Analytical Biochemistry* 360.1 (2007), pp. 75–83. ISSN: 00032697. DOI: 10.1016/j.ab.2006.10.012.
- [53] Lawrence W. Dick et al. “C-terminal lysine variants in fully human monoclonal antibodies: Investigation of test methods and possible causes”. In: *Biotechnology and Bioengineering* 100.6 (2008), pp. 1132–1143. ISSN: 00063592. DOI: 10.1002/bit.21855.
- [54] Bernhard Antes et al. “Analysis of lysine clipping of a humanized Lewis-Y specific IgG antibody and its relation to Fc-mediated effector function”. In: *Journal of Chromatography B* 852.1-2 (2007), pp. 250–256. ISSN: 15700232. DOI: 10.1016/j.jchromb.2007.01.024.

- [55] Sheng Gu et al. “Characterization of trisulfide modification in antibodies”. In: *Analytical Biochemistry* 400.1 (2010), pp. 89–98. ISSN: 00032697. DOI: 10.1016/j.ab.2010.01.019.
- [56] Douglas D. Banks et al. “Removal of Cysteinylation from an Unpaired Sulfhydryl in the Variable Region of a Recombinant Monoclonal IgG1 Antibody Improves Homogeneity, Stability, and Biological Activity”. In: *Journal of Pharmaceutical Sciences* 97.2 (2008), pp. 775–790. ISSN: 00223549. DOI: 10.1002/jps.21014.
- [57] Xiaoping Z. He, Amy H. Que, and Jim J. Mo. “Analysis of charge heterogeneities in mAbs using imaged CE”. In: *Electrophoresis* 30.5 (2009), pp. 714–722. ISSN: 01730835. DOI: 10.1002/elps.200800636.
- [58] Leslie A. Khawli et al. “Charge variants in IgG1”. In: *mAbs* 2.6 (2010), pp. 613–624. ISSN: 1942-0862. DOI: 10.4161/mabs.2.6.13333.
- [59] Hyun Joo An, John W Froehlich, and Carlito B Lebrilla. “Determination of glycosylation sites and site-specific heterogeneity in glycoproteins”. In: *Current Opinion in Chemical Biology* 13.4 (2009), pp. 421–426. ISSN: 13675931. DOI: 10.1016/j.cbpa.2009.07.022.
- [60] J. J. Kattla et al. *Protein glycosylation*. Ed. by Oxford: Pergamon. Comprehens. 2011, pp. 501–520.
- [61] Veysel Kayser et al. “Glycosylation influences on the aggregation propensity of therapeutic monoclonal antibodies”. In: *Biotechnology Journal* 6.1 (2011), pp. 38–44. ISSN: 18606768. DOI: 10.1002/biot.201000091.
- [62] Ricardo J. Solá and Kai Griebenow. “Glycosylation of Therapeutic Proteins: An Effective Strategy to Optimize Efficacy”. In: *BioDrugs* 24.1 (2010), pp. 9–21. ISSN: 1173-8804. DOI: 10.2165/11530550-000000000-00000.
- [63] Susan A. Brooks. “Protein glycosylation in diverse cell systems: implications for modification and analysis of recombinant proteins”. In: *Expert Review of Proteomics* 3.3 (2006), pp. 345–359. ISSN: 1478-9450. DOI: 10.1586/14789450.3.3.345.
- [64] Hans H. Wandall et al. “Global functions of O-glycosylation: promises and challenges in O-glycobiology”. In: *The FEBS Journal* 288.24 (2021), pp. 7183–7212. ISSN: 1742-464X. DOI: 10.1111/febs.16148.
- [65] Erhard Bieberich. “Synthesis, Processing, and Function of N-Glycans in N-Glycoproteins”. In: *Advances in Neurobiology*. Vol. 29. 2023, pp. 65–93. ISBN: 9781493911547. DOI: 10.1007/978-3-031-12390-0_3.

- [66] Wei Wang, Sandeep Nema, and Dirk Teagarden. “Protein aggregation—Pathways and influencing factors”. In: *International Journal of Pharmaceutics* 390.2 (2010), pp. 89–99. ISSN: 03785173. DOI: 10.1016/j.ijpharm.2010.02.025.
- [67] James G. Barnard, Ken Babcock, and John F. Carpenter. “Characterization and Quantitation of Aggregates and Particles in Interferon- β Products: Potential Links Between Product Quality Attributes and Immunogenicity”. In: *Journal of Pharmaceutical Sciences* 102.3 (2013), pp. 915–928. ISSN: 00223549. DOI: 10.1002/jps.23415.
- [68] A. Braun et al. “Protein Aggregates Seem to Play a Key Role Among the Parameters Influencing the Antigenicity of Interferon Alpha (IFN- α) in Normal and Transgenic Mice”. In: *Pharmaceutical Research* 14.10 (1997), pp. 1472–1478.
- [69] Andreas Seidl et al. “Tungsten-Induced Denaturation and Aggregation of Epoetin Alfa During Primary Packaging as a Cause of Immunogenicity”. In: *Pharmaceutical Research* 29.6 (2012), pp. 1454–1467. ISSN: 0724-8741. DOI: 10.1007/s11095-011-0621-4.
- [70] M. Page et al. “Fragmentation of Therapeutic Human Immunoglobulin Preparations”. In: *Vox Sanguinis* 69.3 (1995), pp. 183–194. ISSN: 00429007. DOI: 10.1111/j.1423-0410.1995.tb02592.x.
- [71] Josef Vlasak and Roxana Ionescu. “Fragmentation of monoclonal antibodies”. In: *mAbs* 3.3 (2011), pp. 253–263. ISSN: 1942-0862. DOI: 10.4161/mabs.3.3.15608.
- [72] P. Elliott, A. Hohmann, and J. Spanos. “Protease expression in the supernatant of Chinese Hamster Ovary cells grown in serum-free culture”. In: *Biotechnology Letters* 25.22 (2003), pp. 1949–1952. ISSN: 0141-5492. DOI: 10.1023/B:BILE.0000003992.09492.4b.
- [73] Flavie Robert et al. “Degradation of an Fc-fusion recombinant protein by host cell proteases: Identification of a CHO cathepsin D protease”. In: *Biotechnology and Bioengineering* 104.6 (2009), pp. 1132–1141. ISSN: 00063592. DOI: 10.1002/bit.22494.
- [74] Sharon X. Gao et al. “Fragmentation of a highly purified monoclonal antibody attributed to residual CHO cell protease activity”. In: *Biotechnology and Bioengineering* 108.4 (2011), pp. 977–982. ISSN: 00063592. DOI: 10.1002/bit.22982.

- [75] Flavio Schwarz and Markus Aebi. “Mechanisms and principles of N-linked protein glycosylation”. In: *Current Opinion in Structural Biology* 21.5 (2011), pp. 576–582. ISSN: 0959440X. DOI: 10.1016/j.sbi.2011.08.005.
- [76] Markus Aebi. “N-linked protein glycosylation in the ER”. In: *Biochimica et Biophysica Acta (BBA) - Molecular Cell Research* 1833.11 (2013), pp. 2430–2437. ISSN: 01674889. DOI: 10.1016/j.bbamcr.2013.04.001.
- [77] Shilpa Vashist and Davis T.W. Ng. “Misfolded proteins are sorted by a sequential checkpoint mechanism of ER quality control”. In: *Journal of Cell Biology* 165.1 (2004), pp. 41–52. ISSN: 1540-8140. DOI: 10.1083/jcb.200309132.
- [78] Xudong Wu and Tom A. Rapoport. “Mechanistic insights into ER-associated protein degradation”. In: *Current Opinion in Cell Biology* 53 (2018), pp. 22–28. ISSN: 09550674. DOI: 10.1016/j.ceb.2018.04.004.
- [79] David Brühlmann et al. “Tailoring recombinant protein quality by rational media design”. In: *Biotechnology Progress* 31.3 (2015), pp. 615–629. ISSN: 87567938. DOI: 10.1002/btpr.2089.
- [80] Kelley W. Moremen, Michael Tiemeyer, and Alison V. Nairn. “Vertebrate protein glycosylation: diversity, synthesis and function”. In: *Nature Reviews Molecular Cell Biology* 13.7 (2012), pp. 448–462. ISSN: 1471-0072. DOI: 10.1038/nrm3383.
- [81] Fabian Higél et al. “N-glycosylation heterogeneity and the influence on structure, function and pharmacokinetics of monoclonal antibodies and Fc fusion proteins”. In: *European Journal of Pharmaceutics and Biopharmaceutics* 100 (2016), pp. 94–100. ISSN: 09396411. DOI: 10.1016/j.ejpb.2016.01.005.
- [82] Yutaka Kanda et al. “Comparison of biological activity among nonfucosylated therapeutic IgG1 antibodies with three different N-linked Fc oligosaccharides: the high-mannose, hybrid, and complex types”. In: *Glycobiology* 17.1 (2007), pp. 104–118. ISSN: 1460-2423. DOI: 10.1093/glycob/cw1057.
- [83] Beate Beyer et al. “Microheterogeneity of Recombinant Antibodies: Analytics and Functional Impact”. In: *Biotechnology Journal* 13.1 (2018), p. 1700476. ISSN: 18606768. DOI: 10.1002/biot.201700476.
- [84] Toyohide Shinkawa et al. “The Absence of Fucose but Not the Presence of Galactose or Bisecting N-Acetylglucosamine of Human IgG1 Complex-type Oligosaccharides Shows the Critical Role of Enhancing Antibody-dependent Cellular Cytotoxicity”. In: *Journal of Biological Chemistry* 278.5 (2003), pp. 3466–3473. ISSN: 00219258. DOI: 10.1074/jbc.M210665200.

- [85] T. Shantha Raju. “Terminal sugars of Fc glycans influence antibody effector functions of IgGs”. In: *Current Opinion in Immunology* 20.4 (2008), pp. 471–478. ISSN: 09527915. DOI: 10.1016/j.coi.2008.06.007.
- [86] Robert L. Shields et al. “Lack of Fucose on Human IgG1 N-Linked Oligosaccharide Improves Binding to Human Fc γ RIII and Antibody-dependent Cellular Toxicity”. In: *Journal of Biological Chemistry* 277.30 (2002), pp. 26733–26740. ISSN: 00219258. DOI: 10.1074/jbc.M202069200.
- [87] Akira Okazaki et al. “Fucose Depletion from Human IgG1 Oligosaccharide Enhances Binding Enthalpy and Association Rate Between IgG1 and Fc γ RIIIa”. In: *Journal of Molecular Biology* 336.5 (2004), pp. 1239–1249. ISSN: 00222836. DOI: 10.1016/j.jmb.2004.01.007.
- [88] Riad Abès and Jean-Luc Teillaud. “Impact of Glycosylation on Effector Functions of Therapeutic IgG”. In: *Pharmaceuticals* 3.1 (2010), pp. 146–157. ISSN: 1424-8247. DOI: 10.3390/ph3010146.
- [89] Naoko Yamane-Ohnuki et al. “Establishment of FUT8 knockout Chinese hamster ovary cells: An ideal host cell line for producing completely defucosylated antibodies with enhanced antibody-dependent cellular cytotoxicity”. In: *Biotechnology and Bioengineering* 87.5 (2004), pp. 614–622. ISSN: 0006-3592. DOI: 10.1002/bit.20151.
- [90] Katsuhiko Mori et al. “Engineering Chinese hamster ovary cells to maximize effector function of produced antibodies using FUT8 siRNA”. In: *Biotechnology and Bioengineering* 88.7 (2004), pp. 901–908. ISSN: 0006-3592. DOI: 10.1002/bit.20326.
- [91] Dipa Patel et al. “IgG isotype, glycosylation, and EGFR expression determine the induction of antibody-dependent cellular cytotoxicity in vitro by cetuximab”. In: *Human Antibodies* 19.4 (2010), pp. 89–99. ISSN: 1875869X. DOI: 10.3233/HAB-2010-0232.
- [92] Ann Wright and Sherie L. Morrison. “Effect of altered CH2-associated carbohydrate structure on the functional properties and in vivo fate of chimeric mouse-human immunoglobulin G1.” In: *Journal of Experimental Medicine* 180.3 (1994), pp. 1087–1096. ISSN: 0022-1007. DOI: 10.1084/jem.180.3.1087.
- [93] Jason Hodoniczky, Y.Z. Zheng, and D.C. James. “Control of Recombinant Monoclonal Antibody Effector Functions by Fc N-Glycan Remodeling in

Vitro”. In: *Biotechnology Progress* 21.6 (2005), pp. 1644–1652. ISSN: 8756-7938. DOI: 10.1021/bp050228w.

- [94] Xiaoyu Chen, Y D. Liu, and Gregory C. Flynn. “The effect of Fc glycan forms on human IgG2 antibody clearance in humans”. In: *Glycobiology* 19.3 (2008), pp. 240–249. ISSN: 0959-6658. DOI: 10.1093/glycob/cwn120.
- [95] Thomas A. Millward et al. “Effect of constant and variable domain glycosylation on pharmacokinetics of therapeutic antibodies in mice”. In: *Biologicals* 36.1 (2008), pp. 41–47. ISSN: 10451056. DOI: 10.1016/j.biologicals.2007.05.003.
- [96] Yoshikatsu Kaneko, Falk Nimmerjahn, and Jeffrey V. Ravetch. “Anti-Inflammatory Activity of Immunoglobulin G Resulting from Fc Sialylation”. In: *Science* 313.5787 (2006), pp. 670–673. ISSN: 0036-8075. DOI: 10.1126/science.1129594.
- [97] Bernard J. Scallon et al. “Higher levels of sialylated Fc glycans in immunoglobulin G molecules can adversely impact functionality”. In: *Molecular Immunology* 44.7 (2007), pp. 1524–1534. ISSN: 01615890. DOI: 10.1016/j.molimm.2006.09.005.
- [98] P.N. Boyd, A.C. Lines, and A.K. Patel. “The effect of the removal of sialic acid, galactose and total carbohydrate on the functional activity of Campath-1H”. In: *Molecular Immunology* 32.17-18 (1995), pp. 1311–1318. ISSN: 01615890. DOI: 10.1016/0161-5890(95)00118-2.
- [99] Anatol G. Morell et al. “The Role of Sialic Acid in Determining the Survival of Glycoproteins in the Circulation”. In: *Journal of Biological Chemistry* 246.5 (1971), pp. 1461–1467. ISSN: 00219258. DOI: 10.1016/S0021-9258(19)76994-4.
- [100] Alan R. Flesher et al. “Fluorophore-labeled carbohydrate analysis of immunoglobulin fusion proteins: Correlation of oligosaccharide content with in vivo clearance profile”. In: *Biotechnology and Bioengineering* 47.3 (1995), pp. 405–405. ISSN: 0006-3592. DOI: 10.1002/bit.260470314.
- [101] Gregory C. Flynn et al. “Naturally occurring glycan forms of human immunoglobulins G1 and G2”. In: *Molecular Immunology* 47.11-12 (2010), pp. 2074–2082. ISSN: 01615890. DOI: 10.1016/j.molimm.2010.04.006.
- [102] Johannes Stadlmann et al. “Analysis of immunoglobulin glycosylation by LC-ESI-MS of glycopeptides and oligosaccharides”. In: *PROTEOMICS* 8.14 (2008), pp. 2858–2871. ISSN: 16159853. DOI: 10.1002/pmic.200700968.

- [103] Hongcheng Liu et al. “Impact of IgG Fc-Oligosaccharides on Recombinant Monoclonal Antibody Structure, Stability, Safety, and Efficacy”. In: *Biotechnology Progress* 33.5 (2017), pp. 1173–1181. ISSN: 87567938. DOI: 10.1002/btpr.2498.
- [104] Renato Mastrangeli et al. “The Formidable Challenge of Controlling High Mannose-Type N-Glycans in Therapeutic mAbs”. In: *Trends in Biotechnology* 38.10 (2020), pp. 1154–1168. ISSN: 01677799. DOI: 10.1016/j.tibtech.2020.05.009.
- [105] Patrick H.C. van Berkel et al. “Rapid production of recombinant human IgG With improved ADCC effector function in a transient expression system”. In: *Biotechnology and Bioengineering* 105.2 (2010), pp. 350–357. ISSN: 00063592. DOI: 10.1002/bit.22535.
- [106] Ronald Jay Rothman et al. “Antibody-dependent cytotoxicity mediated by natural killer cells is enhanced by castanospermine-induced alterations of IgG glycosylation”. In: *Molecular Immunology* 26.12 (1989), pp. 1113–1123. ISSN: 01615890. DOI: 10.1016/0161-5890(89)90055-2.
- [107] Marcella Yu et al. “Production, characterization and pharmacokinetic properties of antibodies with N-linked Mannose-5 glycans”. In: *mAbs* 4.4 (2012), pp. 475–487. ISSN: 1942-0862. DOI: 10.4161/mabs.20737.
- [108] Qun Zhou et al. “Development of a simple and rapid method for producing non-fucosylated oligomannose containing antibodies with increased effector function”. In: *Biotechnology and Bioengineering* 99.3 (2008), pp. 652–665. ISSN: 00063592. DOI: 10.1002/bit.21598.
- [109] Austin W. Boesch et al. “Highly parallel characterization of IgG Fc binding interactions”. In: *mAbs* 6.4 (2014), pp. 915–927. ISSN: 1942-0870. DOI: 10.4161/mabs.28808.
- [110] Leslie Alessandri et al. “Increased serum clearance of oligomannose species present on a human IgG1 molecule”. In: *mAbs* 4.4 (2012), pp. 509–520. ISSN: 1942-0862. DOI: 10.4161/mabs.20450.
- [111] David Falck et al. “Glycoform-resolved pharmacokinetic studies in a rat model employing glycoengineered variants of a therapeutic monoclonal antibody”. In: *mAbs* 13.1 (2021). ISSN: 1942-0862. DOI: 10.1080/19420862.2020.1865596.

- [112] M. Butler and A. Meneses-Acosta. “Recent advances in technology supporting biopharmaceutical production from mammalian cells”. In: *Applied Microbiology and Biotechnology* 96.4 (2012), pp. 885–894. ISSN: 0175-7598. DOI: 10.1007/s00253-012-4451-z.
- [113] Roberto Donini, Stuart M. Haslam, and Cleo Kontoravdi. “Glycoengineering Chinese hamster ovary cells: a short history”. In: *Biochemical Society Transactions* 49.2 (2021), pp. 915–931. ISSN: 0300-5127. DOI: 10.1042/BST20200840.
- [114] Roy Jefferis. “Glycosylation as a strategy to improve antibody-based therapeutics”. In: *Nature Reviews Drug Discovery* 8.3 (2009), pp. 226–234. ISSN: 1474-1776. DOI: 10.1038/nrd2804.
- [115] Thomas Amann et al. “Genetic engineering approaches to improve post-translational modification of biopharmaceuticals in different production platforms”. In: *Biotechnology and Bioengineering* 116.10 (2019), pp. 2778–2796. ISSN: 0006-3592. DOI: 10.1002/bit.27101.
- [116] Xun Xu et al. “The genomic sequence of the Chinese hamster ovary (CHO)-K1 cell line”. In: *Nature Biotechnology* 29.8 (2011), pp. 735–741. ISSN: 1087-0156. DOI: 10.1038/nbt.1932.
- [117] Jae Seong Lee et al. “CRISPR/Cas9-mediated genome engineering of CHO cell factories: Application and perspectives”. In: *Biotechnology Journal* 10.7 (2015), pp. 979–994. ISSN: 18606768. DOI: 10.1002/biot.201500082.
- [118] Qurrat Ul Ain, Jee Young Chung, and Yong-Hee Kim. “Current and future delivery systems for engineered nucleases: ZFN, TALEN and RGEN”. In: *Journal of Controlled Release* 205 (2015), pp. 120–127. ISSN: 01683659. DOI: 10.1016/j.jconrel.2014.12.036.
- [119] Laetitia Malphettes et al. “Highly efficient deletion of FUT8 in CHO cell lines using zinc-finger nucleases yields cells that produce completely non-fucosylated antibodies”. In: *Biotechnology and Bioengineering* 106.5 (2010), pp. 774–783. ISSN: 00063592. DOI: 10.1002/bit.22751.
- [120] Simon Fischer et al. “A functional high-content miRNA screen identifies miR-30 family to boost recombinant protein production in CHO cells”. In: *Biotechnology Journal* 9.10 (2014), pp. 1279–1292. ISSN: 18606768. DOI: 10.1002/biot.201400306.

- [121] Sarah Inwood, Michael Betenbaugh, and Joseph Shiloach. “Methods for Using Small Non-Coding RNAs to Improve Recombinant Protein Expression in Mammalian Cells”. In: *Genes* 9.1 (2018), p. 25. ISSN: 2073-4425. DOI: 10.3390/genes9010025.
- [122] S. Weikert et al. “Engineering Chinese hamster ovary cells to maximize sialic acid content of recombinant glycoproteins”. In: *Nature Biotechnology* 17.11 (1999), pp. 1116–1121. ISSN: 1087-0156. DOI: 10.1038/15104.
- [123] Céline Raymond et al. “Production of α 2,6-sialylated IgG1 in CHO cells”. In: *mAbs* 7.3 (2015), pp. 571–583. ISSN: 1942-0862. DOI: 10.1080/19420862.2015.1029215.
- [124] Xiaojie Yu et al. “Engineering Hydrophobic Protein–Carbohydrate Interactions to Fine-Tune Monoclonal Antibodies”. In: *Journal of the American Chemical Society* 135.26 (2013), pp. 9723–9732. ISSN: 0002-7863. DOI: 10.1021/ja4014375.
- [125] Wentao Chen et al. “Stabilizing the CH2 Domain of an Antibody by Engineering in an Enhanced Aromatic Sequon”. In: *ACS Chemical Biology* 11.7 (2016), pp. 1852–1861. ISSN: 1554-8929. DOI: 10.1021/acscchembio.5b01035.
- [126] Cheng-yu Chung et al. “Integrated Genome and Protein Editing Swaps α -2,6 Sialylation for α -2,3 Sialic Acid on Recombinant Antibodies from CHO”. In: *Biotechnology Journal* 12.2 (2017). ISSN: 1860-6768. DOI: 10.1002/biot.201600502.
- [127] Elizabeth Edwards et al. “Strategies to control therapeutic antibody glycosylation during bioprocessing: Synthesis and separation”. In: *Biotechnology and Bioengineering* 119.6 (2022), pp. 1343–1358. ISSN: 0006-3592. DOI: 10.1002/bit.28066.
- [128] Harry Eagle. “Nutrition Needs of Mammalian Cells in Tissue Culture”. In: *Science* 122 (1955), pp. 501–504.
- [129] Ann E. Chapman and John C. Calhoun. “Effects of glucose starvation and puromycin treatment on lipid-linked oligosaccharide precursors and biosynthetic enzymes in Chinese hamster ovary cells in vivo and in vitro”. In: *Archives of Biochemistry and Biophysics* 260.1 (1988), pp. 320–333. ISSN: 00039861. DOI: 10.1016/0003-9861(88)90456-0.

- [130] Gregg B. Nyberg et al. “Metabolic Effects on Recombinant Interferon- γ Glycosylation in Continuous Culture of Chinese Hamster Ovary Cells”. In: *Biotechnology and Bioengineering* 62.5 (2000), pp. 336–347. ISSN: 0018-8646. DOI: 10.1147/rd.445.0770.
- [131] Neil Templeton et al. “Peak antibody production is associated with increased oxidative metabolism in an industrially relevant fed-batch CHO cell culture”. In: *Biotechnology and Bioengineering* 110.7 (2013), pp. 2013–2024. ISSN: 00063592. DOI: 10.1002/bit.24858.
- [132] Zahra Sheikholeslami, Mario Jolicoeur, and Olivier Henry. “Elucidating the effects of postinduction glutamine feeding on the growth and productivity of CHO cells”. In: *Biotechnology Progress* 30.3 (2014), pp. 535–546. ISSN: 87567938. DOI: 10.1002/btpr.1907.
- [133] Markus Schneider, Ian w. Marison, and Urs von Stockar. “The importance of ammonia in mammalian cell culture”. In: *Journal of Biotechnology* 46.3 (1996), pp. 161–185. ISSN: 01681656. DOI: 10.1016/0168-1656(95)00196-4.
- [134] Jong Kwang Hong et al. “Comparative phenotypic analysis of CHO clones and culture media for lactate shift”. In: *Journal of Biotechnology* 283.August (2018), pp. 97–104. ISSN: 01681656. DOI: 10.1016/j.jbiotec.2018.07.042.
- [135] Martin Gawlitzek et al. “Incorporation of ^{15}N from ammonium into the N-linked oligosaccharides of an immunoadhesin glycoprotein expressed in Chinese hamster ovary cells”. In: *Glycobiology* 9.2 (1999), pp. 125–131. ISSN: 0959-6658. DOI: 10.1093/glycob/9.2.125.
- [136] Aziz Cayli et al. “Cell lines with reduced UDP-N-acetylhexosamine pool in the presence of ammonium”. In: *Biotechnology and Bioengineering* 65.2 (1999), pp. 192–200. ISSN: 0006-3592. DOI: 10.1002/(SICI)1097-0290(19991020)65:2<192::AID-BIT9>3.0.CO;2-9.
- [137] P Chen and S Harcum. “Effects of elevated ammonium on glycosylation gene expression in CHO cells”. In: *Metabolic Engineering* 8.2 (2006), pp. 123–132. ISSN: 10967176. DOI: 10.1016/j.ymben.2005.10.002.
- [138] Melissa M. St. Amand et al. “Identification of manipulated variables for a glycosylation control strategy”. In: *Biotechnology and Bioengineering* 111.10 (2014), pp. 1957–1970. ISSN: 00063592. DOI: 10.1002/bit.25251.

- [139] Martin Gawlitzek et al. “Ammonium alters N-glycan structures of recombinant TNFR-IgG: Degradative versus biosynthetic mechanisms”. In: *Biotechnology and Bioengineering* 68.6 (2000), pp. 637–646. ISSN: 0006-3592. DOI: 10.1002/(SICI)1097-0290(20000620)68:6<637::AID-BIT6>3.0.CO;2-C.
- [140] Antti Rivinoja et al. “Elevated Golgi pH impairs terminal N-glycosylation by inducing mislocalization of Golgi glycosyltransferases”. In: *Journal of Cellular Physiology* 220.1 (2009), pp. 144–154. ISSN: 00219541. DOI: 10.1002/jcp.21744.
- [141] Apolline Helfer et al. “Tuning metabolic efficiency for increased product yield in high titer fed-batch Chinese hamster ovary cell culture”. In: *Biotechnology Progress* 39.3 (2023). ISSN: 8756-7938. DOI: 10.1002/btpr.3327.
- [142] Xiaolin Zhang et al. “Feeding tricarboxylic acid cycle intermediates improves lactate consumption and antibody production in Chinese hamster ovary cell cultures”. In: *Biotechnology Progress* 36.4 (2020), pp. 1–9. ISSN: 8756-7938. DOI: 10.1002/btpr.2975.
- [143] Stefania Caso et al. “Effects of pyruvate on primary metabolism and product quality for a high-density perfusion process”. In: *Biotechnology and Bioengineering* 119.4 (2022), pp. 1053–1061. ISSN: 0006-3592. DOI: 10.1002/bit.28033.
- [144] Thomas K. Villiger et al. “High-throughput profiling of nucleotides and nucleotide sugars to evaluate their impact on antibody N-glycosylation”. In: *Journal of Biotechnology* 229 (2016), pp. 3–12. ISSN: 01681656. DOI: 10.1016/j.jbiotec.2016.04.039.
- [145] Kym N. Baker et al. “Metabolic control of recombinant protein N-glycan processing in NS0 and CHO cells”. In: *Biotechnology and Bioengineering* 73.3 (2001), pp. 188–202. ISSN: 0006-3592. DOI: 10.1002/bit.1051.
- [146] Niki S.C. Wong et al. “An investigation of intracellular glycosylation activities in CHO cells: Effects of nucleotide sugar precursor feeding”. In: *Biotechnology and Bioengineering* 107.2 (2010), pp. 321–336. ISSN: 00063592. DOI: 10.1002/bit.22812.
- [147] Michael J. Gramer et al. “Modulation of antibody galactosylation through feeding of uridine, manganese chloride, and galactose”. In: *Biotechnology and Bioengineering* 108.7 (2011), pp. 1591–1602. ISSN: 00063592. DOI: 10.1002/bit.23075.

- [148] Anna E. Hills et al. “Metabolic control of recombinant monoclonal antibody N-glycosylation in GS-NS0 cells”. In: *Biotechnology and Bioengineering* 75.2 (2001), pp. 239–251. ISSN: 0006-3592. DOI: 10.1002/bit.10022.
- [149] Tanaya Surve and Mugdha Gadgil. “Manganese increases high mannose glycoform on monoclonal antibody expressed in CHO when glucose is absent or limiting: Implications for use of alternate sugars”. In: *Biotechnology Progress* 31.2 (2015), pp. 460–467. ISSN: 87567938. DOI: 10.1002/btpr.2029.
- [150] Craig Zupke et al. “Real-time product attribute control to manufacture antibodies with defined N-linked glycan levels”. In: *Biotechnology Progress* 31.5 (2015), pp. 1433–1441. ISSN: 87567938. DOI: 10.1002/btpr.2136.
- [151] Liang Zhang et al. “Combined effects of glycosylation precursors and lactate on the glycoprofile of IgG produced by CHO cells”. In: *Journal of Biotechnology* 289 (2019), pp. 71–79. ISSN: 01681656. DOI: 10.1016/j.jbiotec.2018.11.004.
- [152] David Brühlmann et al. “Cell culture media supplemented with raffinose reproducibly enhances high mannose glycan formation”. In: *Journal of Biotechnology* 252.December 2016 (2017), pp. 32–42. ISSN: 01681656. DOI: 10.1016/j.jbiotec.2017.04.026.
- [153] Christopher K. Crowell et al. “Amino acid and manganese supplementation modulates the glycosylation state of erythropoietin in a CHO culture system”. In: *Biotechnology and Bioengineering* 96.3 (2007), pp. 538–549. ISSN: 00063592. DOI: 10.1002/bit.21141.
- [154] Rhian K. Grainger and David C. James. “CHO cell line specific prediction and control of recombinant monoclonal antibody N-glycosylation”. In: *Biotechnology and Bioengineering* 110.11 (2013), pp. 2970–2983. ISSN: 00063592. DOI: 10.1002/bit.24959.
- [155] Thomas K. Villiger et al. “Controlling the time evolution of mAb N-linked glycosylation, Part I: Microbioreactor experiments”. In: *Biotechnology Progress* 32.5 (2016), pp. 1123–1134. ISSN: 87567938. DOI: 10.1002/btpr.2305.
- [156] Sohye Kang et al. “Metabolic markers associated with high mannose glycan levels of therapeutic recombinant monoclonal antibodies”. In: *Journal of Biotechnology* 203 (2015), pp. 22–31. ISSN: 01681656. DOI: 10.1016/j.jbiotec.2015.03.002.

- [157] Michel Awwad et al. “Modification of monoclonal antibody carbohydrates by oxidation, conjugation, or deoxymannojirimycin does not interfere with antibody effector functions”. In: *Cancer Immunology Immunotherapy* 38.1 (1994), pp. 23–30. ISSN: 0340-7004. DOI: 10.1007/BF01517166.
- [158] A.D. Elbein et al. “Kifunensine, a potent inhibitor of the glycoprotein processing mannosidase I”. In: *Journal of Biological Chemistry* 265.26 (1990), pp. 15599–15605. ISSN: 00219258. DOI: 10.1016/S0021-9258(18)55439-9.
- [159] Jean-Louis Franc et al. “Inhibition of N-linked oligosaccharide processing does not prevent the secretion of thyroglobulin. A study with swainsonine and deoxynojirimycin”. In: *European Journal of Biochemistry* 157.1 (1986), pp. 225–232. ISSN: 0014-2956. DOI: 10.1111/j.1432-1033.1986.tb09660.x.
- [160] Sandhya Pande et al. “Monensin, a small molecule ionophore, can be used to increase high mannose levels on monoclonal antibodies generated by Chinese hamster ovary production cell-lines”. In: *Biotechnology and Bioengineering* 112.7 (2015), pp. 1383–1394. ISSN: 00063592. DOI: 10.1002/bit.25551.
- [161] Dion A Kevin II, Damaris AF Meujo, and Mark T Hamann. “Polyether ionophores: broad-spectrum and promising biologically active molecules for the control of drug-resistant bacteria and parasites”. In: *Expert Opinion on Drug Discovery* 4.2 (2009), pp. 109–146. ISSN: 1746-0441. DOI: 10.1517/17460440802661443.
- [162] Jacek Rutkowski and Bogumil Brzezinski. “Structures and Properties of Naturally Occurring Polyether Antibiotics”. In: *BioMed Research International* 2013 (2013), pp. 1–31. ISSN: 2314-6133. DOI: 10.1155/2013/162513.
- [163] Si Nga Sou et al. “How does mild hypothermia affect monoclonal antibody glycosylation?” In: *Biotechnology and Bioengineering* 112.6 (2015), pp. 1165–1176. ISSN: 00063592. DOI: 10.1002/bit.25524.
- [164] Si Nga Sou et al. “Model-based investigation of intracellular processes determining antibody Fc-glycosylation under mild hypothermia”. In: *Biotechnology and Bioengineering* 114.7 (2017), pp. 1570–1582. ISSN: 10970290. DOI: 10.1002/bit.26225.
- [165] Evelyn Trummer et al. “Process parameter shifting: Part II. Biphasic cultivation—A tool for enhancing the volumetric productivity of batch processes using Epo-Fc expressing CHO cells”. In: *Biotechnology and Bioengineering* 94.6 (2006), pp. 1045–1052. ISSN: 0006-3592. DOI: 10.1002/bit.20958.

- [166] Moritz K. F Wolf et al. “Improved Performance in Mammalian Cell Perfusion Cultures by Growth Inhibition”. In: *Biotechnology Journal* 14.2 (2019), p. 1700722. ISSN: 1860-6768. DOI: 10.1002/biot.201700722.
- [167] Hengameh Aghamohseni et al. “Effects of nutrient levels and average culture pH on the glycosylation pattern of camelid-humanized monoclonal antibody”. In: *Journal of Biotechnology* 186 (2014), pp. 98–109. ISSN: 01681656. DOI: 10.1016/j.jbiotec.2014.05.024.
- [168] “Identification of cell culture conditions to control N -glycosylation site-occupancy of recombinant glycoproteins expressed in CHO cells”. In: *Biotechnology and Bioengineering* 103.6 (2009), pp. 1164–1175. ISSN: 00063592. DOI: 10.1002/bit.22348.
- [169] Jeerawat Soonthornsit et al. “Low cytoplasmic pH reduces ER-Golgi trafficking and induces disassembly of the Golgi apparatus”. In: *Experimental Cell Research* 328.2 (2014), pp. 325–339. ISSN: 00144827. DOI: 10.1016/j.yexcr.2014.09.009.
- [170] Magnus A.B. Axelsson et al. “Neutralization of pH in the Golgi apparatus causes redistribution of glycosyltransferases and changes in the O-glycosylation of mucins”. In: *Glycobiology* 11.8 (2001), pp. 633–644. ISSN: 0959-6658. DOI: 10.1093/glycob/11.8.633.
- [171] Rubin Jiang, Hao Chen, and Sen Xu. “pH excursions impact CHO cell culture performance and antibody N-linked glycosylation”. In: *Bioprocess and Biosystems Engineering* 41.12 (2018), pp. 1731–1741. ISSN: 1615-7591. DOI: 10.1007/s00449-018-1996-y.
- [172] A.E. Schmelzer and W.M. Miller. “Hyperosmotic Stress and Elevated pCO₂ Alter Monoclonal Antibody Charge Distribution and Monosaccharide Content”. In: *Biotechnology Progress* 18.2 (2002), pp. 346–353. ISSN: 8756-7938. DOI: 10.1021/bp010187d.
- [173] Yoshinobu Konno et al. “Fucose content of monoclonal antibodies can be controlled by culture medium osmolality for high antibody-dependent cellular cytotoxicity”. In: *Cytotechnology* 64.3 (2012), pp. 249–265. ISSN: 0920-9069. DOI: 10.1007/s10616-011-9377-2.
- [174] Efren Pacis et al. “Effects of cell culture conditions on antibody N-linked glycosylation-what affects high mannose 5 glycoform”. In: *Biotechnology and Bioengineering* 108.10 (2011), pp. 2348–2358. ISSN: 00063592. DOI: 10.1002/bit.23200.

- [175] J.P. Kunkel et al. “Comparisons of the Glycosylation of a Monoclonal Antibody Produced under Nominally Identical Cell Culture Conditions in Two Different Bioreactors”. In: *Biotechnology Progress* 16.3 (2000), pp. 462–470. ISSN: 8756-7938. DOI: 10.1021/bp000026u.
- [176] W. Chotigeat et al. “Role of environmental conditions on the expression levels, glycoform pattern and levels of sialyltransferase for hFSH produced by recombinant CHO cells”. In: *Cytotechnology* 15.1-3 (1994), pp. 217–221. ISSN: 0920-9069. DOI: 10.1007/BF00762396.
- [177] Marija Ivarsson et al. “Evaluating the impact of cell culture process parameters on monoclonal antibody N-glycosylation”. In: *Journal of Biotechnology* 188 (2014), pp. 88–96. ISSN: 01681656. DOI: 10.1016/j.jbiotec.2014.08.026.
- [178] Zimin Liu et al. “The application of Raman spectroscopy for monitoring product quality attributes in perfusion cell culture”. In: *Biochemical Engineering Journal* 173 (2021), p. 108064. ISSN: 1873295X. DOI: 10.1016/j.bej.2021.108064.
- [179] Jean-Marc Bielser et al. “Perfusion cell culture for the production of conjugated recombinant fusion proteins reduces clipping and quality heterogeneity compared to batch-mode processes”. In: *Journal of Biotechnology* 302 (2019), pp. 26–31. ISSN: 01681656. DOI: 10.1016/j.jbiotec.2019.06.006.
- [180] Daniel J. Karst et al. “Process performance and product quality in an integrated continuous antibody production process”. In: *Biotechnology and Bioengineering* 114.2 (2017), pp. 298–307. ISSN: 00063592. DOI: 10.1002/bit.26069.
- [181] Michel Chartrain and Lily Chu. “Development and Production of Commercial Therapeutic Monoclonal Antibodies in Mammalian Cell Expression Systems: An Overview of the Current Upstream Technologies”. In: *Current Pharmaceutical Biotechnology* 9.6 (2008), pp. 447–467. ISSN: 13892010. DOI: 10.2174/138920108786786367.
- [182] J. Gijs Kuenen. *Continuous Cultures (Chemostats)*. Oxford: Academic Press, 2019, pp. 743–761.
- [183] Jean-Marc Bielser et al. “Perfusion mammalian cell culture for recombinant protein manufacturing – A critical review”. In: *Biotechnology Advances* 36.4 (2018), pp. 1328–1340. DOI: 10.1016/j.biotechadv.2018.04.011.

- [184] Leila Zamani et al. “High Cell Density Perfusion Culture has a Maintained Exoproteome and Metabolome”. In: *Biotechnology Journal* 13.10 (2018), p. 1800036. ISSN: 18606768. DOI: 10.1002/biot.201800036.
- [185] Hui F. Liu et al. “Recovery and purification process development for monoclonal antibody production”. In: *mAbs* 2.5 (2010), pp. 480–499. ISSN: 1942-0862. DOI: 10.4161/mabs.2.5.12645.
- [186] Nripen Singh et al. “Clarification technologies for monoclonal antibody manufacturing processes: Current state and future perspectives”. In: *Biotechnology and Bioengineering* 113.4 (2016), pp. 698–716. ISSN: 00063592. DOI: 10.1002/bit.25810.
- [187] Abhinav A. Shukla et al. “Downstream processing of monoclonal antibodies—Application of platform approaches”. In: *Journal of Chromatography B* 848.1 (2007), pp. 28–39. ISSN: 15700232. DOI: 10.1016/j.jchromb.2006.09.026.
- [188] Allan Matte. “Recent Advances and Future Directions in Downstream Processing of Therapeutic Antibodies”. In: *International Journal of Molecular Sciences* 23.15 (2022), p. 8663. ISSN: 1422-0067. DOI: 10.3390/ijms23158663.
- [189] Sebastian Vogg, Thomas Müller-Späth, and Massimo Morbidelli. “Current status and future challenges in continuous biochromatography”. In: *Current Opinion in Chemical Engineering* 22 (2018), pp. 138–144. ISSN: 22113398. DOI: 10.1016/j.coche.2018.09.001.
- [190] Fabian Steinebach, Thomas Müller-Späth, and Massimo Morbidelli. “Continuous counter-current chromatography for capture and polishing steps in biopharmaceutical production”. In: *Biotechnology Journal* 11.9 (2016), pp. 1126–1141. ISSN: 18606768. DOI: 10.1002/biot.201500354.
- [191] Fabian Steinebach et al. “Design and operation of a continuous integrated monoclonal antibody production process”. In: *Biotechnology Progress* 33.5 (2017), pp. 1303–1313. ISSN: 87567938. DOI: 10.1002/btpr.2522.
- [192] Kevin Botelho Ferreira et al. “Transfer of continuous manufacturing process principles for mAb production in a GMP environment: A step in the transition from batch to continuous”. In: *Biotechnology Progress* 38.4 (2022), pp. 1–13. ISSN: 8756-7938. DOI: 10.1002/btpr.3259.

- [193] Noriko Yoshimoto, Takamitsu Ichihara, and Shuichi Yamamoto. “Connected flow-through chromatography processes as continuous downstream processing of proteins”. In: *MATEC Web of Conferences* 268 (2019). Ed. by A. Orbecido et al., p. 01003. ISSN: 2261-236X. DOI: 10.1051/mateconf/201926801003.
- [194] D. Moyle. “Biomufacturing Technology Roadmap - Modular and Mobile”. In: *Tech. rep. BioPhorum Operations Group Ltd.* (2017).
- [195] Eric Langer. “Continuous Bioprocessing and Perfusion: Wider Adoption Coming as Bioprocessing Matures”. In: *BioProcessing Journal* 13.1 (2014), pp. 43–49. ISSN: 15388786. DOI: 10.12665/J131.Langer.
- [196] Lindsay Arnold et al. “Implementation of Fully Integrated Continuous Antibody Processing: Effects on Productivity and COGm”. In: *Biotechnology Journal* 14.2 (2019), p. 1800061. ISSN: 1860-6768. DOI: 10.1002/biot.201800061.
- [197] Matthew S. Croughan, Konstantin B. Konstantinov, and Charles Cooney. “The future of industrial bioprocessing: Batch or continuous?” In: *Biotechnology and Bioengineering* 112.4 (2015), pp. 648–651. ISSN: 00063592. DOI: 10.1002/bit.25529.
- [198] James Pollock, Sa V. Ho, and Suzanne S. Farid. “Fed-batch and perfusion culture processes: Economic, environmental, and operational feasibility under uncertainty”. In: *Biotechnology and Bioengineering* 110.1 (2013), pp. 206–219. ISSN: 00063592. DOI: 10.1002/bit.24608.
- [199] D. Voisard et al. “Potential of cell retention techniques for large-scale high-density perfusion culture of suspended mammalian cells”. In: *Biotechnology and Bioengineering* 82.7 (2003), pp. 751–765. ISSN: 00063592. DOI: 10.1002/bit.10629.
- [200] Lily Chu and David K. Robinson. “Industrial choices for protein production by large-scale cell culture”. In: *Current Opinion in Biotechnology* 12.2 (2001), pp. 180–187. ISSN: 09581669. DOI: 10.1016/S0958-1669(00)00197-X.
- [201] Yiping Lim et al. “Engineering mammalian cells in bioprocessing – current achievements and future perspectives”. In: *Biotechnology and Applied Biochemistry* 55.4 (2010), pp. 175–189. ISSN: 0885-4513. DOI: 10.1042/BA20090363.

- [202] F. Meuwly et al. “Conversion of a CHO cell culture process from perfusion to fed-batch technology without altering product quality”. In: *Journal of Biotechnology* 123.1 (2006), pp. 106–116. ISSN: 01681656. DOI: 10.1016/j.jbiotec.2005.10.013.
- [203] Jason Walther et al. “The business impact of an integrated continuous biomanufacturing platform for recombinant protein production”. In: *Journal of Biotechnology* 213 (2015), pp. 3–12. ISSN: 01681656. DOI: 10.1016/j.jbiotec.2015.05.010.
- [204] Uwe Gottschalk, Kurt Brorson, and Abhinav A Shukla. “Innovation in biomanufacturing: the only way forward”. In: *Pharmaceutical Bioprocessing* 1.2 (2013), pp. 141–157. ISSN: 2048-9145. DOI: 10.4155/pbp.13.17.
- [205] J Christopher Love, Kerry Routenberg Love, and Paul W. Barone. “Enabling global access to high-quality biopharmaceuticals”. In: *Current Opinion in Chemical Engineering* 2.4 (2013), pp. 383–390. ISSN: 22113398. DOI: 10.1016/j.coche.2013.09.002.
- [206] D Sawyer. “Biomanufacturing Technology Roadmap-Overview”. In: *Biomanufacturing Technol. Roadmap* (2017), pp. 1–48.
- [207] Edward C. Li et al. “Considerations in the early development of biosimilar products”. In: *Drug Discovery Today* 20.S2 (2015), pp. 1–9. ISSN: 13596446. DOI: 10.1016/j.drudis.2014.12.017.
- [208] Paul Saenger. “Ten years of biosimilar recombinant human growth hormone in Europe”. In: *Drug Design, Development and Therapy* Volume 11 (2017), pp. 1505–1507. ISSN: 1177-8881. DOI: 10.2147/DDDT.S130317.
- [209] Jonathan Hummel et al. “Modeling the Downstream Processing of Monoclonal Antibodies Reveals Cost Advantages for Continuous Methods for a Broad Range of Manufacturing Scales”. In: *Biotechnology Journal* 14.2 (2019), p. 1700665. ISSN: 1860-6768. DOI: 10.1002/biot.201700665.
- [210] Stephan Klutz et al. “Cost evaluation of antibody production processes in different operation modes”. In: *Chemical Engineering Science* 141 (2016), pp. 63–74. ISSN: 00092509. DOI: 10.1016/j.ces.2015.10.029.
- [211] Jonathan Coffman et al. “A common framework for integrated and continuous biomanufacturing”. In: *Biotechnology and Bioengineering* 118.4 (2021), pp. 1735–1749. ISSN: 0006-3592. DOI: 10.1002/bit.27690.

- [212] Brian Kelley. “Very Large Scale Monoclonal Antibody Purification: The Case for Conventional Unit Operations”. In: *Biotechnology Progress* 23.5 (2007). ISSN: 8756-7938. DOI: 10.1021/bp070117s.
- [213] Stephan Klutz et al. “Developing the biofacility of the future based on continuous processing and single-use technology”. In: *Journal of Biotechnology* 213 (2015), pp. 120–130. ISSN: 01681656. DOI: 10.1016/j.jbiotec.2015.06.388.
- [214] Fergal Lalor et al. “Sustainability in the biopharmaceutical industry: Seeking a holistic perspective”. In: *Biotechnology Advances* 37.5 (2019), pp. 698–707. ISSN: 07349750. DOI: 10.1016/j.biotechadv.2019.03.015.
- [215] Eri Amasawa et al. “Cost–Benefit Analysis of Monoclonal Antibody Cultivation Scenarios in Terms of Life Cycle Environmental Impact and Operating Cost”. In: *ACS Sustainable Chemistry & Engineering* 9.42 (2021), pp. 14012–14021. ISSN: 2168-0485. DOI: 10.1021/acssuschemeng.1c01435.
- [216] Chaoying Ding et al. “Process design of a fully integrated continuous biopharmaceutical process using economic and ecological impact assessment”. In: *Biotechnology and Bioengineering* 119.12 (2022), pp. 3567–3583. ISSN: 0006-3592. DOI: 10.1002/bit.28234.
- [217] James Pollock et al. “Integrated continuous bioprocessing: Economic, operational, and environmental feasibility for clinical and commercial antibody manufacture”. In: *Biotechnology Progress* 33.4 (2017), pp. 854–866. ISSN: 15206033. DOI: 10.1002/btpr.2492.
- [218] Patrick Hossler, Sarwat F Khattak, and Zheng Jian Li. “Optimal and consistent protein glycosylation in mammalian cell culture”. In: *Glycobiology* 19.9 (2009), pp. 936–949. DOI: 10.1093/glycob/cwp079.
- [219] Daniel J. Karst et al. “Modulation and modeling of monoclonal antibody N-linked glycosylation in mammalian cell perfusion reactors”. In: *Biotechnology and Bioengineering* 114.9 (2017), pp. 1978–1990. ISSN: 00063592. DOI: 10.1002/bit.26315.
- [220] Daniel Johannes Karst, Fabian Steinebach, and Massimo Morbidelli. “Continuous integrated manufacturing of therapeutic proteins”. In: *Current Opinion in Biotechnology* 53 (2018), pp. 76–84. ISSN: 09581669. DOI: 10.1016/j.copbio.2017.12.015.

- [221] William C. Yang et al. “Perfusion seed cultures improve biopharmaceutical fed-batch production capacity and product quality”. In: *Biotechnology Progress* 30.3 (2014), pp. 616–625. ISSN: 87567938. DOI: 10.1002/btpr.1884.
- [222] Veena Warikoo et al. “Integrated continuous production of recombinant therapeutic proteins”. In: *Biotechnology and Bioengineering* 109.12 (2012), pp. 3018–3029. ISSN: 00063592. DOI: 10.1002/bit.24584.
- [223] Rahul Godawat et al. “End-to-end integrated fully continuous production of recombinant monoclonal antibodies”. In: *Journal of Biotechnology* 213 (2015), pp. 13–19. ISSN: 01681656. DOI: 10.1016/j.jbiotec.2015.06.393.
- [224] Michael J. Coolbaugh et al. “Pilot-scale demonstration of an end-to-end integrated and continuous biomanufacturing process”. In: *Biotechnology and Bioengineering* 118.9 (2021), pp. 3287–3301. ISSN: 0006-3592. DOI: 10.1002/bit.27670.
- [225] Sen Xu et al. “Impact of Pluronic® F68 on hollow fiber filter-based perfusion culture performance”. In: *Bioprocess and Biosystems Engineering* 40.9 (2017), pp. 1317–1326. ISSN: 1615-7591. DOI: 10.1007/s00449-017-1790-2.
- [226] Hubert Schwarz et al. “Optimization of medium with perfusion microbioreactors for high density CHO cell cultures at very low renewal rate aided by design of experiments”. In: *Biotechnology and Bioengineering* (2023). ISSN: 0006-3592. DOI: 10.1002/bit.28397.
- [227] S. Metze et al. “Monitoring online biomass with a capacitance sensor during scale-up of industrially relevant CHO cell culture fed-batch processes in single-use bioreactors”. In: *Bioprocess and Biosystems Engineering* 43.2 (2020), pp. 193–205. ISSN: 1615-7591. DOI: 10.1007/s00449-019-02216-4.
- [228] Klaus Joeris et al. “In-situ microscopy: Online process monitoring of mammalian cell cultures”. In: *Cytotechnology* 38.1-3 (2002), pp. 129–134. ISSN: 09209069. DOI: 10.1023/A:1021170502775.
- [229] Konstantin Konstantinov et al. “Real-time biomass-concentration monitoring in animal-cell cultures”. In: *Trends in Biotechnology* 12.8 (1994), pp. 324–333. ISSN: 01677799. DOI: 10.1016/0167-7799(94)90049-3.
- [230] P. Ducommun et al. “On-line determination of animal cell concentration in two industrial high-density culture processes by dielectric spectroscopy”. In: *Biotechnology and Bioengineering* 77.3 (2002), pp. 316–323. ISSN: 0006-3592. DOI: 10.1002/bit.1197.

- [231] Chris L. Davey et al. “Introduction to the dielectric estimation of cellular biomass in real time, with special emphasis on measurements at high volume fractions”. In: *Analytica Chimica Acta* 279.1 (1993), pp. 155–161. ISSN: 00032670. DOI: 10.1016/0003-2670(93)85078-X.
- [232] Moritz Wolf, Jean-Marc Bielser, and Massimo Morbidell. *Perfusion Cell Culture Processes for Biopharmaceuticals: Process Development, Design, and Scale-up*. Cambridge University Press, 2020.
- [233] Adam C. Fisher et al. “The Current Scientific and Regulatory Landscape in Advancing Integrated Continuous Biopharmaceutical Manufacturing”. In: *Trends in Biotechnology* 37.3 (2019), pp. 253–267. ISSN: 01677799. DOI: 10.1016/j.tibtech.2018.08.008.
- [234] Michael A. MacDonald et al. “Perfusion culture of Chinese Hamster Ovary cells for bioprocessing applications”. In: *Critical Reviews in Biotechnology* 42.7 (2022), pp. 1099–1115. ISSN: 0738-8551. DOI: 10.1080/07388551.2021.1998821.
- [235] Cary Matanguihan and Paul Wu. “Upstream continuous processing: recent advances in production of biopharmaceuticals and challenges in manufacturing”. In: *Current Opinion in Biotechnology* 78 (2022), p. 102828. ISSN: 09581669. DOI: 10.1016/j.copbio.2022.102828.
- [236] Marie-Françoise Clincke et al. “Very high density of Chinese hamster ovary cells in perfusion by alternating tangential flow or tangential flow filtration in WAVE bioreactor™—part II: Applications for antibody production and cryopreservation”. In: *Biotechnology Progress* 29.3 (2013), pp. 768–777. ISSN: 8756-7938. DOI: 10.1002/btpr.1703.
- [237] Daniel J. Karst et al. “Characterization and comparison of ATF and TFF in stirred bioreactors for continuous mammalian cell culture processes”. In: *Biochemical Engineering Journal* 110 (2016), pp. 17–26. ISSN: 1369703X. DOI: 10.1016/j.bej.2016.02.003.
- [238] Samantha Wang et al. “Shear contributions to cell culture performance and product recovery in ATF and TFF perfusion systems”. In: *Journal of Biotechnology* 246.November (2017), pp. 52–60. ISSN: 01681656. DOI: 10.1016/j.jbiotec.2017.01.020.
- [239] R. Pavlik. *United States Patent, US 2018/0236407 A1*. 2017.
- [240] R. Pavlik. *Australian Patent, W O 2019/133487 A1*. 2019.
- [241] J. Shevitz. *United States Patent, US 2019/0201820 A1*. 2018.

- [242] Katharina Blaschczok et al. “Investigations on Mechanical Stress Caused to CHO Suspension Cells by Standard and Single-Use Pumps”. In: *Chemie Ingenieur Technik* 85.1-2 (2013), pp. 144–152. ISSN: 0009286X. DOI: 10.1002/cite.201200135.
- [243] William Kelly et al. “Understanding and modeling alternating tangential flow filtration for perfusion cell culture”. In: *Biotechnology Progress* 30.6 (2014), pp. 1291–1300. ISSN: 87567938. DOI: 10.1002/btpr.1953.
- [244] European Medicines Agency. “Guideline on Real Time Release Testing (formerly Guideline on Parametric Release)”. In: *EMA/CHMP/QWP/811210/2009-Rev1* (2012).
- [245] International Conference on Harmonisation of Technical Requirements for Registration of Pharmaceuticals for Human Use. *ICH guideline Q14 on analytical procedure development*. 2022. URL: <http://www.ich.org>.
- [246] Mo Jiang et al. “Opportunities and challenges of real-time release testing in biopharmaceutical manufacturing”. In: *Biotechnology and Bioengineering* 114.11 (2017), pp. 2445–2456. ISSN: 00063592. DOI: 10.1002/bit.26383.
- [247] Adrian D. Shaw et al. “Noninvasive, on-line monitoring of the biotransformation by yeast of glucose to ethanol using dispersive Raman spectroscopy and chemometrics”. In: *Applied Spectroscopy* 53.11 (1999), pp. 1419–1428. ISSN: 00037028. DOI: 10.1366/0003702991945777.
- [248] Nicholas R. Abu-Absi et al. “Real time monitoring of multiple parameters in mammalian cell culture bioreactors using an in-line Raman spectroscopy probe”. In: *Biotechnology and Bioengineering* 108.5 (2011), pp. 1215–1221. ISSN: 00063592. DOI: 10.1002/bit.23023.
- [249] V. Vojinović, J. M.S. Cabral, and L. P. Fonseca. “Real-time bioprocess monitoring: Part I: In situ sensors”. In: *Sensors and Actuators, B: Chemical* 114.2 (2006), pp. 1083–1091. ISSN: 09254005. DOI: 10.1016/j.snb.2005.07.059.
- [250] Karen A. Esmonde-White, Maryann Cuellar, and Ian R. Lewis. “The role of Raman spectroscopy in biopharmaceuticals from development to manufacturing”. In: *Analytical and Bioanalytical Chemistry* 414.2 (2022), pp. 969–991. ISSN: 1618-2642. DOI: 10.1007/s00216-021-03727-4.
- [251] C. V. RAMAN and K. S. KRISHNAN. “A New Type of Secondary Radiation”. In: *Nature* 121.3048 (1928), pp. 501–502. ISSN: 0028-0836. DOI: 10.1038/121501c0.

- [252] Rafael M. Santos et al. “Monitoring mAb cultivations with in-situ raman spectroscopy: The influence of spectral selectivity on calibration models and industrial use as reliable PAT tool”. In: *Biotechnology Progress* 34.3 (2018), pp. 659–670. ISSN: 87567938. DOI: 10.1002/btpr.2635.
- [253] Silvère André et al. “In-line and real-time prediction of recombinant antibody titer by in situ Raman spectroscopy”. In: *Analytica Chimica Acta* 892 (2015), pp. 148–152. ISSN: 00032670. DOI: 10.1016/j.aca.2015.08.050.
- [254] Hemlata Bhatia et al. “In-line monitoring of amino acids in mammalian cell cultures using raman spectroscopy and multivariate chemometrics models”. In: *Engineering in Life Sciences* 18.1 (2018), pp. 55–61. ISSN: 16180240. DOI: 10.1002/elsc.201700084.
- [255] Bence Kozma, András Salgó, and Szilveszter Gergely. “Comparison of multivariate data analysis techniques to improve glucose concentration prediction in mammalian cell cultivations by Raman spectroscopy”. In: *Journal of Pharmaceutical and Biomedical Analysis* 158 (2018), pp. 269–279. ISSN: 07317085. DOI: 10.1016/j.jpba.2018.06.005.
- [256] Thaddaeus A. Webster et al. “Feedback control of two supplemental feeds during fed-batch culture on a platform process using inline Raman models for glucose and phenylalanine concentration”. In: *Bioprocess and Biosystems Engineering* 44.1 (2021), pp. 127–140. ISSN: 1615-7591. DOI: 10.1007/s00449-020-02429-y.
- [257] Jessica Whelan, Stephen Craven, and Brian Glennon. “In situ Raman spectroscopy for simultaneous monitoring of multiple process parameters in mammalian cell culture bioreactors”. In: *Biotechnology Progress* 28.5 (2012), pp. 1355–1362. ISSN: 87567938. DOI: 10.1002/btpr.1590.
- [258] Brandon N. Berry et al. “Quick generation of Raman spectroscopy based in-process glucose control to influence biopharmaceutical protein product quality during mammalian cell culture”. In: *Biotechnology Progress* 32.1 (2016), pp. 224–234. ISSN: 87567938. DOI: 10.1002/btpr.2205.
- [259] Hubert Schwarz et al. “Monitoring of amino acids and antibody N-glycosylation in high cell density perfusion culture based on Raman spectroscopy”. In: *Biochemical Engineering Journal* 182.April (2022), p. 108426. ISSN: 1369703X. DOI: 10.1016/j.bej.2022.108426.

- [260] A. Graf et al. “A Novel Approach for Non-Invasive Continuous In-Line Control of Perfusion Cell Cultivations by Raman Spectroscopy”. In: *Frontiers in Bioengineering and Biotechnology* 10.April (2022), pp. 1–11. ISSN: 2296-4185. DOI: 10.3389/fbioe.2022.719614.
- [261] Gong Chen et al. “Viable cell density on-line auto-control in perfusion cell culture aided by in-situ Raman spectroscopy”. In: *Biochemical Engineering Journal* 172.March (2021), p. 108063. ISSN: 1369703X. DOI: 10.1016/j.bej.2021.108063.
- [262] A.P. Teixeira et al. “Advances in on-line monitoring and control of mammalian cell cultures: Supporting the PAT initiative”. In: *Biotechnology Advances* 27.6 (2009), pp. 726–732. ISSN: 07349750. DOI: 10.1016/j.biotechadv.2009.05.003.
- [263] Carl Rafferty et al. “Analysis of chemometric models applied to Raman spectroscopy for monitoring key metabolites of cell culture”. In: *Biotechnology Progress* 36.4 (2020), pp. 1–16. ISSN: 8756-7938. DOI: 10.1002/btpr.2977.
- [264] Ruth C. Rowland-Jones et al. “Spectroscopy integration to miniature bioreactors and large scale production bioreactors—Increasing current capabilities and model transfer”. In: *Biotechnology Progress* 37.1 (2021), pp. 1–14. ISSN: 8756-7938. DOI: 10.1002/btpr.3074.
- [265] Ruth C. Rowland-Jones et al. “Comparison of spectroscopy technologies for improved monitoring of cell culture processes in miniature bioreactors”. In: *Biotechnology Progress* 33.2 (2017), pp. 337–346. ISSN: 87567938. DOI: 10.1002/btpr.2459.
- [266] Júlia Domján et al. “Raman-based dynamic feeding strategies using real-time glucose concentration monitoring system during adalimumab producing CHO cell cultivation”. In: *Biotechnology Progress* 36.6 (2020). ISSN: 8756-7938. DOI: 10.1002/btpr.3052.
- [267] Brandon Berry et al. “Cross-scale predictive modeling of CHO cell culture growth and metabolites using Raman spectroscopy and multivariate analysis”. In: *Biotechnology Progress* 31.2 (2015), pp. 566–577. ISSN: 87567938. DOI: 10.1002/btpr.2035.
- [268] Ruth C. Rowland-Jones and Colin Jaques. “At-line raman spectroscopy and design of experiments for robust monitoring and control of miniature bioreactor cultures”. In: *Biotechnology Progress* 35.2 (2019), e2740. ISSN: 8756-7938. DOI: 10.1002/btpr.2740.

- [269] Chun Chen, H. Edward Wong, and Chetan T. Goudar. “Upstream process intensification and continuous manufacturing”. In: *Current Opinion in Chemical Engineering* 22 (2018), pp. 191–198. ISSN: 22113398. DOI: 10.1016/j.coche.2018.10.006.
- [270] Laura A. Bailey et al. “Determination of Chinese hamster ovary cell line stability and recombinant antibody expression during long-term culture”. In: *Biotechnology and Bioengineering* 109.8 (2012), pp. 2093–2103. ISSN: 00063592. DOI: 10.1002/bit.24485.
- [271] Sen Xu et al. “Bioreactor productivity and media cost comparison for different intensified cell culture processes”. In: *Biotechnology Progress* 33.4 (2017), pp. 867–878. ISSN: 87567938. DOI: 10.1002/btpr.2415.
- [272] Sadettin S. Ozturk. “Engineering challenges in high density cell culture systems”. In: *Cytotechnology* 22.1-3 (1996), pp. 3–16. ISSN: 0920-9069. DOI: 10.1007/BF00353919.
- [273] Henry Lin et al. “Principles and approach to developing mammalian cell culture media for high cell density perfusion process leveraging established fed-batch media”. In: *Biotechnology Progress* 33.4 (2017), pp. 891–901. ISSN: 87567938. DOI: 10.1002/btpr.2472.
- [274] Rebecca E. McCoy, Nicole A. Costa, and Arvia E. Morris. “Factors that determine stability of highly concentrated chemically defined production media”. In: *Biotechnology Progress* 31.2 (2015), pp. 493–502. ISSN: 87567938. DOI: 10.1002/btpr.2047.
- [275] Olivier Henry, Ezra Kwok, and James M. Piret. “Simpler noninstrumented batch and semicontinuous cultures provide mammalian cell kinetic data comparable to continuous and perfusion cultures”. In: *Biotechnology Progress* 24.4 (2008), pp. 921–931. ISSN: 87567938. DOI: 10.1002/btpr.17.
- [276] Agata Villiger-Oberbek et al. “Development and application of a high-throughput platform for perfusion-based cell culture processes”. In: *Journal of Biotechnology* 212 (2015), pp. 21–29. ISSN: 01681656. DOI: 10.1016/j.jbiotec.2015.06.428.
- [277] Patrick Mayrhofer, Andreas Castan, and Renate Kunert. “Shake tube perfusion cell cultures are suitable tools for the prediction of limiting substrate, CSPR, bleeding strategy, growth and productivity behavior”. In: *Journal of Chemical Technology & Biotechnology* 96.10 (2021), pp. 2930–2939. ISSN: 0268-2575. DOI: 10.1002/jctb.6848.

- [278] Moritz K.F. Wolf et al. “Development of a shake tube-based scale-down model for perfusion cultures”. In: *Biotechnology and Bioengineering* 115.11 (2018), pp. 2703–2713. ISSN: 10970290. DOI: 10.1002/bit.26804.
- [279] Kim Le et al. “A novel mammalian cell line development platform utilizing nanofluidics and optoelectro positioning technology”. In: *Biotechnology Progress* 34.6 (2018), pp. 1438–1446. ISSN: 8756-7938. DOI: 10.1002/btpr.2690.
- [280] Barney Zoro et al. “Development of a novel automated perfusion mini-bioreactor ambr® 250 perfusion”. In: *Cell Culture Engineering XVI*. ECI Symposium Series, 2018.
- [281] Dirk Müller et al. “Process intensification in the biopharma industry: Improving efficiency of protein manufacturing processes from development to production scale using synergistic approaches”. In: *Chemical Engineering and Processing - Process Intensification* 171 (2022), p. 108727. ISSN: 02552701. DOI: 10.1016/j.cep.2021.108727.
- [282] J. Strube et al. “Process intensification in biologics manufacturing”. In: *Chemical Engineering and Processing - Process Intensification* 133.October (2018), pp. 278–293. ISSN: 02552701. DOI: 10.1016/j.cep.2018.09.022.
- [283] Konstantin Konstantinov et al. “The “Push-to-Low” Approach for Optimization of High-Density Perfusion Cultures of Animal Cells”. In: *Advances in Biochemical Engineering/Biotechnology*. Vol. 101. 2006, pp. 75–98. ISBN: 3540340068. DOI: 10.1007/10_016.
- [284] “A two-step procedure for the design of perfusion bioreactors”. In: *Biochemical Engineering Journal* 151.May (2019), p. 107295. ISSN: 1369703X. DOI: 10.1016/j.bej.2019.107295.
- [285] Jean-Marc Bielser et al. “Continuous bleed recycling significantly increases recombinant protein production yield in perfusion cell cultures”. In: *Biochemical Engineering Journal* 169.10 (2021), p. 107966. ISSN: 1369703X. DOI: 10.1016/j.bej.2021.107966.
- [286] Monika Dudek et al. “Raman Optical Activity and Raman spectroscopy of carbohydrates in solution”. In: *Spectrochimica Acta Part A: Molecular and Biomolecular Spectroscopy* 206 (2019), pp. 597–612. ISSN: 13861425. DOI: 10.1016/j.saa.2018.08.017.

- [287] Vincent Dumouilla and Claude Gilles Dussap. “Online analysis of D-glucose and D-mannose aqueous mixtures using Raman spectroscopy: an in silico and experimental approach”. In: *Bioengineered* 12.1 (2021), pp. 4420–4431. ISSN: 2165-5979. DOI: 10.1080/21655979.2021.1955550.
- [288] Ernest Henry Starling. “On the Absorption of Fluids from the Connective Tissue Spaces”. In: *The Journal of Physiology* 19.4 (1896), pp. 312–326. ISSN: 00223751. DOI: 10.1113/jphysiol.1896.sp000596.
- [289] Flaka Radoniqi et al. “Computational fluid dynamic modeling of alternating tangential flow filtration for perfusion cell culture”. In: *Biotechnology and Bioengineering* 115.11 (2018), pp. 2751–2759. ISSN: 10970290. DOI: 10.1002/bit.26813.
- [290] Robert van Reis. *United States Patent, 5,256,294*. 1993.
- [291] Robert van Reis et al. “High performance tangential flow filtration”. In: *Biotechnology and Bioengineering* 56.1 (1997), pp. 71–82. ISSN: 00063592. DOI: 10.1002/(SICI)1097-0290(19971005)56:1<71::AID-BIT8>3.0.CO;2-S.

A Scientific Publications

A.1 Scientific Publication Section I

Advancing Raman model calibration for perfusion bioprocesses using spiked harvest libraries

Abstract

Background: Raman spectroscopy has gained popularity to monitor multiple process indicators simultaneously in biopharmaceutical processes. However, robust and specific model calibration remains a challenge due to insufficient analyte variability to train the models and high cross-correlation of various media components and artifacts throughout the process.

Main Methods: A systematic Raman calibration workflow for perfusion processes enabling highly specific and fast model calibration was developed. Harvest libraries consisting of frozen harvest samples from multiple CHO cell culture bioreactors collected at different process times were established. Model calibration was subsequently performed in an offline setup using a flow cell by spiking process harvest with glucose, raffinose, galactose, mannose, and fructose.

Major Results: In a screening phase, Raman spectroscopy was proven capable not only to distinguish sugars with similar chemical structures in perfusion harvest but also to quantify them independently in process-relevant concentrations. In a second phase, a robust and highly specific calibration model for simultaneous glucose (root mean square error prediction [RMSEP] = 0.32 g L⁻¹) and raffinose (RMSEP = 0.17 g L⁻¹) real-time monitoring was generated and verified in a third phase during a perfusion process.

Implication: The proposed novel offline calibration workflow allowed proper Raman peak decoupling, reduced calibration time from months down to days, and can be applied to other analytes of interest including lactate, ammonia, amino acids, or product titer.

Keywords: flow cell, harvest library, model calibration, MVDA, Raman spectroscopy, spiking

Abbreviations: AOI, analyte of interest; DoE, design of experiments; GA, glucose addition; G_CS, glucose model for calibration set; mAb, monoclonal antibody; PC, principal component; PCA, principal component analysis; PLS, partial least squares; R², coefficients of determination calibration; RA, raffinose addition; R_CS, raffinose model for calibration set; R²CV, coefficients of determination cross validation; RMSE, root mean square error; RMSECV, root mean square error cross validation; RMSEP, root mean square error prediction; R²P, coefficients of determination prediction; RV, reactor volumes; SD, standard deviation; SNV, standard normal variate; VCD, viable cell density; VCV, viable cell volume.

1 Introduction

Encouraged by regulatory authorities, a variety of different process analytical technology (PAT) tools have found their place in (bio)pharmaceutical manufacturing to ensure product quality in complex manufacturing processes [1, 2]. By allowing continuous monitoring of process indicators (e.g., the glucose level in cell culture) connected to their corresponding control systems (e.g., glucose feed), PAT tools would improve the assurance of delivering a product with more consistent critical quality attributes. Spectroscopic techniques are characterized by their speed, non-invasiveness, and relatively low impact on the material under investigation [3]. Raman spectroscopy is arguably the most versatile technology for biotechnological upstream process (USP) monitoring given its low water interferences [4, 5].

The possibility of simultaneous monitoring of multiple process output variables and controlling them using multivariate models in conjunction with feedback loops has been demonstrated by several groups. Calibration models were generated to monitor metabolites (glucose, lactate, ammonia), amino acids, as well as product titer, viable cell density (VCD), viability, and even product quality attributes such as glycosylation [6–11]. Most of these models are exclusively based on *in-situ* collected Raman spectra aligned with reference analytics of process samples trying to capture process variability. However, many media components change concomitantly during the process, leading to difficulties generating chemometric models that are truly based on the fingerprint of the analyte of interest (AOI). This can lead to unawareness about the specificity of the generated models and predictions based on process evolution rather than compound specific Raman bands. The importance to decouple Raman signals to obtain compound specific calibration models was discussed previously, where specific wavenumber regions assigned to glucose and lactate increased model reliability [12]. Furthermore, the model generation by alignment of offline measurements to simultaneously measured Raman spectra is limited to the offline analytics available on the respective site. Thus, Raman model generation for non-routinely measured compounds which might be interesting for developmental activities is difficult to realize and would require changes in the analytical pipeline.

Integrating sufficient analyte variability into the Raman calibration workflow remains one of the biggest challenges to generate robust calibration models. In general, analyte variability can either be integrated into the calibration process by executing a design of experiments (DoE) strategy incorporating variability to a set of bioreactor runs, or by spiking analytes of interest directly into the bioreactor to change their concentrations independently of the process matrix. The DoE strategy

with multiple bioreactor runs was successfully applied for monitoring glucose and lactate concentrations in a cross-scale experiment composed of 5, 200, and 2,000 L bioreactor runs with variability introduced to 5 L bioreactor runs [13]. Furthermore, a miniaturized bioreactorsystem allowing up to 48 simultaneous cultivations at different conditions was shown to facilitate Raman model calibration for reliable glucose and lactate predictions [14]. Spiking strategies to augment analyte variability in the calibration data set were demonstrated insitu [12, 15], at-line [16], and offline [17]. In contrast to the standard calibration approach aligning process spectra to reference analytics, these two strategies allow controlled coverage of the design space to achieve sufficiently high analyte variability for robust Raman calibration which might be especially important for steady-state perfusion processes with inherently low variability. Despite the ability to generate important analyte variability for model generation, these two approaches are very resource intensive. Dedicated bioreactor runs operated at varying setpoints or reactors used for spiking studies need to be executed for Raman model generation, interfering with other ongoing process development activities.

Although most of the reported Raman models were acquired in situ by inserting the Raman probe into the bioreactor, in-line monitoring of perfusion harvest using a flow cell offers an interesting alternative, provided that the harvest is collected through a cell separation device (e.g., ATF or TFF systems). Albeit some cell-related information cannot be extracted when acquiring Raman signals from the filtered harvest, the absence of cells and gas bubbles in the flow cell might be advantageous in terms of signal sensitivity, robustness, and scalability. Models developed in a flow cell can be used independently of the process scale when installed in a bypass loop, facilitating Raman model transfer across different production scales. As such, in-line monitoring of product titer in perfusion harvest using a stainless-steel flow cell was used to optimize an integrated continuous chromatography step [18], whereas others developed a more sophisticated flow cell intensifying Raman signals to detect product breakthrough in a continuous protein A capture step [19].

N-glycosylation is considered a major CQA of therapeutic monoclonalantibodies (mAbs) due to its potential effect on the efficiency and safety profile of the product. The glycosylation pattern of recombinant proteins is highly dependent on the cultivation conditions that need to be well controlled to deliver a consistent product quality [20]. Hence, factors that impact glycosylation need to be monitored and controlled ideally throughout the manufacturing process [21]. To modulate glycosylation patterns during a production process or to match glycosylation patterns to a reference product, feeding sugars such as mannose, galactose, fructose, or raffinose

has been proven an effective way to reach target specifications [22–27]. Direct control with known modulators is of particular interest in quasi-steady-state continuous perfusion processes, where product quality attributes are kept constant throughout the process.

The goal of this study was to develop a systematic Raman calibration workflow to generate highly specific Raman models for perfusion cell culture with inherently low process variability and thereby overcoming limitations of current calibration approaches such as a lack of analyte variability in the calibration data, unsatisfactory analyte specificity due to correlation with simultaneously changing process compounds, or resource and time intensive calibration activities. The novel calibration workflow consisting of a harvest library containing process samples from multiple bioreactor runs covering different process time points enabled rapid model generation by spiking without impacting ongoing bioreactor runs. Model calibration was performed in an offline setup using a flow cell which was finally connected to the perfusion process harvest for real-time predictions. The obtained results show that a systematic spiking approach can build a robust basis for the training of chemometric models particularly for substances having similar chemical structures in complex matrices. This approach not only speeds up a model generation for perfusion cultures from several months down to weeks or even days but more importantly allows breaking correlations of the batch evolution with the analytes of interest.

2 Experimental Section

2.1 Perfusion culture process, monitoring, and control

A proprietary CHO-K1 cell line producing a bispecific mAb was expanded in an incubator (Multitron 4, InforsHT, Bottmingen, Switzerland) for 21 days using a proprietary chemically defined medium (Merck Serono SA, Corsier-sur-Vevey, Switzerland). Perfusion bioreactors (Labfors 5 Cell, Infors HT, Bottmingen, Switzerland) were inoculated with a seeding density of 0.6×10^6 viable cells mL^{-1} . Culture conditions were maintained at $36.5 \text{ }^\circ\text{C}$ with a DO setpoint of 50% (VisiFerm DO Arc, Hamilton, Bonaduz, Switzerland). The pH was controlled at 7.07 ± 0.17 (EasyFerm Plus Arc, Hamilton, Bonaduz, Switzerland) by CO_2 sparging and a $1.1 \text{ M Na}_2\text{CO}_3$ solution. Bioreactors were operated at 2 L working volume and perfusion was started on day 0 and kept constant at 1.3 reactor volumes per day (RV day^{-1}). Bioreactor harvests were gravimetrically controlled to maintain the bioreactor weight constant using either alternating tangential flow filtration (ATF2H, Repligen, Waltham, MA)

or tangential flow filtration (Levitronix technologies Inc, Framingham, MA) with polyether sulfone hollow fibers having a pore size of $0.22\ \mu\text{m}$ (Repligen, Waltham, MA). After an initial growth phase, an online capacitance probe (Incyte Arc, Hamilton, Bonaduz, Switzerland) was used to keep the viable cell volume (VCV) constant at 12%.

2.2 Hardware setup and data acquisition

A custom-made flow cell from stainless steel 316 L with a chamber volume of 0.95 mL was used for all Raman measurements. The flow cell allowed to insert any commercially available bioreactor probe compatible with a bioreactor headplate PG 13.5 thread. The outlet of the chamber was placed at the highest point to prevent bubble formation that could impair spectral acquisition. More details about the flow cell can be found in the Supporting Information section (Supporting Information Figures A.8 and A.9). A Raman spectrometer Multispec Raman (tec5 AG, Steinbach, Germany) using the software MultiSpec Pro II (tec5 AG, Steinbach, Germany) with 785 nm laser excitation wavelength and 500 mW power output was used in combination with the InPhotonics RamanProbe (InPhotonics, Norwood, MA) for the initial screening phase using spectral acquisition time of $6 \times 20\ \text{s}$. For the model calibration and verification, $12 \times 20\ \text{s}$ scans were performed using a Raman Immersible Probe MSR M571 (tec5 AG, Steinbach, Germany) with a ViewPort PG13.5 sensor interface (SCHOTT AG, Landshut, Germany). In the offline setup, light-protected and tempered harvest ($37\ \text{°C}$) was pumped through the flow cell at a flow of $2\ \text{L day}^{-1}$ matching the approximate harvest speed when connected to the perfusion bioreactor, resulting in an average residence time of 40 s.

2.3 Chemometric modeling procedure

Data analysis was performed using The Unscrambler X (CAMO Software, Oslo, Norway). A standard spectral preprocessing procedure was applied for all chemometric modeling activities. Spectra were pre-treated by a 1st derivative with Savitzky-Golay filter (2nd order polynomial, 31 points window) followed by standard normal variate (SNV). Preprocessed spectra were then truncated to wavenumbers from $450 - 1,800\ \text{cm}^{-1}$ and used for further principal component analysis (PCA) and partial least squares (PLS) regression. The number of latent variables was determined by using the standard approach of The Unscrambler X software unless otherwise mentioned. Performance of the models was compared based on the root mean square error (RMSE) of the calibration dataset, five-fold cross-validation (root mean square

error cross validation [RMSECV]) and prediction (root mean square error prediction [RMSEP]), and the corresponding coefficients of determination calibration (R^2), coefficients of determination cross validation (R^2CV), and coefficients of determination prediction (R^2P) as previously described [12, 19].

2.4 Reference analytics

Glucose concentrations and other CPPs such as lactate, ammonia, glutamine, glutamate, VCD, and viability were measured using the Bioprofile Flex2 (Nova Biomedical, Waltham, MA). The supplier indicated an analytical standard deviation (SD) for glucose of 0.07 g L^{-1} . VCV was calculated as follows: [28]

$$VCV = \frac{\frac{4}{3} \cdot \pi \cdot \left(\frac{D}{2}\right)^3 \cdot VCD}{V} \cdot 100 \quad (\text{A.1})$$

where D is the average cell diameter, VCD the viable cell density, and V is the cell culture volume, assuming a spherical shape of the cells. Raffinose was quantified on an Agilent 1,200 HPLC system combined with a refractive index detector (Agilent RID, G1362A). Compounds were separated using a Hiplax H column ($250 \times 4.6 \text{ mm}$, PL1170-6830, Agilent Technologies AG, Basel, Switzerland) with a guard column Hiplax H column ($3 \times 5 \text{ mm}$, PL1670-0830, Agilent Technologies AG, Basel, Switzerland) as described in the literature [29]. The flow rate was adapted to 0.2 mL min^{-1} and the analytical SD was determined to be 0.04 g L^{-1} . Due to the absence of raffinose in the platform perfusion medium, raffinose concentrations during the verification run on day 1 and from day 8 – 13 were assumed to be 0 g L^{-1} .

2.5 Experimental workflow for Raman model calibration

An experimental workflow consisting of three main steps was developed to ensure robust Raman sensor calibration (Figure A.1):

Initial screening phase: Initial screening to assess whether analytes of interest can be distinguished by Raman in the desired concentration range and process matrix.

Model calibration phase: Data acquisition of the AOI for the model calibration using a harvest library.

Model verification phase: Model verification in a perfusion bioreactor run.

During the initial screening phase, a full factorial design with two factors (glucose and one out of the four secondary sugars) with five levels was performed and prepared in duplicates, leading to 50 spectra per glucose-secondary sugar combina-

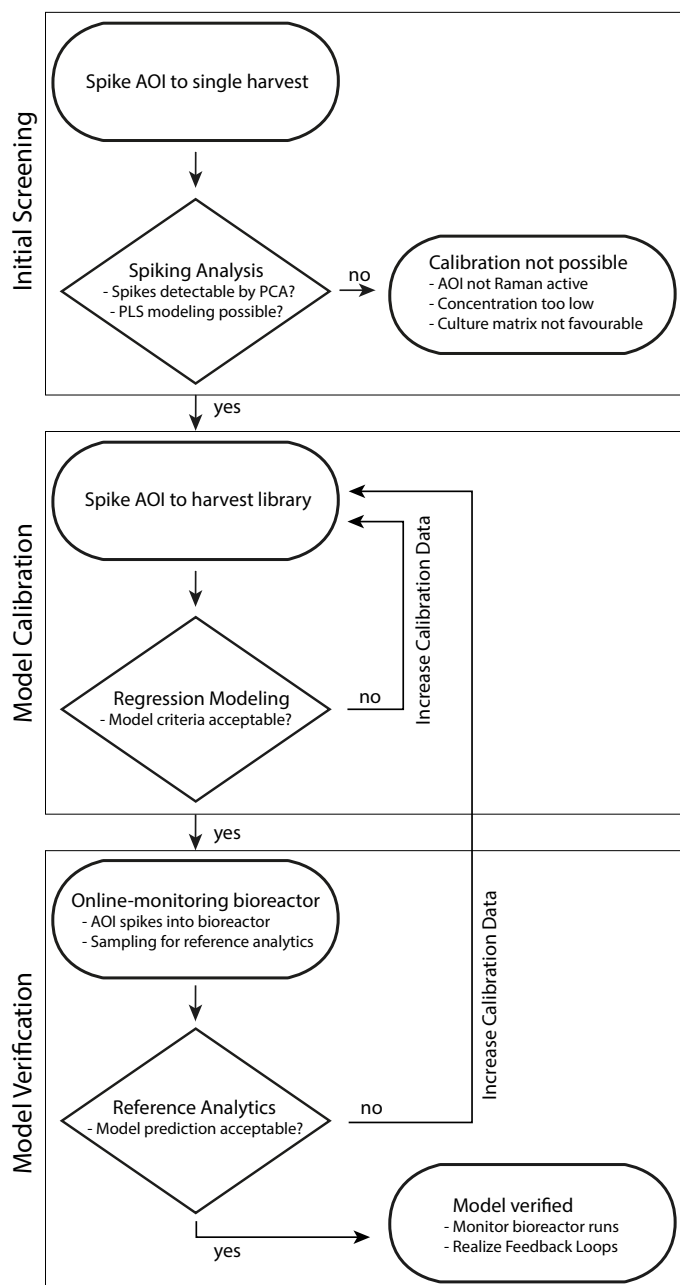


Figure A.1: Spiking chart for the spiking-based Raman calibration workflow. The workflow consists of three phases. Initial screening phase: identification if calibration of a certain analyte is possible. Model calibration phase: actual model calibration using the harvest library. Model verification phase: final stage to verify calibration models with independent bioreactor runs.

tion. As there were four different secondary sugars, a total of 200 spectra resulted in a combined calibration data set. Furthermore, one extra solution of each corner condition and three extra central point solutions were prepared as a test set, resulting in 28 spectra. Glucose levels were equally distributed within a range of 3.45 – 13.45 g L⁻¹. The concentration ranges of secondary sugars were chosen according to the values found to modulate glycosylation patterns in the literature [22, 26].

This resulted in $0 - 4 \text{ g L}^{-1}$ for galactose, mannose, and fructose, and in $0 - 10 \text{ g L}^{-1}$ for raffinose all equally distributed on five levels. Glucose (glucose monohydrate for microbiology, CarlRoth, Karlsruhe, Germany), raffinose (D(+))raffinose pentahydrate, Apollo scientific, Bredbury, UK), galactose (D(+))galactose 99+%, Acros organics, Thermo Fisher Scientific, Waltham, MA), mannose (D(+))mannose 99+%, Acros organics, Thermo Fisher Scientific), and fructose (D(-))fructose, Fisher Scientific, Thermo Fisher Scientific) were weighted and dissolved in 15 mL perfusion harvest for spectral acquisition in the spiking experiments. The same perfusion harvest was used for all the spikes in the initial screening phase to keep the harvest matrix constant.

For the model calibration phase, harvest samples of five different perfusion bioreactor runs, each sampled on five different days to capture intra- as well as inter-process variability were used (Table A.2). Harvests of bioreactor runs R1 and R2 were sampled and directly spiked for model calibration in the flow cell setup. Harvest samples of the three remaining bioreactors (R3, R4, and R5) were light-protected and stored at $-80 \text{ }^{\circ}\text{C}$ thereby building a harvest library. Harvest library samples were thawed and handled in the same way as the fresh harvest once the model calibration was performed (Figure A.2). The variability of the main process parameters was assessed in all the harvests using a Bioprofile Flex2 (Nova Biomedical). Spiking for raffinose ranged from $0 - 10 \text{ g L}^{-1}$, for glucose from $3.3 - 12.7 \text{ g L}^{-1}$, and is summarized in Figure A.3B.

Model verification was performed by connecting the flow cell to the harvest stream of a perfusion bioreactor run and continuous spectra acquisition was performed for 13 days during the stable operation phase. Two raffinose additions (RAs, RA1 and RA2) followed by two glucose additions (GAs, GA1 and GA2) were performed directly into the bioreactor to assess the model prediction performance of the model over the entire calibration range. Raffinose was fed for 4 h with a flow of 2.6 L day^{-1} by exchanging the standard perfusion medium with a medium supplemented with 50 g L^{-1} raffinose. Considering an average VCV of 12.2% during the model verification phase (data not shown) and washing out of the reactor already during the addition phase, a theoretical raffinose peak concentration of 10.9 g L^{-1} for RA1 was calculated based on the bioreactor mass balance (see Supporting Information). For RA2 with a starting concentration of 0.2 g L^{-1} raffinose determined by reference HPLC analytics, a peak concentration of 11.1 g L^{-1} was calculated. Glucose alterations were initiated by adding bolus shots of a 300 g L^{-1} glucose feed. A bolus addition of 50 and 12 mL was executed for GA1 and GA2, respectively. Glucose peak concentrations were calculated to be 11.8 g L^{-1} (GA1) and 5.6 g L^{-1}

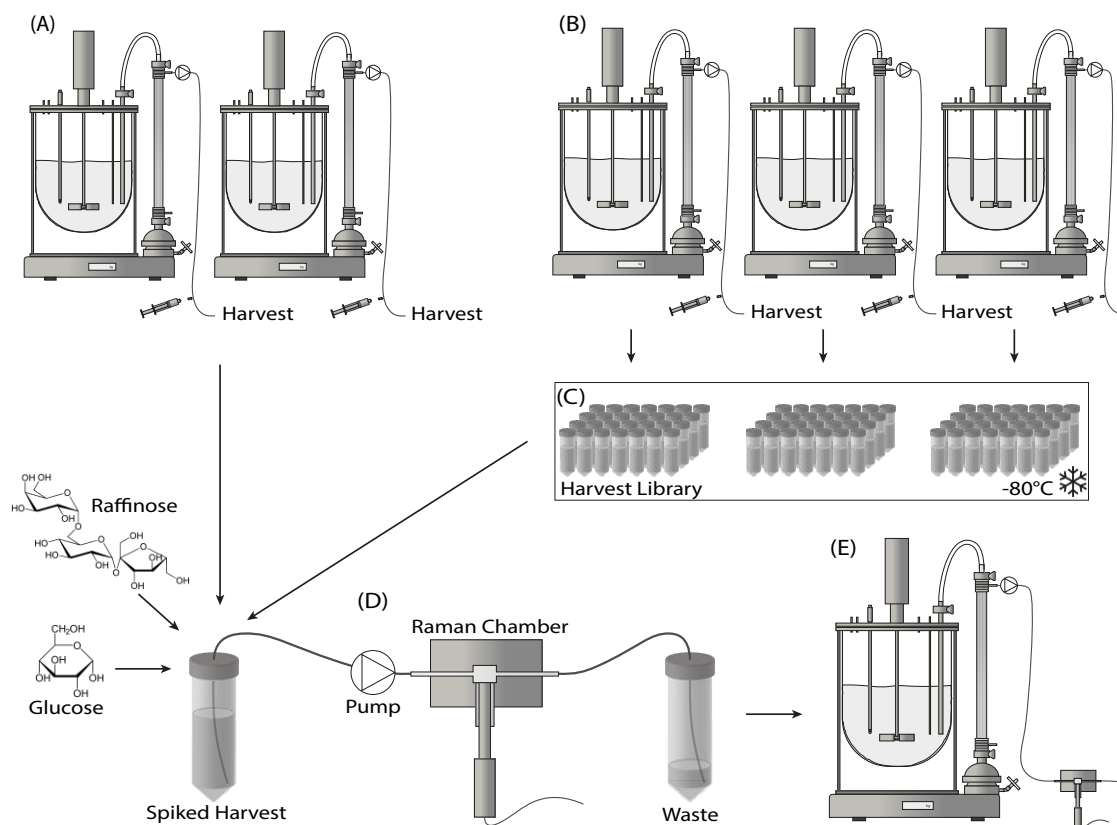


Figure A.2: Schematic of the harvest library spiking approach. Fresh harvest samples of two reactors (A) and harvest samples of three reactors (B) which were frozen and stored in a harvest library (C) were used for model calibration. Harvests were spiked with glucose and/or raffinose and pumped through a Raman flow cell (D) to generate Raman calibration data. The flow cell was then connected directly to the bioreactor run (E) for model verification.

(GA2) considering starting concentrations of 3.2 and 3.6 g L^{-1} , respectively. The bioreactor harvest stream was sampled during alterations for raffinose and glucose reference analytics.

3 Results and Discussion

3.1 Initial screening phase

The purpose of the initial screening phase is to determine whether the different analytes of interest can be distinguished by Raman spectroscopy in a best-case scenario without process disturbances, fluorescence, or other detrimental effects. By using a single harvest for all initial spiking experiments, sugar concentrations could independently be varied without changing the matrix at the same time.

PCA was performed after the standard spectral pretreatment showing distinct

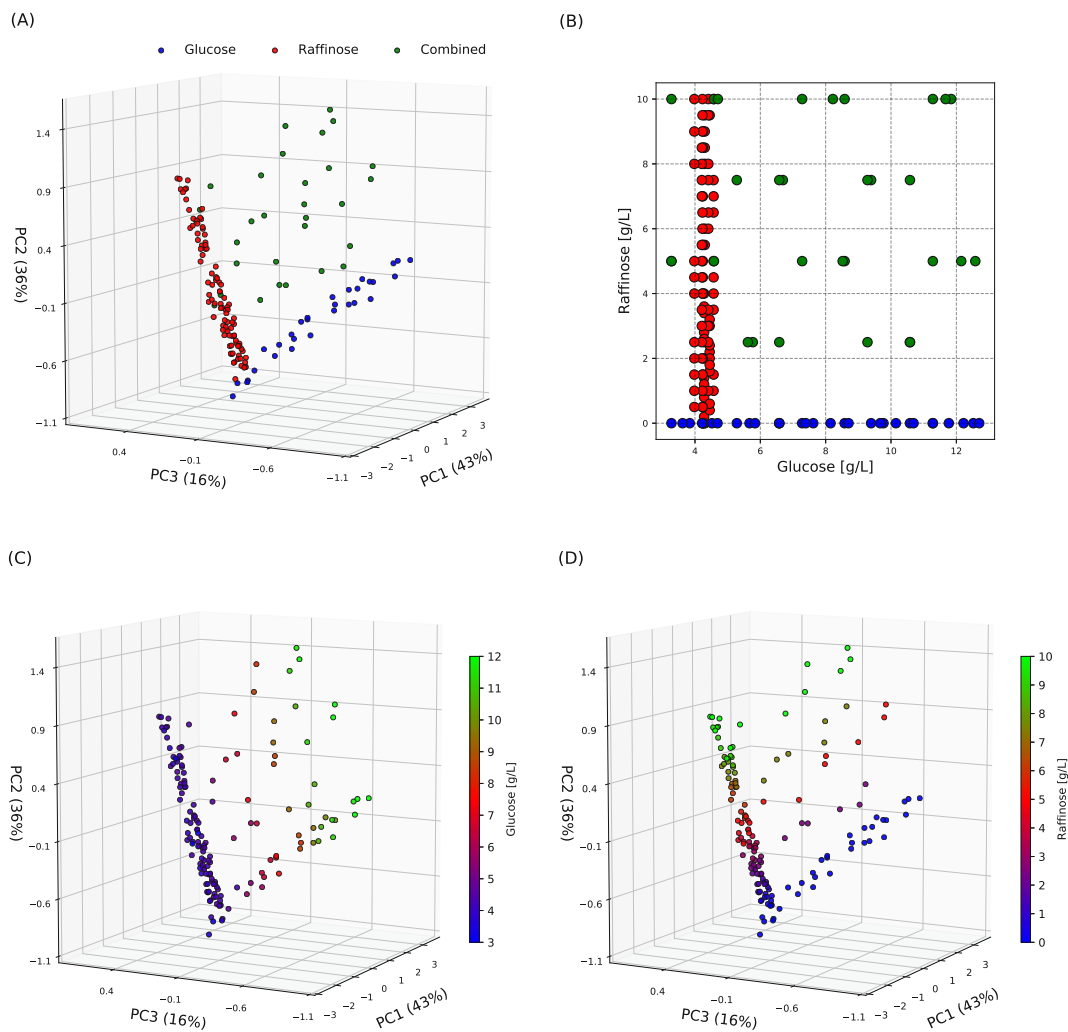


Figure A.3: PCA plot colored by the spiked compounds are depicted in (A) and the corresponding theoretical concentrations in (B). Single raffinose spikes are colored in red, single glucose spikes in blue and mixed spikes in green. CS1 is composed of red samples, CS2 of red and blue samples, CS3 of red, blue, and green samples. PCA plots of the individual sugar concentrations are depicted for glucose in (C) and raffinose concentration in (D). CS, calibration set; PCA, principal component analysis.

clustering of the Raman spectra with spiked sugars. The glucose variability in the spectra is mainly captured by principal component (PC)1 and PC2 (Figure A.4B), whereas variability introduced by other sugars can be explained by PC3 – 5 (Figure A.4A). All spectra containing only a certain glucose concentration but without additional sugar were populating in the center of the PCA plot. With increasing concentrations of the secondary sugar, the recorded spectra shifted into a specific direction away from the common center, the further away, the higher the added concentration of the secondary sugar. This showed not only that the investigated sugars

can be differentiated but can also be quantified within the respective concentration range.

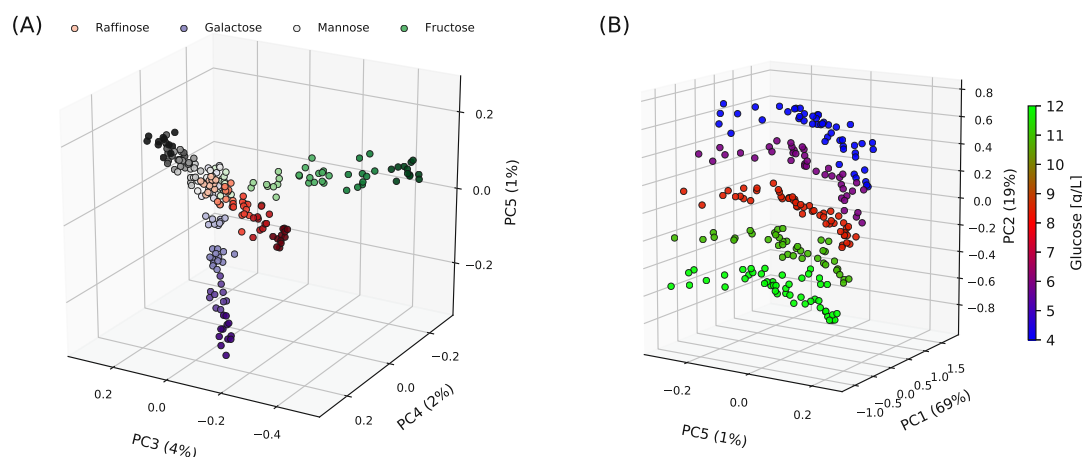


Figure A.4: Principal component analysis (PCA) plots for the initial screening phase for raffinose, galactose, mannose, and fructose with increasing color intensity according to their concentration (A) and glucose (B). Originating from a common center point, all sugars populate in a distinct direction. The higher the concentration, the further away from the center, demonstrating that the Raman spectra can distinguish the various sugars in a concentration-dependent manner.

Table A.1: PLS models were generated for the five different sugars within the specified concentration ranges. The calibration data set consisted of 200 samples, and the test data set of 28 samples. A five-fold cross-validation was performed. LV, latent variables; R^2 , coefficients of determination calibration; R^2CV , coefficients of determination cross validation; RMSE, root mean square error; RMSECV, root mean square error cross validation; RMSEP, root mean square error prediction; R^2P , coefficients of determination prediction.

Sugar	Concentration range [g L ⁻¹]	Suggested LV	RMSE [g L ⁻¹]	RMSECV [g L ⁻¹]	RMSEP [g L ⁻¹]	R^2	R^2CV	R^2P
Glucose	3.45 - 13.5	3	0.45	0.46	0.41	0.984	0.983	0.988
Raffinose	0 - 10	5	0.28	0.31	0.29	0.990	0.988	0.990
Galactose	0 - 4	5	0.20	0.21	0.21	0.969	0.965	0.967
Mannose	0 - 4	5	0.21	0.22	0.26	0.966	0.962	0.948
Fructose	0 - 4	5	0.14	0.14	0.16	0.985	0.983	0.982

PLS modeling results underlined the feasibility of distinguishing and quantifying the investigated sugars within the perfusion harvest matrix (Table A.1). In general, the models featured low RMSE, RMSECV, and RMSEP with R^2 , R^2CV , and $R^2P \geq 0.95$. To identify important wavenumber regions for the different PLS models, min – max normalized regression coefficients were used to color the background of the Raman spectra for the respective sugar models (Figure A.5). Model regression coefficient patterns vary strongly between different sugars. As a first

derivative was applied to the spectra during spectral pre-treatment, peak assignment to functional groups/bonds becomes a challenging task and would go beyond the scope of this work. Nevertheless, the most important regions according to the regression coefficients are in good agreement with specific bands reported in the literature [30, 31]. The highest regression coefficient region for glucose lies between 1,100 and 1,150 cm^{-1} , which is likely the particular COH bending ($\delta(\text{COH})$) at 1,128 cm^{-1} . Raffinose shows the highest regression coefficients between 820 and 860 cm^{-1} , relating to the COC stretching ($\nu(\text{COC})$) at 836 cm^{-1} . Galactose was reported to show a strong distinctive CCO stretching band ($\delta(\text{CCO})$) at 526 cm^{-1} , which corresponds well with the high regression coefficients between 510 and 550 cm^{-1} . Mannose showed particularly high regression coefficients between 460 and 510 cm^{-1} , covering an important mannose peak at 488 cm^{-1} found by others [31]. Fructose showed one particularly important wavenumber region between 610 and 650 cm^{-1} , reported to be a very particular OCO-stretching band ($\delta(\text{OCO})$) at 631 cm^{-1} . A clear color pattern of the spectra according to the concentration is visible in the regions with important regression coefficients for all measured sugars, which can be used as another indication for a compound-specific calibration based on the molecular fingerprint [12].

Overall, the specific sugar clustering seen in the PCA plot, successful PLS modeling with low RMSEP, and the assignment of the most important model regions to molecular vibrations indicated that a Raman calibration for the various sugars in the harvest matrix is possible.

3.2 Model calibration phase

Since glucose is one of the main energy sources in mammalian cell culture, the model for secondary sugars should be reliable also in the presence of varying glucose concentrations. Raffinose is a trisaccharide containing a glucose molecule and was therefore chosen as a worst-case scenario to demonstrate the applicability of the calibration workflow for similar compounds. Galactose, mannose, or fructose exhibited similar strong differences from glucose in the initial screening phase, and thus similar performances can be expected.

Model calibration was based on harvests collected from five different perfusion bioreactor runs once they reached a stable operation. Each reactor was sampled on five different working days to create a diverse set of harvest matrices. In contrast to the initial screening phase, where only a single harvest with a particular matrix composition was used, the model calibration data set is based on spiking experiments with inherent process variability (samples from different process working days) but

Table A.2: Perfusion harvest composition for model calibration. Overview of nutrient compositions, metabolite concentrations, and cell parameters of the five runs (harvest library) used for Raman model calibration and of 12 reference runs. Ranges from the harvest library, mean and SD represent inter-process statistics for the respective data origin. SD, standard deviation; VCD, viable cell density.

Data origin	Statistics	Glutamine [mM]	Glutamate [mM]	Glucose [g L ⁻¹]	Lactate [g L ⁻¹]	Ammonia [mM]	VCD [10 ⁶ cells mL ⁻¹]	Viability [%]
Cal. Runs	Range	0.66 - 1.3	1.23 - 2.2	3.3 - 4.7	0.03 - 0.61	2.31 - 5.94	19.2 - 29.8	68 - 96
Ref. Runs	Range	0.41 - 1.39	0.37 - 1.96	3.1 - 5.8	0 - 0.48	1.85 - 5.75	14.9 - 31.8	92 - 99
Cal. Runs	Mean	0.99	1.69	4.10	0.16	4.19	24.1	89
Ref. Runs	Mean	0.88	1.34	4.71	0.16	3.17	20.5	98
Cal. Runs	SD	0.19	0.22	0.41	0.22	1.18	2.6	8
Ref. Runs	SD	0.13	0.25	0.47	0.11	1.00	1.5	1

Table A.3: Modeling results for final glucose and raffinose models. Models based on calibration sets CS1, CS2, and CS3 for glucose (G) and raffinose (R) were evaluated on their prediction performance in the verification run. Spectra with aligned reference analytics for glucose and raffinose served as a prediction set. RMSEP versus LVs plots for all models can be found in the Supporting Information section (Supporting Information Figure A.11). LV, latent variables; R², coefficients of determination calibration; R²CV, coefficients of determination cross validation; RMSE, root mean square error; RMSECV, root mean square error cross validation; RMSEP, root mean square error prediction; R²P, coefficients of determination prediction. ^a3 LVs were used for the sake of comparison. RMSEP as a function of LVs are provided in the Supporting Information (Figure A.11).

Name	Sugar	Cal. set	Pred. set	LV	RMSE [g L ⁻¹]	RMSECV [g L ⁻¹]	RMSEP [g L ⁻¹]	R ²	R ² CV	R ² P
G_CS1	Gluc	95	18	3	0.08	0.09	1.59	0.741	0.698	0.565
G_CS2	Gluc	125	18	2	0.31	0.33	0.39	0.978	0.977	0.973
G_CS3	Gluc	155	18	2	0.36	0.38	0.32	0.979	0.977	0.982
R_CS1	Raff	95	23	3	0.18	0.18	0.84	0.997	0.996	0.948
R_CS2	Raff	125	23	3 ^a	0.22	0.22	0.17	0.996	0.995	0.998
R_CS3	Raff	155	23	3	0.29	0.30	0.25	0.993	0.992	0.995

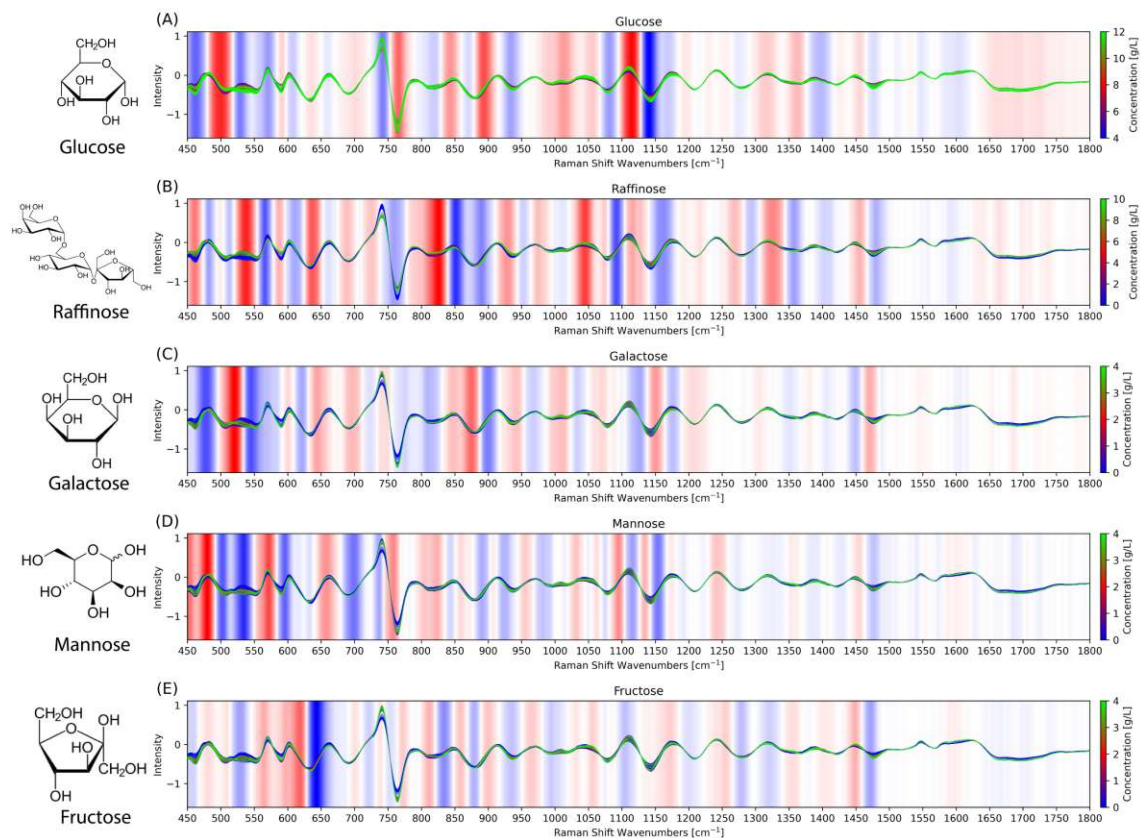


Figure A.5: Raman spectra for glucose (A), raffinose (B), galactose (C), mannose (D), and fructose (E) in perfusion process harvest. All spectra were pretreated with a Savitzky–Golay filter (derivative 1, polynomial = 2, window size = 31) followed by standard normal variate (SNV). Background bands represent the min-max normalized regression coefficient for the respective wavenumber for the individual models. Blue colors show the negative contribution of the wavenumber to the predicted value, whereas red colors indicate a positive contribution. The more intense the coloring, the more important the wavenumber for the respective model.

also inter-process variability (different bioreactor runs). Nutrient and metabolite concentrations as well as cell-specific parameter ranges of the calibration run harvests showed variability as expected from 12 reference runs throughout the steady state perfusion phase (Table A.2), which is a pre-requisite for obtaining robust Raman models. The means and SDs of the calibration and reference runs are close, providing a solid basis for spiking studies for the five calibration runs.

Harvest samples were either directly spiked and used for model calibration or frozen for later use. The spiking scheme in Figure A.3B summarizes which concentrations of glucose and raffinose were present after the spikes were added. Different spiking strategies were assessed to see whether raffinose spiking alone (red points) leads to a robust calibration set (CS1), or if the data set should be augmented (CS2) by glucose spiking (blue points). A third calibration set (CS3) was built including both the raffinose spikes (red points) and glucose spikes (blue points), but also all

the combinations of the two sugars (green points) present in the measured harvest at the same time. As different harvests contained varying starting concentrations of glucose, measurement points with equal amounts of spiked glucose and raffinose scatter slightly along the glucose axis and do not perfectly overlap as one would maybe expect of a DoE approach. The theoretical spiking scheme depicted in Figure A.3B could almost identically be projected by the PCA plot Figure A.3A, just with a small rotation, showing that glucose and raffinose influence the Raman spectra in an independent yet concentration-dependent manner. Raman spectra were then colored according to the glucose concentration (Figure A.3C) and according to the raffinose concentration (Figure A.3D), revealing a distinct separation along the concentration gradient. Already three PCs cover the variability introduced by the spiking approach. A PCA plot colored according to the reactor run origin of the spiked harvest can be found in the Supporting Information (Figure A.10).

PLS regression was performed for the three calibration sets, both for glucose and raffinose (Table A.3). All three models for glucose feature low RMSE ≤ 0.36 g L⁻¹ and RMSECV ≤ 0.38 g L⁻¹. Model glucose model for calibration set (G_CS)1 showed even smaller RMSE and RMSECV of 0.08 and 0.09 g L⁻¹, however, showed rather low R^2 and R^2CV with 0.741 and 0.698. For the other two glucose models, R^2 and R^2CV were above 0.975. A potential explanation for the low R^2 values for G_CS1 is the limited glucose range used for the model calibration of only 3.3 – 4.7 g L⁻¹. For this reason, the model might not be able to distinguish the free glucose from the glucose molecule present in the raffinose molecule as peaks are not ideally decoupled. Despite the low RMSE and RMSECV of model G_CS1, the PLS results must be taken with care and proper verification data should be considered. Raffinose models showed low RMSE ≤ 0.29 g L⁻¹ and RMSECV ≤ 0.30 g L⁻¹ with all R^2 and $R^2CV \geq 0.992$. Again, the model containing only raffinose spikes (raffinose model for calibration set [R_CS]1) showed the lowest RMSE and RMSECV, however with high R^2 values. In general, the obtained RMSE for glucose are in a similar range as models reported in the literature [6, 9–11], even in the presence of a secondary sugar like raffinose.

To assess whether concentration changes of untracked harvest component or freeze-thawing of harvest library samples (Run 3, 4, and 5) showed different concentration predictability compared to freshly spiked harvest samples (Run 1 and 2), a leave-one-out regression analysis was performed based on the largest calibration set CS3 (Supporting Information Table A.4). Therefore, one of the five runs was removed from the calibration set and used as a test set. This was iteratively done for all five runs leading to predictions for glucose and raffinose. The resulting RMSEP

for glucose and raffinose does not drastically deviate from the overall model based on all five runs for CS3, therefore underlining that the five chosen runs indeed cover process variability well and the harvest library approach is legitimate for Raman model generation.

3.3 Model verification phase

The initial screening phase and the model calibration phase were performed in an offline setup, meaning the flow cell was not connected directly to a bioreactor harvest stream. For the model verification phase, the flow cell was connected to the harvest stream of a perfusion bioreactor run and online predictions were made for glucose and raffinose (Figure A.6) using the six models built in the model calibration phase (Table A.3). Due to the absence of raffinose in the standard perfusion medium, two RAs into the bioreactor of 10.9 g L^{-1} were made on day 1 (RA1) and 11.1 g L^{-1} on day 4 (RA2) to assess the model performance on a wide concentration range. Furthermore, two GAs were performed on day 10 (GA1) and day 12 (GA2) to investigate the raffinose model performance in the presence of changing glucose concentrations. The GA1 addition targeted a bioreactor concentration of 11.8 g L^{-1} glucose to simulate a very strong glucose deviation. The addition of GA2 on the other hand simulated smaller glucose drift up to 5.6 g L^{-1} being more realistic for steady-state perfusion process fluctuations.

Raffinose predictions based on CS1 (Figure A.6A) led to a reasonable performance on RA1 and RA2, even though the target peak concentrations of raffinose were slightly underpredicted. After stopping RA, a slow decrease of the raffinose concentration due to consumption and washing out by the perfusion process was measured. Glucose predictions during the raffinose alterations are in close alignment with the reference points, showing no interference of the raffinose with the glucose prediction. However, strong prediction deviations for the glucose and raffinose models (G_CS1 and R_CS1) occurred when glucose was added at 11.8 g L^{-1} (GA1). These models are not able to distinguish raffinose from glucose, leading to a prediction of up to 3 g L^{-1} raffinose when there was no raffinose present at all. Glucose on the other hand was strongly underpredicted with 6.4 g L^{-1} instead of 11.8 g L^{-1} . Even for the smaller GA2 of 5.6 g L^{-1} , a similar behavior was observed, resulting in an RMSEP for glucose of 1.59 g L^{-1} and raffinose of 0.84 g L^{-1} (Table A.3). Glucose variability during the process was not sufficient to properly train the raffinose model, clearly demonstrating a need to extend the calibration range to make the model more robust in case of glucose fluctuations during the process. Proper model verification by performing compound spiking into the verification run should

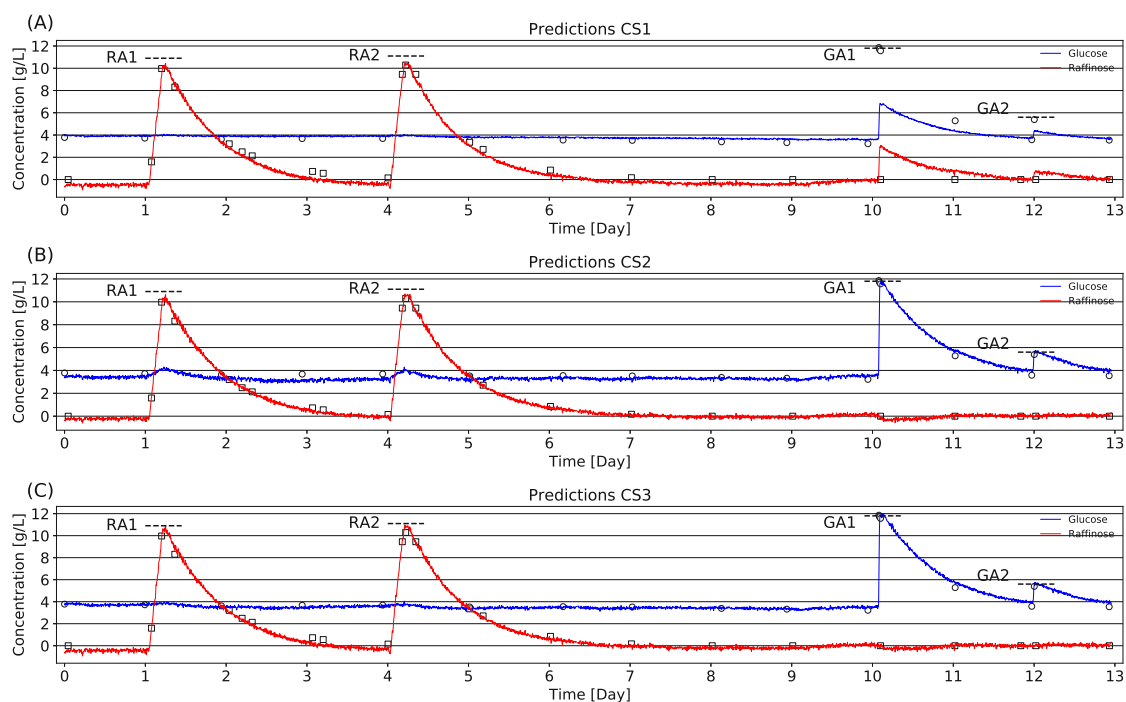


Figure A.6: Raman predictions of the verification run using models based on calibration set CS1 (A), CS2 (B), and CS3 (C). RA1 and RA2 represent raffinose additions of 10.9 and 11.1 g L⁻¹ to the bioreactor, whereas GA1 is a glucose addition of 11.8 g L⁻¹ and GA2 a glucose addition of 5.6 g L⁻¹. Raw predictions without moving average are shown and aligned with reference values for glucose (circles) and raffinose (squares). CS, calibration set; GA, glucose addition; RA, raffinose addition.

therefore routinely be done to assess model accuracy, robustness, and reliability as PLS regression metrics alone proved to be insufficient.

Raffinose models based on CS2 (Figure A.6B) showed good predictive power for the RAs RA1 and RA2 throughout the whole run. Only a marginal drop of 0.1 – 0.2 g L⁻¹ raffinose prediction was detected during the large GA GA1. No impact on raffinose prediction for GA2 was observed, simulating a realistic glucose deviation during the process. Thus, the raffinose model R_CS2 can be considered a specific and robust model for process monitoring. The glucose prediction by G_CS2 during the raffinose spikes showed small increases in the glucose prediction of about 0.2 – 0.3 g L⁻¹, indicating some leftover correlation between the two sugars. Nevertheless, glucose predictions by G_CS2 were in good alignment with the target concentration and the reference analytics during GAs GA1 and GA2. An overall low RMSEP of 0.39 g L⁻¹ for glucose and 0.17 g L⁻¹ for raffinose resulted in CS2 (Table A.3).

The prediction model for raffinose R_CS3 based on the largest calibration set CS3 including combination spikes in the calibration data showed good alignment with reference analytics (Figure A.6C). Compared to R_CS2, this model led to a

slightly higher RMSEP of 0.25 g L^{-1} , meaning that combination spiking did not bring any significant benefit during the perfusion run verification. Combination spiking however had a positive impact on the glucose predictions with an RMSEP of 0.32 g L^{-1} , even artifacts of raffinose during RAs RA1 and RA2 could be removed.

Comparing regression coefficients of the glucose model G_CS1, which was generated by simply aligning offline glucose measurements with Raman spectra, to the regression coefficients of the glucose model G_CS2 and G_CS3, clear differences in the absolute values are visible (Figure A.7A). The regression coefficient of the G_CS1 model show not only much lower absolute values, but peaks are less defined and noisier, being a sign of weak model calibration. This demonstrated that the G_CS1 model had not enough glucose variability in the calibration data to generate a robust and specific model for glucose. Albeit the overall regression coefficients are similar in structure for all raffinose models, the numeric contributions at the fingerprint regions are slightly more pronounced for R_CS2 and R_CS3 (Figure A.7B). The largest difference distinguishing R_CS1 from the other models (R_CS2 and R_CS3) arises between $1,100$ and $1,150 \text{ cm}^{-1}$. The more robust raffinose models R_CS2 and R_CS3 show much lower regression coefficients around $1,128 \text{ cm}^{-1}$, being exactly the very particular glucose COH bending ($\delta(\text{COH})$) at $1,128 \text{ cm}^{-1}$, and higher regression coefficients toward $1,150 \text{ cm}^{-1}$. The decoupling of the Raman bands for glucose and raffinose in this particular region by glucose spiking is most likely responsible for the higher specificity of the Raman prediction and demonstrates the necessity of proper spiking studies to decouple Raman bands.

Overall, successful model verification demonstrated that the developed model calibration approach spiking fresh harvest or a harvest library showed significant advantages compared to the traditional *in-situ* model calibration. Once a harvest library is established, new calibration models can be created at any time by thawing harvest and spiking it with analytes of interest. In this way, the Raman fingerprint of an analyte in a complex matrix is used to calibrate models while lowering matrix and process effects, constituting an alternative for perfusion cell culture to the relative resource and time-intensive DoE calibration strategies with parallelized bioreactor runs operated at varying process setpoints to induce sufficient process variability [13, 14]. Although all three calibration sets CS1, CS2, and CS3 showed good raffinose predictions during the first 10 days without larger glucose fluctuation, significant prediction deviations occurred when challenged by glucose alterations for the models with no glucose spikes (G_CS1 and R_CS1). The inherent glucose variability of the different harvest samples was not sufficient for the PLS regression to distinguish glucose from raffinose, and spiking proved to be necessary to achieve proper peak

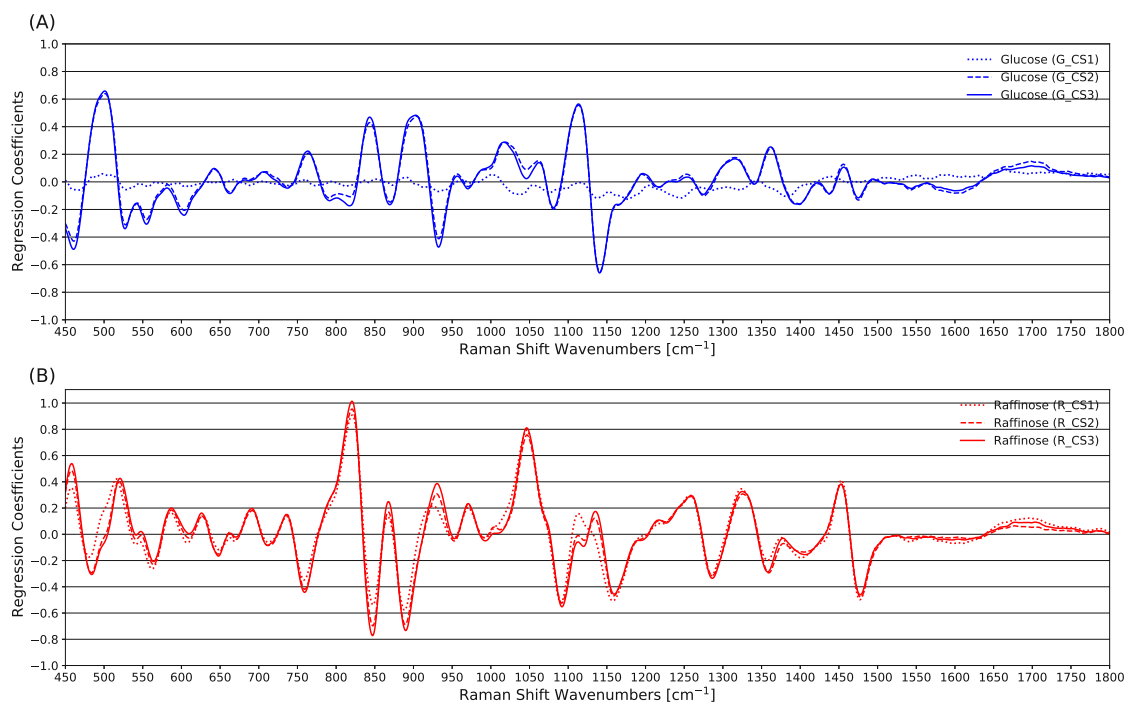


Figure A.7: Regression coefficients for glucose models (A) and raffinose models (B).

decoupling to generate compound-specific model predictions. In contrast to successful previous spiking studies where only one or a few spikes were added directly to a set of bioreactor runs [12, 15], the proposed spiking approach for perfusion cell culture increases spiking capabilities and flexibility as spikes are performed externally of the bioreactor in a small harvest volume. Whether combination spiking is necessary, or if single compound spiking is sufficient as demonstrated by the raffinose model R_CS2, remains an open question and might depend on the respective compounds being modeled. With the increasing number of components to be spiked at the same time, the DoE approach might show an advantage of significantly reducing the number of experiments. With raffinose, it was demonstrated that calibration models for analytes absent in the standard perfusion process can be created offline without the need of adding the analyte to a single bioreactor.

The novel calibration approach has been applied to a steady-state perfusion process for an mAb producing CHO cell line to extend calibration ranges and improve the decoupling of process compounds. Dynamic perfusion cultures with the presence of a cell-free harvest stream would equally profit from this calibration approach. Whether harvest-based calibration data acquisitions are sufficient to enable robust generic models such as for different media and cell lines remains an open question. The rapidity of generating adequate Raman spectra using the spiked harvest library approach would certainly facilitate the development of process specific as well as

general Raman models. Generating representative library samples for batch and fed-batch cultivations without a filtration device is more challenging due to the presence of cells. Thus, applying a similar design-of-experiment spiking approach to a fresh culture sample represents a promising method to decouple concomitant changing culture compounds.

4 Conclusion and Outlook

In this work, a systematic spiking-based Raman calibration workflow using a harvest library was developed to calibrate chemometric models and to monitor analyte concentrations using a flow cell connected to the harvest stream of a perfusion process. In a showcase to generate models of molecularly similar compounds, well-decoupled calibration models for glucose and raffinose with an RMSEP of 0.32 and 0.17 g L⁻¹, respectively, were achieved.

Providing appropriate calibration data sets in place of observations around normal operating points is paramount for chemometric modeling, whether standard PLS regression or more advanced mathematical regression techniques are used. The developed calibration workflow can be applied to other nutrients or metabolites as long as their concentration is in a Raman detectable range, eliminating the need for complex and time-consuming offline data alignment.

Ultimately, the presented workflow may pave the way for advanced monitoring and control of a number of critical cell culture components that can have a significant impact on critical quality attributes including post-translation modifications such as glycosylation or glycation.

Acknowledgements

The authors would like to thank Pavel Dagorov and his workshop team (FHNW) for building the Raman flow cell, Martin Held and Tsvetan Kardashliev (D-BSSE, ETH Zürich) for support in HPLC sugar analysis, and Damian von Blarer (FHNW) for automation support. Christian Ott (SCHOTT AG), Sebastian Dederer, and Christian Lux (tec5 AG) kindly assisted with the Raman device setup. Moreover, the authors would like to acknowledge Merck Serono SA (an affiliate of Merck KGaA) for material support and specifically the Bioprocess Sciences (BPS) team for valuable discussions and support throughout the project, especially Martin Jordan, Golzar Mesbah, Loic Chappuis, Alexandre Chatelin, Arnaud Perilleux, Hervé Broly, and Jonathan Souquet.

Conflict of interest

The authors declare that they have no known competing financial interests or personal relationships that could have appeared to influence the work reported in this paper.

Data availability statement

The data that support the findings of this study are available from the corresponding author upon reasonable request.

Supporting Information

$$V \cdot \frac{dc}{dt} = Q \cdot (c_{in} - c) \quad (\text{A.2})$$

Where c is the concentration of the analyte in the bioreactor, c_{in} the feed concentration, Q the flow rate, and V the bioreactor volume.

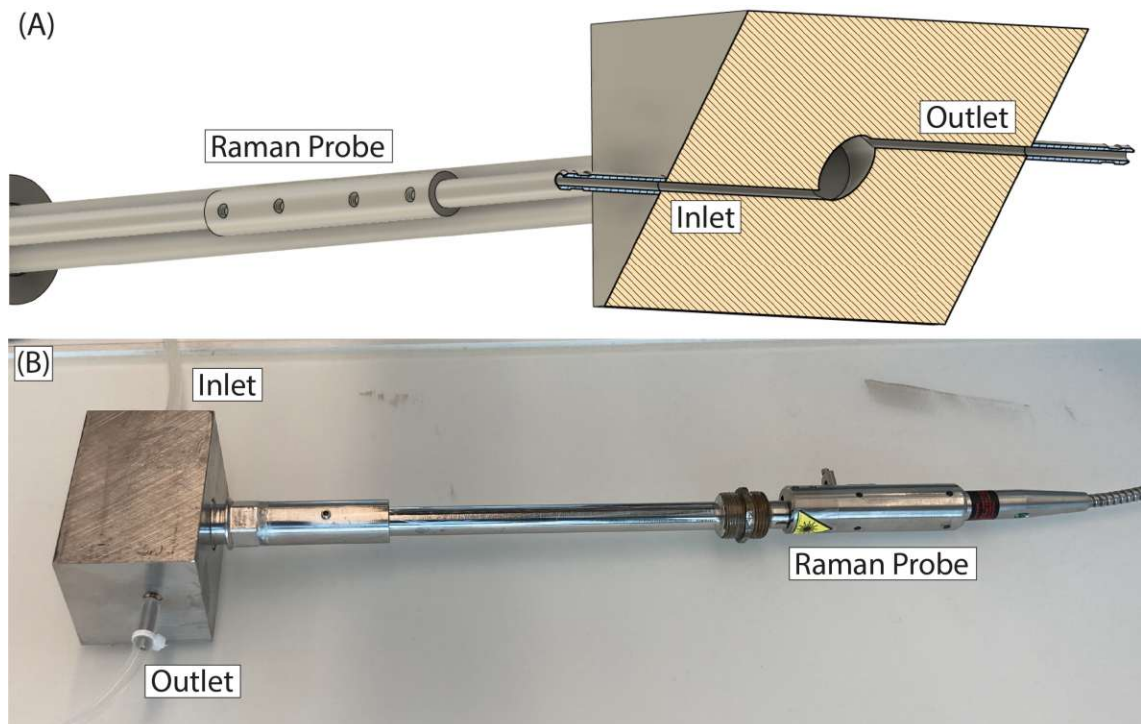


Figure A.8: Illustration of the Raman flow cell using a diagonal cut to show the flow chamber with the inlet (lower left side, close to Raman probe) and outlet (upper right side, further away from Raman sensor) (A). This design enabled efficient bubble removing ensuring stable operation. Picture of Raman flow cell setup connected to a perfusion harvest stream (B).

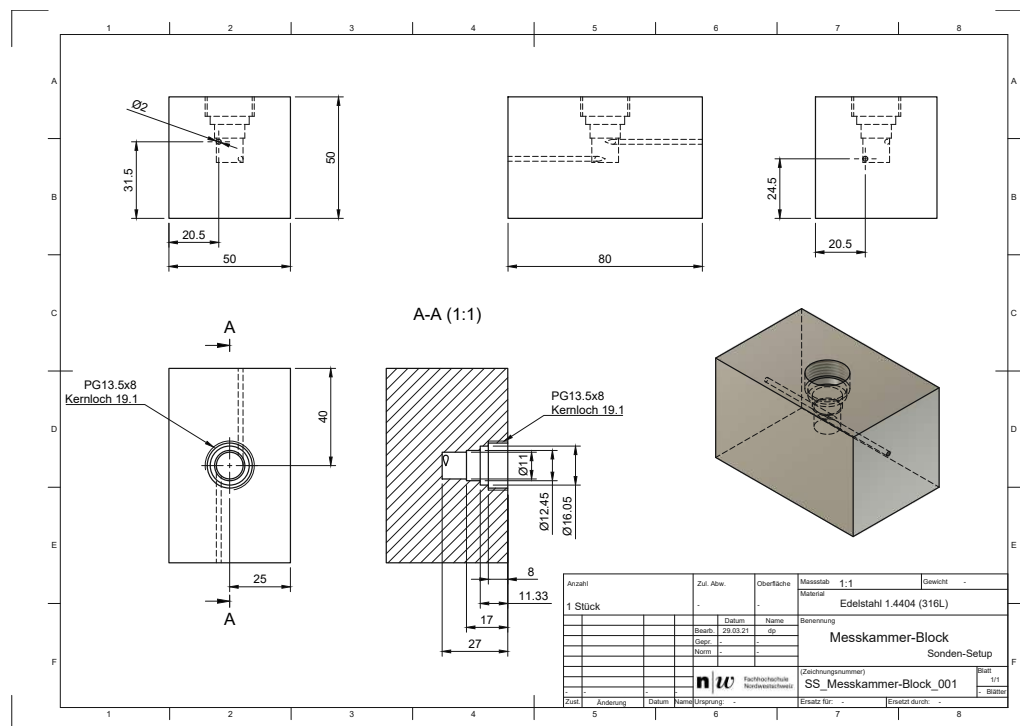


Figure A.9: Detailed drawing of the Raman flow cell, dimensions given in mm.

Table A.4: Modeling results of leave-one-out validation for glucose and raffinose. Based on calibration set CS3, glucose and raffinose models were built by leaving out data from a specific run, which was then used as prediction set. The removed data was used as a test set. All-R1 means that data from all runs except Run 1 are included to build the model, and the data from Run 1 was used as a test set in this particular case. For the models names “All”, all data from all five runs was included and an independent test set of the validation run was used.

Name	Sugar	Cal. Set	Pred. Set	RMSEC	RMSECV	RMSEP	R ² C	R ² CV	R ² P
All	Glucose	155	18	0.36	0.38	0.32	0.979	0.977	0.982
All-R1	Glucose	100	55	0.33	0.34	0.39	0.986	0.986	0.974
All-R2	Glucose	116	39	0.29	0.30	0.20	0.989	0.998	0.997
All-R3	Glucose	143	12	0.18	0.19	0.29	0.993	0.993	0.990
All-R4	Glucose	131	24	0.27	0.28	0.30	0.986	0.985	0.988
All-R5	Glucose	131	24	0.25	0.26	0.28	0.987	0.986	0.989
All	Raffinose	155	23	0.29	0.30	0.25	0.993	0.992	0.995
All-R1	Raffinose	100	55	0.33	0.36	0.17	0.992	0.990	0.997
All-R2	Raffinose	116	39	0.27	0.29	0.40	0.994	0.993	0.985
All-R3	Raffinose	143	12	0.29	0.30	0.34	0.993	0.992	0.992
All-R4	Raffinose	131	24	0.25	0.27	0.46	0.994	0.993	0.985
All-R5	Raffinose	131	24	0.28	0.30	0.36	0.993	0.992	0.990

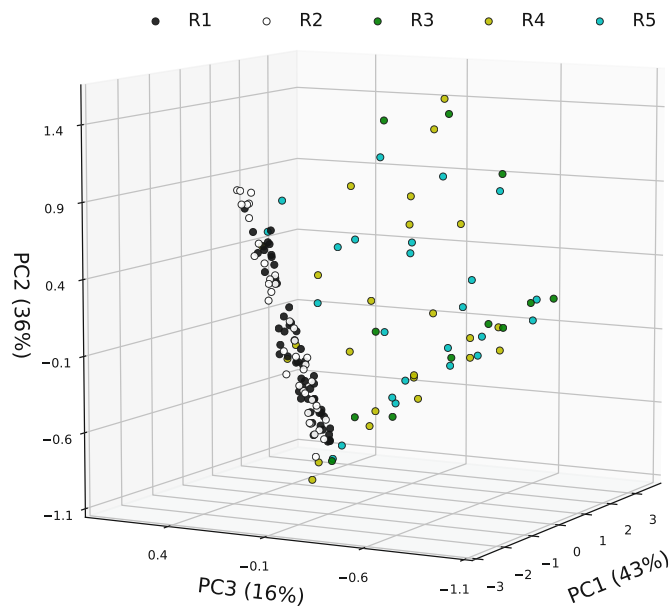


Figure A.10: PCA plot for glucose and raffinose model calibration using the harvest library colored according to the base harvest origin.

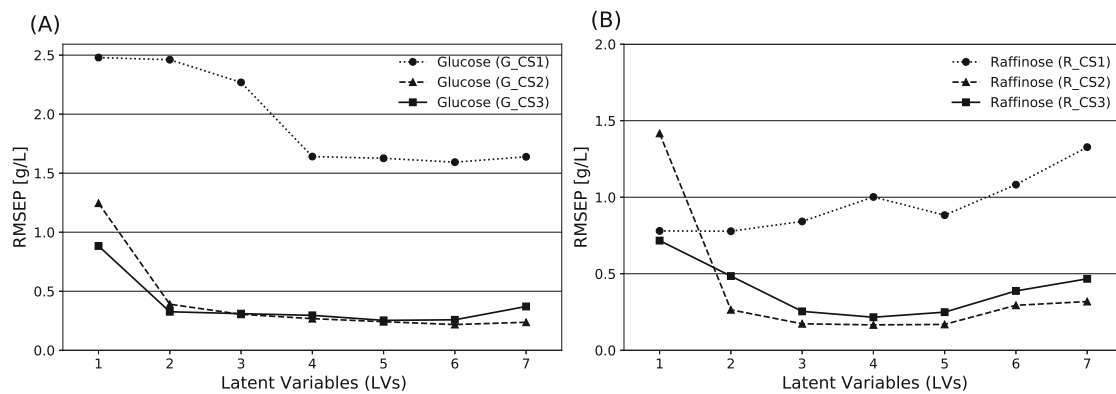


Figure A.11: RMSEP for glucose models (A) and raffinose models (B) according to the number of latent variables (LVs) used for PLS regression.

References

- [1] International Conference on Harmonisation of Technical Requirements for Registration of Pharmaceuticals for Human Use. *ICH Harmonised Tripartite Guideline: Pharmaceutical Development Q8(R2)*. 2009. URL: <http://www.ich.org/>.
- [2] International Conference on Harmonisation of Technical Requirements for Registration of Pharmaceuticals for Human Use. *ICH Harmonised Tripartite Guideline: Development and Manufacture of Drug Substances (Chemical Entities and Biotechnological/Biological Entities) Q11*. 2011. URL: <http://www.ich.org/>.
- [3] Adrian D. Shaw et al. “Noninvasive, on-line monitoring of the biotransformation by yeast of glucose to ethanol using dispersive Raman spectroscopy and chemometrics”. In: *Applied Spectroscopy* 53.11 (1999), pp. 1419–1428. ISSN: 00037028. DOI: 10.1366/0003702991945777.
- [4] Jean-Marc Bielser et al. “Perfusion mammalian cell culture for recombinant protein manufacturing – A critical review”. In: *Biotechnology Advances* 36.4 (2018), pp. 1328–1340. DOI: 10.1016/j.biotechadv.2018.04.011.
- [5] V. Vojinović, J. M.S. Cabral, and L. P. Fonseca. “Real-time bioprocess monitoring: Part I: In situ sensors”. In: *Sensors and Actuators, B: Chemical* 114.2 (2006), pp. 1083–1091. ISSN: 09254005. DOI: 10.1016/j.snb.2005.07.059.
- [6] Nicholas R. Abu-Absi et al. “Real time monitoring of multiple parameters in mammalian cell culture bioreactors using an in-line Raman spectroscopy probe”. In: *Biotechnology and Bioengineering* 108.5 (2011), pp. 1215–1221. ISSN: 00063592. DOI: 10.1002/bit.23023.
- [7] Silvére André et al. “In-line and real-time prediction of recombinant antibody titer by in situ Raman spectroscopy”. In: *Analytica Chimica Acta* 892 (2015), pp. 148–152. ISSN: 00032670. DOI: 10.1016/j.aca.2015.08.050.
- [8] Hemlata Bhatia et al. “In-line monitoring of amino acids in mammalian cell cultures using raman spectroscopy and multivariate chemometrics models”. In: *Engineering in Life Sciences* 18.1 (2018), pp. 55–61. ISSN: 16180240. DOI: 10.1002/elsc.201700084.

- [9] Bence Kozma, András Salgó, and Szilveszter Gergely. “Comparison of multivariate data analysis techniques to improve glucose concentration prediction in mammalian cell cultivations by Raman spectroscopy”. In: *Journal of Pharmaceutical and Biomedical Analysis* 158 (2018), pp. 269–279. ISSN: 07317085. DOI: 10.1016/j.jpba.2018.06.005.
- [10] Thaddaeus A. Webster et al. “Feedback control of two supplemental feeds during fed-batch culture on a platform process using inline Raman models for glucose and phenylalanine concentration”. In: *Bioprocess and Biosystems Engineering* 44.1 (2021), pp. 127–140. ISSN: 1615-7591. DOI: 10.1007/s00449-020-02429-y.
- [11] Jessica Whelan, Stephen Craven, and Brian Glennon. “In situ Raman spectroscopy for simultaneous monitoring of multiple process parameters in mammalian cell culture bioreactors”. In: *Biotechnology Progress* 28.5 (2012), pp. 1355–1362. ISSN: 87567938. DOI: 10.1002/btpr.1590.
- [12] Rafael M. Santos et al. “Monitoring mAb cultivations with in-situ raman spectroscopy: The influence of spectral selectivity on calibration models and industrial use as reliable PAT tool”. In: *Biotechnology Progress* 34.3 (2018), pp. 659–670. ISSN: 87567938. DOI: 10.1002/btpr.2635.
- [13] Brandon Berry et al. “Cross-scale predictive modeling of CHO cell culture growth and metabolites using Raman spectroscopy and multivariate analysis”. In: *Biotechnology Progress* 31.2 (2015), pp. 566–577. ISSN: 87567938. DOI: 10.1002/btpr.2035.
- [14] Ruth C. Rowland-Jones and Colin Jaques. “At-line raman spectroscopy and design of experiments for robust monitoring and control of miniature bioreactor cultures”. In: *Biotechnology Progress* 35.2 (2019), e2740. ISSN: 8756-7938. DOI: 10.1002/btpr.2740.
- [15] Carl Rafferty et al. “Analysis of chemometric models applied to Raman spectroscopy for monitoring key metabolites of cell culture”. In: *Biotechnology Progress* 36.4 (2020), pp. 1–16. ISSN: 8756-7938. DOI: 10.1002/btpr.2977.
- [16] Ruth C. Rowland-Jones et al. “Spectroscopy integration to miniature bioreactors and large scale production bioreactors—Increasing current capabilities and model transfer”. In: *Biotechnology Progress* 37.1 (2021), pp. 1–14. ISSN: 15206033. DOI: 10.1002/btpr.3074.

- [17] Júlia Domján et al. “Raman-based dynamic feeding strategies using real-time glucose concentration monitoring system during adalimumab producing CHO cell cultivation”. In: *Biotechnology Progress* 36.6 (2020). ISSN: 8756-7938. DOI: 10.1002/btpr.3052.
- [18] Denizhan Yilmaz et al. “Application of Raman spectroscopy in monoclonal antibody producing continuous systems for downstream process intensification”. In: *Biotechnology Progress* 36.3 (2020). ISSN: 15206033. DOI: 10.1002/btpr.2947.
- [19] Fabian Feidl et al. “A new flow cell and chemometric protocol for implementing in-line Raman spectroscopy in chromatography”. In: *Biotechnology Progress* 35.5 (2019), pp. 1–10. ISSN: 15206033. DOI: 10.1002/btpr.2847.
- [20] Jyoti Batra and Anurag S. Rathore. “Glycosylation of monoclonal antibody products: Current status and future prospects”. In: *Biotechnology Progress* 32.5 (2016), pp. 1091–1102. ISSN: 15206033. DOI: 10.1002/btpr.2366.
- [21] “Quality attributes of recombinant therapeutic proteins: An assessment of impact on safety and efficacy as part of a quality by design development approach”. In: *Biotechnology Progress* 28.3 (2012), pp. 608–622. ISSN: 87567938. DOI: 10.1002/btpr.1548.
- [22] David Brühlmann et al. “Cell culture media supplemented with raffinose reproducibly enhances high mannose glycan formation”. In: *Journal of Biotechnology* 252.December 2016 (2017), pp. 32–42. ISSN: 01681656. DOI: 10.1016/j.jbiotec.2017.04.026.
- [23] Michael J. Gramer et al. “Modulation of antibody galactosylation through feeding of uridine, manganese chloride, and galactose”. In: *Biotechnology and Bioengineering* 108.7 (2011), pp. 1591–1602. ISSN: 00063592. DOI: 10.1002/bit.23075.
- [24] Tanaya Surve and Mugdha Gadgil. “Manganese increases high mannose glycoform on monoclonal antibody expressed in CHO when glucose is absent or limiting: Implications for use of alternate sugars”. In: *Biotechnology Progress* 31.2 (2015), pp. 460–467. ISSN: 87567938. DOI: 10.1002/btpr.2029.
- [25] Thomas K. Villiger et al. “Controlling the time evolution of mAb N-linked glycosylation, Part I: Microbioreactor experiments”. In: *Biotechnology Progress* 32.5 (2016), pp. 1123–1134. ISSN: 87567938. DOI: 10.1002/btpr.2305.

- [26] Liang Zhang et al. “Combined effects of glycosylation precursors and lactate on the glycoprofile of IgG produced by CHO cells”. In: *Journal of Biotechnology* 289 (2019), pp. 71–79. ISSN: 01681656. DOI: 10.1016/j.jbiotec.2018.11.004.
- [27] Craig Zupke et al. “Real-time product attribute control to manufacture antibodies with defined N-linked glycan levels”. In: *Biotechnology Progress* 31.5 (2015), pp. 1433–1441. ISSN: 87567938. DOI: 10.1002/btpr.2136.
- [28] S. Metze et al. “Monitoring online biomass with a capacitance sensor during scale-up of industrially relevant CHO cell culture fed-batch processes in single-use bioreactors”. In: *Bioprocess and Biosystems Engineering* 43.2 (2020), pp. 193–205. ISSN: 1615-7591. DOI: 10.1007/s00449-019-02216-4.
- [29] Bin Lai et al. “Simultaneous Determination of Sugars , Carboxylates , Alcohols and Aldehydes from Fermentations by High Performance Liquid Chromatography”. In: (2016). DOI: 10.3390/fermentation2010006.
- [30] Monika Dudek et al. “Raman Optical Activity and Raman spectroscopy of carbohydrates in solution”. In: *Spectrochimica Acta Part A: Molecular and Biomolecular Spectroscopy* 206 (2019), pp. 597–612. ISSN: 13861425. DOI: 10.1016/j.saa.2018.08.017.
- [31] Vincent Dumouilla and Claude Gilles Dussap. “Online analysis of D-glucose and D-mannose aqueous mixtures using Raman spectroscopy: an in silico and experimental approach”. In: *Bioengineered* 12.1 (2021), pp. 4420–4431. ISSN: 2165-5979. DOI: 10.1080/21655979.2021.1955550.

A.2 Scientific Publication Section II

Raman-controlled pyruvate feeding to control metabolic activity and product quality in continuous biomanufacturing

This section is based on the following publication: P. Romann, S. Schneider, D. Tobler, M. Jordan, A. Perilleux, J. Souquet, C. Herwig, J-M. Bielser, and T. K. Villiger, **Raman-controlled pyruvate feeding to control metabolic activity and product quality in continuous biomanufacturing**, 2023, Under review in *Biotechnology Journal*.

Abstract

Background: Despite technological advances ensuring stable cell culture perfusion operation over prolonged time, reaching a cellular steady-state metabolism remains a challenge for certain manufacturing cell lines. This study investigated the stabilization of a steady-state perfusion process producing a bispecific antibody with drifting product quality attributes, caused by shifting metabolic activity in the cell culture.

Main Methods: A novel on-demand pyruvate feeding strategy was developed, leveraging lactate as an indicator for tricarboxylic acid (TCA) cycle saturation. Real-time lactate monitoring was achieved through in-line Raman spectroscopy, enabling accurate control at predefined target setpoints.

Major Results: The implemented feedback control strategy resulted in a 3-fold reduction of ammonium accumulation and stabilized product quality profiles. Stable and flat glycosylation profiles were achieved with standard deviations below 0.2% for high mannose and fucosylation. Whereas galactosylation and sialylation were stabilized in a similar manner, varying lactate setpoints might allow for fine tuning of these glycan forms.

Implication: The Raman-controlled pyruvate feeding strategy represents a valuable tool for continuous manufacturing, stabilizing metabolic activity and preventing product quality drifting in perfusion cell cultures. Additionally, this approach effectively reduced high mannose, helping to mitigate increases associated with process intensification, such as extended culture durations or elevated culture densities.

Keywords: steady-state perfusion, Raman feedback control, pyruvate, glycosylation stabilization, continuous manufacturing

Abbreviations: AOI, analyte of interest; DS, drug substance; LV, latent variable; PAT, process analytical technology; PLS, partial least squares; R^2 , coefficient of determination calibration; R^2CV , coefficient of determination cross validation; R^2P , coefficient of determination prediction; RMSE, root mean square error calibration; RMSECV, root mean square error cross validation; RMSEP, root mean square error prediction; RV, reactor volumes; SD, standard deviation; SNV, standard normal variate; TCA cycle, tricarboxylic acid cycle; VCD, viable cell density; VCV, viable cell volume.

1 Introduction

The biopharmaceutical industry is experiencing a shift from conventional batch processes to integrated and continuous biomanufacturing [1]. Continuous manufacturing enables process intensification, resulting in a smaller facility footprint and various benefits like reduced capital expenditure, shorter lead time for plant construction, increased flexibility in responding to demand changes, and improved product quality consistency [2–6]. The transition implies a significant change in upstream and downstream processing influencing various aspects such as process control strategy, quality monitoring, and regulatory matters [7].

Several small-scale studies have demonstrated feasibility of continuous biomanufacturing [8–11] and first successful pilot scale and GMP productions were reported [12, 13]. Depending on the downstream strategy, either stable process intermediates were generated and pooled at the end of a manufacturing run to define a batch [12], or several lots were created from one bioreactor run, treated as individual drug substance (DS) batches for end-product testing [13]. Storing stable process intermediates at manufacturing scale can require large storage capacities exceeding 20,000 L and requires in-process hold studies to demonstrate product stability [14]. Generating multiple DS batches from one manufacturing offers various advantages in terms of storage capacity reduction, reduced residence time for labile proteins and flexibility with respect to the process duration even at manufacturing scale. In this case however, consistent product quality is required at any time during the continuous manufacturing process as no final product pooling is performed and each DS batch must fulfil the quality expectations.

Steady-state perfusion upstream processing represents the first step in the continuous manufacturing process. Even though the name steady-state perfusion would not only imply constant component addition and removal but also constant cellular metabolism, biological reaction rates are not always constant and might change with proceeding runtime [15]. This is supported by transcriptomic and proteomic studies demonstrating that some transcripts of CHO cells in steady-state perfusion never reached a steady-state concentration [16]. Significant fluctuations of metabolites during steady-state perfusion operation were reported in the literature, consequently resulting in drifting product quality attributes. As such, lactate levels were observed to drop after an initial peak, ammonium levels were observed to rise with proceeding runtime and changes in cell diameter were observed, all indicating that the cell culture is not in the desired steady-state [17].

Metabolic profiling of CHO cells revealed high glycolytic activity with lactate

production and reduced tricarboxylic acid (TCA) cycling in the exponential growth phase of batch or fed-batch cultures [18–21]. When the culture proceeded into the stationary phase, lactate consumption and maximal TCA cycling indicated high oxidative phosphorylation in the mitochondria. Even though lower catabolism of amino acids was reported in the stationary phase compared to the growth phase, still a substantial fraction of amino acids was replenishing the TCA cycle [20, 22–24]. The preferred metabolic state of cells in steady-state perfusion cultures is somewhere at the edge between growth phase and stationary phase; cell division is still desired to keep a stable culture with high viability, but at a much-reduced rate compared to the regular growth phase to reduce the bleed fraction. Accordingly, after an initial lactate peak in the exponential growth phase, the metabolic shift resulted in consumption of the accumulated lactate. Once the lactate had been consumed, amino acid catabolism had to replenish the TCA cycle, resulting in increased ammonium levels and a drift of quality attributes towards less complex glycoforms in perfusion cultures [17]. Similar glycoform shifts were observed for elevated ammonium concentrations in fed-batch processes [25–27]. Ammonium was reported to interfere with the glycosylation machinery by altering nucleotide sugar synthesis and transport [28–30], changing protein expression [26], misslocalizing glycosyltransferases or changing pH in the Golgi apparatus impacting enzymatic activity [27, 31]. Therefore, ensuring constant ammonium levels in steady-state perfusion cultures is critical to deliver consistent product quality for continuous biomanufacturing. Product quality levers must be defined, and appropriate control strategies must be implemented in order to alleviate the influence of to the changing cellular metabolism on product quality.

TCA cycle intermediates and molecules entering the TCA cycle such as lactate or pyruvate represent an interesting toolbox to influence metabolic activity of the cell culture. Whereas in fed-batch processes TCA cycle intermediates and lactate have been identified to increase process titer when fed in the stationary phase [32, 33], in steady-state perfusion cultures a constant pyruvate addition of $2 \text{ g L}^{-1} \text{ day}^{-1}$ has been demonstrated to stabilize the product quality profile [17]. In all cases, the feeding of these metabolites clearly decreased the ammonium production, indicating a reduced pressure on amino acid catabolism to replenish the TCA cycle [23]. To achieve the full potential benefits, the challenge remains to stay close at the optimal feeding rate. Overfeeding should be avoided to prevent excessive lactate accumulation whereas insufficient feeding would cause a metabolic switch back to amino acid catabolism, leading to increased ammonium concentrations. Considering that metabolic activity is not truly stable over time in perfusion processes [15], previ-

ously published constant feeding strategies might not be appropriate depending on the manufacturing cell line. Therefore, it becomes crucial to devise advanced pyruvate feeding strategies that can adjust to the specific needs of the cell culture. Such adaptable strategies offer a versatile solution for stabilizing both the perfusion cell cultures and the product quality.

The aim of this study is to stabilize the metabolic activity during an industrial steady-state perfusion cell culture process producing a bispecific antibody. Raman spectroscopy integrated into the cell free perfusion harvest stream allowed accurate and robust real-time lactate monitoring and control at target concentration. A novel Raman-based feedback control was realized continuously feeding pyruvate to maintain stable lactate levels, adapting to changing culture need with run progression. As a result, the TCA cycle was saturated by pyruvate throughout the entire 40-day perfusion process which significantly reduced amino acid catabolism. Subsequently, ammonium accumulation was prevented and product glycosylation such as high mannose, fucosylation and galactosylation were successfully stabilized to consistent quality profiles suitable for fully integrated continuous manufacturing processes.

2 Materials and Methods

2.1 Perfusion bioreactor setup and operation

A proprietary CHO-K1 cell line producing a bispecific mAb was expanded in an incubator (Multitron, Infors HT, Bottmingen, Switzerland) for 21 days using a proprietary chemically defined perfusion platform medium (Merck KGaA, Corsier-sur-Vevey, Switzerland). Perfusion bioreactors (Labfors 5 Cell, Infors HT, Bottmingen, Switzerland) were inoculated at a seeding density of 0.6×10^6 viable cells mL^{-1} . Culture conditions were maintained at $36.5 \text{ }^\circ\text{C}$ with a dissolved oxygen setpoint at 50% (VisiFerm DO Arc, Hamilton, Bonaduz, Switzerland). The pH was controlled at 7.07 ± 0.17 (EasyFerm Plus Arc probe Hamilton, Bonaduz, Switzerland) by sparging CO_2 and a $1.1 \text{ M Na}_2\text{CO}_3$ solution. Bioreactors were operated at 2 L working volume. Perfusion started on day 0 and was kept constant at 1.3 reactor volumes per day (RV day^{-1}) until the end of the run. Bioreactor harvests were gravimetrically controlled to maintain the bioreactor weight constant with a cell retention device consisting of a hollow fiber filter having a pore size of $0.22 \text{ } \mu\text{m}$ (Repligen, Waltham, Massachusetts, USA) driven by centrifugal pumps (Levitronix, Zurich, Switzerland). After an initial growth phase, an online capacitance

probe (Incyte Arc, Hamilton, Bonaduz, Switzerland) was used to keep the viable cell volume (VCV) constant at 12%. Next to standard perfusion runs (controls), two perfusion runs with Raman-controlled pyruvate feeding were performed to keep lactate concentration constant at a target setpoint. For those runs, a Raman flow cell was inserted into the cell-free harvest stream. Based on lactate predictions by Raman, a pyruvate feed was added to the cell culture by a PI-controlled feed pump (Ismatec Reglo ICC, Ismatec SA, Barrington, USA) to keep lactate concentration on setpoint. The pyruvate feed consisted of perfusion media supplemented with 100 g L⁻¹ sodium-pyruvate (CAS: 113-24-6, Thermo Fisher Scientific, Waltham, Massachusetts, USA) and was placed on a balance to calculate pyruvate addition rates. The first run was performed with a lactate setpoint of 0.7 g L⁻¹ where the feedback control was active from day 5 – 41. The second run was controlled at 0.3 g L⁻¹ lactate from day 6 – 39 and an additional supplementation of 5 mmol L⁻¹ ammonium was added to the culture media from day 21 – 35.

2.2 Raman Hardware Setup and Data Acquisition

A Raman spectrometer Multispec[®] Raman (tec5 AG, Steinbach, Germany) using the software MultiSpec[®] Pro II (tec5 AG, Steinbach, Germany) with 785 nm laser excitation wavelength and 500 mW power output was used in combination with the InPhotonics RamanProbe[™] (InPhotonics, Norwood, USA). The Raman probe was inserted into a custom-made flow cell made from stainless steel 316 L with a chamber volume of 0.95 mL [34]. Spectral acquisition time was 12 × 20 s. For in-process control, a spectra every 300 s was recorded.

2.3 Raman Model Calibration

Model calibration was performed by spiking a harvest library as described previously [34]. A peristaltic pump (Ismatec Reglo ICC, Ismatec SA, Barrington, USA) connected to the Raman flow cell was used as an offline calibration setup for rapid spectral acquisition. Flow rates through the Raman chamber were matching flow rates of a perfusion bioreactor operated at 1.3 RV day⁻¹ and a bleed rate of 20%, resulting in approximately 2 L day⁻¹. To get a representative harvest library, harvests of three perfusion bioreactors were sampled on different days to capture intra- as well as inter-process variability. Spiked analytes of interest for model generation were lactate, glucose, pyruvate and ammonium (Table A.5). A total of 286 Raman spectra were recorded with this offline calibration setup. Additionally, 72 in-process Raman spectra where the flow cell was directly inserted into the harvest stream of

a perfusion bioreactor were recorded and implemented into the calibration data set. Overall, 358 Raman spectra were combined to build the calibration data set.

Table A.5: PLS models were generated for lactate, glucose, pyruvate and ammonium within the specified concentration ranges. The calibration data set consisted of 286 spiked samples and 71 in-process samples, the spike validation (Figure A.12) served as test set. 5-fold cross-validation was performed.

Compound	Concentration Range	LV	RMSE	RMSECV	RMSEP	R ²	R ² CV	R ² P
Lactate	0.0 - 2.2 g L ⁻¹	4	0.08	0.09	0.11	0.980	0.978	0.799
Glucose	3.5 - 7.0 g L ⁻¹	4	0.14	0.14	0.15	0.975	0.974	0.940
Pyruvate	0.0 - 2.0 g L ⁻¹	1	0.07	0.09	0.08	0.987	0.983	0.798
Ammonium	0.0 - 6.0 mmol L ⁻¹	7	0.45	0.49	1.32	0.895	0.877	0.192

2.4 Chemometric Modelling

The Unscrambler X (CAMO Software, Oslo, Norway) was used for multivariate data analysis. All spectra were preprocessed by a 1st derivative with Savitzky-Golay filter (2nd order polynomial, 31 points window) followed by standard normal variate (SNV). Preprocessed spectra were then truncated to wavenumbers from 450 – 1,800 cm⁻¹ prior to partial least squares regression (PLS). The number of latent variables (LV) suggested by The Unscrambler X software was chosen for prediction models. During the regression modelling, prediction models were assessed based on the root mean square error (RMSE) of the calibration dataset and a 5-fold cross-validation (RMSECV). Further, the corresponding coefficients of determination R² and R²CV were considered as previously described [35, 36].

2.5 Model Verification

Model verification studies were performed by spiking various components directly into a perfusion bioreactor with the Raman flow cell connected to the harvest stream. Reference samples were taken before and after bolus additions for reference analytics. The analytes of interest lactate, glucose, pyruvate and ammonium but also sodium chloride were added as bolus at process relevant concentrations (Table A.6) to validate the impact of the spiked compound on the previously generated Raman prediction models. The model parameters RMSEP and R²P were calculated based on the Raman predictions of the spike recovery experiment and reference compound concentrations measured by at-line or offline analytics.

Table A.6: Spiked compounds as well as stock solution, effectively increase of compound concentration in bioreactor (spike addition) and added spike volume. Spike solutions were prepared in perfusion harvest.

Spiking Time [days]	Compound	Stock Solution [g L ⁻¹]	Spike Addition [g L ⁻¹]	Spike Volume [mL]
0.5	Ammonium	2.88	0.01 (= 0.5 mmol L ⁻¹)	6.3
0.7	Sodium-chloride	100	1	20.0
1.6	Glucose	400	2	10.0
2.7	Lactate	79.5	1	25.2
3.6	Pyruvate	78.9	0.5	12.7
4.4	Ammonium	2.88	0.04 (= 2.0 mmol L ⁻¹)	25.0

2.6 Analytics

Cell density, viability, cell diameter, glucose, lactate, ammonium, and pH were measured using a BioProfile FLEX2 (Nova Biomedical, Waltham, USA). Perfusion bioreactors were automatically sampled by the FLEX2 On-Line Autosampler (Nova Biomedical, Waltham, USA) and samples were fractionated using a Teledyne Cetac ASX-7200 (Teledyne CETAC Technologies, Omaha, Nebraska, USA). Viable cell volume (VCV) was calculated as follows [37]:

$$\text{VCV} = \frac{\frac{4}{3} \cdot \pi \cdot \left(\frac{D}{2}\right)^3 \cdot \text{VCD}}{V} \cdot 100 \quad (\text{A.3})$$

Where D is the average cell diameter, VCD the viable cell density, and V is the cell culture volume, assuming a spherical shape of the cells. Osmolality was measured by an osmometer OM 819 (Vogel MedTech GmbH, Fernwald, Germany). Pyruvate was quantified on an Agilent 1200 HPLC system combined with a refractive index detector (Agilent RID, G7162A) as described in the literature [38]. Compounds were separated using a ReproGel H column (250 × 4.6 mm, Su.9.h0.s2546, Dr. Maisch, Germany) with a guard column ReproGel H column (5 × 4.6 mm, Su.9.h0.s0046, Dr. Maisch, Germany). The flow rate and the column temperature were adapted to 0.5 mL min⁻¹ and 55 °C with a runtime of 15 min. Process titer was determined using a protein affinity high performance liquid chromatography device (PA-HPLC, Waters, Milford, Massachusetts, USA). Amino-acid concentrations were measured using ultra-performance liquid chromatography (UPLC, Waters, Milford, Massachusetts, USA). To quantify protein glycosylation, mAbs were purified on Phytips (PhytipsVR, PhyNexus, San Jose, CA, USA), followed by a multi attribute method (MAM) which is based on high performance liquid chromatography-mass spectrometry (LC-MS, Vanquish™ Horizon UHPLC System

and Q ExactiveTM Plus, Thermo Fisher Scientific, Waltham, Massachusetts, USA).

2.7 Calculation of net specific consumption rates

Viable cell volume net specific consumption rates (q_{AOI}) for various analytes of interest (AOI) were calculated according to formula A.5. For the net consumption rate of pyruvate (q_{Pyr}), the additional pyruvate feed had to be included according to formula A.5:

$$q_{AOI} = \frac{Q_{Perf} \cdot (c_{in} - c_{out}) - \frac{c_{t1} - c_{t2}}{t_2 - t_1}}{X} \quad (A.4)$$

$$q_{Pyr} = \frac{Q_{Perf} \cdot (c_{in} - c_{out}) + Q_{Feed} \cdot c_{Feed} - \frac{c_{t1} - c_{t2}}{t_2 - t_1}}{X} \quad (A.5)$$

Where t_1 and t_2 were the measurement timepoints (days), Q_{Perf} the perfusion rate (vvd), c_{in} the AOI concentration in the media (g L^{-1} or mmol L^{-1}), c_{out} the AOI concentration in the harvest averaged between the two timepoints (g L^{-1} or mmol L^{-1}), c_{t1} and c_{t2} the measured analyte concentrations at the respective timepoint (g L^{-1} or mmol L^{-1}), Q_{Feed} the pyruvate feed rate ($\text{L RV}^{-1} \text{ day}^{-1}$), c_{Feed} the pyruvate feed concentration (g L^{-1}) and X the averaged VCV between the two timepoints (%).

3 Results and Discussion

3.1 Raman model calibration and spike validation

Raman model calibration for lactate, glucose, pyruvate, and ammonium by harvest-library spiking [34] led to RMSE and RMSECV values below 0.15 g L^{-1} (lactate, glucose and pyruvate) and below 0.5 mmol L^{-1} for ammonium predictions (Table A.5). A spike validation was subsequently performed to assess the accuracy and robustness of the models during a steady-state perfusion process by adding defined amounts of the corresponding component as a bolus to the bioreactor and evaluate the impact on the prediction models (Table A.6). An immediate sharp increase of the prediction signal for the spiked component to the expected concentration is a strong indication for direct measurements based on spectral peaks, being required for robust prediction models. On the other hand, an immediate sharp prediction increase by

adding a different component than the model was calibrated for is indicative of insufficient peak decoupling and does not qualify for model robustness. A slow change of the prediction signal when spiking other components can come from a metabolic perturbation resulting in increased or decreased consumption rates of the predicted component. As long as the changes can be confirmed by reference analytics, the model can be considered accurate and robust.

The glucose model immediately responded to the glucose bolus addition and correctly predicted the concentration confirmed by reference analytics (Figure A.12A). Slight glucose prediction increases were monitored upon addition of lactate, pyruvate and the larger ammonium spike of 2 mmol L⁻¹. As increases were not immediate and could be confirmed by reference analytics, this can be explained by impacted cellular metabolic activity changing glucose levels upon addition of lactate, pyruvate or ammonium. Overall, the glucose predictions aligned well with reference data points that were taken prior and after the spike additions and the model can be considered robust and accurate with a RMSEP of 0.15 g L⁻¹. Similar independence of models to different spiked compounds and high accuracy could be demonstrated for lactate (Figure A.12B) and pyruvate (Figure A.12D) with RMSEP of 0.11 g L⁻¹ and 0.08 g L⁻¹ respectively. The ammonium model on the other hand did not react to ammonium spikes of 0.5 mmol L⁻¹ and 2 mmol L⁻¹ (Figure A.12C). Ammonium predictions were constantly around 2 – 3 mmol L⁻¹ and slight changes were observed for sodium-chloride, lactate and pyruvate addition. These results are in sharp contrast to reported cases about apparently good ammonium models for fed-batch cultivations [39–41] or perfusion runs [42]. A possible explanation for the unsuccessful ammonium prediction model might be that reported ammonium models rely on correlations of ammonium with other process components rather than being based on ammonium specific Raman bands. In such a case the model would fail during spike validation. In fact, this is congruent with earlier reports where no ammonium corresponding peaks were detected when spiking ammonium into water, suggesting that direct ammonium Raman models might not be possible at process relevant concentrations [43, 44]. Whereas RMSEP below 0.15 g L⁻¹ based on spike validation data confirmed low RMSE and RMSECV of Raman models for lactate, glucose and pyruvate, a significantly higher RMSEP (from RMSECV of 0.49 mmol L⁻¹ to RMSEP of 1.32 mmol L⁻¹) was computed for ammonium (Table A.5). RMSE, RMSECV and RMSEP were plotted versus the number of latent variables used for the models and is provided in the Supporting Information section (Figure A.18). Although only one Raman model is required for feedback control, proper decoupling of other compounds such as glucose and pyruvate by harvest library spiking is of

crucial importance to obtain independent and accurate Raman prediction models [34]. Furthermore, spike validation is required to distinguish models purely relying on correlation to other process compounds from models based on compound specific Raman bands rendering them suitable for real-time monitoring and feedback control.

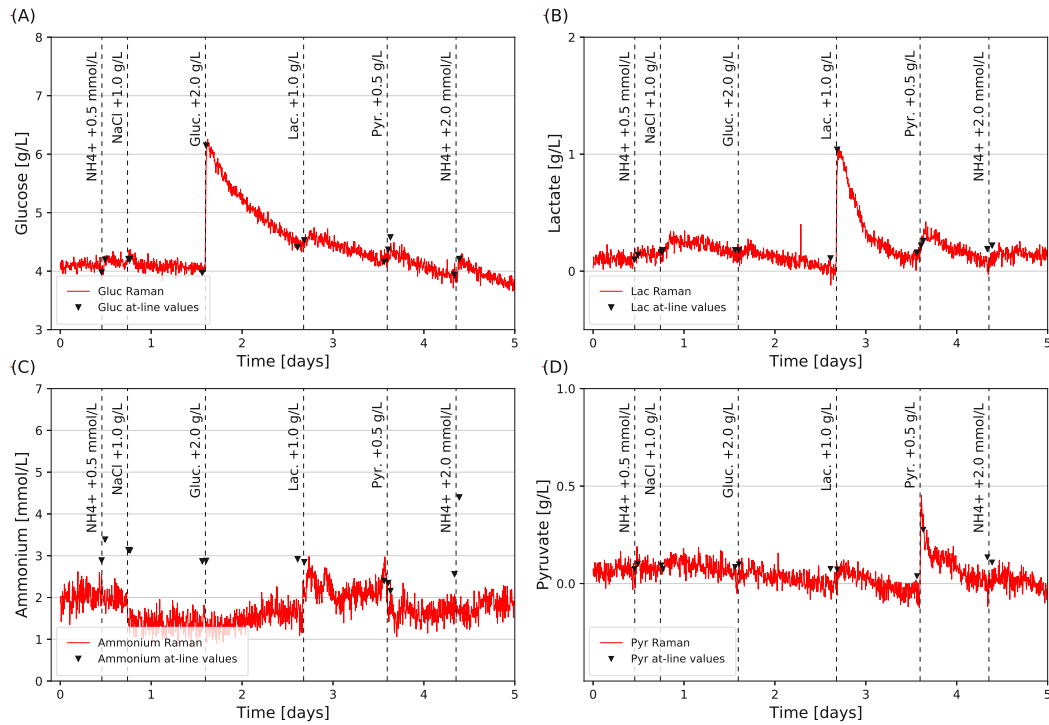


Figure A.12: Spike validation of Raman models during steady-state perfusion. Glucose model (A), lactate model (B), ammonium model (C) and pyruvate model (D) were evaluated by addition of spiked compounds (Table A.6). Vertical dashed lines represent the time of the respective spike addition.

3.2 Steady-state perfusion cell culture stabilization by Raman controlled pyruvate feeding

Aiming to stabilize a perfusion process by minimizing ammonium production through Raman-controlled pyruvate feeding, it seemed most practical to adopt a Raman ammonium model that would maintain ammonium levels at a predefined setpoint. However, spike validation revealed that real-time ammonium monitoring to control pyruvate feed addition upon ammonium increase was not possible due to poor model performance. The next strategy would be to feed pyruvate and feed to a defined target value. As pyruvate is quickly converted to lactate by the cells (Figure A.12B), pyruvate concentration within the culture tends to be very low and complicates a

feedback control (Figure A.14D). Lactate on the other hand, assuming it is only produced by the culture when enough pyruvate is present to supply the TCA cycle, represents the ideal metabolite to realize a feedback control loop ensuring TCA saturation by pyruvate addition (Figure A.13A). Feeding pyruvate on demand by Raman feedback control such that the lactate concentration was kept stable at a defined setpoint to ensure sufficient pyruvate availability for the TCA cycle was therefore evaluated with the intention to reduce anaplerotic reactions such as amino acid catabolism with the byproduct ammonium (Figure A.13B). Stabilized cellular metabolism and reduced ammonium production in turn could subsequently mitigate product quality drifts.

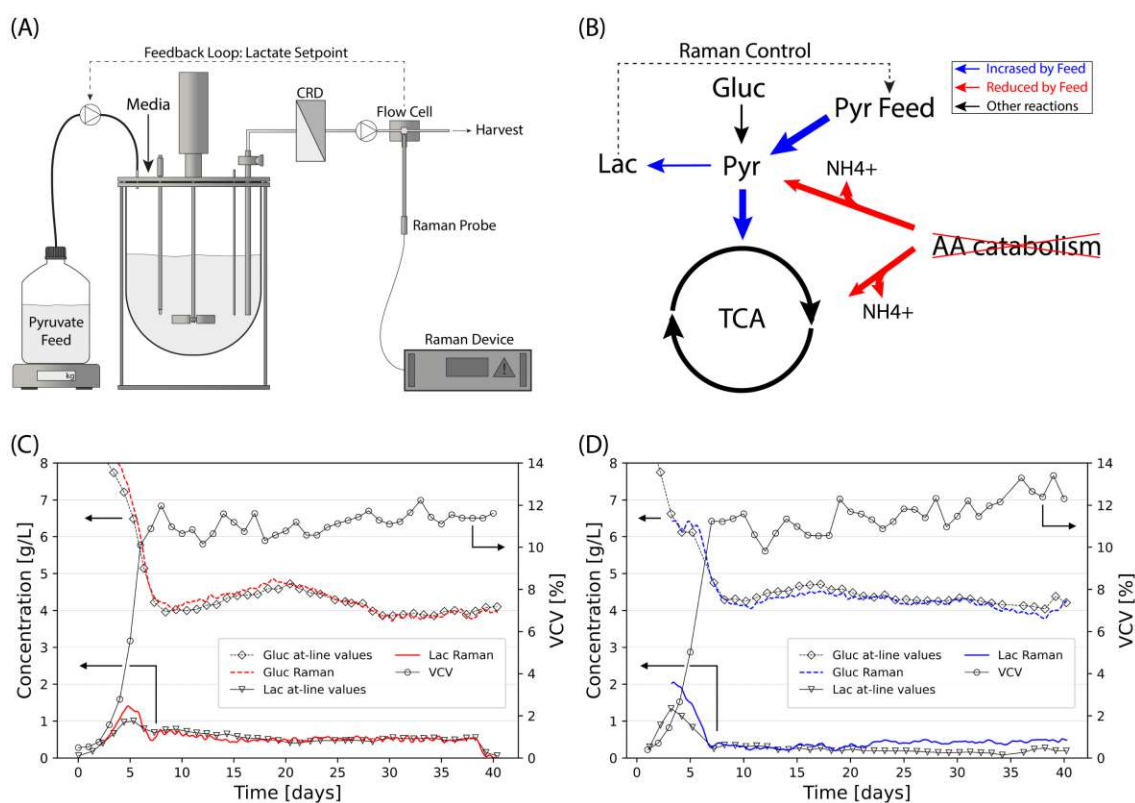


Figure A.13: Raman controlled feeding strategy. Schematic setup of perfusion bioreactor with Raman flow cell after cell retention device (CRD) in harvest stream predicting lactate concentration and controlling pyruvate feed addition (A). Simplified metabolic scheme of feeding strategy (B). Real-time Raman predictions and corresponding at-line reference measurements for a perfusion run with 0.7 g L⁻¹ lactate setpoint (C) and a perfusion run with a lower lactate setpoint of 0.3 g L⁻¹ (D).

Lactate setpoints for Raman controlled pyruvate feeding were set to 0.7 g L⁻¹ and 0.3 g L⁻¹. The setpoint of 0.7 g L⁻¹ was defined based on the initial lactate peak concentration of approximately 1.4 g L⁻¹ for the standard perfusion processes without pyruvate feed addition (Figure A.14C). By controlling at 0.7 g L⁻¹ lactate,

corresponding to half of the initial peak concentration, a clear effect on ammonium product was expected without impacting culture viability. A second lower lactate setpoint was defined to assess whether varying lactate concentrations could be used to fine-tune product quality, or if product quality is independent of the lactate concentration as long as it is not fully depleted corresponding to a saturated TCA cycle by pyruvate. This second setpoint with 0.3 g L^{-1} was a low concentration but still sufficiently high to be accurately quantified by the lactate Raman prediction model with a RMSEP of 0.11 g L^{-1} .

Real-time Raman predictions for the 0.7 g L^{-1} lactate setpoint run (Figure A.13C) and for the 0.3 g L^{-1} lactate setpoint run (Figure A.13D) are well aligned with reference analytics during the steady-state operation. Slight deviations occurred during the initial growth phase, where the lactate models predicted slightly higher than the reference values. Glucose models predicted well during steady-state operation and the initial growth phase, potentially as the glucose concentration is manyfold higher than the lactate concentration. Pyruvate predictions are not shown as the pyruvate concentration remained below 0.2 g L^{-1} for all perfusion runs (Figure A.14D). The slight deviation of the lactate predictions early in the process can be explained as the Raman calibration set consisted solely of samples during the steady-state operation, not including matrix changes of the initial growth phase. If models are required to correctly predict during steady-state operation as well as during the first days of the culture, additional early process samples could be included into the data set. This is however of no concern in this study as the models were designed to accurately predict during the steady-state operation and predictions during the initial growth phase are not required for any feedback control.

Standard perfusion culture runs without pyruvate feed (Ctr. 1 – 3) achieved stable operation within 6 days after inoculation and remained at high culture viability above 87% throughout the entire run time of 40 days or longer (Figure A.14A). After an initial lactate peak, the lactate concentration dropped below the detection limit of the at-line analyzer of 0.1 g L^{-1} for the remaining process time (Figure A.14C). Similarly, pyruvate concentration was depleted throughout the entire run time (Figure A.14D). Ammonium started to accumulate once the initial lactate peak was fully consumed and reached its maximum of $6 - 7 \text{ mmol L}^{-1}$ around process day 20. Subsequently, ammonium concentrations decreased slowly back to the starting concentration of $2 - 3 \text{ mmol L}^{-1}$ on day 6. Glucose levels, after the initial decrease during the growth phase, slightly increased from below 4 g L^{-1} to almost 5 g L^{-1} until day 20, followed by a decreasing trend towards the end of the process (Figure A.14H). pH was maintained stable within the defined dead band (Figure A.14G)

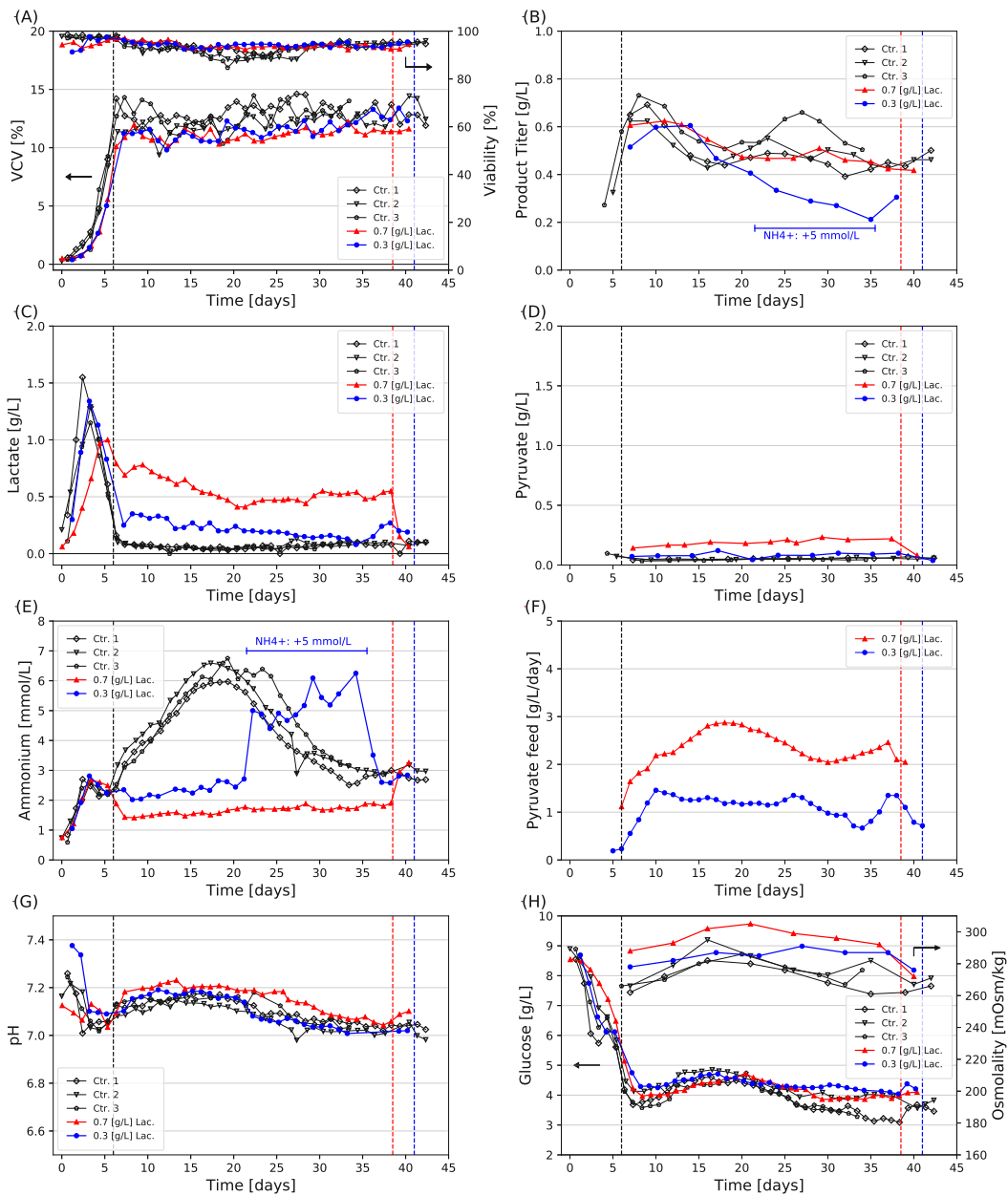


Figure A.14: Cell culture parameter, nutrient and metabolite trends for steady-state perfusion cultivations. VCV and viability (A), product titer (B), lactate (C), pyruvate (D), ammonium (E), pyruvate feed rate (F), culture pH (G), glucose and osmolality (H). The vertical black lines represent the start of Raman controlled pyruvate feeding and the blue and red vertical line represent the end of pyruvate feeding of the respective runs. Blue horizontal lines represent a phase of ammonium addition of 5 mmol L⁻¹ to the perfusion media in the perfusion run with 0.3 g L⁻¹ lactate setpoint.

and osmolality remained relatively stable as well (Figure A.14H).

Fluctuating nutrient and metabolite levels as observed for ammonium clearly indicated that no metabolic steady-state was achieved despite stable perfusion operation. As a consequence, product quality attributes were impacted and drifted accordingly during the perfusion operation (Figure A.15). High mannose correlated with the increase in ammonium and reached its peak of up to 4% around day 20 (Figure A.15A). This is in agreement with the literature reporting increased high mannose levels at elevated ammonia concentrations [25–27]. Fucosylation showed its lowest concentration of below 94% on day 20 – 25, before rising back to almost 98% (Figure A.15B). A lower degree of fucosylation and a simultaneous increase in high mannose can be explained by a general decrease in the progression of the glycosylation pathways. A-galactosylation with G0 (Figure A.15C), and galactosylation with G1 (Figure A.15D) and G2 (Figure A.15E) showed furthermore fluctuation with G0 being at its highest around day 20 – 25, whereas G1 and G2 were at their lowest around day 20 – 25. A-sialylation (Figure A.15F), mono-sialylation (Figure A.15G) and di-sialylation (Figure A.15H) were drifting towards the end of the run but to a much lower extent below 1% compared to other glycoforms.

Raman controlled pyruvate feeding at 0.7 g L^{-1} and 0.3 g L^{-1} lactate concentration setpoints was started on day 6 when stable operation as achieved and did not impact culture viability (Figure A.14A). Lactate levels could be stabilized between $0.5 - 0.8 \text{ g L}^{-1}$ for the 0.7 g L^{-1} setpoint and between $0.1 - 0.4 \text{ g L}^{-1}$ for the 0.3 g L^{-1} setpoint (Figure A.14C), representing a significantly tighter control compared to previously published lactate levels when applying a constant pyruvate feed of $2 \text{ g L}^{-1} \text{ day}^{-1}$ [17]. Pyruvate was only slightly elevated up to 0.2 g L^{-1} for the 0.7 g L^{-1} lactate setpoint run, whereas it remained depleted for the 0.3 g L^{-1} lactate setpoint (Figure A.14D). This underlines that even though accurate Raman prediction models were achieved, controlling based on pyruvate concentration is difficult due to very low pyruvate concentrations in the bioreactor. Ammonium accumulation was successfully prevented and stayed below 2 mmol L^{-1} for the higher lactate setpoint of 0.7 g L^{-1} until feed stopping on day 38 and slightly above 2 mmol L^{-1} for the 0.3 g L^{-1} lactate setpoint until day 20 (Figure A.14E). On day 21 – 35, ammonium was added to the fresh media in the 0.3 g L^{-1} lactate setpoint run to assess the impact of ammonium to modulate product quality. Ammonium levels increased rapidly to $5 - 6 \text{ mmol L}^{-1}$. The higher lactate setpoint of 0.7 g L^{-1} indeed led to a further reduction of ammonium by almost 1 mmol L^{-1} , demonstrating that elevating lactate concentration by pyruvate feeding comprises a tool to adjust ammonium concentrations. Higher lactate setpoints in turn require larger pyruvate feed rates which were

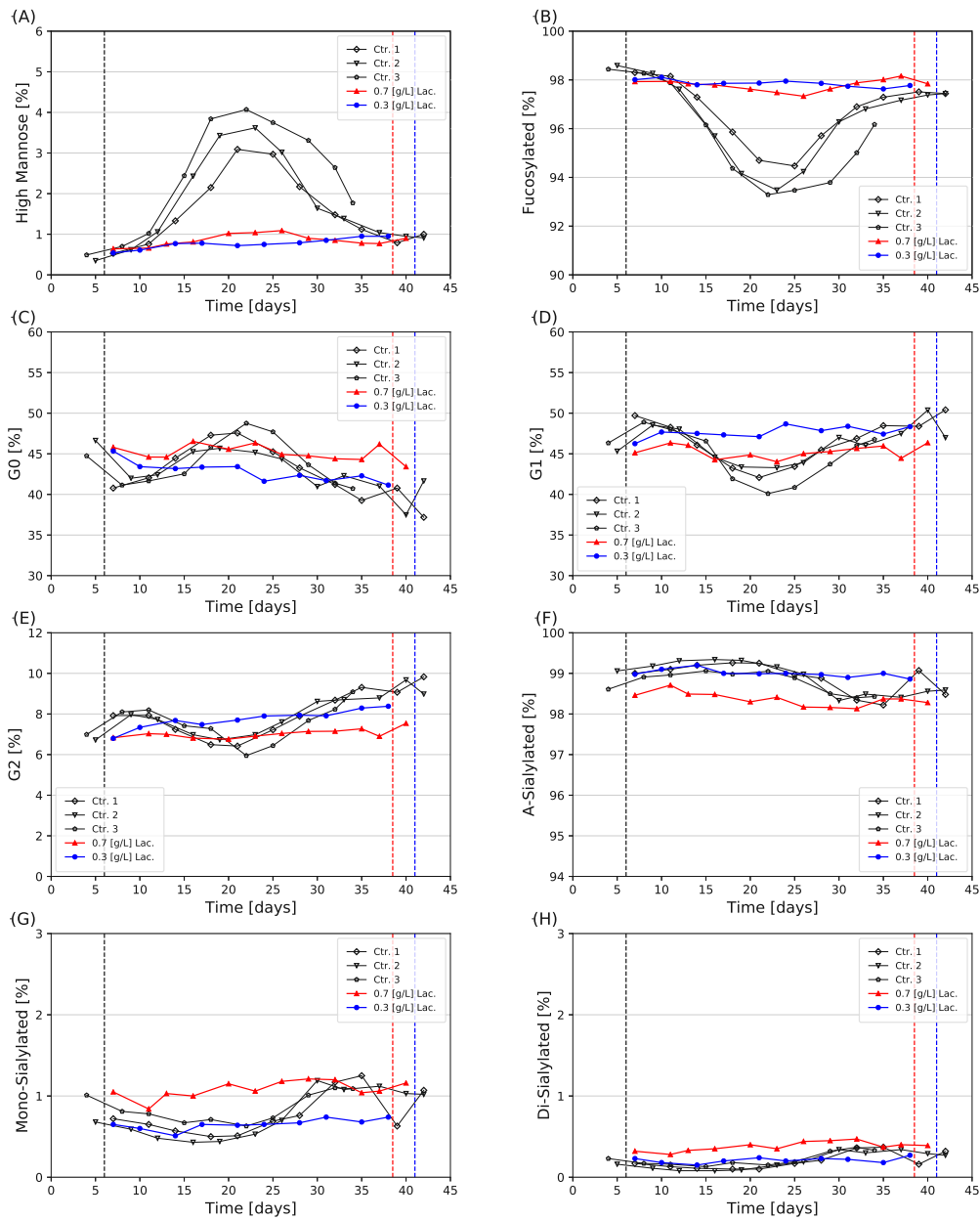


Figure A.15: Product glycosylation profiles for steady-state perfusion cultivations. High mannose (A), fucosylation (B), G0 (C), G1 (D), G2 (E), a-sialylation (F), mono-sialylation (G) and di-sialylation (H). The vertical black lines represent the start of Raman controlled pyruvate feeding and the blue and red vertical line represent the end of pyruvate feeding of the respective runs. Blue horizontal lines represent a phase of ammonium addition of 5 mmol L^{-1} to the perfusion media in the perfusion run with 0.3 g L^{-1} lactate setpoint.

in this study 2 – 3 times larger for the 0.7 g L^{-1} setpoint compared to the 0.3 g L^{-1} setpoint (Figure A.14F). Fluctuations in the pyruvate feed rate especially for the higher lactate setpoint demonstrate the benefits of Raman controlled feeding rather than constant feeding at a predefined feeding rate to attain stable metabolite profiles. The pH remained within the dead band despite pyruvate feeding and no base nor CO_2 additions were required. Glucose concentrations were stabilized compared to the control run and remained closer to the 4 g L^{-1} mark throughout the entire run when pyruvate was fed. Possible explanations might be that cellular metabolism got reduced at peak ammonium concentrations or that glucose consumption got reduced by switching to more active amino acid catabolism during standard perfusion runs. Osmolality was slightly increased for the perfusion runs with pyruvate feed, remained however around or below 300 mOsm kg^{-1} . Product titer remained unchanged independently of the pyruvate feeding. Only when ammonium was fed during day 21 – 35 in the 0.3 g L^{-1} lactate run, the titer dropped. In contrast to other studies feeding TCA cycle intermediates, no beneficial effect on product titer was observed [32, 33].

Raman controlled pyruvate feeding significantly stabilized product quality resulting in flat glycosylation profiles (Figure A.15). Whereas high mannose started at 0.5% and increased up to 4.1% during the standard perfusion runs, resulting in a delta change of up to 3.6%, maximal delta changes of 0.5% were achieved for perfusion cultures with pyruvate feeding (Figure A.15A). Accordingly, proper lactate control by pyruvate feeding addresses the need to expand the scarce toolbox of high mannose reducing approaches in cell culture [45]. This might become especially useful when increased high mannose concentrations arise upon perfusion process intensification by pushing cell densities to the limits or optimizing cell specific perfusion rates [11]. Similarly, delta changes of up to 5.1% for standard perfusion runs were reduced to delta changes of maximally 0.8% for fucosylated species (Figure A.15B). No difference on high mannose and fucosylation levels were observed for 0.3 g L^{-1} or 0.7 g L^{-1} lactate setpoints. All other glycoforms showed a similar trend with significantly stabilized concentration levels throughout the entire run time, however different lactate concentration setpoints resulted in different absolute glycoform concentration levels. As such, the higher lactate setpoint of 0.7 g L^{-1} resulted in an increase of G0 (Figure A.15C), mono-sialylated (Figure A.15G) and di-sialylated species (Figure A.15H), whereas G1 (Figure A.15D), G2 (Figure A.15E) and a-sialylated species (Figure A.15F) were slightly lower than for the 0.3 g L^{-1} lactate setpoint. Standard deviations (SD) of all glycoforms were significantly reduced by Raman controlled pyruvate feeding down to 0.1% as in the case of high

mannose.

A similarly stable recombinant antibody quality profile during a 30-day perfusion process was reported in a study with a human hybrid cell line F2N78 without additional pyruvate feed [46]. Interestingly, lactate concentration was constant at around 2 g L^{-1} and ammonium remained below 2 mmol L^{-1} for the entire 30 days. Whereas Raman controlled pyruvate feeding was not required in the reported study due to sufficiently high lactate levels, the CHO-K1 cell line used in this study required additional pyruvate supplementation to reach the same stabilizing effect. Raman controlled pyruvate feeding represents therefore a valuable tool to stabilize perfusion cell culture runs for cell lines otherwise consuming the entire lactate and switching to amino acids catabolism. The achieved product quality trends for the previously unstable perfusion process can therefore be considered as time-independent, enabling splitting the perfusion batch into multiple DS batches without the need to generate stable process intermediates. Additionally, accurate lactate control further enables product quality fine-tuning by varying the lactate setpoint for a multitude of glycosylation attributes. Stabilization metrics are summarized in a numerical form in Table A.7 for the three most stabilized glycoforms, metrics for remaining glycoforms can be found in the Supporting Information section (Table A.8).

Interestingly, the ammonium addition into the fresh medium during day 21 – 35 of the 0.3 g L^{-1} lactate setpoint run did not impact product quality. This result was not expected considering diverse studies demonstrating that elevated ammonium concentrations and spikes of ammonium can impact product quality in fed-batch cultures [25–27]. The external ammonium addition with a concentration of $4.5 - 6.5 \text{ mmol L}^{-1}$ reached the same region as during the peak of the standard perfusion runs showing clear impact on product quality, however not on product titer. By externally adding ammonium the opposite trend was observed with no impact on product quality but on product titer. The correlation between increased ammonium and reduced titer has also been observed in fed-batch processes and was explained by reduced cellular activity at elevated ammonia levels [32]. One possible explanation for unchanged product quality upon ammonia feeding might be that the impact of ammonium on product quality was somehow mitigated due to the continuing lactate control by pyruvate feeding. However, further research to understand this observation would be necessary and goes beyond the scope of this study.

Table A.7: Process stabilization metrics for control runs and Raman controlled perfusion runs. Minimal and maximal fraction of glycoforms (Min, Max), the difference of lowest and highest measured fraction of glycoforms during the same perfusion run (Delta), Mean and standard deviation (SD) are provided for the respective glycoforms.

Run	Min [%]	Max [%]	Delta [%]	Mean [%]	SD [%]
High mannose					
Control 1	0.5	3.1	2.6	1.6	0.8
Control 2	0.4	3.6	3.3	1.7	1.1
Control 3	0.5	4.1	3.6	2.4	1.3
0.3 g L ⁻¹ Lac	0.5	1.0	0.4	0.8	0.1
0.7 g L ⁻¹ Lac	0.6	1.1	0.5	0.9	0.1
Fucosylation					
Control 1	94.5	98.3	3.8	96.7	1.3
Control 2	93.5	98.6	5.1	96.4	1.6
Control 3	93.3	98.4	5.1	95.7	1.9
0.3 g L ⁻¹ Lac	97.6	98.1	0.5	97.9	0.1
0.7 g L ⁻¹ Lac	97.3	98.2	0.8	97.8	0.2
G0					
Control 1	37.2	47.6	10.4	42.6	3.1
Control 2	37.5	46.6	9.2	42.9	2.5
Control 3	40.7	48.8	8.0	43.8	2.7
0.3 g L ⁻¹ Lac	41.2	45.3	4.2	42.8	1.2
0.7 g L ⁻¹ Lac	43.4	46.5	3.1	45.1	0.9

3.3 Understanding the impact of pyruvate feeding on cellular metabolism

Amino acid concentrations were analysed for all perfusion cultures to gain deeper insight into the metabolic activity of the cell culture. Alanine concentrations were about 2 mmol L⁻¹ higher for the perfusion runs with pyruvate feed addition (Figure A.16A). Glycine concentrations showed a rise from initially 1 mmol L⁻¹ to 3 mmol L⁻¹ on day 20, after which they returned to the initial concentration of 1 mmol L⁻¹ towards the end of the process (Figure A.16B). Glutamine showed no significant differences between the control run and the 0.3 g L⁻¹ lactate setpoint run, yet increased up to 3 mmol L⁻¹ for the 0.7 g L⁻¹ lactate setpoint (Figure A.16C). Glutamate levels remained low throughout the entire process time and were slightly lower when pyruvate feeding was present (Figure A.16D). Asparagine did not show differences when pyruvate feeding was present (Figure A.16E), but lower aspartate levels were observed with pyruvate feeding (Figure A.16F). Remaining amino acid

concentrations were comparable between standard perfusion runs and perfusion runs with Raman controlled pyruvate feeding (Figure A.19).

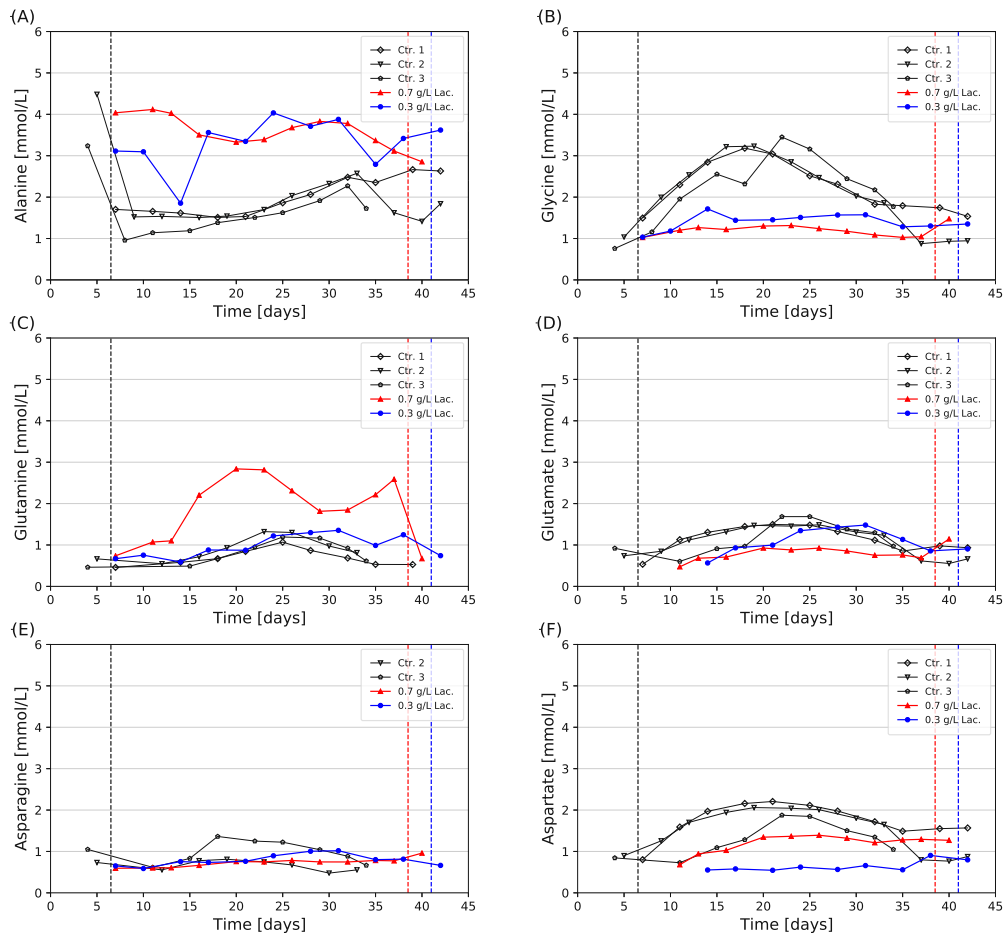


Figure A.16: Amino acid profiles during steady-state perfusion cultivation. Alanine (A), glycine (B), glutamine (C), glutamate (D), asparagine (E) and aspartate (F). The vertical black lines represent the start of Raman controlled pyruvate feeding and the blue and red vertical line represent the end of pyruvate feeding of the respective runs.

Calculation of consumption rates for these amino acids revealed that asparagine was by far the most consumed amino acid (Figure A.17A), corresponding with observations by others [21, 47] and consumption rates even slightly increased with pyruvate feed addition. Alanine consumption rates however changed drastically upon pyruvate feed addition (Figure A.17C). Whilst alanine was catabolised from the medium without pyruvate feed, alanine was produced with rates of around $0.2 \text{ mmol } \%^{-1} \text{ day}^{-1}$. As alanine is generated from pyruvate and ammonium by alanine aminotransferase, supplying sufficient pyruvate as precursor to capture ammonium can be one of the major explanations for the significantly reduced ammonium levels

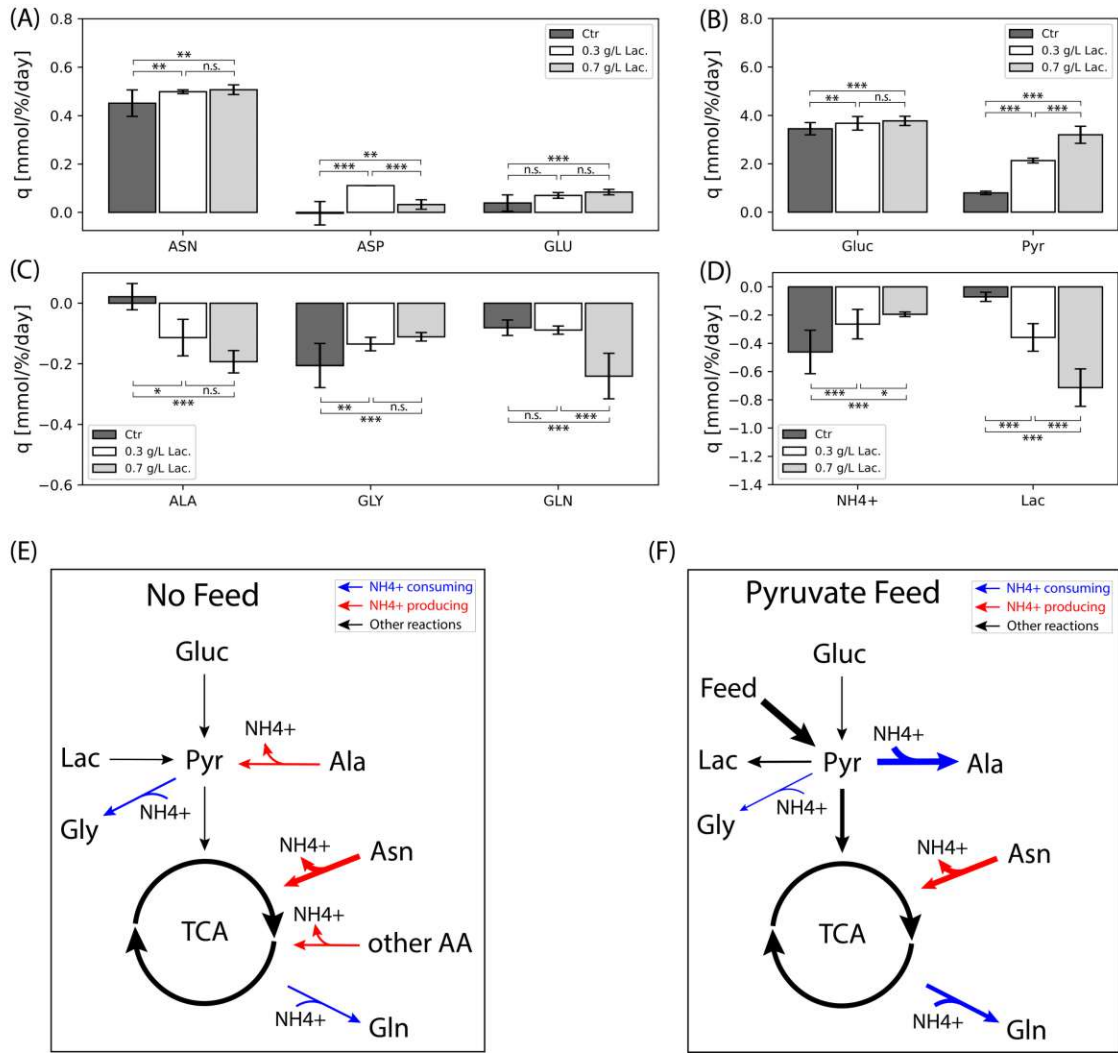


Figure A.17: Consumption rate of nutrients, metabolites and amino acids during steady-state perfusion cell culture. Steady-state data was used to calculate consumption rates, three control runs were combined for the calculation of control data. Consumption rates of net consumed amino acids (A) and nutrients (B), consumption rates of net produced amino acids (C) and nutrients and metabolites (D). The Welch's test was applied to determine statistical significance (* $P < 0.05$, ** $P < 0.01$, *** $P < 0.001$, n.s. not significant). Simplified schematic representation of cellular metabolism without pyruvate feed (E) and with Raman controlled pyruvate feeding (F).

during pyruvate feeding in perfusion cultures [17]. Increased glutamine production was also observed at high pyruvate feeding with the 0.7 g L^{-1} lactate setpoint (Figure A.17C), which might explain the even lower ammonium levels at 0.7 g L^{-1} lactate setpoint compared to 0.3 g L^{-1} lactate setpoint (Figure A.14E). The peak in glycine production for standard perfusion runs could potentially be explained by increased threonine catabolism, producing the TCA cycle precursor acetyl-CoA and glycine as a byproduct. Moreover, an increased conversion from serine to glycine by the enzyme serine hydroxymethyltransferase initiated by enhanced serin biosynthe-

sis activity due to elevated ammonium levels could be an explanation. As threonine and serine concentration levels did not significantly vary between pyruvate feeding and standard perfusion runs (Figure A.19), no final explanation for the glycine stabilization by pyruvate feeding could be drawn in this study. Aspartate and glutamate remained at rather low consumption rates below $0.1 \text{ mmol \%}^{-1} \text{ day}^{-1}$ for all tested conditions (Figure A.17A).

Pyruvate consumption rates increased the more pyruvate was fed and were almost 4-fold larger for the 0.7 g L^{-1} lactate setpoint run compared to the standard perfusion runs (Figure A.17B). Albeit pyruvate is partially converted to lactate (Figure A.17C) and was washed out of the perfusion culture, significantly more pyruvate is available to enter the TCA cycle or serve as precursor for amino acid anabolism such as alanine. Glucose consumption rates remained rather constant for all conditions and revealed that glucose was still the major energy source for the cells (Figure A.17B). Nevertheless, the increase in pyruvate addition to the culture achieved a 3-fold reduction of the ammonium production from up to $0.6 \text{ mmol \%}^{-1} \text{ day}^{-1}$ down to as little as $0.2 \text{ mmol \%}^{-1} \text{ day}^{-1}$. Whereas asparagine, alanine and many other amino acids were catabolized without additional pyruvate feeding (Figure A.17E), alanine and glutamine synthesis acted as major ammonium sinks when sufficient pyruvate was fed into the TCA cycle (Figure A.17F). Combined with an overall decreased amino acid catabolism, ammonium production was minimized and stabilized throughout the entire perfusion culture.

4 Conclusion and Outlook

This study aimed to stabilize a steady-state perfusion process producing a bispecific antibody, which was experiencing drifting product quality attributes despite stable operation. A shifting metabolic activity was identified as the cause of the variability, and a stabilization strategy was implemented to improve the consistency of the product quality.

Pyruvate as a potential glycosylation modulating lever by reducing amino acid catabolism and saturating the TCA cycle has been leveraged to develop a novel on-demand feeding strategy. Lactate, exclusively produced from pyruvate when sufficient TCA cycle precursors are present in the cell culture, served as ideal indicator for TCA cycle saturation which was monitored in real-time by Raman spectroscopy. Inserting the Raman probe into the cell free harvest stream of the perfusion process enabled fast and robust prediction model generation and allowed for accurate lactate level monitoring. In contrast to lactate depletion after an initial peak during the

growth phase of the standard perfusion process and thereby indicating insufficient TCA cycle precursors, Raman controlled pyruvate feeding enabled to control the lactate concentration at a desired setpoint concentration. Concomitantly, the TCA cycle got optimally saturated with the precursor pyruvate thereby minimizing amino acid catabolism, resulting in a 3-fold reduction of ammonium accumulation. Stabilized metabolic activity of the cell culture ultimately stabilized the product quality profiles. High mannose and fucosylation showed stable concentration levels with a standard deviation of less than 0.2% and were independent of the lactate setpoint. Other glycosylation species such as galactosylation or sialylation were stabilized in an analogous way and could additionally be fine-tuned by varying lactate setpoint levels.

The presented feedback control strategy represents a valuable tool for continuous manufacturing to stabilize metabolic activity of cells throughout the entire perfusion culture which would otherwise result in product quality drifting. Hence, the novel Raman-controlled pyruvate feeding strategy comprises one of the scarce approaches to effectively reduce high mannose which might increase with proceeding culture duration or process intensification activities.

Acknowledgements

The authors would like to thank Philip Giller (FHNW) for supporting experimental work on perfusion processes and Pavel Dagorov, Georg Hasler and Theo Walser (FHWN) for building the Raman flow cell. Moreover, the authors would like to acknowledge specifically the Global Drug Substance Development (GDSD) team of Merck Serono SA (an affiliate of Merck KGaA, Darmstadt, Germany) for material and analytical support and for valuable discussions and support throughout the project, especially Loïc Chappuis, Alexandre Châtelin and the analytical team.

Conflict of interest

The authors declare that they have no known competing financial interests or personal relationships that could have appeared to influence the work reported in this paper.

Data availability statement

The data that support the findings of this study are available from the corresponding author upon reasonable request.

Supporting Information

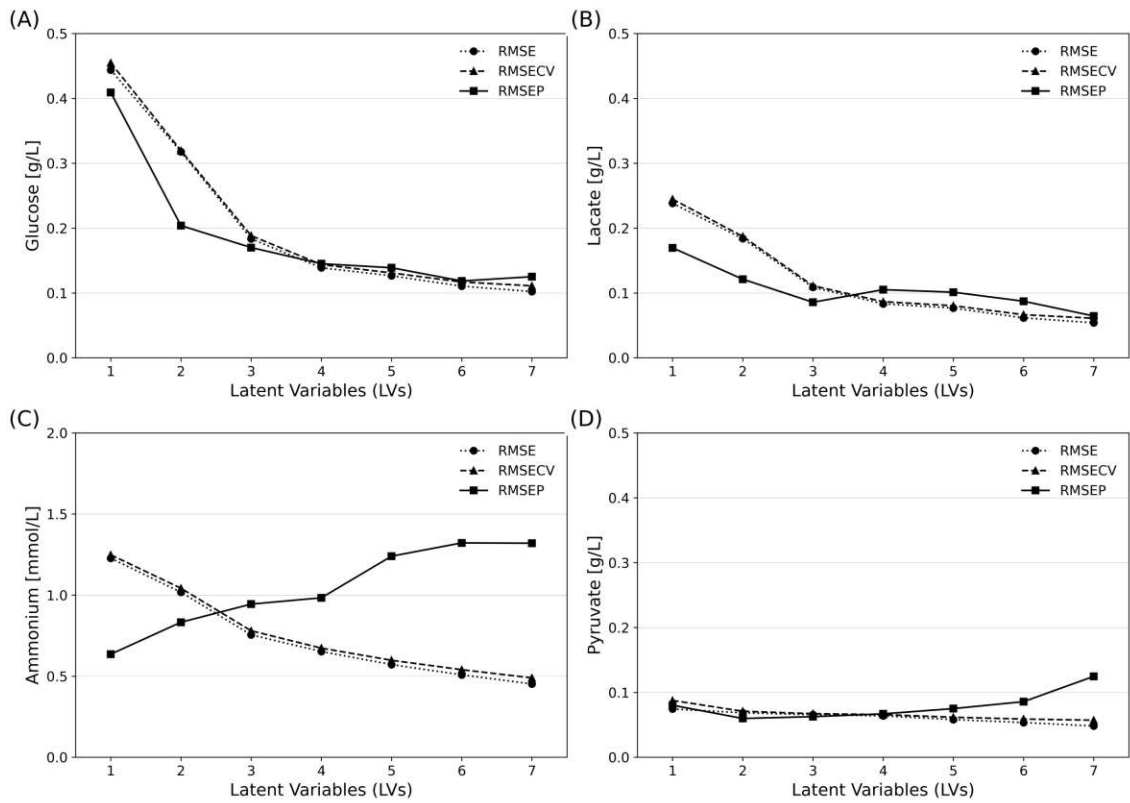


Figure A.18: RMSE, RMSECV and RMSEP versus the amount of latent variables. Glucose prediction model (A), lactate (B), ammonium (C) and pyruvate (D).

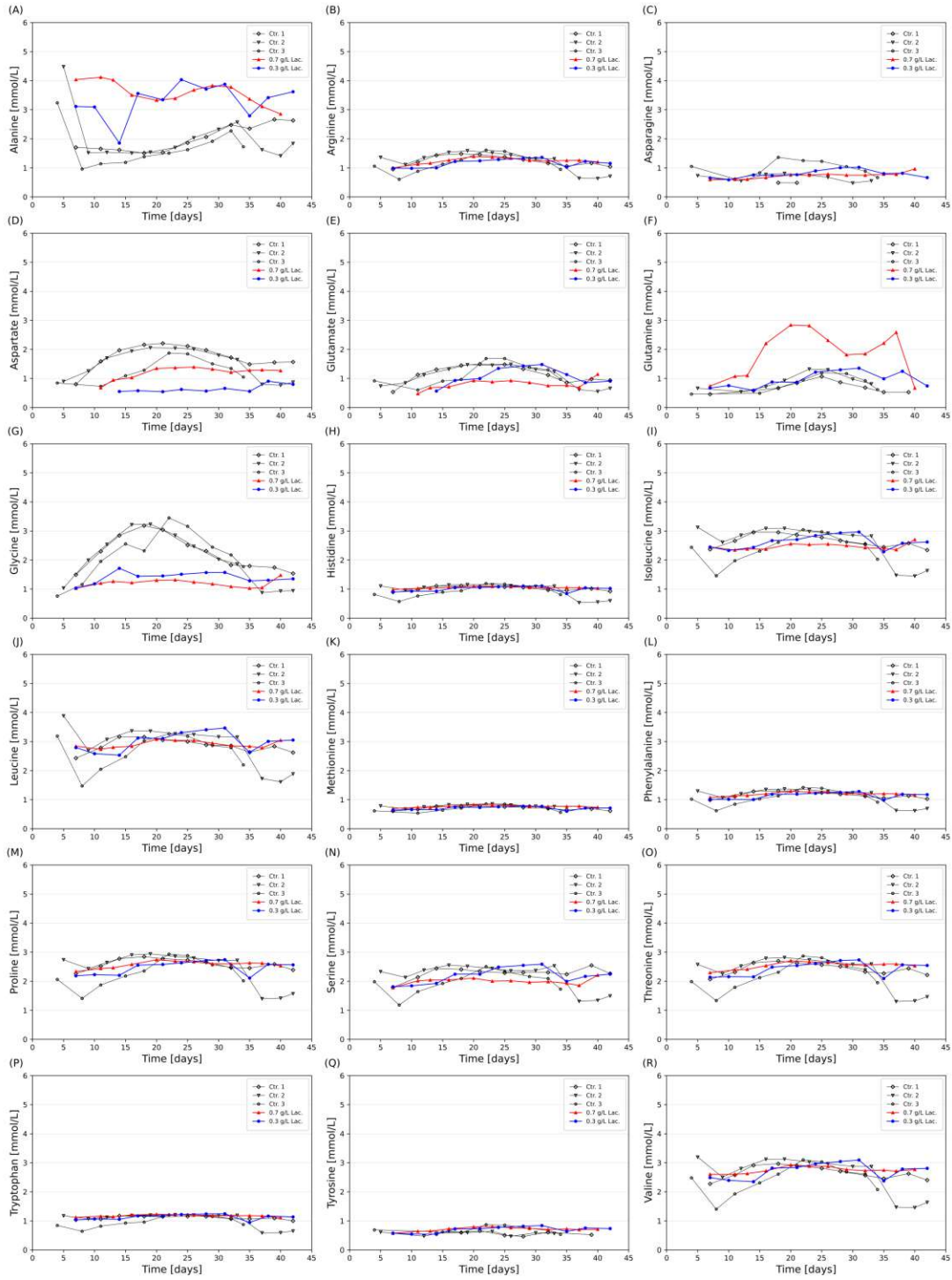


Figure A.19: Amino acid profiles during steady-state perfusion cultivation for all measured amino acids.

Table A.8: Process stabilization metrics for control runs and Raman controlled perfusion runs. Minimal and maximal fraction of glycoforms (min, max), the difference of lowest and highest measured fraction of glycoforms during the same perfusion run (Delta), mean and standard deviation (SD) are provided for the respective glycoforms.

Run	Min [%]	Max [%]	Delta [%]	Mean [%]	SD [%]
High mannose					
Control 1	0.5	3.1	2.6	1.6	0.8
Control 2	0.4	3.6	3.3	1.7	1.1
Control 3	0.5	4.1	3.6	2.4	1.3
0.3 g L ⁻¹ Lac	0.5	1.0	0.4	0.8	0.1
0.7 g L ⁻¹ Lac	0.6	1.1	0.5	0.9	0.1
Fucosylation					
Control 1	94.5	98.3	3.8	96.7	1.3
Control 2	93.5	98.6	5.1	96.4	1.6
Control 3	93.3	98.4	5.1	95.7	1.9
0.3 g L ⁻¹ Lac	97.6	98.1	0.5	97.9	0.1
0.7 g L ⁻¹ Lac	97.3	98.2	0.8	97.8	0.2
G0					
Control 1	37.2	47.6	10.4	42.6	3.1
Control 2	37.5	46.6	9.2	42.9	2.5
Control 3	40.7	48.8	8.0	43.8	2.7
0.3 g L ⁻¹ Lac	41.2	45.3	4.2	42.8	1.2
0.7 g L ⁻¹ Lac	43.4	46.5	3.1	45.1	0.9
G1					
Control 1	42.1	50.4	8.3	46.6	2.6
Control 2	43.3	50.4	7.1	46.2	2.1
Control 3	40.1	48.9	8.8	44.9	2.9
0.3 g L ⁻¹ Lac	46.3	48.7	2.4	47.7	0.7
0.7 g L ⁻¹ Lac	44.0	46.4	2.3	45.3	0.8
G2					
Control 1	6.4	9.8	3.4	8.0	1.1
Control 2	6.7	9.7	3.0	8.0	1.0
Control 3	6.0	9.1	3.1	7.5	0.9

Run	Min [%]	Max [%]	Delta [%]	Mean [%]	SD [%]
0.3 g L ⁻¹ Lac	6.8	8.4	1.6	7.7	0.4
0.7 g L ⁻¹ Lac	6.8	7.5	0.8	7.0	0.2
A-sialylation					
Control 1	98.2	99.3	1.0	98.9	0.4
Control 2	98.3	99.3	1.0	98.9	0.4
Control 3	98.4	99.1	0.7	98.8	0.3
0.3 g L ⁻¹ Lac	98.9	99.2	0.3	99.0	0.1
0.7 g L ⁻¹ Lac	98.1	98.7	0.6	98.4	0.2
Mono-sialylation					
Control 1	0.5	1.3	0.8	0.8	0.3
Control 2	0.4	1.2	0.8	0.8	0.3
Control 3	0.6	1.1	0.5	0.9	0.2
0.3 g L ⁻¹ Lac	0.5	0.7	0.2	0.7	0.1
0.7 g L ⁻¹ Lac	0.8	1.2	0.4	1.1	0.1
Di-sialylation					
Control 1	0.1	0.4	0.3	0.2	0.1
Control 2	0.1	0.3	0.3	0.2	0.1
Control 3	0.1	0.4	0.2	0.2	0.1
0.3 g L ⁻¹ Lac	0.1	0.3	0.2	0.2	0.1
0.7 g L ⁻¹ Lac	0.2	0.5	0.3	0.3	0.1

References

- [1] Clive Badman et al. “Why We Need Continuous Pharmaceutical Manufacturing and How to Make It Happen”. In: *Journal of Pharmaceutical Sciences* 108.11 (2019), pp. 3521–3523. ISSN: 00223549. DOI: 10.1016/j.xphs.2019.07.016.
- [2] Jason Walther et al. “The business impact of an integrated continuous biomanufacturing platform for recombinant protein production”. In: *Journal of Biotechnology* 213 (2015), pp. 3–12. ISSN: 18734863. DOI: 10.1016/j.jbiotec.2015.05.010.
- [3] Jason Walther et al. “Perfusion Cell Culture Decreases Process and Product Heterogeneity in a Head-to-Head Comparison With Fed-Batch”. In: *Biotechnology Journal* 14.2 (2019), pp. 1–10. ISSN: 18607314. DOI: 10.1002/biot.201700733.
- [4] Konstantin B. Konstantinov and Charles L. Cooney. “White Paper on Continuous Bioprocessing May 20–21 2014 Continuous Manufacturing Symposium”. In: *Journal of Pharmaceutical Sciences* 104.3 (2015), pp. 813–820. ISSN: 00223549. DOI: 10.1002/jps.24268.
- [5] James Pollock et al. “Integrated continuous bioprocessing: Economic, operational, and environmental feasibility for clinical and commercial antibody manufacture”. In: *Biotechnology Progress* 33.4 (2017), pp. 854–866. ISSN: 15206033. DOI: 10.1002/btpr.2492.
- [6] Ohnmar Khanal and Abraham M. Lenhoff. “Developments and opportunities in continuous biopharmaceutical manufacturing”. In: *mAbs* 13.1 (2021). ISSN: 19420870. DOI: 10.1080/19420862.2021.1903664.
- [7] Adam C. Fisher et al. “The Current Scientific and Regulatory Landscape in Advancing Integrated Continuous Biopharmaceutical Manufacturing”. In: *Trends in Biotechnology* 37.3 (2019), pp. 253–267. ISSN: 01677799. DOI: 10.1016/j.tibtech.2018.08.008.
- [8] Fabian Steinebach et al. “Design and operation of a continuous integrated monoclonal antibody production process”. In: *Biotechnology Progress* 33.5 (2017), pp. 1303–1313. ISSN: 15206033. DOI: 10.1002/btpr.2522.
- [9] Veena Warikoo et al. “Integrated continuous production of recombinant therapeutic proteins”. In: *Biotechnology and Bioengineering* 109.12 (2012), pp. 3018–3029. ISSN: 00063592. DOI: 10.1002/bit.24584.

- [10] Rahul Godawat et al. “End-to-end integrated fully continuous production of recombinant monoclonal antibodies”. In: *Journal of Biotechnology* 213 (2015), pp. 13–19. ISSN: 01681656. DOI: 10.1016/j.jbiotec.2015.06.393.
- [11] Daniel J. Karst et al. “Process performance and product quality in an integrated continuous antibody production process”. In: *Biotechnology and Bioengineering* 114.2 (2017), pp. 298–307. ISSN: 00063592. DOI: 10.1002/bit.26069.
- [12] Kevin Botelho Ferreira et al. “Transfer of continuous manufacturing process principles for mAb production in a GMP environment: A step in the transition from batch to continuous”. In: *Biotechnology Progress* 38.4 (2022), pp. 1–13. ISSN: 8756-7938. DOI: 10.1002/btpr.3259.
- [13] Michael J. Coolbaugh et al. “Pilot-scale demonstration of an end-to-end integrated and continuous biomanufacturing process”. In: *Biotechnology and Bioengineering* 118.9 (2021), pp. 3287–3301. ISSN: 0006-3592. DOI: 10.1002/bit.27670.
- [14] Jonathan Coffman et al. “A common framework for integrated and continuous biomanufacturing”. In: *Biotechnology and Bioengineering* 118.4 (2021), pp. 1735–1749. ISSN: 0006-3592. DOI: 10.1002/bit.27690.
- [15] Jean-Marc Bielser et al. “Perfusion mammalian cell culture for recombinant protein manufacturing – A critical review”. In: *Biotechnology Advances* 36.4 (2018), pp. 1328–1340. ISSN: 07349750. DOI: 10.1016/j.biotechadv.2018.04.011.
- [16] Vania Bertrand et al. “Transcriptome and proteome analysis of steady-state in a perfusion CHO cell culture process”. In: *Biotechnology and Bioengineering* 116.8 (2019), pp. 1959–1972. ISSN: 0006-3592. DOI: 10.1002/bit.26996.
- [17] Stefania Caso et al. “Effects of pyruvate on primary metabolism and product quality for a high-density perfusion process”. In: *Biotechnology and Bioengineering* 119.4 (2022), pp. 1053–1061. ISSN: 10970290. DOI: 10.1002/bit.28033.
- [18] Camila A. Wilkens, Claudia Altamirano, and Ziomara P. Gerdtzen. “Comparative metabolic analysis of lactate for CHO cells in glucose and galactose”. In: *Biotechnology and Bioprocess Engineering* 16.4 (2011), pp. 714–724. ISSN: 12268372. DOI: 10.1007/s12257-010-0409-0.

- [19] Francesca Zagari et al. “Lactate metabolism shift in CHO cell culture: The role of mitochondrial oxidative activity”. In: *New Biotechnology* 30.2 (2013), pp. 238–245. ISSN: 18716784. DOI: 10.1016/j.nbt.2012.05.021.
- [20] Neil Templeton et al. “Peak antibody production is associated with increased oxidative metabolism in an industrially relevant fed-batch CHO cell culture”. In: *Biotechnology and Bioengineering* 110.7 (2013), pp. 2013–2024. ISSN: 00063592. DOI: 10.1002/bit.24858.
- [21] Mathilde Coulet et al. “Metabolic Profiling of CHO Cells during the Production of Biotherapeutics”. In: *Cells* 11.12 (2022), p. 1929. ISSN: 2073-4409. DOI: 10.3390/cells11121929.
- [22] Zahra Sheikholeslami, Mario Jolicoeur, and Olivier Henry. “Elucidating the effects of postinduction glutamine feeding on the growth and productivity of CHO cells”. In: *Biotechnology Progress* 30.3 (2014), pp. 535–546. ISSN: 87567938. DOI: 10.1002/btpr.1907.
- [23] Markus Schneider, Ian w. Marison, and Urs von Stockar. “The importance of ammonia in mammalian cell culture”. In: *Journal of Biotechnology* 46.3 (1996), pp. 161–185. ISSN: 01681656. DOI: 10.1016/0168-1656(95)00196-4.
- [24] Jong Kwang Hong et al. “Comparative phenotypic analysis of CHO clones and culture media for lactate shift”. In: *Journal of Biotechnology* 283 (2018), pp. 97–104. ISSN: 01681656. DOI: 10.1016/j.jbiotec.2018.07.042.
- [25] Thomas K. Villiger et al. “Controlling the time evolution of mAb N-linked glycosylation, Part I: Microbioreactor experiments”. In: *Biotechnology Progress* 32.5 (2016), pp. 1123–1134. ISSN: 15206033. DOI: 10.1002/btpr.2305.
- [26] Melissa M. St. Amand et al. “Identification of manipulated variables for a glycosylation control strategy”. In: *Biotechnology and Bioengineering* 111.10 (2014), pp. 1957–1970. ISSN: 00063592. DOI: 10.1002/bit.25251.
- [27] Martin Gawlitzek et al. “Ammonium alters N-glycan structures of recombinant TNFR-IgG: Degradative versus biosynthetic mechanisms”. In: *Biotechnology and Bioengineering* 68.6 (2000), pp. 637–646. ISSN: 00063592. DOI: 10.1002/(SICI)1097-0290(20000620)68:6<637::AID-BIT6>3.0.CO;2-C.
- [28] Martin Gawlitzek et al. “Incorporation of ¹⁵N from ammonium into the N-linked oligosaccharides of an immunoadhesin glycoprotein expressed in Chinese hamster ovary cells”. In: *Glycobiology* 9.2 (1999), pp. 125–131. ISSN: 0959-6658. DOI: 10.1093/glycob/9.2.125.

- [29] Aziz Cayli et al. “Cell lines with reduced UDP-N-acetylhexosamine pool in the presence of ammonium”. In: *Biotechnology and Bioengineering* 65.2 (1999), pp. 192–200. ISSN: 0006-3592. DOI: 10.1002/(SICI)1097-0290(19991020)65:2<192::AID-BIT9>3.0.CO;2-9.
- [30] P Chen and S Harcum. “Effects of elevated ammonium on glycosylation gene expression in CHO cells”. In: *Metabolic Engineering* 8.2 (2006), pp. 123–132. ISSN: 10967176. DOI: 10.1016/j.ymben.2005.10.002.
- [31] Antti Rivinoja et al. “Elevated Golgi pH impairs terminal N-glycosylation by inducing mislocalization of Golgi glycosyltransferases”. In: *Journal of Cellular Physiology* 220.1 (2009), pp. 144–154. ISSN: 00219541. DOI: 10.1002/jcp.21744.
- [32] Apolline Helfer et al. “Tuning Metabolic Efficiency for Increased Product Yield in High Titer Fed-Batch CHO Cell Culture”. In: *Biotechnology Progress* (2023). ISSN: 8756-7938. DOI: 10.1002/btpr.3327.
- [33] Xiaolin Zhang et al. “Feeding tricarboxylic acid cycle intermediates improves lactate consumption and antibody production in Chinese hamster ovary cell cultures”. In: *Biotechnology Progress* 36.4 (2020), pp. 1–9. ISSN: 8756-7938. DOI: 10.1002/btpr.2975.
- [34] Patrick Romann et al. “Advancing Raman model calibration for perfusion bioprocesses using spiked harvest libraries”. In: *Biotechnology Journal* 17.11 (2022). ISSN: 1860-6768. DOI: 10.1002/biot.202200184.
- [35] Fabian Feidl et al. “A new flow cell and chemometric protocol for implementing in-line Raman spectroscopy in chromatography”. In: *Biotechnology Progress* 35.5 (2019), pp. 1–10. ISSN: 15206033. DOI: 10.1002/btpr.2847.
- [36] Rafael M. Santos et al. “Monitoring mAb cultivations with in-situ raman spectroscopy: The influence of spectral selectivity on calibration models and industrial use as reliable PAT tool”. In: *Biotechnology Progress* 34.3 (2018), pp. 659–670. ISSN: 87567938. DOI: 10.1002/btpr.2635.
- [37] S. Metze et al. “Monitoring online biomass with a capacitance sensor during scale-up of industrially relevant CHO cell culture fed-batch processes in single-use bioreactors”. In: *Bioprocess and Biosystems Engineering* 43.2 (2020), pp. 193–205. ISSN: 1615-7591. DOI: 10.1007/s00449-019-02216-4.
- [38] Bin Lai et al. “Simultaneous Determination of Sugars, Carboxylates, Alcohols and Aldehydes from Fermentations by High Performance Liquid Chromatography”. In: (2016). DOI: 10.3390/fermentation2010006.

- [39] Thaddaeus A. Webster et al. “Development of generic raman models for a GS-KOTM CHO platform process”. In: *Biotechnology Progress* 34.3 (2018), pp. 730–737. ISSN: 15206033. DOI: 10.1002/btpr.2633.
- [40] Brandon Berry et al. “Cross-scale predictive modeling of CHO cell culture growth and metabolites using Raman spectroscopy and multivariate analysis”. In: *Biotechnology Progress* 31.2 (2015), pp. 566–577. ISSN: 15206033. DOI: 10.1002/btpr.2035.
- [41] Nicholas R. Abu-Absi et al. “Real time monitoring of multiple parameters in mammalian cell culture bioreactors using an in-line Raman spectroscopy probe”. In: *Biotechnology and Bioengineering* 108.5 (2011), pp. 1215–1221. ISSN: 00063592. DOI: 10.1002/bit.23023.
- [42] Hubert Schwarz et al. “Monitoring of amino acids and antibody N-glycosylation in high cell density perfusion culture based on Raman spectroscopy”. In: *Biochemical Engineering Journal* 182 (2022), p. 108426. ISSN: 1369703X. DOI: 10.1016/j.bej.2022.108426.
- [43] Ruth C. Rowland-Jones et al. “Comparison of spectroscopy technologies for improved monitoring of cell culture processes in miniature bioreactors”. In: *Biotechnology Progress* 33.2 (2017), pp. 337–346. ISSN: 15206033. DOI: 10.1002/btpr.2459.
- [44] Ruth C. Rowland-Jones et al. “Spectroscopy integration to miniature bioreactors and large scale production bioreactors—Increasing current capabilities and model transfer”. In: *Biotechnology Progress* 37.1 (2021), pp. 1–14. ISSN: 8756-7938. DOI: 10.1002/btpr.3074.
- [45] Renato Mastrangeli et al. “The Formidable Challenge of Controlling High Mannose-Type N-Glycans in Therapeutic mAbs”. In: *Trends in Biotechnology* 38.10 (2020), pp. 1154–1168. ISSN: 01677799. DOI: 10.1016/j.tibtech.2020.05.009.
- [46] Joon Serk Seo et al. “Characteristics of human cell line, F2N78, for the production of recombinant antibody in fed-batch and perfusion cultures”. In: *Journal of Bioscience and Bioengineering* 121.3 (2016), pp. 317–324. ISSN: 13474421. DOI: 10.1016/j.jbiosc.2015.07.007.
- [47] Nuno Carinhas et al. “Metabolic signatures of GS-CHO cell clones associated with butyrate treatment and culture phase transition”. In: *Biotechnology and Bioengineering* 110.12 (2013), pp. 3244–3257. ISSN: 00063592. DOI: 10.1002/bit.24983.

A.3 Scientific Publication Section III

Maduramycin, a novel glycosylation modulator for mammalian fed-batch and steady-state perfusion processes

Die approbierte gedruckte Originalversion dieser Dissertation ist an der TU Wien Bibliothek verfügbar.
The approved original version of this doctoral thesis is available in print at TU Wien Bibliothek.

This section is based on the following publication: P. Romann, T. Vuillemin, S. Pavone, M. Jordan, A. Perilleux, J. Souquet, J-M. Bielser, C. Herwig, and T. K. Villiger, **Maduramycin, a novel glycosylation modulator for mammalian fed-batch and steady-state perfusion processes**, 2023, Under review in *Journal of Biotechnology*.

Abstract

Controlling high-mannose (HM) content of therapeutic proteins during process intensification, reformulation for subcutaneous delivery, antibody-drug conjugate or biosimilar manufacturing represents an ongoing challenge. Even though a range of glycosylation levers to increase HM content exist, modulators specially increasing M5 glycans are still scarce. Several compounds of the polyether ionophore family were screened for their ability to selectively increase M5 glycans of mAb products and compared to the well-known α -mannosidase I inhibitor kifunensine known to increase mainly M8 – M9 glycans. Maduramycin, amongst other promising polyether ionophores, showed the desired effect on different cell lines. For fed-batch processes, a double bolus addition modulator feed strategy was developed maximizing the effect on glycosylation by minimizing impact on culture performance. Further, a continuous feeding strategy for steady-state perfusion processes was successfully developed, enabling consistent product quality at elevated HM glycan levels. With kifunensine and maduramycin showing inverse effects on the relative HM distribution, a combined usage of these modulators was further evaluated to fine-tune a desired HM glycan pattern. The discovered HM modulators expand the current HM modulating toolbox for biotherapeutics. Their application not only for fed-batch processes, but also steady-state perfusion processes, make them a universal tool with regards to fully continuous manufacturing processes.

Keywords: N-linked glycosylation, HM modulation, M5 glycans, fed-batch, steady-state perfusion

Abbreviations: ADC, antibody-drug-conjugate; ADCC, antibody dependent cell cytotoxicity; ECE, enzyme conversion efficiency; ER, endoplasmic reticulum; GnTI, N-acetylglucosaminyltransferase I; HM, high mannose; M5 – M9, HM glycans with 5 – 9 mannose residues; mAb, monoclonal antibodies; ST, shake tubes; STR, stirred tank reactor; VCD, viable cell density; VCV, viable cell volume.

1 Introduction

With over 162 approved therapies world-wide and an ever-increasing demand due to rising incidences of chronic diseases and cancer, monoclonal antibodies (mAbs) make the largest and fastest growing class of biologics [1–3]. The majority of mAbs have a conserved N-glycosylation site in the Fc-domain which is critical for molecular stability, effector function and pharmacokinetics [4]. During the production of these mAbs, a mannose rich oligosaccharide chain is attached to a predefined and specific region in the protein (Asn-X-Ser/Thr). This process is called N-linked glycosylation and occurs in the endoplasmic reticulum (ER)[5, 6]. The oligosaccharide undergoes a series of modifications as it passes through the secretory pathway (ER and cis-Golgi). This includes trimming by glycosidases and mannosidases resulting in range of high mannose-type N-glycans (HM), reaching from HM glycans with 9 mannose residues (M9) to mostly 5 mannose residues (M5). HM glycans are of particular importance given their impact on pharmacokinetics and effector function. In general, higher antibody dependent cell cytotoxicity (ADCC) [7–11], reduced complement dependent cytotoxicity [8, 12], and reduced serum half-time are reported for HM-type mAbs [10, 13–15]. Enzymes in the medial Golgi can further modify the HM glycan structure, leading to the formation of complex glycans, followed by further branching and capping reactions in the trans-golgi and trans-golgi network [16, 17]. The way that mAbs are manufactured has a direct impact on the glycosylation profile, resulting in a heterogeneous mixture of complex-, hybrid- and HM-type N-glycans [4, 18].

Process intensification to meet the increasing demand and market supply, reformulation of drugs for subcutaneous delivery, rising interest in antibody-drug conjugates (ADCs), and biosimilar manufacturing heavily depend on proper control of HM content [19]. Especially for biosimilars, where 22 of the 37 licensed biosimilars are glycosylated monoclonal antibodies [20], careful control of HM levels is necessary to demonstrate biosimilarity to the reference product.

Naturally occurring mAbs contain relatively low levels of HM, but levels can be significantly increased up to 10% for commercially produced products [21]. Historical processes in contrast to newer processes tend to induce more HM species, particularly M5. Better process control, improved media formulation or shifts towards advanced manufacturing methods such as perfusion cell culture might be the reason for this discrepancy.

Many approaches to increase HM content in a biosimilar in order to match glycosylation of a reference product have been described and summarized in the

literature [16, 19, 22]. As such, changes in pH [19, 23], in osmolality [23, 24], hypothermia [25], or sugar additives are reported to increase HM glycans [26, 27]. Many of these approaches do however not allow large changes in HM content, do not specifically increase M5 species, and often come with negative impact on culture performance and product titer.

Larger changes in HM content could be achieved with enzyme-specific inhibitors such as kifunensine, swainsonin or deoxymannojirimycin [28–30]. Kifunensine as the most popular α -mannosidase I inhibitor in the ER has extensively been used in mammalian cell culture to drastically increase HM without significant impact on product titer but increased predominantly M8/M9 structures [7, 11, 29, 31].

Although it was demonstrated that higher mannose-type glycans (M6 – M9) show similar ADCC and pharmacokinetic properties than M5 glycans in intravenous administration [8, 10], the presence of M6 – M9 might be mitigated by serum α -mannosidases cleaving higher mannose-type glycans to M5 glycans [13, 15, 32]. With an increasing interest in subcutaneous administration of biologics, where no serum α -mannosidase activity is available, M6 – M9 glycans cannot be trimmed to M5 glycans [33]. Potential interaction of higher mannose-type glycans (M6 – M9) with C-type lectin receptors might trigger immunogenic reactions and increases interest in selective M5 glycan modulators [34, 35]. Furthermore, for biosimilar manufacturing where exact product quality matching is necessary, methods to particularly increase M5 glycans are of high interest.

Approaches to selectively increase M5 glycans are scarce, expensive, or patented and therefore not available for commercial mAb manufacturing. Raffinose for example used as sugar additive to the culture media has been identified to selectively increase M5 in a fed-batch process, showed however negative impact on culture growth and titer at higher concentrations [36]. M5 could be increased up to 7%, but at a significant rise in media cost due to raffinose supplementation.

Monensin, a sodium-hydrogen ionophore inhibiting glycan processing by increasing the pH in the Golgi, has been identified and patented to selectively increase M5 glycans for mAbs in a cell line independent and dose dependent manner [37]. Monensin belongs to the polyether ionophore compound family, a large group of relatively cheap antimicrobials extensively used in beef cattle production [38, 39]. In a perfusion process retaining the product in the bioreactor, monensin was bolused at a 500 nM dose and kept constant for 24 h, after which the monensin addition was stopped to reach the desired glycan target at the end of the run. Continuous monensin feeding was suggested in order to hold the HM concentration at a pre-defined target level throughout the production run, was however not demonstrated [37].

With continuous manufacturing of mAbs including perfusion upstream processing and continuous downstream processing on the rise [40–42], continuous modulator feeding is the only choice to achieve stable quality profiles at defined target set-points over time. Applicability for steady-state perfusion processes of such potent glycosylation modulators must therefore be assessed.

This study initially focused on finding alternatives to monensin within the polyether ionophore compound family to address the need for further potent M5 glycan increasing modulators. Maduramycin was identified as a novel HM modulator predominantly increasing M5 glycans of mAbs. Subsequently, feeding strategies of maduramycin for fed-batch and steady-state perfusion processes were evaluated using shake tubes (ST), automated miniature bioreactor systems and stirred tank bioreactors (STR). With a strong focus on the development of fully continuous manufacturing processes, continuous feeding of maduramycin during steady-state perfusion processes was successfully applied to control HM at a target setpoint and compared to continuous kifunensine feeding. This study further reports a novel combination to use maduramycin and kifunensine to target a specific HM glycan distribution at a defined absolute HM level.

2 Materials and Methods

2.1 Cell Lines

Three different CHO-S cell lines were used for fed-batch cultivations. Cell line A and B produced classical monoclonal antibodies (IgG1), whereas cell line C produced a fusion protein composed of a Fc-domain of IgG1 linked to a protein of interest. For perfusion cell cultures, a proprietary CHO-K1 cell line producing a bispecific monoclonal antibody (cell line D) was used (Table A.9).

Table A.9: Description of cell lines, products and glycosylation sites.

Cell line	Host cell line	Product	Glycosylation site	Cell culture system
A	CHO-S	IgG	1 Fc	Shake tubes, ambr15
B	CHO-S	IgG	1 Fc	ambr15, ambr250
C	CHO-S	IgG-fusion protein	1 Fc + 2 fusion protein	ambr15
D	CHO-K1	Bispecific IgG	1 Fc	Shake tubes, 2 L bioreactors

2.2 Modulator Stock Solutions

Maduramycin (CAS: 84878-61-5, Sigma-Aldrich, St. Louis, Missouri, USA) was dissolved in DMSO (DMSO Anhydrous, Invitrogen, Waltham, USA) at a stock con-

centration of 17.1 mM. Kifunensine (CAS: 109944-15-2, Sigma-Aldrich, St. Louis, Missouri, USA) stock solution was prepared in water at a concentration of 0.144 mM. Narasin (CAS: 55134-13-9, Sigma-Aldrich, St Louis, Missouri, USA) was dissolved in DMSO (Sigma-Aldrich, St Louis, Missouri, USA) at a stock concentration of 20.9 mM. Salinomycin (CAS: 53003-10-4, Sigma-Aldrich, St Louis, Missouri, USA) was dissolved in DMSO at a stock concentration of 24.5 mM. All stock solutions were stored at -20 °C.

2.3 Shake Tube Compound Screening

Cell line A was transferred into 50 mL ST (TubeSpin®), TPP, Trasadingen, Switzerland) after 24 days of expansion for fed-batch cultivation over 14 days. Cells were incubated at 36.5 °C, 5% CO₂, 320 rpm in an incubator with an orbital throw of 25 mm and a shaking angle of 90° (Multitron 4, Infors HT, Bottmingen, Switzerland). Cells were cultivated in a proprietary chemically defined medium (Merck Serono SA, Corsier-sur-Vevey, Switzerland) and a glycosylation modulating compound was added (Table A.10). Cells were fed on days 3, 5, 7 and 10 with a proprietary chemically defined main feed and a cysteine/tyrosine feed. A glucose feed was also added in the cell culture on days 3, 5, 7, 10 and 12 according to glucose consumption.

Table A.10: Experimental conditions for polyether ionophore compound screening.

Cell line	Compound	Concentration [nM]
A	Maduramycin	10, 25, 40, 50, 100
A	Narasin	1, 5, 20
A	Salinomycin	1, 5, 20
B, C	Maduramycin	10, 20, 40
B, C	Narasin	1, 5
B, C	Salinomycin	1, 5

2.4 Semi-continuous Perfusion in Shake Tubes

Cell culture (cell line D) from a 2 L steady-state STR perfusion bioreactor were transferred into 50 mL ST (TubeSpin®), TPP, Trasadingen, Switzerland) for semi-continuous cultivation [43]. The culture volume was 10 mL at a viable cell volume (VCV) of 10%, which was readjusted daily by bleeding based on VCV measurements. Cells were incubated at 36.5 °C, 5% CO₂, 270 rpm in an incubator with an orbital throw of 25 mm and a shaking angle of 90° (Multitron 4, Infors HT, Bottmingen, Switzerland). Cells were cultivated at 1 reactor volume per day (RV

day⁻¹) using a proprietary chemically defined medium (Merck Serono SA, Corsier-sur-Vevey, Switzerland) or with the same media supplemented with glycosylation modulators. Daily media change was performed by centrifugation for 5 min at 200 g (Centrifuge 5810 R, Eppendorf SE, Hamburg, Germany). Samples were 0.22 μm filtered prior to further analysis.

To screen the effect of maduramycin, kifunensine and the combination of both modulators on mAb glycosylation, a full factorial experimental design was chosen with four levels for maduramycin (0, 12.5, 25 and 50 nM) and four levels for kifunensine (0, 25, 50 and 100 nM). Antibody glycosylation was analysed on cultivation day 3, after 72 hours of incubation in modulator media.

2.5 Glycosylation Flux Analysis and Response Surface Modelling

Flux analysis for the initial glycosylation pathway was performed by assuming a linear pathway starting from the M9 structure to M5 (Figure A.24A). The connectivity of the network is described by the stoichiometric matrix S . Assuming a pseudo steady state of the system, the fluxes v are constrained to [44]:

$$S \cdot v = 0 \quad (\text{A.6})$$

It is worth mentioning, that the assumption of pseudo-steady-state holds for most conditions since a slow transient behaviour where no internal accumulation or depletion of species during the investigated timeframe is sufficient and a true steady-state is not required. The measured glycosylation species can be therefore seen as constant fluxes, v_e , out of the Golgi apparatus which can be used to calculate the internal fluxes, v_i , inside the network. Species M9 was assumed to be the only structure entering the late ER and Golgi apparatus. Consequently, formula A.7 can be split accordingly:

$$S_i \cdot v_i + S_e \cdot v_e = 0 \quad (\text{A.7})$$

where S_e is the stoichiometric matrix for the measured fluxes and S_i for the calculated internal fluxes. The inverse $(S_i)^{-1}$ is used to solve formula A.8:

$$v_i = -(S_i)^{-1} \cdot S_e \cdot v_e \quad (\text{A.8})$$

Assuming a fully linear pathway, the system is fully determined, and the result of formula A.9 is in this case unique. The ratio of the incoming flux and the outgoing flux was used as measure of the enzyme conversion rate as follows:

$$ECE_i [\%] = \frac{v_i}{v_{i-1}} \cdot 100 \quad (\text{A.9})$$

Multiple linear regression was performed to model the relationship between the two factors (kifunensine and maduramycin concentration) and the responses (total HM, enzyme conversion efficiency and relative HM distribution). A quadratic function was used for all response surface models (formula A.10):

$$Y = \beta_0 + \beta_1 \cdot X_1 + \beta_2 \cdot X_2 + \beta_3 \cdot X_1^2 + \beta_4 \cdot X_2^2 \quad (\text{A.10})$$

Where Y represents the dependent variable (response), β_{0-4} the regression coefficients, X_1 and X_2 the independent variables (factors). The `statsmodels` library in Python [45] was used to perform multiple linear regression.

For reversibility assessment at high modulator concentration, modulator media (200 nM maduramycin and 1 μM kifunensine) was used from cultivation day 0 – 4 and switched back to standard media without modulator from cultivation day 4 – 8. Samples for glycosylation analysis were collected every day to get time resolved glycosylation data.

2.6 Ambr15 Fed-Batch Cultivation

Cell line A was transferred into 15 mL automated mini bioreactor (ambr15®), Sartorius, Göttingen, Germany) after 24 days (cell line B: 19 days; cell line C: 28 days) of expansion for fed-batch cultivation over 17 days (cell line B and C: 14 days). The seeding density was 0.3×10^6 cells mL^{-1} (cell line B: 0.2×10^6 cells mL^{-1} ; cell line C: 0.2×10^6 cells mL^{-1}). Cells were grown at 37 °C for 5 days then at 33 °C until the end of the culture (cell line B: 36.5 °C for 6 days then at 33 °C until the end of the culture; cell line C: always at 36.5 °C). Stirring speed was kept constant at 800 rpm. pH was controlled by CO_2 and base addition in a defined range. Dissolved oxygen was controlled at 40% by sparging air and oxygen. Cells were cultivated in a proprietary chemically defined medium (Merck Serono SA, Corsier-sur-Vevey, Switzerland) into which a glycosylation modulating compound at varying concentrations was added

(Table A.10 for screening experiments; Table A.11 for maduramycin vs. kifunensine comparison). Cells were fed on days 3, 5, 7, 10 and 14 with a proprietary chemically defined main feed and a cysteine/tyrosine feed (cell line B: 3, 5, 7 and 10; cell line C: 3, 5, 7 and 10). A glucose feed was added daily to the cell culture starting on day 3 until the end of the culture according to glucose consumption (cell line B and C: 3, 5, 7, 10 and 12).

Table A.11: Experimental conditions for maduramycin vs. kifunensine comparison in ambr15 fed-batch processes.

Cell line	Compound	Concentration [nM]
A	Maduramycin	10, 25, 40
A	Kifunensine	25, 50, 75
B, C	Maduramycin	10, 20, 40
B, C	Kifunensine	50, 100, 1000

2.7 Ambr250 Fed-Batch Cultivation

Cell line B were transferred into 250 mL automated mini bioreactor (ambr250®), Sartorius, Göttingen, Germany) after 24 days of expansion for fed-batch cultivation over 12 days at a seeding density of 6.0×10^6 cells mL⁻¹. Cells were grown at 36.5 °C for 4 days then at 32 °C until the end of the culture, 500 rpm in an ambr250 automated system (ambr15®), Sartorius, Göttingen, Germany). pH was controlled by CO₂ and base addition in a defined range and dissolved oxygen controlled at 50%. Cells were cultivated in a proprietary chemically defined medium (Merck Serono SA, Corsier-sur-Vevey, Switzerland) with maduramycin at 40 nM, 50 nM and 80 nM. A further condition starting with 40 nM maduramycin and a second maduramycin addition of 40 nM on day 5 was performed. Cells were continuously fed for the whole duration of the culture with a proprietary chemically defined main feed and a cysteine/tyrosine feed on days 2, 5 and 8. A glucose feed was also added in the cell culture for the whole culture duration according to glucose consumption. Each condition was performed in duplicates but pooled for titer and glycosylation analysis.

2.8 Lab-scale 2 L STR Perfusion Cell Culture

Cell line D was expanded in an incubator (Multitron 4, Infors HT, Bottmingen, Switzerland) for 21 days using a proprietary chemically defined medium (Merck Serono SA, Corsier-sur-Vevey, Switzerland). Perfusion bioreactors (Labfors 5 Cell,

Infors HT, Bottmingen, Switzerland) were inoculated with a seeding density of 0.6×10^6 viable cells mL^{-1} . Culture conditions were maintained at 36.5°C with a dissolved oxygen setpoint of 50% (VisiFerm DO Arc, Hamilton, Bonaduz, Switzerland). The pH was controlled at 7.07 ± 0.17 (EasyFerm Plus Arc, Hamilton, Bonaduz, Switzerland) by CO_2 sparging and a 1.1 M Na_2CO_3 solution. Bioreactors were operated at 2 L working volume and perfusion was started on day 0 and kept constant at 1.3 RV day^{-1} . Bioreactor harvests were gravimetrically controlled to maintain the bioreactor weight constant using alternating tangential flow filtration (ATF2H, Repligen, Waltham, Massachusetts, USA) with polyether sulfone hollow fibers having a pore size of $0.22 \mu\text{m}$ (Repligen, Waltham, Massachusetts, USA). After an initial growth phase, an online capacitance probe (Incyte Arc, Hamilton, Bonaduz, Switzerland) was used to keep the VCV constant at 12%. Different modulator media for kifunensine and maduramycin based on the standard proprietary chemically defined media were prepared at 25 nM, 50 nM and 100 nM concentration. These media were connected to the bioreactor depending on the run design according to Table A.12, whereas modulator-free standard media was used for the entire control run.

Table A.12: Overview of 2L steady-state STR perfusion cell culture media compositions.

Change	Ctr run		Kif run		Mad run		Mad const. run	
	Media	Day	Media	Day	Media	Day	Media	Day
Start	Standard	0	Standard	0	Standard	0	Standard	0
#1	x	x	50 nM	11	50 nM	8	50 nM	11
#2	x	x	25 nM	19	25 nM	15	x	x
#3	x	x	100 nM	26	100 nM	22	x	x
#4	x	x	Standard	33	Standard	29	x	x

2.9 Analytical Methods

Cell density, viability, cell diameter, glucose, lactate, ammonia, and pH were measured using a BioProfile FLEX2 (Nova Biomedical, Waltham, USA). Lab-scale 2 L bioreactors were automatically sampled by the FLEX2 On-Line Autosampler (Nova Biomedical, Waltham, USA) and samples were fractionated using a Teledyne Cetac ASX-7200 (Teledyne CETAC Technologies, Omaha, Nebraska, USA). Viable cell volume (VCV) was calculated as follows [46]:

$$\text{VCV} = \frac{\frac{4}{3} \cdot \pi \cdot \left(\frac{D}{2}\right)^3 \cdot \text{VCD}}{V} \cdot 100 \quad (\text{A.11})$$

Where D is the average cell diameter, VCD the viable cell density, and V is the cell culture volume, assuming a spherical shape of the cells.

Process titers were determined using a protein affinity high performance liquid chromatography device (PA-HPLC, Waters, Milford, Massachusetts, USA).

To quantify protein glycosylation, mAbs were purified on Phytips (PhytipsVR, PhyNexus, San Jose, CA, USA). Product glycosylation for cell line A, B and C was quantified through 2-amino-benzamide labelling UPLC on a 100 mm column (Waters Corporation, Milford, MA, USA). For cell line D, a multi attribute method (MAM) which is based on high performance liquid chromatography-mass spectrometry (LC-MS, Vanquish™ Horizon UHPLC System and Q Exactive™ Plus, Thermo Fisher Scientific, Waltham, Massachusetts, USA) was used.

3 Results

3.1 Glycosylation Modulation in Fed-batch Processes

The polyether ionophores maduramycin, narasin and salinomycin were screened in ST with cell line A in a fed-batch process. All three polyether ionophores showed growth inhibition (Figure A.20A) and impact on cell viability (Figure A.20B) at elevated concentrations. For maduramycin, concentrations above 40 nM started to impact cell growth, whereas for narasin and salinomycin already 20 nM resulted in almost no cell growth. The desired increase of particularly M5 species was most pronounced for maduramycin with total HM concentrations of over 30% (Figure A.20C). Narasin and salinomycin increased total HM concentration to a much lower extent, but still by mainly increasing M5 species. Even though narasin and salinomycin could increase HM to a similar extent as maduramycin on cell line B and cell line C (Supporting Information Figure A.27), maduramycin was the chosen glycosylation modulator for further studies due to its applicability for all screened cell lines.

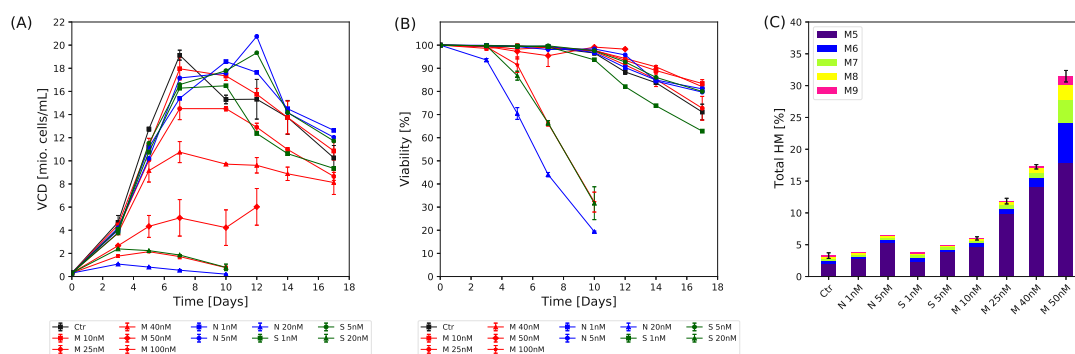


Figure A.20: HM modulator screening for cell line A in ST. Maduramycin, narasin and salinomycin, abbreviated with M, N and S were used at nM concentrations supplemented to the cell culture. VCD (A), viability (B) and total HM (C) for a fed-batch process. Conditions with error bars were performed in duplicates ($n=2$).

Consequently, the effect of maduramycin on product glycosylation was compared to the known α -mannosidase I inhibitor kifunensine in ambr15 bioreactors for fed-batch processes. Again, maduramycin concentration of 40 nM showed an impact on the cell growth of cell line A (Figure A.21A) and to a lower extent as well for cell line B (Figure A.21B) and cell line C (Figure A.21C). Accordingly, process titer was slightly reduced for the 40 nM maduramycin conditions (Figure A.21J, K and L). Kifunensine, except for the 1 μ M condition with cell line C, showed no impact on cell growth nor process titer. The total HM could be increased with

both modulators in a concentration dependent manner, varied however strongly between the different cell lines at similar modulator concentrations. At 40 nM maduramycin for example, cell line A reached a total HM level of 15.7% (Figure A.21D), cell line B a total HM level of 34.7% (Figure A.21E), and cell line C a total HM level of 20.7% (Figure A.21F). Similar trends were found for kifunensine, where total HM of the highest tested modulator concentration of 1 μ M ranged from 30.8% in cell line B to 82.1% in cell line C. The HM distributions showed the expected differences between kifunensine and maduramycin (Figure A.21G, H and I). Maduramycin almost exclusively increased the M5 species and resulted in a relative M5 distribution of about 80% or higher for all three cell lines, independent of the total HM level. Kifunensine showed decreasing relative M5 levels with increasing modulator concentration. Interestingly, kifunensine could still increase the absolute M5 levels at 100 nM modulator concentration or lower compared to the control in cell line B and C. When dosed at much higher concentrations of 1 μ M however, the higher mannose-type glycans such as M8 and M9 were significantly increased at the cost of M5 and M6 glycans.

As elevated modulator concentrations of maduramycin in the culture media reduced cell growth and product titer (Figure A.21), a double bolus feed strategy was evaluated for a high-seed fed-batch process for cell line B in the ambr250 bioreactor system. Rather than adding the entire modulator dose of 80 nM at the beginning of the process, a first addition of 40 nM on the starting day and a second dose of 40 nM on day 5 was performed. The VCD of the single bolus additions of 80 nM maduramycin at the beginning of the run resulted in significant growth reduction with a maximal VCD of 16.6×10^6 cells mL⁻¹, compared to the much higher VCD in the control run of 30.9×10^6 cells mL⁻¹ (Figure A.22A). The single bolus addition of 50 nM showed only a slightly reduced growth rate in the beginning and reached similar maximal VCD of 30.1×10^6 cells mL⁻¹. The double bolus condition with 40 nM maduramycin until day 5 showed also slightly reduced growth rate, reaching a high maximal cell density of 30.3×10^6 cells mL⁻¹. After adding the second bolus of another 40 nM maduramycin, VCD and viability started to decline faster compared to the control (Figure A.22B), however less than for the 80 nM single bolus addition. Considering the impact on product glycosylation, the single bolus additions resulted in a concentration dependent increase of the total HM of up to 28.6% for the 80 nM maduramycin condition (Figure A.22C). Relative HM distributions for all conditions showed that M5 was by far the most abundant mannose form for all conditions as expected for maduramycin. The double bolus addition 40 nM + 40 nM reached even higher total HM of 36.3%. Product titer decrease for the single bolus additions

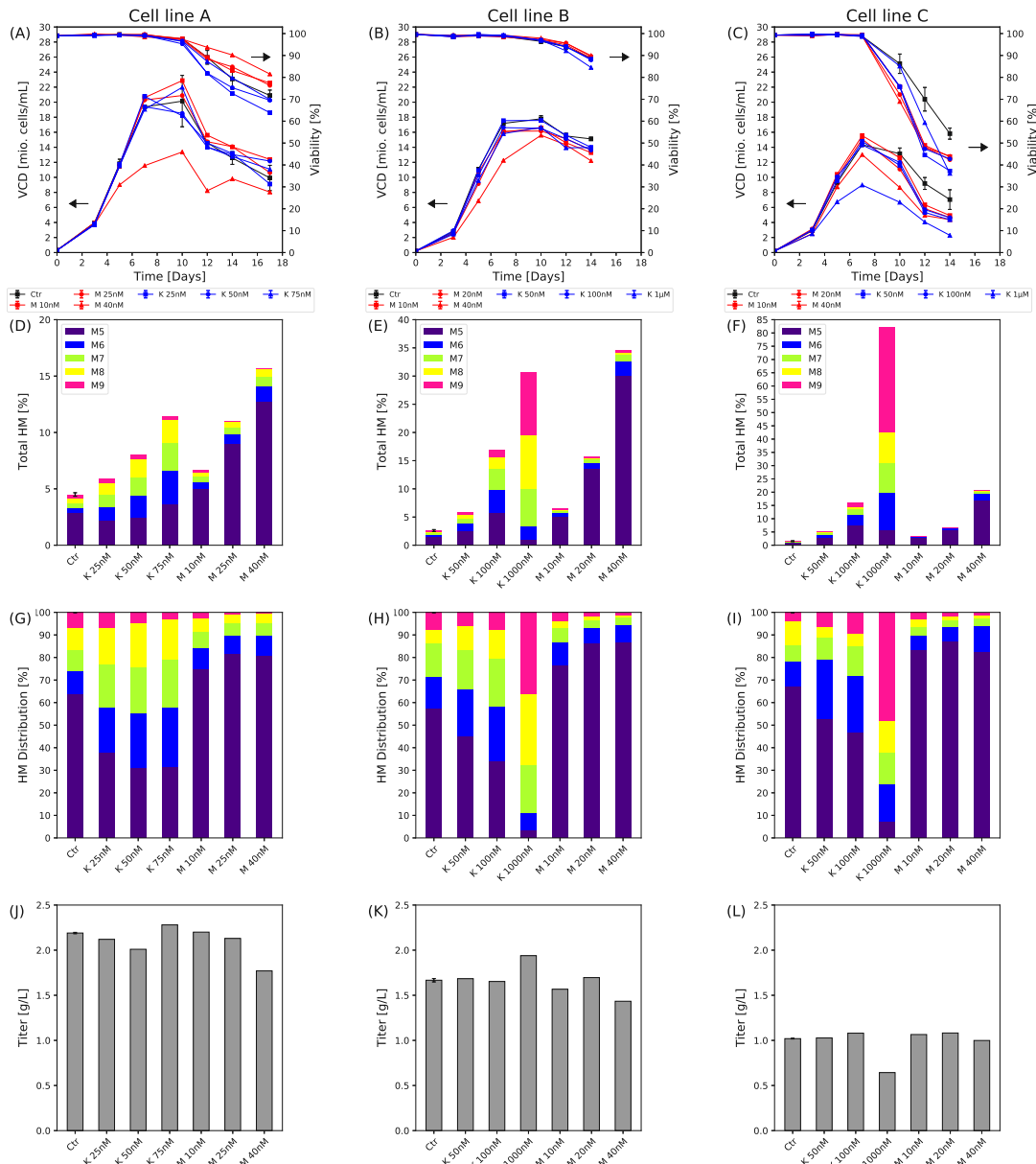


Figure A.21: HM modulator comparison in ambr15 fed-batch process for cell line A (first column), cell line B (second column) and cell line C (third column). Kifunensine and maduramycin, abbreviated with K, respectively M, were investigated at nM concentrations supplemented to the cell culture. VCD and viability (A, B, C), total HM (D, E, F), HM distribution (G, H, I) and product titer (J, K, L). Conditions with error bars were performed in duplicates (n=2).

in a concentration dependent manner, reaching the lowest concentration for the 80 nM condition of 2.3 g L⁻¹ compared to the control titer of 6 g L⁻¹ (Figure A.22D). The double bolus addition resulted in improved titer of 4 g L⁻¹, almost comparable to the 50 nM single bolus addition with 4.4 g L⁻¹, but with a more than doubled total HM level.

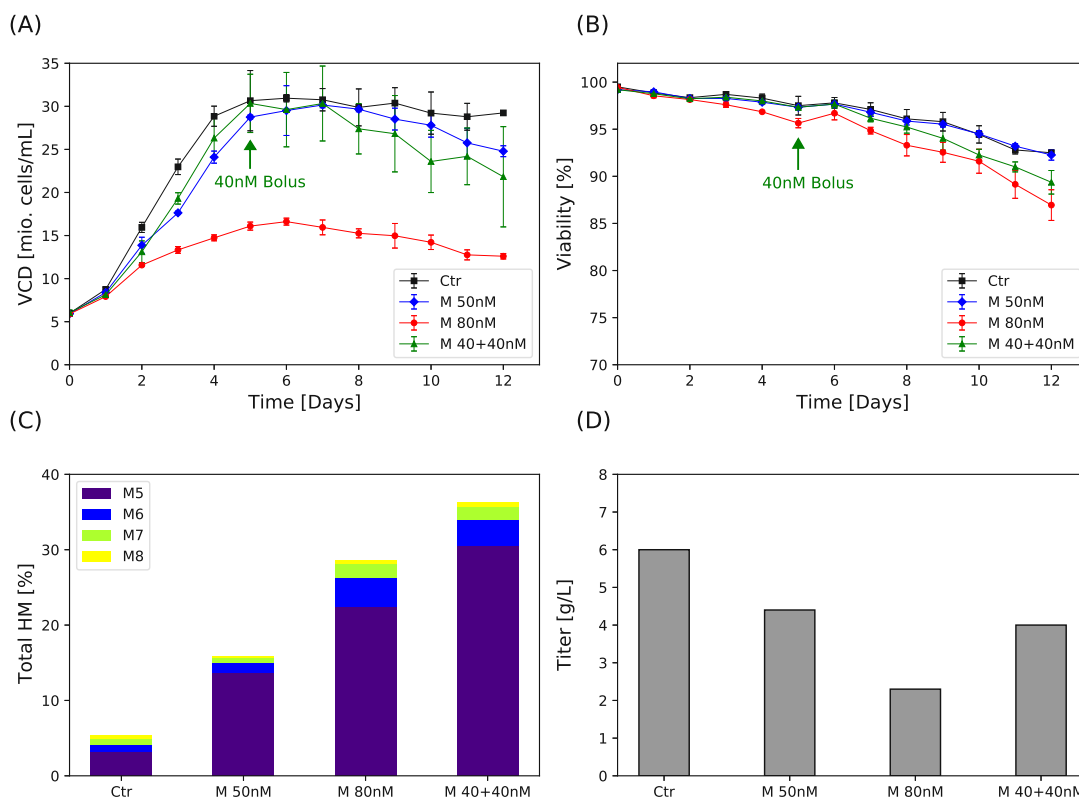


Figure A.22: Feeding strategy evaluation in ambr250 high-seed fed-batch process for cell line B. VCD (A), cell viability (B), total HM (C) and process titer (D). The green arrow represents the seconds Maduramycin addition for the condition M 40+40 nM. Conditions were performed in duplicates and pooled for titer and glycosylation analysis (n=2).

3.2 Glycosylation Modulation in Perfusion Processes

In contrast to fed-batch processes, the media in steady-state perfusion processes gets added in a continuous manner and product is harvested simultaneously. To assess the applicability of the new modulator maduramycin to steady-state perfusion processes with continuous modulator enriched media exchange, semi-continuous perfusion cultures in ST with a perfusion cell line (cell line D) were performed. Cultures were kept at a modulator concentration of 1 μ M of kifunensine and 200 nM of maduramycin for 4 days at steady-state cell density and no impact on cell viability and VCV was observed despite the high modulator concentrations (Figure A.23A and B). Total HM increased rapidly after modulator addition and reached steady-state glycosylation after around 2 days. Upon removal of the modulator media on day 4 back to modulator free media, total HM decreased again back to the original glycopattern on day 0 within 2 – 3 days for both kifunensine (Figure A.23C) and maduramycin (Figure A.23D). Knowing glycosylation reaches a steady-state within 2 days, a screening for lower modulator concentrations was performed by analysing

the glycosylation after 3 days in modulator media. Kifunensine at concentration of 25 nM and 50 nM did not drastically increase total HM, yet reduced the M5 type fraction by increasing M6 – M9. The 100 nM kifunensine conditions increased the total HM to 15.5% with a relative HM distribution with all HM glycan forms at roughly equal levels (Figure A.23E). Maduramycin at 12.5 nM did not increase total HM, while the relative HM distribution moved towards M5. The 25 nM maduramycin condition reached 5.8% total HM and the 50 nM maduramycin condition reached 15.7% total HM. In both conditions, the relative HM distribution contained mainly M5 type glycans as expected (Figure A.23F).

Having two different modulators increasing total HM, one increasing rather M6 – M9 (kifunensine) while the other almost exclusively increases M5 (maduramycin), a combination screening was performed in semi- continuous perfusion ST to develop a tool to target specific total HM levels with a customizable relative HM distribution. From glycosylation results of the mixed screening, overall enzymatic conversion efficiencies (efficiency of enzymes to catalyse a specific glycosylation reaction) were calculated and represented as contour plots (Figure A.24A upper row). Kifunensine demonstrated its expected effect to inhibit mannosidases catalyzing all the reactions from M9 – M5 with increasing modulator concentration. Maduramycin showed no or minor impact on the mannosidase activities for conversions from M9 – M7, but some impact on mannosidase activities for conversions from M7 – M5. N-acetylglucosaminyltransferase I (GnTI) compared to the mannosidases showed much stronger inhibition by maduramycin, and no inhibition by kifunensine at low concentrations to slight inhibition at higher concentrations. Contour plots of the relative HM distribution show clearly that M6 – M9 fractions can be increased by adding kifunensine to the culture media. For M5 however, the fraction decreases when increasing kifunensine concentration. With almost horizontal contour lines in all relative HM distribution plots, maduramycin seems not to change the HM distributions significantly no matter of the concentrations (Figure A.24A lower row). Considering the total HM contour plot showing increasing total HM levels for both modulators (Figure A.24B), the mixing of kifunensine and maduramycin represents an effective tool to achieve a desired total HM with a particular relative HM distribution. As such, by adding kifunensine to the culture media, the relative HM distribution can be tailored. By further adding maduramycin, the total HM level can be increased without impacting the tailored relative HM distribution. For example, targeting a relative M5 fraction of 35 – 40%, kifunensine must be chosen at a concentration of 25 nM and maduramycin can be supplemented depending on the targeted total HM level (Figure A.24C). By increasing kifunensine and keeping the

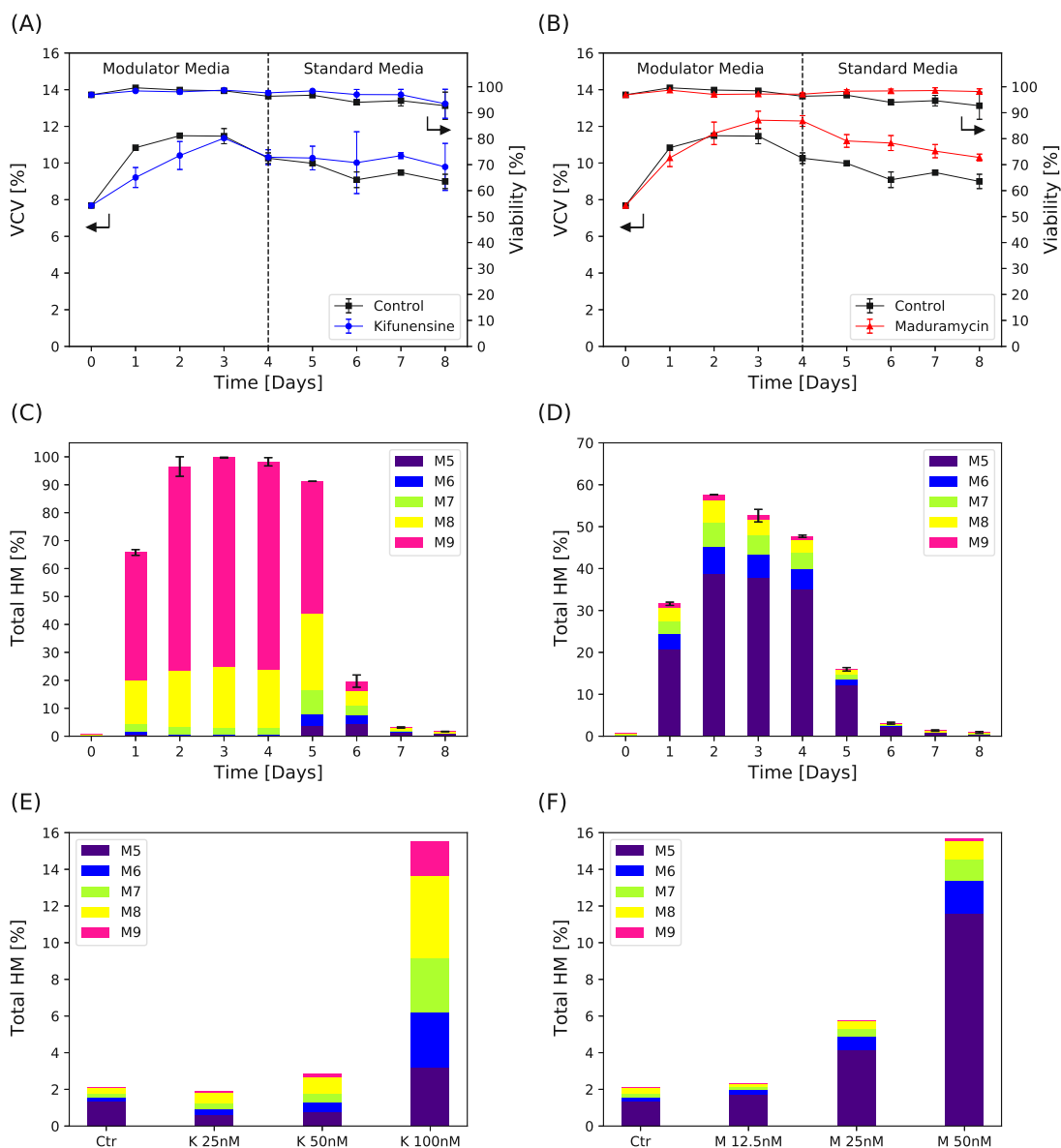


Figure A.23: Semi-continuous perfusion ST experiment evaluating reversibility of maduramycin and kifunensine effects on cell line D. VCV and viability (A) and HM glycoforms (C) for kifunensine cultures at 1 μ M. VCV and cell viability (B) and HM glycoforms (D) for maduramycin cultures at 200 nM. Dashed lines indicate the switch from modulator media to modulator-free perfusion media. HM glycoforms for kifunensine (E) and maduramycin (F) screening in ST stopped after 3 days. Conditions with error bars were performed in duplicates ($n=2$).

maduramycin at for example 12.5 nM, not only the total HM increased but also the relative HM distribution changed towards higher mannose-type glycans (Figure A.24D). Cell culture viability was not impacted by combined addition of kifunensine and maduramycin (Table A.13). Predicted vs. actual plots for all response surface models and model equations are provided in the Supporting Information section

(Figure A.29 and Table A.14).

Validation of the semi-continuous perfusion ST screening was subsequently performed in 2 L steady-state STR perfusion bioreactors at modulator concentration of 25 nM, 50 nM and 100 nM according to Table A.12. VCV and culture viability (Figure A.25A) was not impacted by changing kifunensine concentrations (Figure A.25C) or maduramycin concentrations (Figure A.25D). Time resolved glycosylation trends for the kifunensine run (Figure A.25E) and for the maduramycin run (Figure A.25F) changed accordingly to the modulator concentration within the bioreactor. It is worth noting that total HM levels are fully reversible for both modulators upon switching back to modulator free media. Steady-state glycosylation levels, calculated based on the data of the last 3 days prior to a media change, are provided for kifunensine (Figure A.25G) and maduramycin (Figure A.25H). The averaged total HM levels for the kifunensine run of 2.5% for 25 nM, 3.0% for 50 nM and 12.0% for 100 nM modulator concentration are in well agreement with the semi-continuous perfusion ST screening (Figure A.23E), where total HM levels of 1.9% for 25 nM, 2.8% for 50 nM and 15.5% for 100 nM modulator concentration were observed. Similarly, total HM levels for the maduramycin run (25 nM: 5.4%; 50 nM: 13.4%) were comparable to the ST screening (25 nM: 5.8%; 50 nM: 15.7%) in Figure A.23F. The 12.5 nM condition was not evaluated at the 2 L bioreactor scale as no increase in total HM was observed in the screening and therefore replaced by the 100 nM condition leading to total HM of 20.6%. Next to total HM levels, also the relative HM distributions were comparable to the ST screening. Process titers during the perfusion runs were comparable to the control run (Figure A.25B).

The ultimate goal of this study was to develop a tool to increase and control total and individual HM glycoforms with a particular focus on M5 for a fully continuous manufacturing process and keep product quality stable over time. Therefore, maduramycin was fed constantly at 50 nM throughout an entire steady-state perfusion run. VCV and cell viability were not impacted by the modulator addition (Figure A.28A) and titer remained comparable to the control run (Figure A.28B). Total HM increased upon maduramycin addition from 0.7% to 12.2% and remained over 10% until the end of the run (Figure A.26A). The major fraction of the relative HM distribution was clearly the M5 form always remaining above 8%. All other HM glycans from M6 – M9 remained around 1% or lower (Figure A.26B). At the same time to an increase of HM species, a concomitant decrease of complex glycans was observed. As such, galactosylation decreased from around 55% to 25% (Figure A.26G), and afucosylation increased from approximately 2% to 8% (Figure A.26D). A-sialylation remained rather constant between 98 – 100% (Figure A.26C). Other

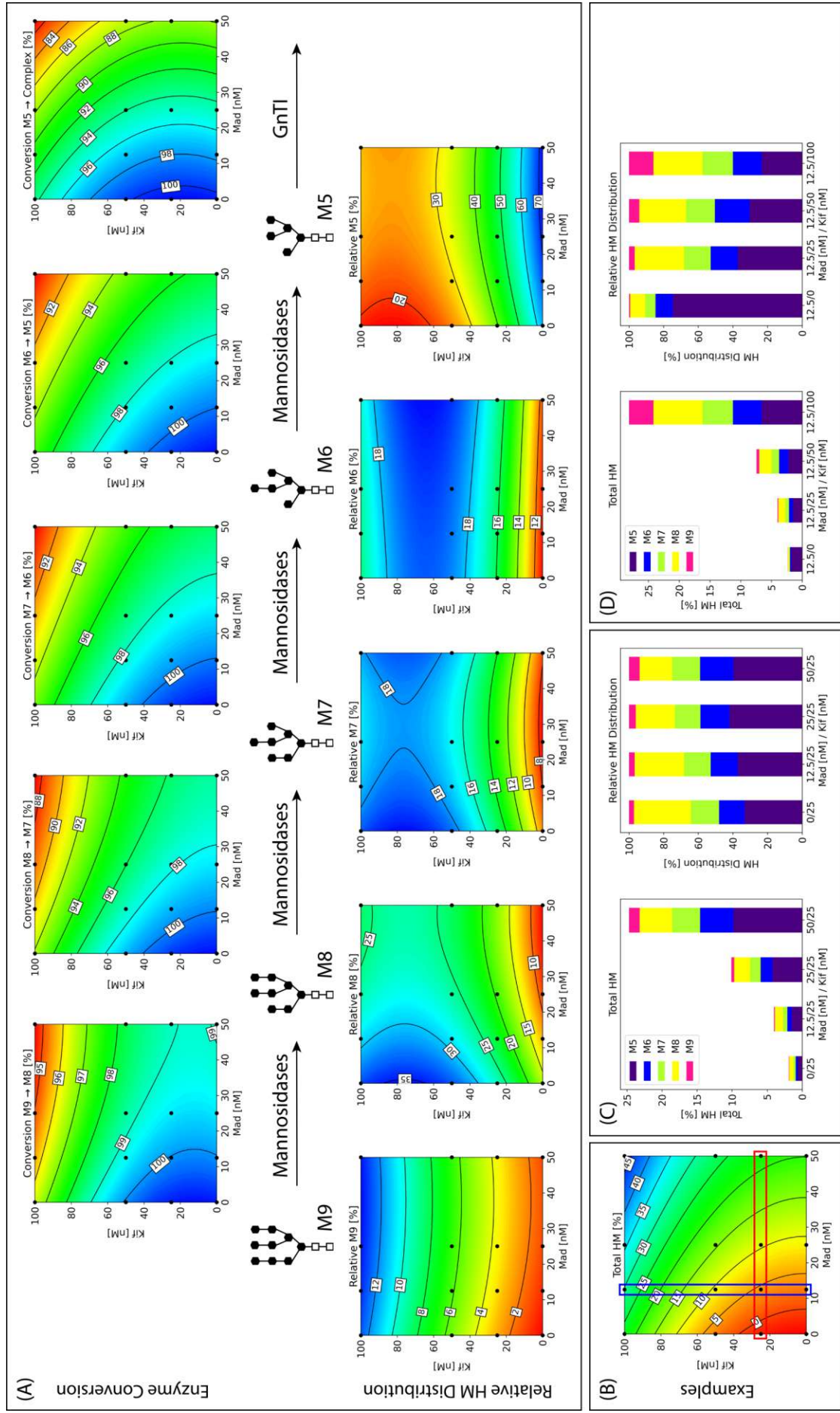


Figure A.24: HM fine-tuning experimental data of cell line D in semi-continuous ST by supplementing maduramycin, kifunensine or a combination of both compounds. Response surface plots for enzyme conversion efficiency are shown in the top row in (A), the relative HM distributions for the specific HM forms in the lower row. Total HM response surface is shown in (B), the red rectangle highlights data used for the total HM and the HM distribution plot in (C), the blue rectangle for the total HM and the HM distribution plot in (D). Black dots on the response surface correspond to experimental data points used for modelling.

glycoforms, including A1 (Figure A.26E), A2 and A2G1 (Figure A.26F), FA1 and FA2 (Figure A.26I) and FA2G1 and FA2G2 (Figure A.26J) also show constant glycosylation levels over time even though absolute levels changed for some glycoforms compared to the control run.

4 Discussion

Using polyether ionophores as glycosylation modulator is an attractive method to increase and fine tune HM glycans of mAbs with a predominant tendency of increasing the M5 glycoform. Next to the previously identified modulator monensin [9], this study screened three novel polyether ionophores for their propensity to act as HM modulators. Maduramycin showed the desired effect on all tested cell lines, whereas narasin and salinomycin showed similar performance on two cell lines, reduced effects on a third cell line were observed (Figure A.20). Furthermore, absolute HM levels varied strongly between the tested cell lines, demonstrating that each cell line reacts different to a particular dose of a specific polyether ionophore modulator. This is in agreement with previous studies, where varying HM levels were observed upon treatment with the same dose of monensin [37]. Whereas maduramycin was the preferred modulator in this study due to its effect on all tested cell lines, narasin or salinomycin might be suitable alternatives in case maduramycin shows insufficient effect on a new cell line.

For fed-batch processes, total HM could significantly be increased using maduramycin. The same fed-batch processes supplemented with kifunensine clearly demonstrated the differences between the two modulators. With increasing kifunensine concentration, the relative M5 fraction decreased significantly and relative M6 – M9 fractions were increasing (Figure A.21). It is worth mentioning that also kifunensine increased lower mannose-type glycans (M5 – M7) species when supplemented at lower doses, higher mannose-type glycans (M8 – M9) prevailed only when kifunensine was supplemented at high doses of 1 μ M. Maduramycin in contrast increased the relative M5 fraction compared to the modulator free control runs on all tested cell lines and kept high M5 distributions irrelevantly of the dose. At elevated modulator concentrations, maduramycin and kifunensine showed growth inhibition leading to lower maximal cell densities in the fed-batch processes, resulting in reduced process titer. Growth inhibition for kifunensine was also detected by others, however without impacting process titer [11], and minimal impact on culture performance for the polyether ionophore monensin was observed [37]. The growth inhibition threshold for maduramycin was reached earlier compared to kifunensine and a special feeding strategy for maduramycin was therefore developed in this work, splitting the maduramycin dose into two bolus additions (Figure A.22). The first bolus at the beginning of the process was dosed in order not to impact cell growth. Once the maximal cell density was reached, a second bolus was added to boost the HM level in the product. This strategy not only increased the total HM level but also improved

process titer due to higher maximal cell densities compared to the single bolus addition. This feeding strategy might be similarly applied to other polyether ionophores such as narasin, salinomycin, as all of them showed concentration dependent impact on cell growth.

With increasing attention to continuous manufacturing, steady-state perfusion processes are gaining interest within the manufacturing space of biopharmaceuticals. Even though monensin has been evaluated in a perfused bioreactor retaining the product [37], this is the first report to the authors' knowledge evaluating continuous maduramycin and kifunensine addition in a steady-state perfusion process with continuous product harvesting. To assess the applicability of maduramycin and kifunensine for continuous feeding, semi-continuous ST were used to cultivate a perfusion adapted cell line producing a bispecific mAb (Figure A.23). During the initial phase with daily replaced modulator enriched culture media, steady-state glycosylation was reached within 3 days for kifunensine as well as for maduramycin. Upon switching back to modulator free media, glycosylation patterns returned to the initial low HM levels within 2 – 3 days. This demonstrates that neither maduramycin nor kifunensine accumulate within the cells and both compounds can be readily washed out once modulator free media is fed. Looking at relative glycosylation patterns highlights the drastic difference between kifunensine producing mainly M8 and M9 glycans, and maduramycin producing mainly M5 glycans. With two complementary HM increasing modulators inversely affecting the relative HM distribution, a further screening including the combined use of kifunensine and maduramycin was performed (Figure A.24). The HM glycan trimming is a complex process with multiple different mannosidases involved and occurs in the ER as well as in the Golgi [19, 22] and the acquired data set did not allow to distinguish between all the different enzymes involved. For simplification, the overall conversion efficiencies from a particular HM glycan to the following HM glycan (e.g., from M9 – M8) were analysed. A clear trend of kifunensine mainly reducing enzymatic activity of mannosidases and maduramycin mainly reducing GnTI activity was detected. This novel approach to mix kifunensine with maduramycin enables to target a specific total HM level with a customized relative HM distribution. Therefore, the kifunensine concentration can be chosen to target a specific relative HM distribution and maduramycin can be added on top to reach the targeted total HM level. For biosimilar process development, where matching exact glycosylation patterns is crucial, the usage of polyether ionophores such as maduramycin in combination with kifunensine might represent a valid approach.

As the main goal of this study was to increase total HM exclusively by increasing

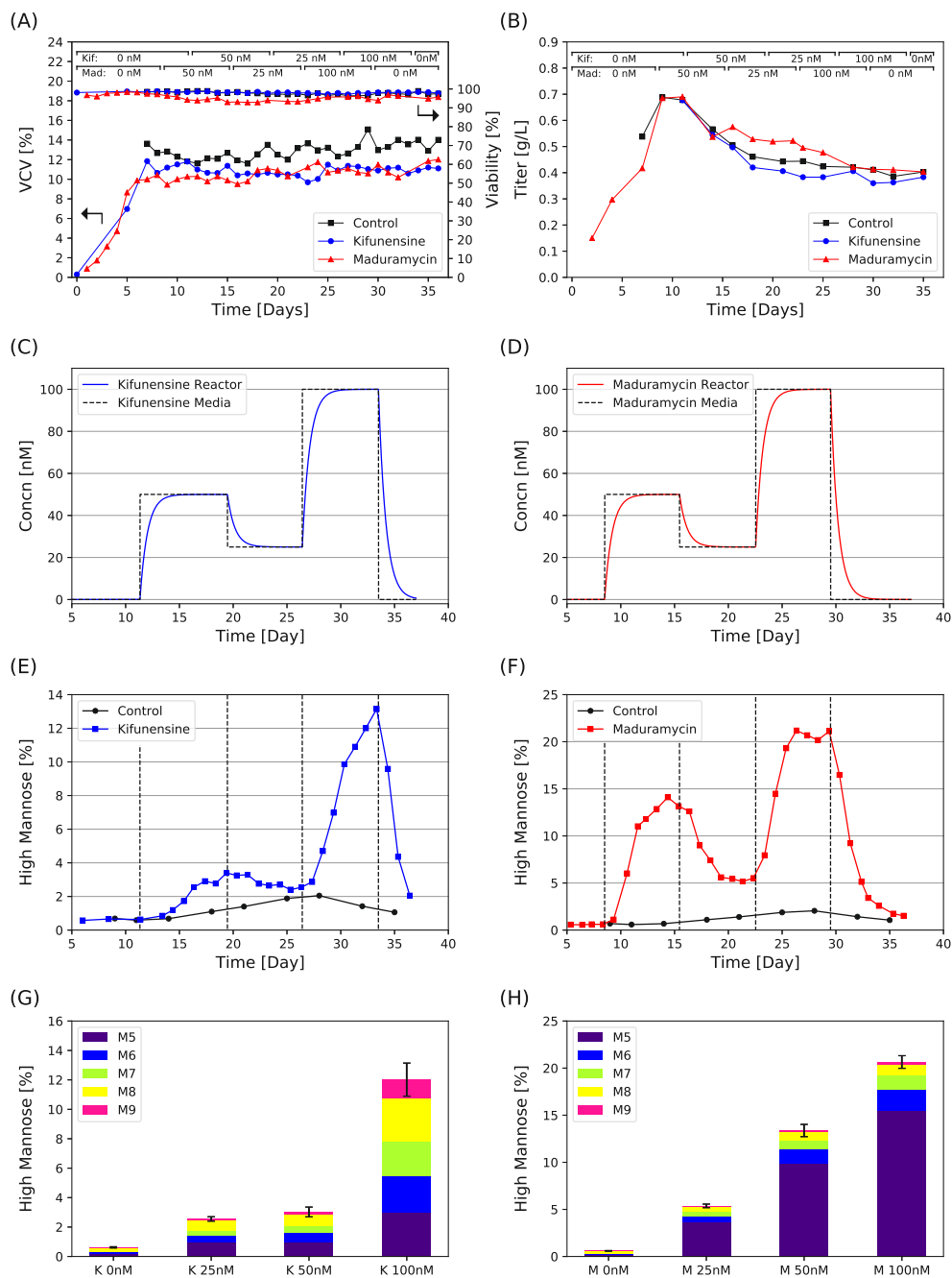


Figure A.25: Steady-state perfusion process data at 2 L bioreactor scale for control run, kifunensine and maduramycin run using cell line D. VCV and viability (A), process titer (B), feeding strategy and calculated modulator concentration in the bioreactor for kifunensine run (C) and for maduramycin run (D), with respective absolute HM levels for kifunensine run (E) and maduramycin (F). Steady-state HM glycoforms averaged over last 3 days before media change for kifunensine run (G) and for maduramycin run (H).

M5, maduramycin supplementation alone was further evaluated in real steady-state 2 L perfusion bioreactors operated for up to 36 days and compared to kifunensine (Figure A.25). Reversibility observed in semi-continuous ST after changing modulator concentration could be validated in steady-state perfusion bioreactors. The glycosylation pattern followed, with a couple of days delay, the modulator concentration within the bioreactor and was fully reversible after switching to modulator free media. Thinking of possible real-time monitoring of critical quality attributes (CQA) in the near future with emerging technologies, adaptive modulator addition based on feedback control might be an interesting tool to modulate product quality and adapt to process changes in real time. Steady-state glycosylation levels in the 2 L perfusion bioreactors matched well with the glycosylation levels obtained after 3-day semi-continuous ST screening. Semi-continuous ST screenings can therefore be a fast tool to assess the cell line specific response to polyether ionophores or other modulators prior to stirred tank bioreactor runs.

In a steady-state continuous manufacturing scenario, product quality must be held constant throughout the entire perfusion process to enable a fully integrated, continuous downstream processing. With commercially produced mAb product of up to 10% HM [21], a perfusion process of cell line D with a standard HM level of 0.5 – 2% was tried to be increased to 10% by continuous maduramycin addition. This was achieved by feeding 50 nM maduramycin, determined by the previous ST screening and a 2 L steady-state perfusion run at varying modulator levels (Figure A.26). The HM level was stably increased and maintained at the elevated level for almost 25 days. Almost exclusively M5 was present among the HM species. At the same time, also more complex glycoforms changed in their absolute level, but remained stable at the new level throughout the perfusion run. This can be explained partly as increasing HM levels directly lead to reduced levels of more processed glycosylation forms. Additionally, it seems that maduramycin does not only act on the enzyme GnTI leading to increased M5, but also on further enzyme more downstream in the glycosylation pathway. Considering that maduramycin belongs to the same group of polyether ionophores as monensin, which is believed to change neutralize the pH within the Golgi [47, 48], all pH sensitive enzymes might be impacted in the glycosylation pathway. Modelling and tuning of more complex glycoforms goes however beyond the scope of this study. In contrast to fed-batch processes, no impact on culture viability and process titer was observed for both modulators, even though maduramycin was used at higher concentration up to 200 nM. This might either be a cell line specific characteristic, might be related to the highly reduced cell division rate during steady-state operation or comes due

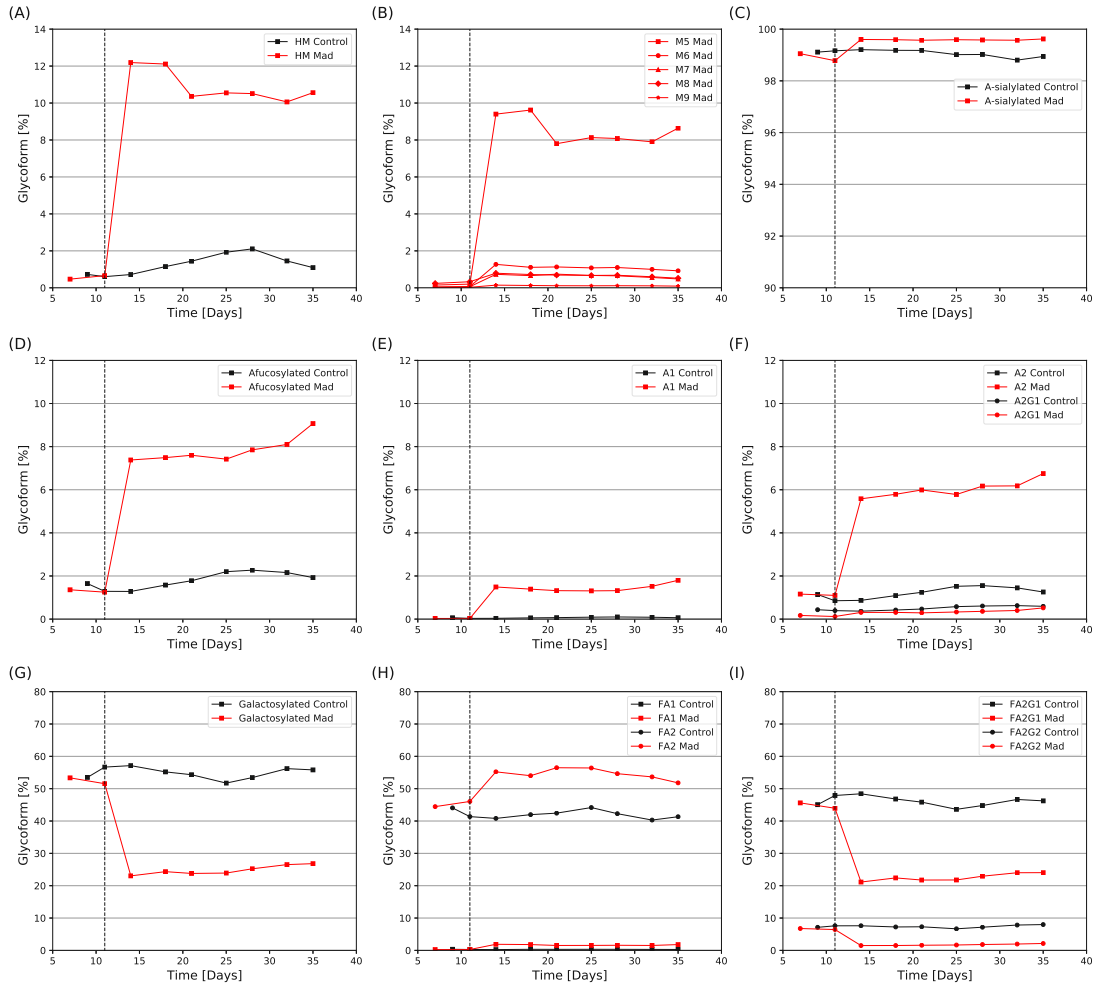


Figure A.26: Glycosylation data of steady-state perfusion process at 2 L bioreactor scale for continuous 50 nM maduramycin run and control run using cell line D. Absolute HM (A), HM glycoforms for maduramycin run (B), a-sialylated species (C), afucosylated species (D), A1 form (E), A2 and A2G1 forms (F), galactosylated species (G), FA1 and FA2 forms (H), FA2G1 and FA2G2 forms (I). The dashed lines represent the change to 50 nM maduramycin media on day 11.

to the optimal nutrient supplementation and waste product removal due to the perfusion operation. Further, the increased biomass to modulator ratio during the perfusion cell cultures might be an explanation for the findings. In any case, it is recommended to start with the continuous modulator feeding once the target VCV of the cell culture is reached to avoid inhibiting cell growth during the initial exponential growth phase.

5 Conclusion

This study evaluated amongst other polyether ionophores the use of maduramycin, a novel HM modulator specifically increasing M5 type glycans, and compared its effect to kifunensine. Whereas a double bolus addition in fed-batch processes of maduramycin enabled highest total HM levels with minimal titer reduction, a continuous feeding strategy for steady-state perfusion processes was successfully established. The study further suggested a novel combination to utilize maduramycin and kifunensine, demonstrating an interesting tool to fine-tune or control the relative HM distribution independently of the targeted total HM level.

Acknowledgements

The authors would like to thank Philip Giller and Sebastian Schneider (FHNW) for supporting experimental work on perfusion processes. Moreover, the authors would like to acknowledge specifically the Bioprocess Sciences (BPS) team of Merck Serono SA (an affiliate of Merck KGaA) for material and analytical support and for valuable discussions and support throughout the project, especially Alexandre Châtelin and the analytical team.

Conflict of interest

The authors declare that they have no known competing financial interests or personal relationships that could have appeared to influence the work reported in this paper.

Data availability statement

The data that support the findings of this study are available from the corresponding author upon reasonable request.

Supporting Information

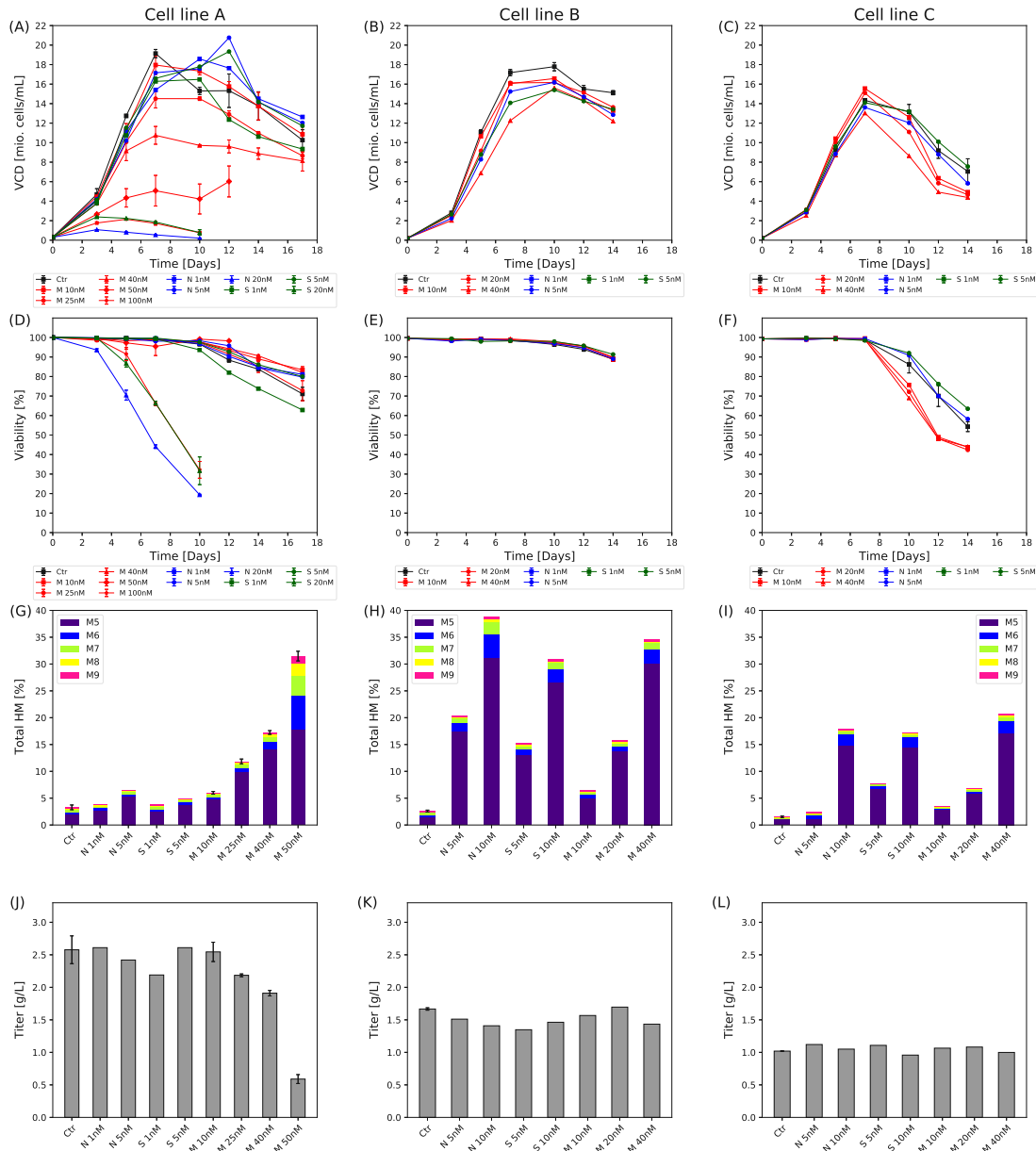


Figure A.27: Polyether ionophore screening in ST bioreactors for cell line A (first column), and in ambr15 fed-batch process for cell line B (second column) and cell line C (third column). Narasin, salinomycin and maduramycin with the respective abbreviation N, S and M were evaluated. VCD (A, B, C), viability (D, E, F), total HM (G, H, I) and product titer (J, K, L). Conditions with error bars were performed in duplicates (n=2).

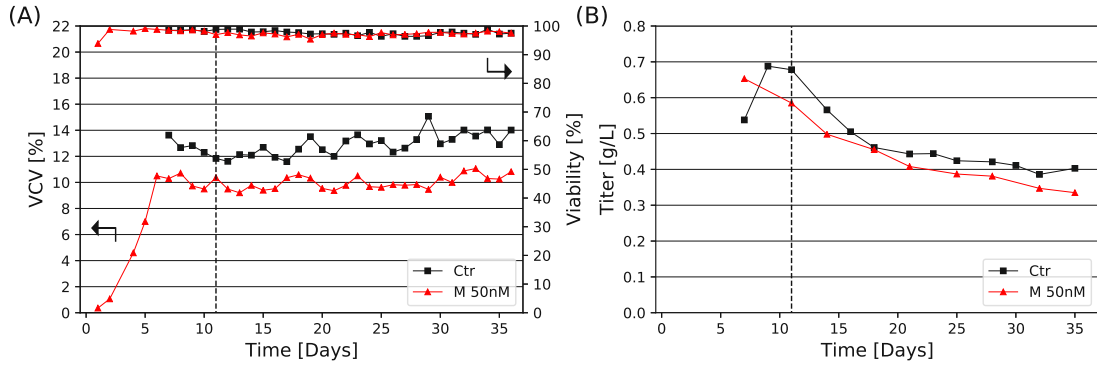


Figure A.28: VCV and cell viability (A) and process titer (B) of continuous 50 nM maduramycin feeding during steady-state perfusion process and a control run. The dashed line represents the start of the continuous maduramycin feeding.

Table A.13: Cell culture parameters for combined utilization of maduramycin and kifunensine in ST bioreactors.

Name	Mad [nM]	Kif [nM]	Viability [%]	Cell Diam. [μm]	VCV [%]
WD0	0	0	87.5	22.01	10.35
0/25	0	25	94.0	23.16	10.08
0/50	0	50	94.6	22.87	9.75
0/100	0	100	93.6	23.05	9.37
12.5/0	12.5	0	96.8	23.11	9.95
25/0	25	0	92.9	22.75	8.34
50/0	50	0	93.4	22.89	9.46
12.5/25	12.5	25	93.7	22.92	9.47
12.5/50	12.5	50	92.3	22.94	9.09
12.5/100	12.5	100	95.3	22.98	9.71
25/25	25	25	92.4	23.00	8.59
25/50	25	50	93.8	23.07	9.21
25/100	25	100	91.4	23.10	9.27
50/50	50	50	87.5	22.72	8.61
50/25	50	25	90.5	22.78	9.02
50/100	50	100	92.5	23.10	9.98
0/0	0	0	90.0	22.87	8.58

Table A.14: Response surface model equations for the HM fine-tuning experimental data of cell line D in semi-continuous ST bioreactors.

Name	Equation
Conversion M9 \rightarrow M8	$Y = 100.811595 + -0.070179X_1 + 0.014238X_2 + 0.000663X_1^2 + -0.000584X_2^2$
Conversion M8 \rightarrow M7	$Y = 101.718196 + -0.159924X_1 + -0.005934X_2 + 0.001252X_1^2 + -0.000894X_2^2$
Conversion M7 \rightarrow M6	$Y = 101.260511 + -0.099831X_1 + -0.006405X_2 + 0.000307X_1^2 + -0.000589X_2^2$
Conversion M6 \rightarrow M5	$Y = 101.221842 + -0.098855X_1 + -0.014174X_2 + 0.000043X_1^2 + -0.000486X_2^2$
Conversion M5 \rightarrow Complex	$Y = 100.400464 + -0.211775X_1 + 0.042188X_2 + -0.000781X_1^2 + -0.001104X_2^2$
Relative M9	$Y = 0.341824 + 0.058320X_1 + 0.084876X_2 + -0.000770X_1^2 + 0.000384X_2^2$
Relative M8	$Y = 16.267734 + -0.396442X_1 + 0.506230X_2 + 0.004178X_1^2 + -0.003338X_2^2$
Relative M7	$Y = 9.183410 + -0.120694X_1 + 0.275201X_2 + 0.002047X_1^2 + -0.001800X_2^2$
Relative M6	$Y = 10.916158 + 0.007931X_1 + 0.249038X_2 + 0.000126X_1^2 + -0.001943X_2^2$
Relative M5	$Y = 63.290875 + 0.450884X_1 + -1.115345X_2 + -0.005582X_1^2 + 0.006698X_2^2$
Total HM	$Y = -3.591360 + 0.521934X_1 + -0.004014X_2 + -0.000958X_1^2 + 0.002728X_2^2$

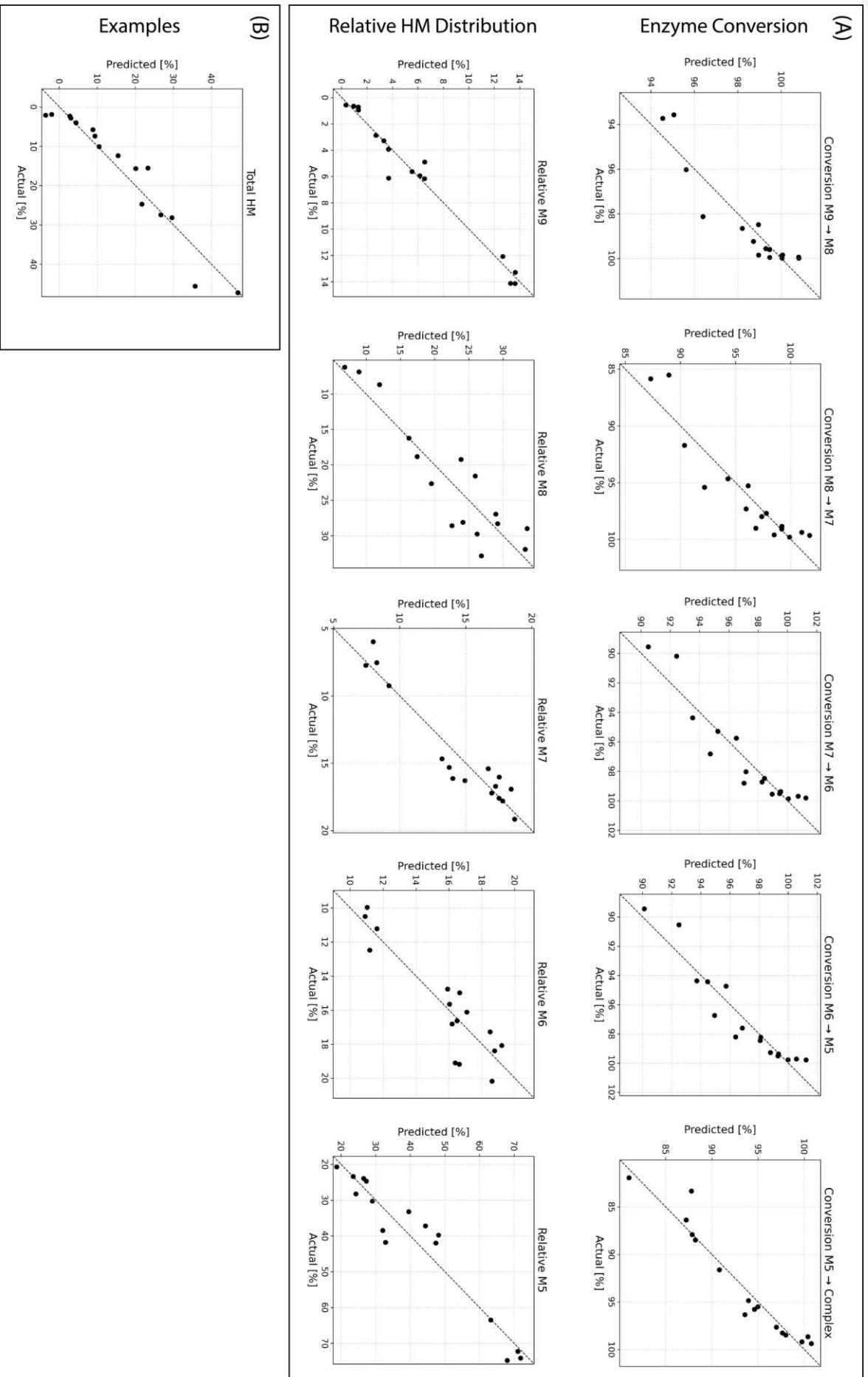


Figure A.29: Predicted vs. actual plots for the MLR plots of the HM fine-tuning experiment of cell line D in semi-continuous ST bioreactors. Predicted vs. actual plots for the enzyme conversion efficiency plots are provided in the upper row of (A), for the relative HM distributions in the lower row of (B) and for the total HM in (B).

References

- [1] Xiaochen Lyu et al. “The global landscape of approved antibody therapies”. In: *Antibody Therapeutics* 5.4 (2022), pp. 233–257. ISSN: 2516-4236. DOI: 10.1093/abt/tbac021.
- [2] Theo Vos et al. “Global, regional, and national incidence, prevalence, and years lived with disability for 301 acute and chronic diseases and injuries in 188 countries, 1990–2013: a systematic analysis for the Global Burden of Disease Study 2013”. In: *The Lancet* 386.9995 (2015), pp. 743–800. ISSN: 01406736. DOI: 10.1016/S0140-6736(15)60692-4.
- [3] Christina Fitzmaurice et al. “Global, regional, and national cancer incidence, mortality, years of life lost, years lived with disability, and disability-adjusted life-years for 32 cancer groups, 1990 to 2015: A Systematic Analysis for the Global Burden of Disease Study Global Burden ”. In: *JAMA Oncology* 3.4 (2017), pp. 524–548. ISSN: 23742445. DOI: 10.1001/jamaoncol.2016.5688.
- [4] Fabian Higel et al. “N-glycosylation heterogeneity and the influence on structure, function and pharmacokinetics of monoclonal antibodies and Fc fusion proteins”. In: *European Journal of Pharmaceutics and Biopharmaceutics* 100 (2016), pp. 94–100. ISSN: 18733441. DOI: 10.1016/j.ejpb.2016.01.005.
- [5] Markus Aebi. “N-linked protein glycosylation in the ER”. In: *Biochimica et Biophysica Acta (BBA) - Molecular Cell Research* 1833.11 (2013), pp. 2430–2437. ISSN: 01674889. DOI: 10.1016/j.bbamcr.2013.04.001.
- [6] Flavio Schwarz and Markus Aebi. “Mechanisms and principles of N-linked protein glycosylation”. In: *Current Opinion in Structural Biology* 21.5 (2011), pp. 576–582. ISSN: 0959440X. DOI: 10.1016/j.sbi.2011.08.005.
- [7] Patrick H.C. van Berkel et al. “Rapid production of recombinant human IgG With improved ADCC effector function in a transient expression system”. In: *Biotechnology and Bioengineering* 105.2 (2010), pp. 350–357. ISSN: 00063592. DOI: 10.1002/bit.22535.
- [8] Yutaka Kanda et al. “Comparison of biological activity among nonfucosylated therapeutic IgG1 antibodies with three different N-linked Fc oligosaccharides: The high-mannose, hybrid, and complex types”. In: *Glycobiology* 17.1 (2007), pp. 104–118. ISSN: 14602423. DOI: 10.1093/glycob/cw1057.

- [9] Ronald Jay Rothman et al. “Antibody-dependent cytotoxicity mediated by natural killer cells is enhanced by castanospermine-induced alterations of IgG glycosylation”. In: *Molecular Immunology* 26.12 (1989), pp. 1113–1123. ISSN: 01615890. DOI: 10.1016/0161-5890(89)90055-2.
- [10] Marcella Yu et al. “Production, characterization and pharmacokinetic properties of antibodies with N-linked Mannose-5 glycans”. In: *mAbs* 4.4 (2012), pp. 475–487. ISSN: 1942-0862. DOI: 10.4161/mabs.20737.
- [11] Qun Zhou et al. “Development of a simple and rapid method for producing non-fucosylated oligomannose containing antibodies with increased effector function”. In: *Biotechnology and Bioengineering* 99.3 (2008), pp. 652–665. ISSN: 00063592. DOI: 10.1002/bit.21598.
- [12] Austin W. Boesch et al. “Highly parallel characterization of IgG Fc binding interactions”. In: *mAbs* 6.4 (2014), pp. 915–927. ISSN: 1942-0870. DOI: 10.4161/mabs.28808.
- [13] Leslie Alessandri et al. “Increased serum clearance of oligomannose species present on a human IgG1 molecule”. In: *mAbs* 4.4 (July 2012), pp. 509–520. ISSN: 1942-0862. DOI: 10.4161/mabs.20450.
- [14] David Falck et al. “Glycoform-resolved pharmacokinetic studies in a rat model employing glycoengineered variants of a therapeutic monoclonal antibody”. In: *mAbs* 13.1 (2021). ISSN: 1942-0862. DOI: 10.1080/19420862.2020.1865596.
- [15] Andrew M. Goetze et al. “High-mannose glycans on the Fc region of therapeutic IgG antibodies increase serum clearance in humans”. In: *Glycobiology* 21.7 (2011), pp. 949–959. ISSN: 09596658. DOI: 10.1093/glycob/cwr027.
- [16] David Brühlmann et al. “Tailoring recombinant protein quality by rational media design”. In: *Biotechnology Progress* 31.3 (2015), pp. 615–629. ISSN: 15206033. DOI: 10.1002/btpr.2089.
- [17] Kelley W. Moremen, Michael Tiemeyer, and Alison V. Nairn. “Vertebrate protein glycosylation: diversity, synthesis and function”. In: *Nature Reviews Molecular Cell Biology* 13.7 (July 2012), pp. 448–462. ISSN: 1471-0072. DOI: 10.1038/nrm3383.
- [18] Beate Beyer et al. “Microheterogeneity of Recombinant Antibodies: Analytics and Functional Impact”. In: *Biotechnology Journal* 13.1 (2018), pp. 1–11. ISSN: 18607314. DOI: 10.1002/biot.201700476.

- [19] Renato Mastrangeli et al. “The Formidable Challenge of Controlling High Mannose-Type N-Glycans in Therapeutic mAbs”. In: *Trends in Biotechnology* 38.10 (2020), pp. 1154–1168. ISSN: 18793096. DOI: 10.1016/j.tibtech.2020.05.009.
- [20] Joel Welch et al. “The Mannose in the Mirror: A Reflection on the Pharmacokinetic Impact of High Mannose Glycans of Monoclonal Antibodies in Biosimilar Development”. In: *Clinical Pharmacology & Therapeutics* 0.0 (2022), pp. 1–8. ISSN: 0009-9236. DOI: 10.1002/cpt.2783.
- [21] Gregory C. Flynn et al. “Naturally occurring glycan forms of human immunoglobulins G1 and G2”. In: *Molecular Immunology* 47.11-12 (2010), pp. 2074–2082. ISSN: 01615890. DOI: 10.1016/j.molimm.2010.04.006.
- [22] Helen H. Shi and Chetan T. Goudar. “Recent advances in the understanding of biological implications and modulation methodologies of monoclonal antibody N-linked high mannose glycans”. In: *Biotechnology and Bioengineering* 111.10 (2014), pp. 1907–1919. ISSN: 10970290. DOI: 10.1002/bit.25318.
- [23] Rubin Jiang, Hao Chen, and Sen Xu. “pH excursions impact CHO cell culture performance and antibody N-linked glycosylation”. In: *Bioprocess and Biosystems Engineering* 41.12 (2018), pp. 1731–1741. ISSN: 1615-7591. DOI: 10.1007/s00449-018-1996-y.
- [24] Efren Pacis et al. “Effects of cell culture conditions on antibody N-linked glycosylation-what affects high mannose 5 glycoform”. In: *Biotechnology and Bioengineering* 108.10 (2011), pp. 2348–2358. ISSN: 00063592. DOI: 10.1002/bit.23200.
- [25] Sha Sha et al. “N-Glycosylation Design and Control of Therapeutic Monoclonal Antibodies”. In: *Trends in Biotechnology* 34.10 (2016), pp. 835–846. ISSN: 18793096. DOI: 10.1016/j.tibtech.2016.02.013.
- [26] Tanaya Surve and Mugdha Gadgil. “Manganese increases high mannose glycoform on monoclonal antibody expressed in CHO when glucose is absent or limiting: Implications for use of alternate sugars”. In: *Biotechnology Progress* 31.2 (2015), pp. 460–467. ISSN: 87567938. DOI: 10.1002/btpr.2029.
- [27] Craig Zupke et al. “Real-time product attribute control to manufacture antibodies with defined N-linked glycan levels”. In: *Biotechnology Progress* 31.5 (2015), pp. 1433–1441. ISSN: 87567938. DOI: 10.1002/btpr.2136.

- [28] Michel Awwad et al. “Modification of monoclonal antibody carbohydrates by oxidation, conjugation, or deoxymannojirimycin does not interfere with antibody effector functions”. In: *Cancer Immunology Immunotherapy* 38.1 (1994), pp. 23–30. ISSN: 0340-7004. DOI: 10.1007/BF01517166.
- [29] A.D. Elbein et al. “Kifunensine, a potent inhibitor of the glycoprotein processing mannosidase I”. In: *Journal of Biological Chemistry* 265.26 (1990), pp. 15599–15605. ISSN: 00219258. DOI: 10.1016/S0021-9258(18)55439-9.
- [30] Jean-Louis Franc et al. “Inhibition of N-linked oligosaccharide processing does not prevent the secretion of thyroglobulin. A study with swainsonine and deoxynojirimycin”. In: *European Journal of Biochemistry* 157.1 (1986), pp. 225–232. ISSN: 0014-2956. DOI: 10.1111/j.1432-1033.1986.tb09660.x.
- [31] Chao Yu et al. “Use of the α -mannosidase I inhibitor kifunensine allows the crystallization of apo CTLA-4 homodimer produced in long-term cultures of Chinese hamster ovary cells”. In: *Acta Crystallographica Section F: Structural Biology and Crystallization Communications* 67.7 (2011), pp. 785–789. ISSN: 17443091. DOI: 10.1107/S1744309111017672.
- [32] Xiaoyu Chen, Diana Liu, and Gregory C. Flynn. “The effect of Fc glycan forms on human IgG2 antibody clearance in humans”. In: *Glycobiology* 19.3 (2009), pp. 240–249. ISSN: 09596658. DOI: 10.1093/glycob/cwn120.
- [33] Michael R. Turner and Sathy V. Balu-Iyer. “Challenges and Opportunities for the Subcutaneous Delivery of Therapeutic Proteins”. In: *Journal of Pharmaceutical Sciences* 107.5 (2018), pp. 1247–1260. ISSN: 15206017. DOI: 10.1016/j.xphs.2018.01.007.
- [34] Hadar Feinberg et al. “Mechanism of pathogen recognition by human dectin-2”. In: *Journal of Biological Chemistry* 292.32 (2017), pp. 13402–13414. ISSN: 1083351X. DOI: 10.1074/jbc.M117.799080.
- [35] Nithinan Sawettanai et al. “Synthetic Lipomannan Glycan Microarray Reveals the Importance of α (1,2) Mannose Branching in DC-SIGN Binding”. In: *Journal of Organic Chemistry* 84.12 (2019), pp. 7606–7617. ISSN: 15206904. DOI: 10.1021/acs.joc.8b02944.
- [36] David Brühlmann et al. “Cell culture media supplemented with raffinose reproducibly enhances high mannose glycan formation”. In: *Journal of Biotechnology* 252 (2017), pp. 32–42. ISSN: 18734863. DOI: 10.1016/j.jbiotec.2017.04.026.

- [37] Sandhya Pande et al. “Monensin, a small molecule ionophore, can be used to increase high mannose levels on monoclonal antibodies generated by Chinese hamster ovary production cell-lines”. In: *Biotechnology and Bioengineering* 112.7 (2015), pp. 1383–1394. ISSN: 00063592. DOI: 10.1002/bit.25551.
- [38] Dion A Kevin II, Damaris AF Meujo, and Mark T Hamann. “Polyether ionophores: broad-spectrum and promising biologically active molecules for the control of drug-resistant bacteria and parasites”. In: *Expert Opinion on Drug Discovery* 4.2 (2009), pp. 109–146. ISSN: 1746-0441. DOI: 10.1517/17460440802661443.
- [39] Jacek Rutkowski and Bogumil Brzezinski. “Structures and Properties of Naturally Occurring Polyether Antibiotics”. In: *BioMed Research International* 2013 (2013), pp. 1–31. ISSN: 2314-6133. DOI: 10.1155/2013/162513.
- [40] Kevin Botelho Ferreira et al. “Transfer of continuous manufacturing process principles for mAb production in a GMP environment: A step in the transition from batch to continuous”. In: *Biotechnology Progress* 38.4 (2022), pp. 1–13. ISSN: 8756-7938. DOI: 10.1002/btpr.3259.
- [41] Michael J. Coolbaugh et al. “Pilot-scale demonstration of an end-to-end integrated and continuous biomanufacturing process”. In: *Biotechnology and Bioengineering* 118.9 (2021), pp. 3287–3301. ISSN: 0006-3592. DOI: 10.1002/bit.27670.
- [42] Daniel J. Karst et al. “Process performance and product quality in an integrated continuous antibody production process”. In: *Biotechnology and Bioengineering* 114.2 (2017), pp. 298–307. ISSN: 00063592. DOI: 10.1002/bit.26069.
- [43] Moritz K F Wolf et al. “Development of a shake tube - based scale - down model for perfusion cultures”. In: *Biotechnology and Bioengineering* 115.March (2018), pp. 2703–2713. DOI: 10.1002/bit.26804.
- [44] Ivan Hang et al. “Analysis of site-specific N-glycan remodeling in the endoplasmic reticulum and the Golgi”. In: *Glycobiology* 25.12 (2015), pp. 1335–1349. ISSN: 14602423. DOI: 10.1093/glycob/cwv058.
- [45] Skipper Seabold and Josef Perktold. “Statsmodels : Econometric and Statistical Modeling with Python”. In: *9th Python in Science Conference*. Scipy. 2010, pp. 92–96.

- [46] S. Metze et al. “Monitoring online biomass with a capacitance sensor during scale-up of industrially relevant CHO cell culture fed-batch processes in single-use bioreactors”. In: *Bioprocess and Biosystems Engineering* 43.2 (2020), pp. 193–205. ISSN: 1615-7591. DOI: 10.1007/s00449-019-02216-4.
- [47] RT Kubo and ML Pigeon. “Expression of membrane IGM by a human B lymphoblastoid cell line in the presence of monensin”. In: *Molecular Immunology* 20.3 (1983), pp. 345–348.
- [48] Hilton H. Mollenhauer, D. James Morr , and Loyd D. Rowe. “Alteration of intracellular traffic by monensin; mechanism, specificity and relationship to toxicity”. In: *Biochimica et Biophysica Acta (BBA) - Molecular Cell Research* 1031.2 (1990), pp. 225–246.

A.4 Scientific Publication Section IV

Maximizing yield of perfusion cell culture processes: Evaluation and scale-up of continuous bleed recycling

Abstract

Bleed recycling is a novel method to increase the yield of steady-state perfusion processes by concentrating process bleed to selectively remove biomass and recycle the liquid fraction. This results in significant product saving which otherwise would go to waste. As long as cells can be concentrated and separated, existing cell separation devices can be used for such an application. However, limited information comparing operation modes and efficiency for bleed recycling applications is available. For the first time, inclined gravity settling has been used as bleed recycling technology and was compared to acoustic separation. Except for lower debris removal, inclined gravity settling showed similar bleed recycling efficiency and no negative impact on cell viabilities, nutrient and metabolite levels and product quality. Additionally considering reduced system complexity and facilitated scale-up, inclined gravity settling was the preferred technology for further evaluation during a 42-day lab-scale perfusion process. Up to a 3.5-fold bleed reduction and an average harvest rate increase of 19% was achieved. Scalability was subsequently tested with a large-scale inclined gravity settler suitable for a 2,000 L perfusion process confirming performance of lab-scale experiments. Bleed recycling characterization data from screening experiments combined with scalability demonstration facilitates decision making when considering bleed recycling for novel perfusion process settings to reduce perfusion waste, increase process sustainability and boost overall process yield.

Keywords: monoclonal antibody production, steady-state perfusion, bleed recycling characterization, acoustic separation, inclined gravity settling, scale-up

Abbreviations: AS, acoustic separator; CRD, cell retention device; IS, inclined gravity settler; mAb, monoclonal antibodies; SE, separation efficiency; VCD, viable cell density; VCV, viable cell volume.

1 Introduction

Recent reports about perfusion cell culture have shown increasing volumetric productivities, more homogenous product quality profiles, and benefits due to reduced product residence time in the bioreactor for labile proteins [1–4]. Continuous manufacturing of monoclonal antibodies consists of a steady-state perfusion cell culture process followed by a continuous capture step and multiple polishing steps [5, 6]. To achieve a steady-state perfusion operation not only a cell retention device (CRD) for cell free harvesting, but also a waste stream (bleed) to remove excessive biomass is required. Bleeding is not a selective operation since the bleed has the same composition as the culture in the bioreactor. Assuming a process viable cell volume (VCV) of 10% means a bleed composition of 10% biomass and 90% liquid fraction. As bleeding is required to maintain target cell density in a stable perfusion process, this causes a large amount of liquid (containing the product of interest) to be wasted along with excessive biomass.

When calculating process yield for perfusion processes, the product concentration (harvest titer) and the harvest rate must be considered [7]. Large process bleed rates are therefore undesirable in terms of process intensification as they lead to reduced harvest rates. Despite major improvements in harvest titer within the industry, little attention was put on perfusion bleed rate reduction.

A first strategy to improve process yield consists of reducing the overall process bleed rate. Growth inhibition by cell cycle inhibitors or temperature shifts were reported in literature [8]. Despite improved process yields, growth inhibition showed changes in product quality. Furthermore, the process bleed rate corresponds to the cell division rate. While low cell division rates might initially lead to improved process yields, this approach can jeopardize high long-term cell culture viability and stability.

A second strategy concentrates the bleed stream in order to reduce the liquid fraction that is wasted concomitantly with the biomass in the bleed stream. Only the concentrated biomass is directed to waste and the clarified liquid stream is directed back to the bioreactor, resulting in an increased perfusion harvest rate and process yield. The bleed stream coming from the bioreactor, corresponding to the cell division rate, is not reduced in this scenario, but a significant liquid fraction thereof is recycled back to the bioreactor. As such, a recent proof-of-concept study implementing a solid-liquid separation step using an acoustic separator to concentrate the biomass in the bleed stream of a perfusion process was conducted and specified as bleed recycling [9]. Good separation efficiency and no changes

in product quality or metabolite profile were detected at a VCV of 5%, tested during a period of 4 days at 2 L scale. A liquid-solid separation device instead of growth inhibition could mitigate the risk of long-term process stability by keeping bleed rates sufficiently high without reducing culture performance. The study by Bielser et al. [9] was the first report of bleed recycling in the literature, and further research is needed to explore its potential benefits at higher VCV and under different perfusion process conditions. Furthermore, scalability of acoustic separation for bleed recycling has not been demonstrated.

Acoustic separators use an acoustic resonance field to cause individual cells to group together and form larger cell aggregates. These cell aggregates show enhanced settling properties due to their larger size and settle faster once the acoustic waves are interrupted [10, 11]. Whereas very promising separation results could be achieved with acoustic settlers used as CRD in small scale [12–14] a limited amount of information is available about large-scale application of acoustic separators. Acoustic separators were successfully tested up to a clarification volume of 200 L day⁻¹ and further scale-up by merging multiple smaller acoustic chambers was suggested [15]. Development of larger scale acoustic separators seems very difficult due to the significant power input required for cell separation, causing heat generation within the device [16, 17]. A multi-chamber system might solve the problem of heat dissipation but increases system complexity drastically, raising a need to explore further technologies as bleed recycling alternatives. These technologies should be less complex and easier to scale, nevertheless showing similar performance characteristics.

Next to acoustic separation, inclined gravity settling has been successfully used as CRD to maintain stable perfusion processes [17–19]. In contrast to acoustic separators, inclined gravity settlers were extensively studied and used for large-scale production bioreactors due to their relatively low complexity and good scalability [20, 21], rendering them an interesting alternative to acoustic separation for bleed recycling. As the particles, in this case cells, settle down within the inclined channel, a higher density slurry is formed at the bottom of the channel. Driven by gravity, the slurry slips down the surface, generating a convective flow that enhances the settling process, described as “Boycott Effect” [22]. As no aggregation support by an acoustic resonance field is available, inclined gravity settlers tend to be larger than acoustic separators. This comes with an increased culture residence time within the inclined gravity settler, with unknown impact on culture performance when used for bleed recycling.

Even though settling technology does not guarantee 100% clarified culture harvest, which led to the widespread use of filter-based cell retention devices with a

predominant use of tangential flow filtration (TFF) and alternating flow filtration (ATF) in combination with hollow fiber modules [3, 17, 23, 24], the technological requirements for bleed recycling are different. In the case of bleed recycling, the main purpose of the bleed recycling device is to concentrate cells as much as possible rather than providing a complete cell free harvest stream. The clarified recycle stream, even if containing some remaining cells, will be directed back to the bioreactor and ultimately increase the harvest stream. Filtration for further downstream process operations is performed by the main cell retention device and not by the bleed recycling device. Since not only whole cells but also smaller particles such as cell debris can be recycled into the bioreactor, possible negative effects of cell debris on fouling of cell retention filters should be investigated [25, 26]. Defining critical process debris levels and corresponding correlation to filter fouling has not yet been demonstrated and most likely changes depending on chosen process parameters, equipment, and operation mode.

The aim of this study is to demonstrate the application of bleed recycling for process intensification of industrially relevant perfusion processes. For the first time, inclined gravity settling is used as bleed recycling device and compared to acoustic separation with respect to bleed recycling efficiency, metabolite profiles, product quality attributes, cell debris removal, and ease of operation. A wide range of perfusion scenarios covering process VCV, process bleed rates and settler operation parameters were investigated at lab-scale, to quantify the potential of process intensification by bleed recycling for a wide range of cases. Scalability of bleed recycling was demonstrated by building a large-scale inclined gravity settler and recycling bleed streams of a 2,000 L perfusion bioreactor with 1,500 L filling volume. Details of the successful outcomes are reported, focusing on the performance of bleed recycling technologies, and even more importantly, on the impact of bleed recycling on cell culture performance and product quality.

2 Materials and Methods

2.1 Lab-scale perfusion culture process

A proprietary CHO-K1 cell line producing a bispecific monoclonal antibody (mAb1) was expanded in an incubator (Multitron 4, Infors HT, Bottmingen, Switzerland) for 21 days using a proprietary chemically defined medium (Merck Serono SA, Corsier-sur-Vevey, Switzerland). Perfusion bioreactors (Labfors 5 Cell, Infors HT, Bottmingen, Switzerland) were inoculated with a seeding density of 0.6×10^6 viable cells

mL^{-1} . Culture conditions were maintained at $36.5\text{ }^{\circ}\text{C}$ with a dissolved oxygen (DO) setpoint of 50% (VisiFerm DO Arc, Hamilton, Bonaduz, Switzerland). The pH was controlled at 7.07 ± 0.17 (EasyFerm Plus Arc, Hamilton, Bonaduz, Switzerland) by CO_2 sparging and a 1.1 M Na_2CO_3 solution. Bioreactors were operated at 2 L working volume and perfusion was started on day 0 and kept constant at 1.3 reactor volumes per day (RV day^{-1}). Bioreactor harvests were gravimetrically controlled to maintain the bioreactor weight constant using alternating tangential flow filtration (ATF2H, Repligen, Waltham, Massachusetts, USA) with polyether sulfone hollow fibers having a pore size of $0.22\text{ }\mu\text{m}$ (Repligen, Waltham, Massachusetts, USA). After an initial growth phase, an online capacitance probe (Incyte Arc, Hamilton, Bonaduz, Switzerland) was used to keep VCV constant at 12%.

2.2 Pilot-scale perfusion cell culture

Another proprietary CHO-K1 cell line producing a bispecific monoclonal antibody (mAb2) was cultivated in a 200 L perfusion bioreactor (Mobius 200 L Bioreactor, Merck KGaA, Darmstadt, Germany). VCV was kept constant at 8% with an online capacitance probe (Incyte Arc, Hamilton, Bonaduz, Switzerland). Bioreactor harvests were gravimetrically controlled to maintain the bioreactor weight constant using either alternating tangential flow filtration (XCell ATF[®] 6 single use, Repligen, Waltham, Massachusetts, USA) with polyether sulfone hollow fibers having a pore size of $0.22\text{ }\mu\text{m}$ (Repligen, Waltham, Massachusetts, USA) to retain the cells. When the production was finished, the remaining cell culture was used to test the large-scale inclined gravity settler (Constructions Inoxydables SA, Châtel-St-Denis, Switzerland) with flowrates representative for a 2,000 L perfusion bioreactor. During the experiment, cell culture was agitated and maintained at $35\text{ }^{\circ}\text{C}$. The pH was controlled at 6.95 ± 0.15 (InPro3253i, Mettler Toledo, Greifensee, Switzerland) using CO_2 or 1.1 M Na_2CO_3 and DO was maintained at 50% (InPro6860i/12/120/nA, Mettler Toledo, Greifensee, Switzerland). Perfusion and capacitance controls were stopped.

2.3 Large-scale perfusion cell culture

A 2,000 L bioreactor (Mobius 2,000 L Bioreactor, Merck KGaA, Darmstadt, Germany) was inoculated at 0.67×10^6 viable cells mL^{-1} (mAb1) with a constant working volume of 1,500 L. The pH was controlled at 6.95 ± 0.15 (InPro3253i, Mettler Toledo, Greifensee, Switzerland) using CO_2 or 1.1 M Na_2CO_3 and DO was maintained at 50% (InPro6860i/12/120/nA, Mettler Toledo, Greifensee, Switzerland).

During the growth phase, the temperature was kept at 36.5 °C and was then shifted to 33 °C once the capacitance setpoint was reached. VCV was kept constant at 8% with an online capacitance probe (Incyte Arc, Hamilton, Bonaduz, Switzerland). A flowmeter (LFS-03SU-Z-SC1-G25, Levitronix, Zurich, Switzerland) was used on the process bleed line to monitor the flow and deduct the amount from the overall target harvest rate. Perfusion rate was gradually increased during growth phase until 1.3 RV day⁻¹ from when it was kept constant until the end of the run. Product of interest was harvested through two single use alternating tangential flow devices in parallel (XCell ATF[®] 10 single use, Repligen, Waltham, Massachusetts, USA) with polyether sulfone hollow fibers having a pore size of 0.22 μm (Repligen, Waltham, Massachusetts, USA) to retain the cells. Harvest flowrates were controlled by flowmeters (LFS-03SU-Z-SC1-G25, Levitronix, Zurich, Switzerland) after each ATF10 (Repligen, Waltham, Massachusetts, USA) and addition of fresh media was controlled with gravimetric addition to maintain the weight of the bioreactor constant.

2.4 Inclined gravity settler lab-scale design and scale-up

Good separation efficiency of the settling device is a prerequisite for bleed recycling applications. Depending on the inlet flow rate the settler is designed for, the optimal settler size must be defined in order to reduce the residence time as much as possible whilst keeping high separation efficiencies. The inclined gravity settlers (Figure A.30B and D) were designed and scaled up based on the PNK (Ponder, Nakamura and Kuroda) theory. The design-acceptance criteria were chosen based on the theory-related suggestions (see Supporting Information). Settler dimensions and design parameter are summarized in Table A.15. The constructional drawings for the lab-scale and the large-scale settler can be found in the Supporting Information section (Figure A.38 and A.39)

2.5 Continuous bleed recycling and control strategy for 2 L perfusion process

Bleed recycling was realized by connecting the bleed stream coming from the bioreactor to the settler inlet, coupling the waste outlet of the settler to a waste container and returning the recycle stream to the bioreactor (Figure A.30A). To operate a bleed recycling device at a defined recycle rate, two Ismatec Reglo ICC peristaltic pumps were required to control the three flows (Ismatec SA, Barrington, USA). The first pump was placed between bioreactor and settler inlet (process bleed pump) and

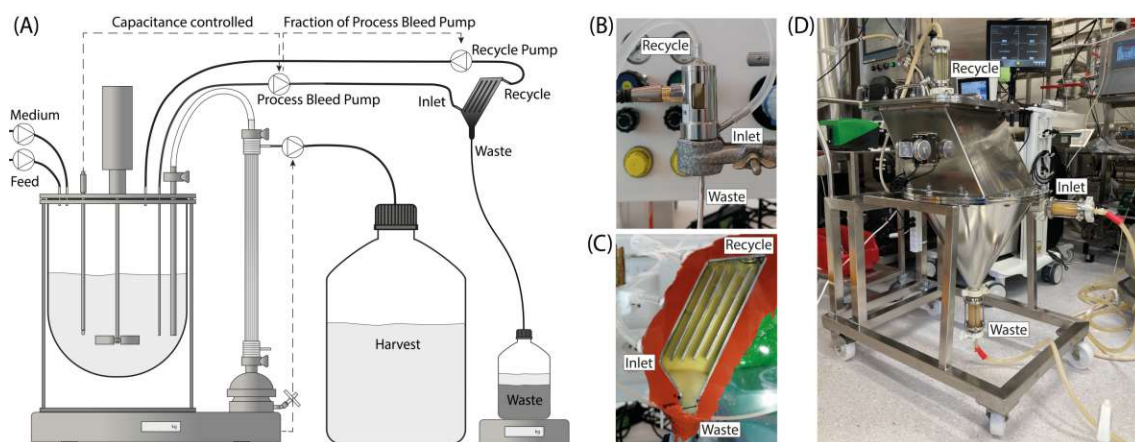


Figure A.30: Schematic representation of the bleed recycling setup (A), lab-scale acoustic settler (B), lab-scale inclined gravity settler (C) and large-scale inclined gravity settler (D).

Table A.15: Separator and settler specifications used to concentrate the bleed stream. *Residence time was calculated using inlet flow rates of 0.5 L day^{-1} for lab-scale operation and 500 L day^{-1} for large-scale operation.

Parameter	Acoustic Separator (Lab-Scale)	Inclined Gravity Settler (Lab-scale)	Inclined Gravity Settler (Large-scale)
Number of channels	-	5	40
Plate length (cm)	-	6.8	30
Plate width (cm)	-	1.0	29.7
Distance between two plates (cm)	-	0.5	0.5
Horizontal settling area (cm^2)	-	17.0	17820
Settler inner volume (L)	0.7×10^{-3}	24×10^{-3}	30.4
Fluid clarification rate (mL s^{-1})	11.6×10^{-3}	4.8×10^{-3}	4.6
Estimated settler residence time (h) *	0.03	1.15	1.46

was controlled by a capacitance-based feedback-loop to regulate the process bleed stream. The second pump (recycle pump) was placed in the recycle loop, whereas the third flow was defined by the flow difference going into the waste container. The bleed rate in this setup was based on the capacitance signal. As a result, the control system had to account for fluctuations and automatically adapt waste and clarified stream flows to maintain a defined settler recycle rate. Therefore, the recycle pump was operated at a fraction of the process bleed pump. Given a certain recycle rate setpoint, the recycle pump speed was recalculated every 15 s by the bioreactor control system based on the process bleed pump speed.

2.6 Offline performance evaluation for inclined gravity settler and acoustic separator

Performance of the in-house developed inclined gravity settler (Figure A.30B) was compared in an offline setup to a commercially available acoustic cell separator BioSep 1 L with Mini BioSep Controller (Applikon Biotechnology, Delft, Netherlands) (Figure A.30C). Acoustic separation was driven by a control unit with power output 0.7 W, 3 min run time and 3 s stop time. Settler feed streams of both devices and the recycle stream of the inclined gravity settler were operated by Ismatec Reglo ICC peristaltic pumps (Ismatec SA, Barrington, USA). The recycle stream of the acoustic separator was operated by a MasterFlex L/S pump with model 07514-10 pump head (MasterFlex, Dinkelscherben, Germany). Both bleed recycling devices were fed from a common stirred vessel to ensure identical starting conditions. The entire experimental setup is illustrated in the Supporting Information (Figure A.40). Various inlet VCV ranging from 4% to 35% were loaded to the settlers by hourly sampling a steady-state 2 L perfusion bioreactor at 12% VCV and adjusting the VCV either by diluting with harvest or concentrating by centrifugation (800 g, 1 min) using a centrifuge 5810 R (Eppendorf SE, Hamburg, Germany). Cells were gently stirred during the loading to the bleed recycling devices to avoid sedimentation or aggregation using the IKA RET basic C magnetic stirrer (IKA Werke GmbH & Co. KG, Staufen im Breisgau, Germany). Experiments were performed at a stable inlet flow rate of 0.5 L day⁻¹, simulating 2 L perfusion process at 1.3 RV day⁻¹ with approximately 20% bleed rate. The duration of each experiment was over 6 h to ensure a stable operation was achieved within the devices, after which all the settler streams (inlet, waste and recycle stream) were sampled for evaluation of settling performance, cell parameters, nutrients and metabolites, debris removal and product quality. For high debris experiments, sonication of cell culture was performed using a Branson sonifier 250 (Branson Ultrasonics, Brookfield, US) with a tapered microtip at maximum power output over 30 min prior to loading to the bleed recycling devices.

2.7 Large-scale inclined gravity settler operation

For performance evaluation, the inclined gravity settler (Figure A.30D) was connected to the 200 L bioreactor. A pump with a flowmeter (LFS-03SU-Z-SC1-G25, Levitronix, Zurich, Switzerland) was used to control inlet flowrate into the gravity settler. A calibrated pump (Serie 520 U, Watson-Marlow, Pendennis Court, Falmouth Business Park, Falmouth TR11 4SZ, United Kingdom) was placed on the

bottom outlet of the gravity settler, to ensure no return of the concentrated cells back into the settler. Outlet flow at the top was monitored by a second flowmeter (LFS-03SU-Z-SC1-G25, Levitronix, Zurich, Switzerland). Performance of the large-scale gravity settler was evaluated by loading the 200 L culture volume to the inclined gravity settler at a speed matching an operation at 2,000 L bioreactor filling volume at 1.3 vvd perfusion rate with bleed rates of 18% (470 L day⁻¹), 23% (600 L day⁻¹) and 28% (730 L day⁻¹). At the same time, settler recycle rates of 75% were targeted. For at-scale evaluation, the inclined gravity settler was connected on the bleed line of the 2,000 L bioreactor with a filling volume of 1,500 L in the control state. The inlet flow (process bleed stream) was regulated by the capacitance probe. Clarified recycle (top of gravity settler) and concentrated waste (bottom of the device) were connected to two separated tanks. As another control system than for the 2 L perfusion run was present, the control strategy had to be changed. Instead of adapting the flow rates based on the process bleed stream, a fixed pump speed of the concentrated waste on the settler was set to reach a recycle rate of roughly 70%. Based on an average process bleed of 430 L day⁻¹, the concentrated bleed pump was set to 130 L day⁻¹. To stabilize the process bleed stream, an upper limit for the process bleed flow was set to 450 L day⁻¹.

2.8 Analytical methods

Cell density, viability, cell diameter, glucose, lactate, ammonia, and pH were measured using a BioProfile FLEX2 (Nova Biomedical, Waltham, USA) for lab-scale experiments. Lab-scale 2L bioreactors were automatically sampled by the FLEX2 On-Line Autosampler (Nova Biomedical, Waltham, USA) and samples were fractionated using a Teledyne Cetac ASX-7200 (Teledyne CETAC Technologies, Omaha, Nebraska, USA). For large-scale experiments, cell parameters were analysed using a Vi-CELL XR analyzer (Beckman Coulter, Brea, California, USA) and metabolites using a Vi-CELL MetaFLEX™ bioanalyte analyzer (Beckman Coulter, Brea, California, USA). VCV was calculated as follows [27]:

$$\text{VCV} = \frac{\frac{4}{3} \cdot \pi \cdot \left(\frac{D}{2}\right)^3 \cdot \text{VCD}}{V} \cdot 100 \quad (\text{A.12})$$

where D is the average cell diameter, VCD the viable cell density, and V is the cell culture volume, assuming a spherical shape of the cells.

Separation efficiency (SE) for bleed recycling devices was calculated using formula A.13, where VCV_R corresponds to the viable cell volume of the recycle stream

and VCV_{In} to the viable cell volume of the inlet stream.

$$SE = 1 - \frac{VCV_R}{VCV_{In}} \quad (\text{A.13})$$

Process titers were determined using a protein affinity high performance liquid chromatography device (PA-HPLC, Waters, Milford, Massachusetts, USA).

Protein glycosylation was quantified through a multi attribute method (MAM) which is based on high performance liquid chromatography-mass spectrometry (LC-MS, Vanquish™ Horizon UHPLC System and Q Exactive™ Plus, Thermo Fisher Scientific, Waltham, Massachusetts, USA).

Optical Density OD_{600} was measured in cell culture supernatant after centrifugation for 10 min at 3,200 g using the UV-Vis spectrometer Genesys 10 Bio (Thermo Fisher Scientific, Waltham, Massachusetts, USA). For debris particle counting, the fluid imaging device FlowCam (Fluid Imaging Technologies Inc., Scarborough, Maine, USA) with Olympus UPLFLN 10X objective (Olympus, Shinjuku, Japan) was used to quantify particles with diameter $> 1 \mu m$. The samples were diluted 1:10 in deionized water and loaded to the flow camera at a flow rate of 0.15 mL min^{-1} and 15 frames s^{-1} without any size filter applied, resulting in an estimated capture efficiency of 20%.

3 Results and Discussion

3.1 Offline performance evaluation of inclined gravity settler and acoustic separator

Bleed recycling on a perfusion bioreactor splits the bleed stream into a concentrated waste stream and a clarified recycle stream that is recirculated back to the bioreactor (Figure A.30A). As inclined gravity settling as technology for bleed recycling has never been used before, a comparison to a previously applied technology such as acoustic separation [9] in term of performance was necessary. During bleed recycling, the fluid in the process bleed and recirculation loop (before and after concentration) is not in a controlled environment (pH, DO, Temperature). Therefore, it was important to understand if the increased residence time of the inclined gravity settler compared to acoustic separation would impact the cell culture or some of the product quality attributes.

As cell culture fluids from different perfusion runs and different process times

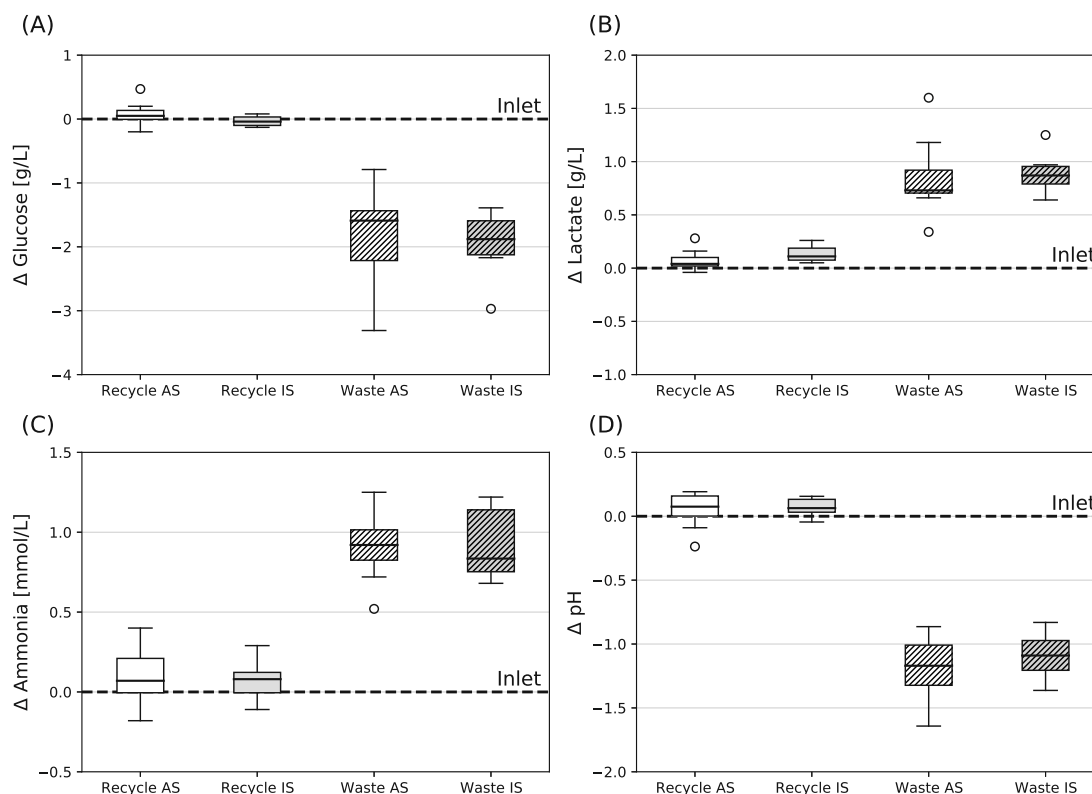


Figure A.31: Difference in glucose (A), lactate (B), ammonia (C) and pH (D) of the inlet stream into the settler (dashed zero line) compared the respective recycle and waste stream for acoustic separator (AS) and inclined gravity settler (IS) ($n = 8$).

were used for settling experiments coming from a sampled steady-state perfusion bioreactor, inlet concentrations of analytes varied depending on the sampling day. On a specific day however, exactly the same culture was used to assess both acoustic separation and inclined gravity settling as described in the Supporting Information (Figure A.40). Therefore, the data was normalized with respect to the inlet concentrations and Figure A.31 shows the difference of the waste and clarified stream compared to the respective inlet stream. Recycle stream concentrations for the acoustic separator and the inclined gravity settler were comparable to the inlet concentrations for glucose (Figure A.31A), lactate (Figure A.31B) and ammonia (Figure A.31C). Furthermore, there was no detectable shift in pH (Figure A.31D). Despite significant changes in the composition of the waste stream, there was no impact on the recycle stream for either settler type. Product glycosylation from samples of the inlet stream were compared to glycosylation measurements of clarified recycle stream samples. No significant changes in product quality between the inlet stream and the recycle stream for both the acoustic separator and the inclined gravity settler were detected, indicating that the increased residence time of the culture in the

inclined settler had no impact on clarified harvest composition as well as on product quality (Figure A.32).

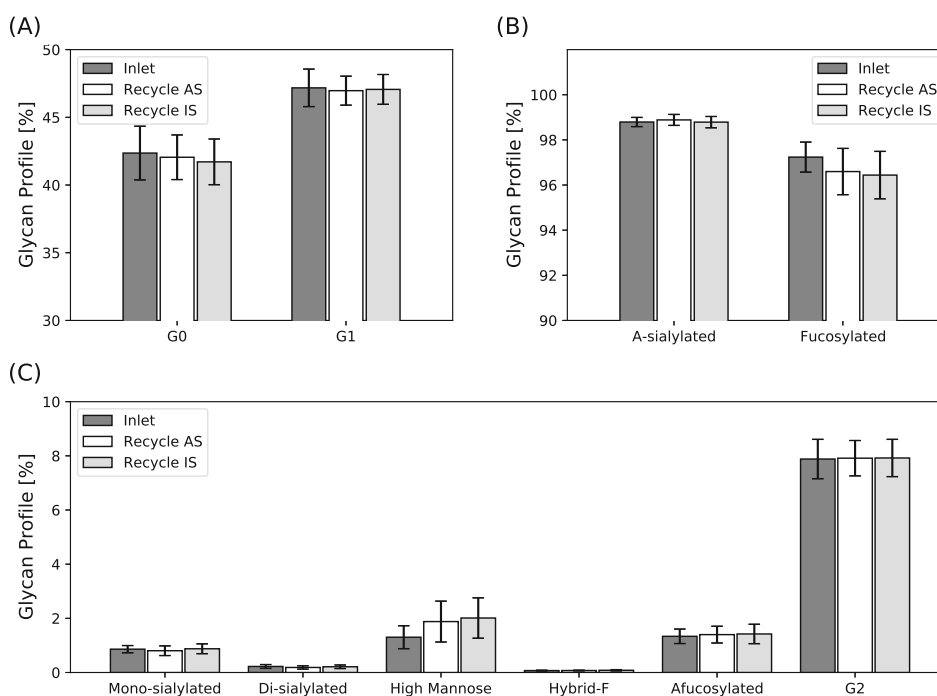


Figure A.32: Glycan forms of antibodies in the recycle stream of the acoustic settler (AS) and inclined gravity settler (IS) compared to the inlet stream for the offline experiment ($n = 14$).

Cell debris as a concern for cell retention device clogging or cause for product sieving is desired to keep at low levels during the production process [25,28]. In a standard perfusion process, a fraction of the cell debris is constantly removed via the process bleed together with excess cells and harvest. When using a bleed recycling device, the waste bleed stream is significantly reduced and a large fraction of clarified harvest is returned to the bioreactor. Therefore, offline experiments were designed to investigate the particle clearance capacity of the acoustic separator and the inclined gravity settler.

Optical density measurements (OD_{600}) were used to quantify the smallest particles that were remaining in the liquid phase after sample centrifugation. These optical density measurements resulted in a slightly higher debris measurements for the inclined gravity settler compared to acoustic separation (Figure A.33A). Particle counts based on picture analysis with a minimal particle detection size of $1 \mu\text{m}$ in the clarified harvest streams confirmed that the acoustic settler favours particle removal compared to the inclined gravity settler. A clear deviation from the

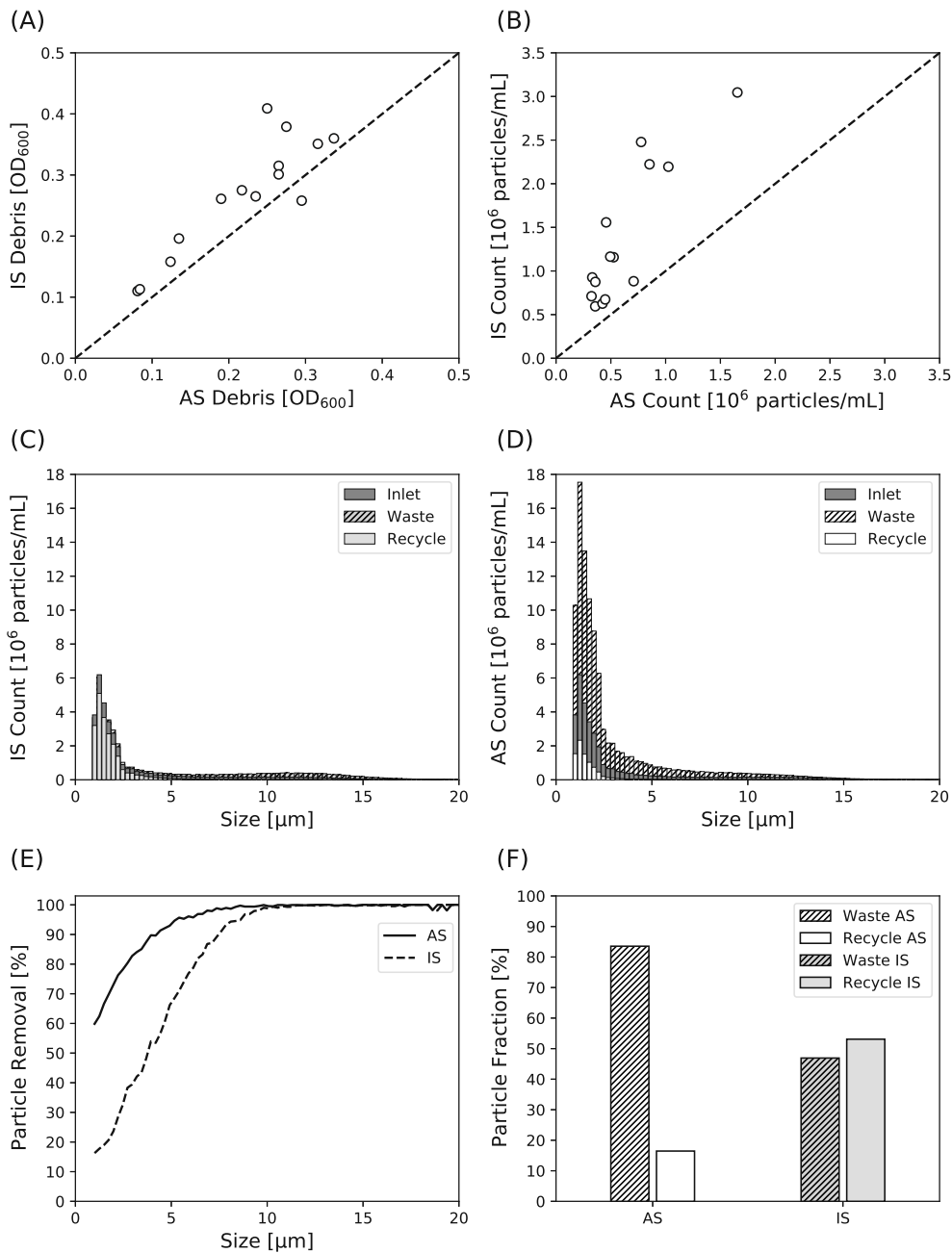


Figure A.33: Offline debris investigation of recycle streams using the UV-Vis spectrometer (A) and the fluid imaging device FlowCam (B). Layered histogram of intensified debris experiment showing the debris size distribution for the lab-scale inclined gravity settler (C) and the lab-scale acoustic settler (D), particle removal rate for specific debris size (E) and the calculated effectively returned particle amount considering a recycle rate of 80% irrespectively of their size (F). Acoustic settler (AS), Inclined Gravity Settler (IS).

dashed similarity line towards the inclined gravity settler further demonstrates that the inclined gravity settler leads to a higher residual particle concentration when using identical inlet streams (Figure A.33B). For a more detailed investigation of the difference between the acoustic and the inclined gravity settler, a concentrated high debris suspension was created by sonication of cell culture samples and inserted into both settling devices. Particle counts resolved to particle size are shown for the inclined gravity settler (Figure A.33C) and the acoustic settler (Figure A.33D). Identical inlet particle distribution resulted in much higher debris concentrations in the waste stream of the acoustic settler compared to the inclined gravity settler, consequently leading to reduced residual particle counts in the clarified recycle stream. Calculating the removal efficiency according to the particle size (Figure A.33E) reveals that both settler types completely remove particles larger than $10\ \mu\text{m}$, while separation efficiency drops for smaller particles. Whilst the acoustic settler still removed more than 60% of the smallest measured particles of $1\ \mu\text{m}$, the inclined gravity settler performed worse for smaller sized particle removal. Calculating the effectively removed particle fraction with a recycle rate of 80% (Figure A.33F), the acoustic settler removed roughly 84% of the particles, whereas the inclined gravity settler removed 47% of the particles for this particular debris enhanced scenario. Altogether, both settlers removed larger particles efficiently, but lost efficiency for smaller particles. Wang et al. [26] demonstrated that debris in the size of 20 – 200 nm can contribute to product retention and membrane plugging with similar range pore size. As the acoustic wave separator was predominantly better at removing larger particles with only slightly higher removal of submicron particles, it is questionable whether a clear benefit to avoid product retention for acoustic separation would be observable.

To balance additional operational complexity with benefits of increased process yield, many parameters such as process VCV setpoint, process bleed rate and settler recycle rate must be considered. VCV as a key parameter for bleed recycling is defined by the VCD count and the average cell diameter (Figure A.34A). The grey point represents an example simulating a process bleed of approximately 20% ($0.5\ \text{L}\ \text{day}^{-1}$ for $2\ \text{L}$ perfusion at $1.3\ \text{RV}\ \text{day}^{-1}$) for the utilized cell line producing mAb1. In order to maximize the process yield increase with a bleed recycling system, it is beneficial to operate the settling systems at higher recycle rates. However, operation at too high recycle rates can lead to accumulation of cells within the settling device due to limitations in compacting cells being removed with the smaller remaining waste stream.

The acoustic separator and the inclined gravity settler were therefore evaluated

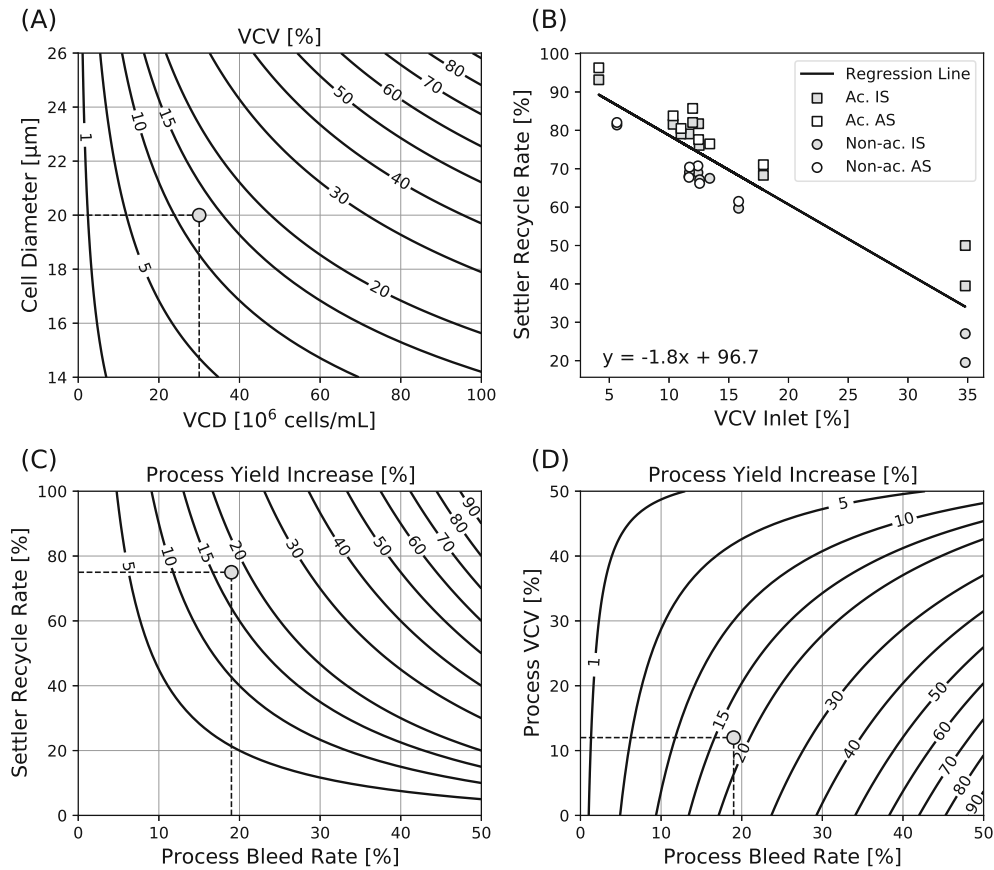


Figure A.34: Bleed recycling efficiency data and performance calculations. VCV contour plot showing the relationship of VCD and average cell diameter for VCV (A). Experimental data to evaluate optimal recycle rates by accumulating and non-accumulating settler experiments (B). The straight line represents an expected accumulation limit based on linear regression of all data points. Process yield increase contour plot relating process bleed rate to settler recycle rate (C) or process VCV setpoint (D) assuming optimal settler recycle rate as evaluated by the regression line in (B). The points in (A), (C) and (D) serve as an example for a process bleed of approximately 20% with the specified VCV of roughly 12%. Acoustic settler (AS), Inclined Gravity Settler (IS).

at non-accumulating conditions and accumulating conditions with a bleed of roughly 20% to approximate the optimal operation conditions of each settling device. Inlet VCV values were chosen from 4% to 35%, covering a wide range of process set-points (Figure A.34B). As no significant difference between the two bleed recycling technologies was detected, the optimal operation conditions were calculated by combining both data sets and performing a linear regression. Despite favoured debris removal, the acoustic separator did not achieve significantly higher recycle rates before entering the accumulating stage. This is a possible indication that although the cells tend to aggregate due to the acoustic waves, they do not result in a more compact cell suspension after gravity settling than with the inclined gravity settler.

To calculate potential process yield increases, not only the gained knowledge about achievable recycling rates without cell accumulation, but also process bleed rates must be considered. It was therefore assumed that bleed recycling device volumes are scaled accordingly when changing process bleed rates to maintain high separation efficiency. Having a properly scaled separation device, yield increases were plotted as contour plots with either settler recycle rate (Figure A.34C) or process VCV setpoint (Figure A.34D) versus the respective process bleed rate. These plots help to estimate potential yield increases given a particular perfusion process assuming optimal settler performances evaluated in Figure A.34B. For the example process indicated by the grey points, a potential process yield increase of 18% can be achieved. In general, the lower the process VCV setpoint and the higher the process bleed rate, the higher the yield increase can be expected.

In brief, the offline investigation to compare acoustic separation to inclined gravity settling showed no difference in nutrients, metabolites, product quality and settler efficiency. The acoustic separation results are in good agreement with Bielser et al. [9], demonstrating similar inlet stream and recycle stream characteristics. Despite the larger settler volume required for inclined gravity settling resulting in increased settler residence time (Table A.15), no difference to acoustic separation was detected in this study. Acoustic waves seem therefore to facilitate cell aggregation and accelerate the settling process, which allows a reduction in the volume of the settling chambers, and subsequently reduced residence time within the separation chamber. But acoustic waves do not lead to higher compaction of the cell biomass in the waste stream, as similar performances were obtained with both technologies. Solely for debris removal, acoustic settling showed superior performance compared to inclined gravity settling. Due to the experimental data demonstrating that the increased residence time within the inclined settler compared to the acoustic separator had no impact on bleed recycling performance, culture parameters and product quality attributes, and for reasons of lower system complexity and simplified scale-up, all further experiments were conducted using inclined gravity settling.

3.2 Bleed Recycling in Lab-scale Perfusion Cultivation

A long-term steady-state perfusion run at 2 L scale was performed with a gravity settler connected to the process bleed stream to demonstrate improved process performance and operability over prolonged time. The inclined gravity settler was started on day 9 with a secure recycle rate of 50%, immediately increasing the process harvest rate from roughly to 90% compared to 72% in the control run (Figure A.35E). During 17 days of inclined settler operation, the recycle rate was stepwise

increase up to 66% without accumulation within the settler (Figure A.35C), keeping the harvest rate (on average 92%) significantly above the harvest rate of the control run (on average 77%) as demonstrated by the blue area in Figure A.35E. The process bleed decreased from initially 30% down to 20%, which is related to slower cell division rates. With an average bleed rate of 23% and an average settler recycle rate of 56% during these 17 days, a process yield increase of about 16% was predicted by Figure A.34C. It has to be mentioned that all predictions are based on the assumption that the harvest titer remains unchanged, and the process yield increase is solely increased due to higher harvest volumes.

Experimental result showed good agreement with an accumulated harvest volume increase of 19% by bleed recycling (Figure A.35G). As process yield can not only be increased by increased harvest volume, but also by increasing harvest titers, the actual process yield increase during this bleed recycling period was higher. Harvest titer was slightly increased in the bleed recycling run leading to a process yield increase of 24% rather than the 19% coming from increased harvest volume (Figure A.35H). The reason for the titer increase cannot be explained by the presented data as bleed recycling should have no impact on harvest titer. Despite a slight titer increase and an increase of debris (Figure A.35F), all other process parameters such as VCV and viability (Figure A.35A), glucose and lactate (Figure A.35B), ammonia and pH (Figure A.35D) and product quality (Figure A.36) were comparable to the control run. This is in agreement with previous results from the offline screening, where no significant difference between settler inlet and return could be identified in terms of nutrients and metabolites (Figure A.31), as well as for product quality (Figure A.32). Further, the inclined gravity settlers showed reduced removal efficiency for smaller particles (Figure A.33), subsequently accumulating within the bioreactor when operated for prolonged time. The experienced levels of debris did however not cause any problems with the cell retention device as harvest titers was not impacted compared to the control and showed even slightly higher concentrations.

Bleed recycling was stopped between day 26 – 34, leading to a decrease in cell debris. This debris reduction can be explained by the fact that once bleed recycling is stopped, all debris in the bleed stream goes to the waste as no bleed is recycled anymore. The settler was restarted on day 34 to confirm accumulating conditions predicted by the regression line (Figure A.34B). At 12% biomass an accumulating recycle rate of approximately 75% was predicted. Therefore, the recycle rate was increased step by step (Figure A.35C), until it reached accumulating conditions at 75% on day 38, confirming the expected performance. An average bleed rate of 21% was observed in the control run during this second period of bleed recycling. A

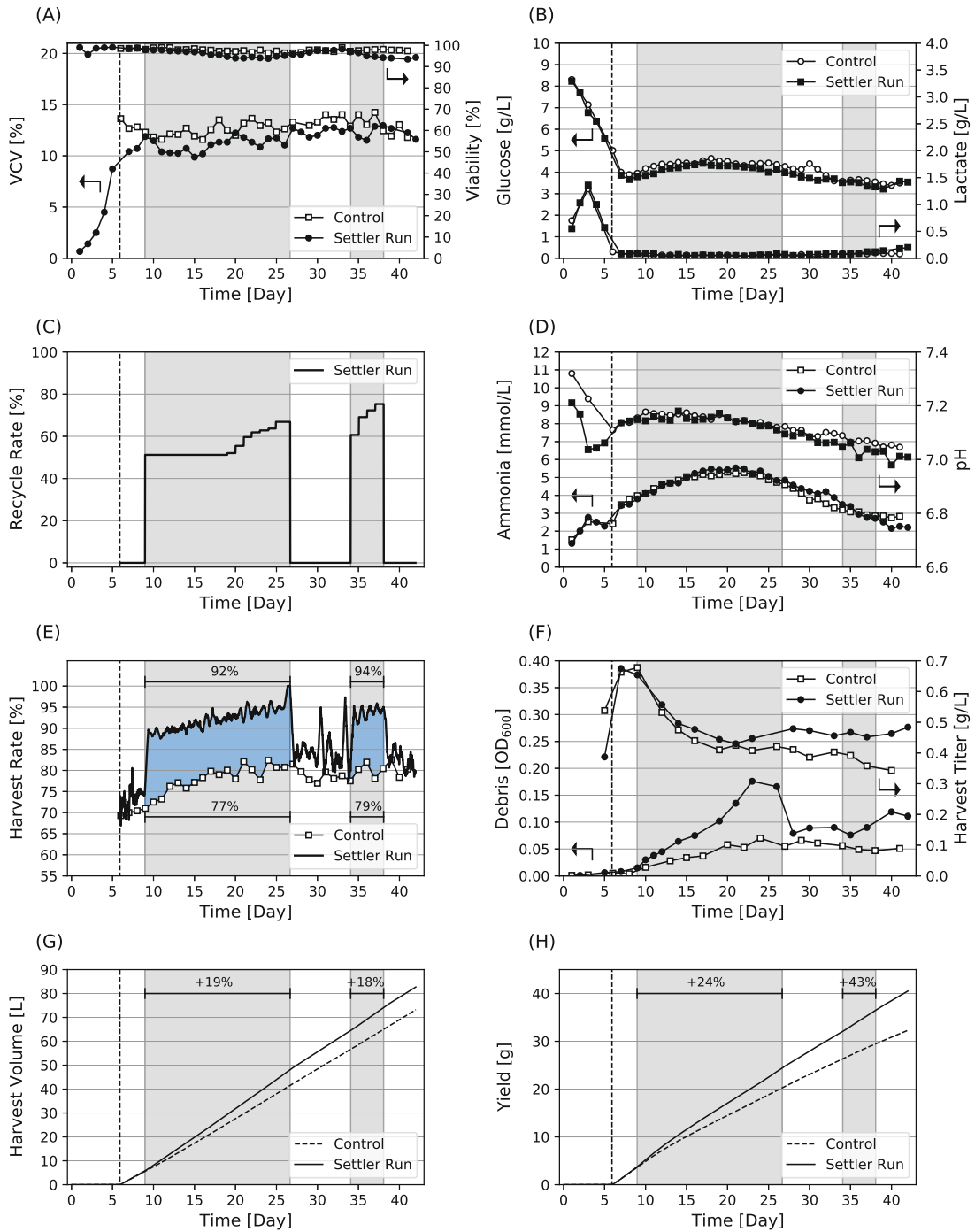


Figure A.35: Process data of lab-scale 2 L perfusion settler run compared with a standard control run without bleed recycling for mAb1. VCV and viability (A), glucose and lactate concentration (B), theoretical recycle rate setpoint (C), ammonia and pH profile (D), process harvest rate (E), harvest titer and debris trend (F), cumulative harvest volume (G) and cumulative process yield (H). Grey areas represent process phases where bleed recycling was performed, whereas bleed recycling was turned off during white process phases.

significant bleed rate reduction down to an average of 6% was achieved by applying an average settler recycle rate of 69%, leading to a predicted 18% process yield increase (Figure A.34C). This matched the experimentally determined 18% harvest volume increase (Figure A.35G) assuming no change in harvest titer. As harvest titer difference to the control got larger with proceeding run time, the product yield increase for the second bleed recycling phase increased even by 43% (Figure A.35H). The discrepancy in harvest titer cannot be explained by the presented data as all other process parameters were comparable to the control run and should not be overrated. Important is the fact that the harvest volume could significantly be increased during both bleed recycling phases without impacting the cell culture (Figure A.35) and product quality (Figure A.36), which is doubtlessly attributable to bleed recycling.

Overall, bleed recycling was successfully applied to a steady-state perfusion bioreactor run of 42 days and confirmed recycle rate and yield improvement estimation based on harvest volume increase. The automation setup around the settler enabled seamless operation. No operator intervention was necessary, the settler waste and clarified streams were self-adjusting to the process bleed fluctuations. Additionally, to a previous bleed recycling proof of concept study performed with very high bleed rate and relatively low VCV setpoint of 5%, a best-case scenario for a proof-of-concept [9], this data shows that bleed recycling can be applied to more industrially relevant viable cell volumes above 10% and for extended periods.

3.3 Bleed recycling scale-up for 2,000 L perfusion processes

The large-scale inclined gravity settler was designed to manage bleed recycling at a volumetric flow rate of 500 L day⁻¹ (Table A.15). This would correspond to a 2,000 L perfusion process with a perfusion rate of 1.3 RV day⁻¹ with roughly 20% of it as bleed rate. The evaluation was started with a process bleed rate of 18% (470 L day⁻¹), slightly below the foreseen maximal capacity of the inclined gravity settler. Recycle rates between 58% and 75% resulted, in the setup that was used, in an almost cell free recycle streams (Figure A.37A) with separation efficiencies above 97% (Figure A.37B). Subsequently, the process bleed rate was increased to 23% (600 L day⁻¹) and 28% (730 L day⁻¹), keeping high recycle rates of 76% and 75%, respectively. These process bleed rates were above the foreseen settler capacity and the separation efficiency decreased to 94% and 87%. Cell viabilities in the recycle stream however were not impacted. It is acceptable that the separation efficiency is not close to 100% as long as the process is not negatively impacted. Potentially, cells traveling through the bleed recycling loop could suffer from the absence of pH

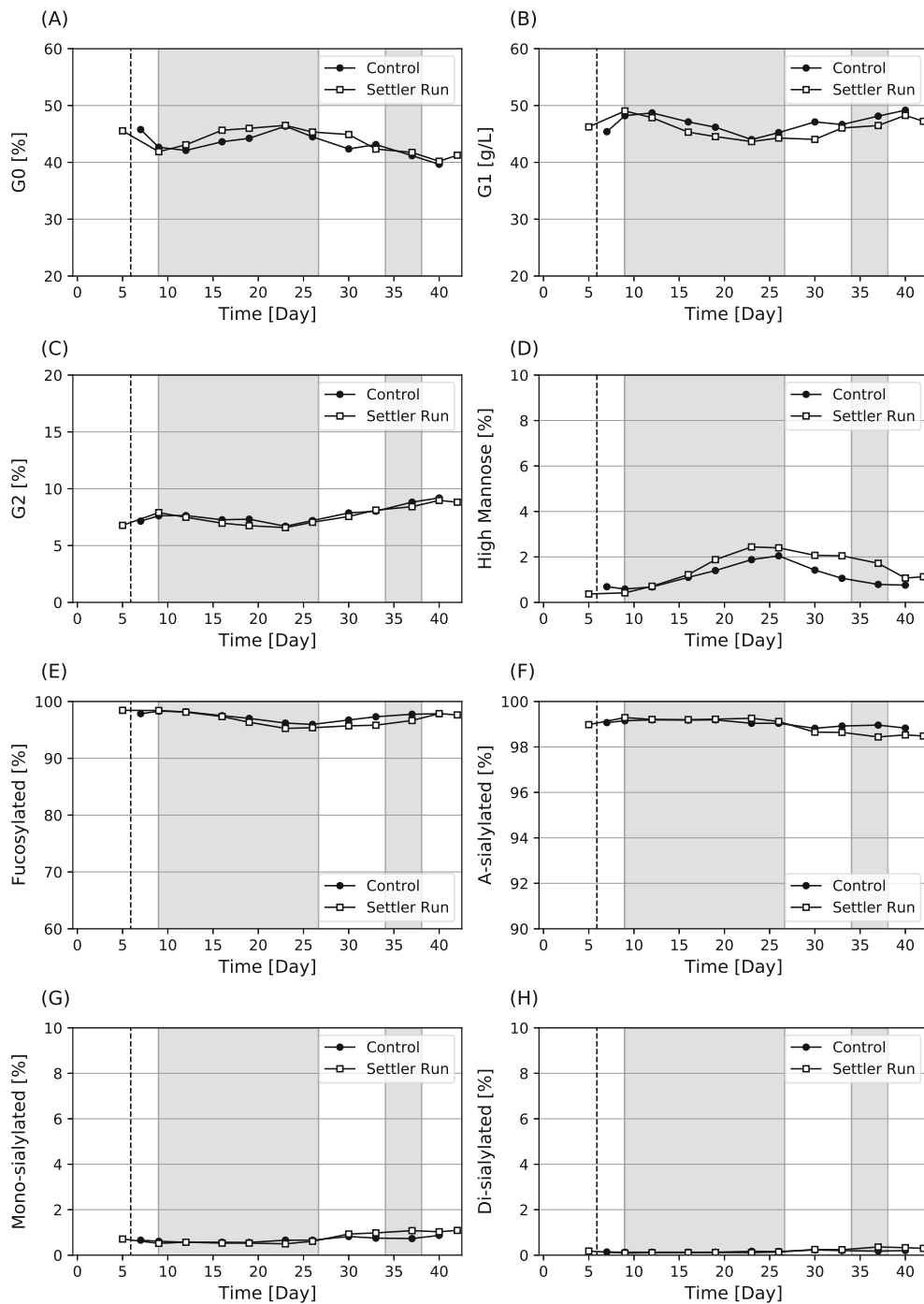


Figure A.36: CQA trends of lab-scale 2 L perfusion settler run compared with a standard control run without bleed recycling for mAb1. Galactosylation G0 (A), galactosylation G1 (B), galactosylation G2 (C), high-mannose (D), fucosylation (E), a-sialylation (F), mono-sialylation (G), and di-sialylation (H). Grey areas represent process phases where bleed recycling was performed, whereas bleed recycling was turned off during white process phases.

and pO_2 control. The high viability measured in the recycle stream gives confidence that the cells were not suffering from this (Figure A.37C). To avoid the presence of cells in the recycle stream at higher process bleed rates, the settler size should be increased respectively. Given a production process with a bioreactor volume of 2,000 L, 1.3 RV day^{-1} perfusion rate, a recycle rate of 75% and a process bleed rate of 18 – 28%, this experiment showed that a yield increase of 17 – 28% can be achieved with the large-scale inclined gravity settler (Figure A.37D). No significant changes in product quality were detected and data is summarized in the Supporting Information section (Table A.16). Previously, inclined gravity settlers were used as cell retention devices in mammalian cell culture [20,21]. The main goal of this application is to retain cells within the bioreactor and keep high cell viability at the same time. Cells are ideally relatively quickly returned to the bioreactor after entering the uncontrolled environment within the inclined gravity settler to avoid negative impact on culture viability. This is usually achieved with rather high inlet and return (return stream on the bottom of inclined gravity settler containing cells) compared to the clarified harvest stream (on top of the inclined gravity settler). Here, it has been demonstrated that large-scale inclined gravity settlers can also be used as bleed recycling devices, enabling selective bleed operation. By operating the waste stream (on the bottom of the inclined gravity settler) at a relatively low flow compared to the inlet and recycle stream (clarified stream on top of the inclined gravity settler), it has been possible to concentrate biomass without impacting the recycle stream to the bioreactor (clarified stream on top of the inclined gravity settler).

The settler was then connected to a 2,000 L perfusion bioreactor (filling volume of 1,500 L) with fluctuating process bleed controlled by the capacitance signal and processed an average bleed of 430 L day^{-1} . The inclined gravity settler achieved an overall recycle rate of 70% and showed high separation efficiency of $> 99\%$ throughout the entire operation time (Figure A.37E). There was no quality drift detected from the start of the operation until the end of the operation (Supporting Information Table A.17). Even though operation lasted only for approximately 15 h, the operating times corresponds to roughly ten times the calculated residence time in the large-scale inclined gravity settler (Table A.15). Proof of concept for large-scale bleed recycling could therefore be demonstrated. To optimize the efficiency, an adaptive control strategy could be implemented as described for the 2 L perfusion system. This would reduce the concentrated bleed stream once the inlet stream decreases, which would ultimately lead to improved overall recycle rates.

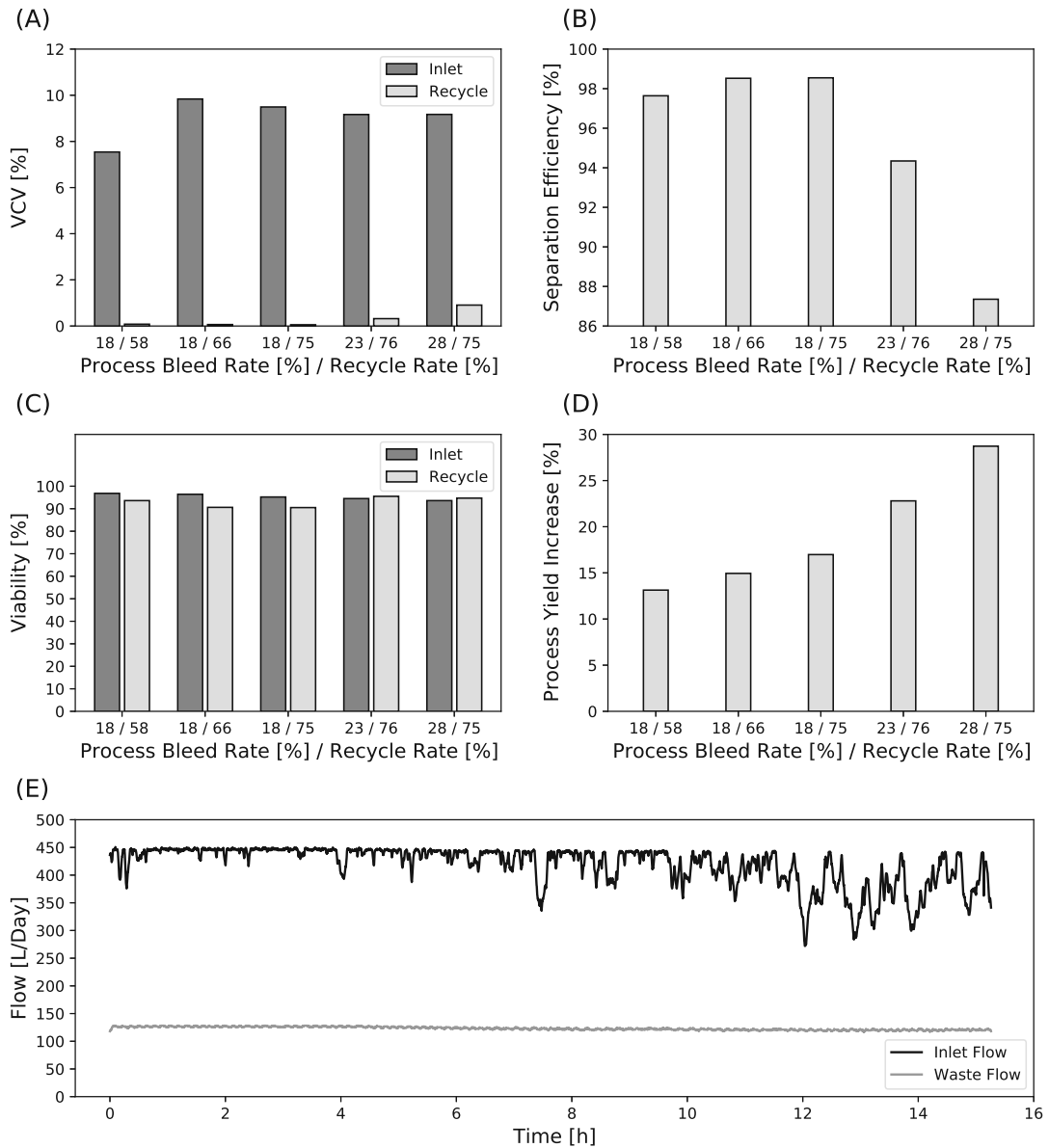


Figure A.37: Offline large-scale 2,000 L perfusion process settler evaluation for various process bleed rates and recycle rates showing VCV of inlet and recycle streams (A), separation efficiency (B), cell viabilities (C) and process yield increase (D). Inline, real-time data of flow rates of inclined gravity settler connected to the 2,000 L perfusion run (E).

4 Conclusion and Outlook

This study for the first time used inclined gravity settling for bleed recycling applications in steady-state perfusion processes and compared it to the previously used acoustic separation technology. In lab-scale experiments, acoustic separation and inclined gravity settling showed similar bleed recycling efficiency and had no impact on nutrients, metabolites as well as on product quality. Solely for cell debris removal,

the acoustic settler showed superior performance in removing smaller particles.

For reasons of simplified scale-up and reduced system complexity, inclined gravity settling was the chosen technology for long-term steady state perfusion bleed recycling. It was tested at lab-scale during a 42-day perfusion cell culture and was then scaled-up for a 2,000 L perfusion process. An adaptive automation strategy was developed and tested to successfully operate the settling device at optimal setpoints despite fluctuations in process bleed rates.

For a perfusion process at lab-scale with a VCV setpoint of 12% and a bleed rate between 20% and 25%, the waste stream could be reduced by up to 3.5 times down to 6% effective bleed rate, resulting in a harvest rate increase of 19%. The large-scale inclined gravity settler connected to a 2,000 L perfusion bioreactor with a filling volume of 1,500 L was able to process an average bleed stream of 430 L day⁻¹ with a recycle rate of 70%, constantly maintaining a separation efficiency of higher than 99%. Even higher bleed streams of 600 L day⁻¹ were successfully concentrated with separation efficiencies above 94%, representing a perfusion run with 2,000 L filling volume and 23% bleed rate. To the authors knowledge, this is the first time bleed-recycling has been performed at manufacturing scale using an inclined gravity settler. No impact on product quality was observed at both scales. The insights gained on bleed recycling builds the basis of a rational support in decision making when considering this technology to improve process yield for an existing or new perfusion process with specific target process VCV, perfusion rate and process bleed rate. Similarly, this knowledge could be applied to other emerging technologies for bleed recycling such as continuous centrifuges, once they are available in right dimensions and allow stable operation throughout the entire runtime of a perfusion cell culture process.

Acknowledgements

The authors would like to thank Pavel Dagorov and his workshop team (FHNW) for building the lab-scale settler and designing the large-scale settler, and Miroslav Soos (UCT Prague) for support in scale-up. We also thank Paulin Tsague Nguetsop from Construction Inoxydable (Châtel-St-Denis, Switzerland) for the flexibility and enthusiasm for the collaboration on the large-scale settler construction. Marc De Poli and his team kindly assisted in large-scale cell culture evaluation. Moreover, the authors would like to acknowledge specifically the Bioprocess Sciences (BPS) team of Merck Serono SA (an affiliate of Merck KGaA) for material and analytical support and for valuable discussions and support throughout the project, especially Alexandre Chatelin and the analytical team.

Conflict of interest

The authors declare that they have no known competing financial interests or personal relationships that could have appeared to influence the work reported in this paper.

Data availability statement

Data will be made available on request.

Supporting Information

For inclined gravity settlers (IS), the otherwise low-efficient settling is enhanced by the Boycott effect [22]. As the particles (cells) settle down within the inclined channel, a higher density slurry is formed at the lower side of the channel. Driven by gravity, the slurry slips down the surface, generating a convective flow that enhances the settling process. The kinetics of this process are described by an elementary model invented by E. Ponder, N. Nakamura, and K. Kuroda [28]. The model was later confirmed using continuum mechanics equations [29]. The kinetic relationship is known as the PNK theory and describes the rate of the clarified fluid production as a product of the particle settling velocity and the horizontal projection of the channel area available for settling described by formula A.14:

$$S = v_p \cdot n \cdot w \cdot (l \cdot \sin \theta + b \cdot \cos \theta) \quad (\text{A.14})$$

where v_p is the particle settling velocity, n is the number of channels in the IS, w is the width of the settler, l is the length of lamellae, b is the distance between 2 plates in orthogonal direction, and Θ is the angle of the lamellae to the vertical direction [30].

The PNK theory, however, holds only under mild flow conditions. Shen and Yanagimachi [30] suggested that formula A.14 should only be used if Reynolds number of the flow (Re_f) is within 0 – 10 and the ratio (Λ) between the Grashof number for settling (Gr_s) and Reynolds number for settling (Re_s) is within 10^4 to 10^7 . The dimensionless numbers are described by formulas A.14 - A.17:

$$Re_f = \frac{v \cdot b \cdot \rho_l}{\eta_l} \quad (\text{A.15})$$

$$Re_s = \frac{v_p \cdot h \cdot \rho_l}{\eta_l} \quad (\text{A.16})$$

$$Gr_s = \frac{h^3 \cdot g \cdot \rho_l \cdot (\rho_p - \rho_l) \cdot \phi_p}{\eta^2} \quad (\text{A.17})$$

where subscripts p and l are related to the particle and liquid, respectively, v is

settling velocity, ρ is the density, η is the viscosity, h is the characteristic settling distance (given by the relationship $b \cdot \cos \Theta$), v is the flow velocity, b is the distance between 2 plates in the orthogonal direction, and ϕ is the particle volume fraction [30].

Both the lab-scale and large-scale settler were designed in a way to fit the acceptance ranges of these criteria for at least 70% recycle rate of the respective expected bleed rate. Furthermore, a settler inner volume limit was set to be maximally 1.5-fold the volume corresponding to a 1-hour residence time. This limit was proposed to decrease the time cells spend in an uncontrolled environment of the settler in contact with the product. Different designs were then screened and the best ones of those fitting the evaluation criteria were selected for construction.

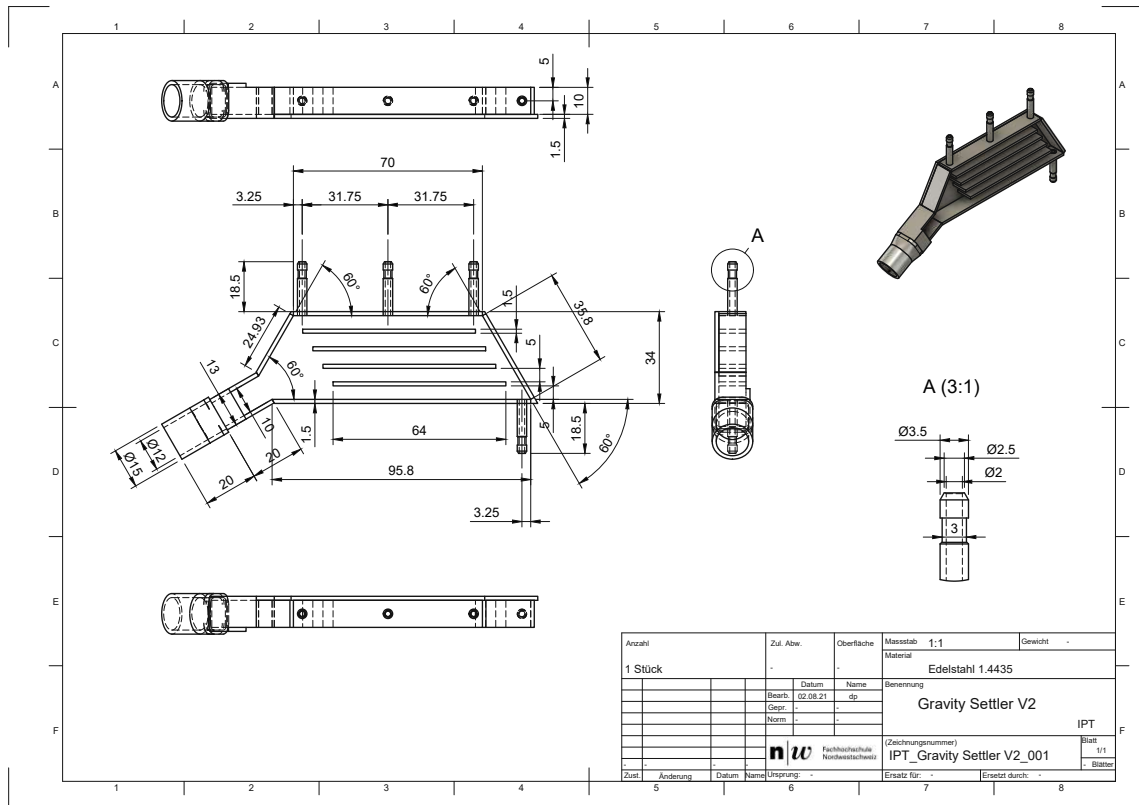


Figure A.38: Detailed drawing of the lab-scale inclined gravity settler, dimensions given in mm.

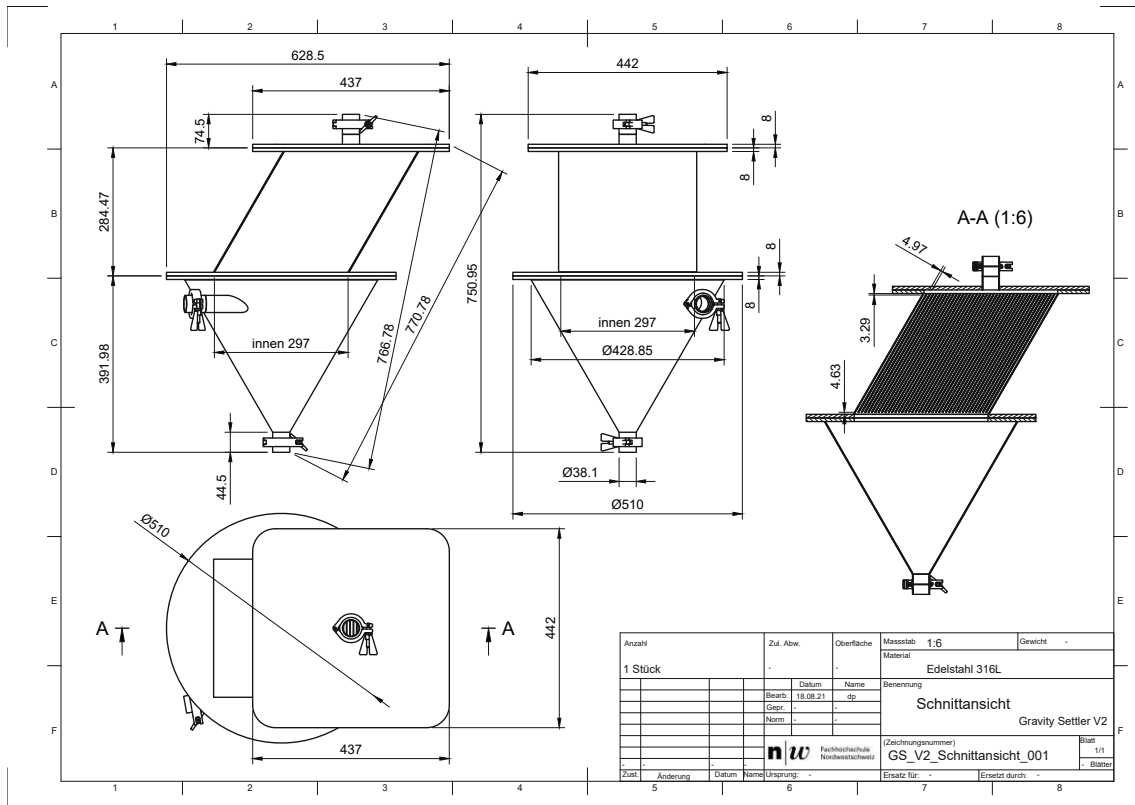


Figure A.39: Detailed drawing of the large-scale inclined gravity settler, dimensions given in mm.

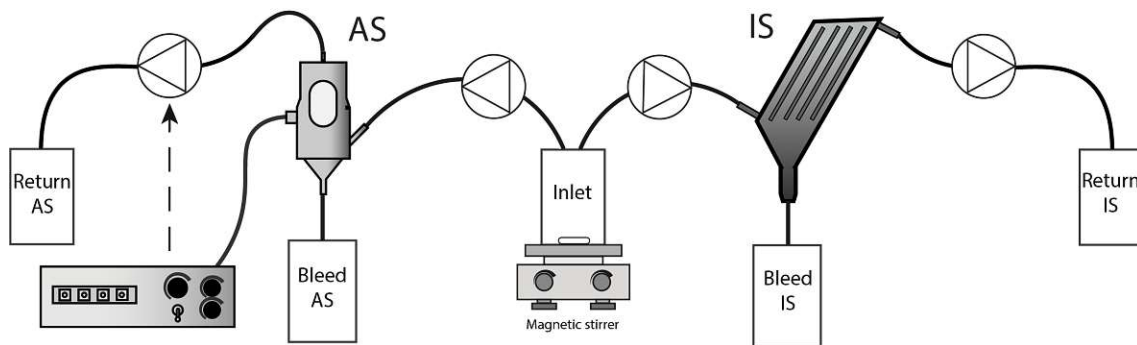


Figure A.40: Experimental offline setup of Inclined Settler (IS) and acoustic separator (AS). Both bleed recycling devices are fed from a common stirred vessel (Inlet). The return pump of the acoustic separator is turned on and off synchronously with the on and off times of the ultrasound input. The outlet streams (Bleed and Return) for both devices are collected in separate vessels for further analyses

Table A.16: Absolute CQA changes for offline large-scale settler evaluation. Absolute CQA changes were calculated by subtracting the recycle CQA from the inlet CQA. The tested mAb2 contained 3 different glycosylation sites, which were all analyzed for their glycosylation changes.

Site	Experiment (Process Bleed Rate / Recycle Rate [%])	High Mannose [%]	Total Sialylated [%]	Total NGNA [%]	Total Fucosylated [%]	G0 [%]	G1 [%]	G2 [%]
N77	18 / 58	-0.10	0.64	0.29	0.06	-0.10	-0.16	-0.31
N77	18 / 66	0.01	0.19	-0.35	0.02	-0.07	-0.01	-0.08
N77	18 / 75	0.03	-0.23	-0.45	-0.04	0.02	0.13	0.03
N77	23 / 76	-0.13	1.17	0.11	0.12	-0.12	-0.36	-0.56
N77	28 / 75	0.07	-0.31	-0.59	-0.11	0.10	0.07	0.01
N109	18 / 58	-0.01	0.03	0.04	0.00	0.00	0.00	-0.03
N109	18 / 66	0.02	0.05	-0.33	-0.01	-0.01	-0.02	-0.03
N109	18 / 75	0.03	-0.10	-0.12	-0.04	0.01	0.00	0.06
N109	23 / 76	-0.01	0.00	0.00	0.01	-0.01	-0.01	0.04
N109	28 / 75	-0.01	0.02	-0.03	0.02	-0.02	-0.02	0.05
N208	18 / 58	-0.01	0.02	0.13	0.00	0.50	-0.02	-0.38
N208	18 / 66	-0.01	-0.06	0.25	-0.03	0.06	0.22	0.38
N208	18 / 75	0.01	-0.01	0.00	0.00	-0.35	0.41	-0.18
N208	23 / 76	-0.05	0.02	0.20	-0.01	-0.42	0.31	-0.35
N208	28 / 75	0.02	0.02	-0.08	-0.01	-0.85	-0.42	0.68

Table A.17: Absolute CQA changes for inline large-scale settler evaluation. Absolute CQA changes for mAb1 were calculated by subtracting the recycle CQA from the inlet CQA.

Time [h]	A- sialylated [%]	Mono- sialylated [%]	Di- sialylated [%]	High Mannose [%]	Hybrid- F [%]	Fucosyl- ated [%]	Afucosyl- ated [%]	G0 [%]	G1 [%]	G2 [%]
0	0.11	-0.07	-0.03	-0.02	0.00	0.04	-0.01	1.08	-0.85	-0.10
15	-0.06	0.05	0.01	-0.03	-0.01	0.01	0.02	-0.05	0.09	-0.06

References

- [1] Anurag S. Rathore et al. “Continuous Processing for Production of Biopharmaceuticals”. In: *Preparative Biochemistry and Biotechnology* 45.8 (2015), pp. 836–849. ISSN: 15322297. DOI: 10.1080/10826068.2014.985834.
- [2] Sen Xu et al. “Bioreactor productivity and media cost comparison for different intensified cell culture processes”. In: *Biotechnology Progress* 33.4 (2017), pp. 867–878. ISSN: 15206033. DOI: 10.1002/btpr.2415.
- [3] Jean-Marc Bielser et al. “Perfusion mammalian cell culture for recombinant protein manufacturing – A critical review”. In: *Biotechnology Advances* 36.4 (2018), pp. 1328–1340. ISSN: 07349750. DOI: 10.1016/j.biotechadv.2018.04.011.
- [4] Jean Marc Bielser et al. “Perfusion cell culture for the production of conjugated recombinant fusion proteins reduces clipping and quality heterogeneity compared to batch-mode processes”. In: *Journal of Biotechnology* 302 (2019), pp. 26–31. ISSN: 18734863. DOI: 10.1016/j.jbiotec.2019.06.006.
- [5] Veena Warikoo et al. “Integrated continuous production of recombinant therapeutic proteins”. In: *Biotechnology and Bioengineering* 109.12 (2012), pp. 3018–3029. ISSN: 00063592. DOI: 10.1002/bit.24584.
- [6] Fabian Steinebach et al. “Design and operation of a continuous integrated monoclonal antibody production process”. In: *Biotechnology Progress* 33.5 (2017), pp. 1303–1313. ISSN: 15206033. DOI: 10.1002/btpr.2522.
- [7] Mona Bausch, Christian Schultheiss, and Jochen B. Sieck. “Recommendations for Comparison of Productivity Between Fed-Batch and Perfusion Processes”. In: *Biotechnology Journal* 14.2 (2019), pp. 4–7. ISSN: 18607314. DOI: 10.1002/biot.201700721.
- [8] Moritz K.F. Wolf et al. “Improved Performance in Mammalian Cell Perfusion Cultures by Growth Inhibition”. In: *Biotechnology Journal* 14.2 (2019), pp. 1–9. ISSN: 18607314. DOI: 10.1002/biot.201700722.
- [9] Jean Marc Bielser et al. “Continuous bleed recycling significantly increases recombinant protein production yield in perfusion cell cultures”. In: *BioPharm International* 34.10 (2021), pp. 48–51. ISSN: 19391862. DOI: 10.1016/j.bej.2021.107966.

- [10] Th Gaida et al. “Selective retention of viable cells in ultrasonic resonance field devices”. In: *Biotechnology Progress* 12.1 (1996), pp. 73–76. ISSN: 87567938. DOI: 10.1021/bp950040k.
- [11] E. Benes and F. Hager. *Separation of dispersed particles by drifting ultrasonic resonance fields*. Ultrasonics International 91, 1991. ISBN: 9780750603898. DOI: 10.1016/C2013-0-04523-9.
- [12] Thomas Ryll et al. “Performance of small-scale CHO perfusion cultures using an acoustic cell filtration device for cell retention: Characterization of separation efficiency and impact of perfusion on product quality”. In: *Biotechnology and Bioengineering* 69.4 (2000), pp. 440–449. ISSN: 0006-3592. DOI: 10.1002/1097-0290(20000820)69:4<440::AID-BIT10>3.0.CO;2-0.
- [13] Volker M. Gorenflo et al. “Characterization and optimization of acoustic filter performance by experimental design methodology”. In: *Biotechnology and Bioengineering* 90.6 (2005), pp. 746–753. ISSN: 00063592. DOI: 10.1002/bit.20476.
- [14] Irfan Z. Shirgaonkar, Stephane Lanthier, and Amine Kamen. “Acoustic cell filter: a proven cell retention technology for perfusion of animal cell cultures”. In: *Biotechnology Advances* 22.6 (2004), pp. 433–444. ISSN: 07349750. DOI: 10.1016/j.biotechadv.2004.03.003.
- [15] Volker M. Gorenflo et al. “Scale-up and optimization of an acoustic filter for 200 L/day perfusion of a CHO cell culture”. In: *Biotechnology and Bioengineering* 80.4 (2002), pp. 438–444. ISSN: 0006-3592. DOI: 10.1002/bit.10386.
- [16] Hans Cappon and Karel J. Keesman. “Design basis of industrial acoustic separators”. In: *2013 IEEE International Ultrasonics Symposium (IUS)*. IEEE, 2013, pp. 299–302. ISBN: 978-1-4673-5686-2. DOI: 10.1109/ULTSYM.2013.0077.
- [17] D. Voisard et al. “Potential of cell retention techniques for large-scale high-density perfusion culture of suspended mammalian cells”. In: *Biotechnology and Bioengineering* 82.7 (2003), pp. 751–765. ISSN: 00063592. DOI: 10.1002/bit.10629.
- [18] Brian C. Batt, Robert H. Davis, and Dhinakar S. Kompala. “Inclined Sedimentation for Selective Retention of Viable Hybridomas in a Continuous Suspension Bioreactor”. In: *Biotechnology Progress* 6.6 (1990), pp. 458–464. ISSN: 15206033. DOI: 10.1021/bp00006a600.

- [19] James Searles, Paul Todd, and Dhinakar Kompala. “Viable Cell Recycle with an Inclined Settler in the Perfusion Culture of Suspended Recombinant Chinese Hamster Ovary Cells”. In: *Biotechnology Progress* 10.2 (1994), pp. 198–206. ISSN: 8756-7938. DOI: 10.1021/bp00026a600.
- [20] Hans Jürgen Henzler. “Continuous fermentation with animal cells. Part 2. Techniques and methods of cell retention”. In: *Chemie-Ingenieur-Technik* 84.9 (2012), pp. 1482–1496. ISSN: 15222640. DOI: 10.1002/cite.201200003.
- [21] Michael Pohlscheidt et al. “Optimizing capacity utilization by large scale 3000 L perfusion in seed train bioreactors”. In: *Biotechnology Progress* 29.1 (2013), pp. 222–229. ISSN: 87567938. DOI: 10.1002/btpr.1672.
- [22] A. E. Boycott. “Sedimentation of Blood Corpuscles”. In: *Nature* 668.4 (1920), pp. 98–105.
- [23] Cary Matanguihan and Paul Wu. “Upstream continuous processing: recent advances in production of biopharmaceuticals and challenges in manufacturing”. In: *Current Opinion in Biotechnology* 78 (2022), p. 102828. ISSN: 09581669. DOI: 10.1016/j.copbio.2022.102828.
- [24] Daniel J. Karst et al. “Characterization and comparison of ATF and TFF in stirred bioreactors for continuous mammalian cell culture processes”. In: *Biochemical Engineering Journal* 110 (2016), pp. 17–26. ISSN: 1369703X. DOI: 10.1016/j.bej.2016.02.003.
- [25] Samantha Wang et al. “Shear contributions to cell culture performance and product recovery in ATF and TFF perfusion systems”. In: *Journal of Biotechnology* 246 (2017), pp. 52–60. ISSN: 01681656. DOI: 10.1016/j.jbiotec.2017.01.020.
- [26] Samantha Wang et al. “Larger Pore Size Hollow Fiber Membranes as a Solution to the Product Retention Issue in Filtration-Based Perfusion Bioreactors”. In: *Biotechnology Journal* 14.2 (2019), pp. 1–17. ISSN: 18607314. DOI: 10.1002/biot.201800137.
- [27] S. Metze et al. “Monitoring online biomass with a capacitance sensor during scale-up of industrially relevant CHO cell culture fed-batch processes in single-use bioreactors”. In: *Bioprocess and Biosystems Engineering* 43.2 (2020), pp. 193–205. ISSN: 1615-7591. DOI: 10.1007/s00449-019-02216-4.
- [28] Eric Ponder. “On Sedimentation and Rouleaux Formation - II”. In: *Quarterly Journal of Experimental Physiology* January (1926).

- [29] Robert H Davis. “Sedimentation of noncolloidal particles at low Reynolds numbers”. In: *Annual Review of Fluid Mechanics* 2.17 (1985), pp. 91–118. DOI: 0066--4189/85/0115-0091\$02.00.
- [30] Yuyi Shen and Kurt Yanagimachi. “CFD-aided cell settler design optimization and scale-up: Effect of geometric design and operational variables on separation performance”. In: *Biotechnology Progress* 27.5 (2011), pp. 1282–1296. ISSN: 87567938. DOI: 10.1002/btpr.636.

A.5 Scientific Publication Section V

Co-current filtrate flow in TFF perfusion processes: Decoupling transmembrane pressure from crossflow to improve product sieving

This section is based on the following publication: P. Romann, P. Giller, A. Sibia, C. Herwig, A. Zydne, A. Perilleux, J. Souquet, J-M. Bielser, and T. K. Villiger, **Co-current filtrate flow in TFF perfusion processes: Decoupling transmembrane pressure from crossflow to improve product sieving**, 2023, Under review in *Biotechnology and Bioengineering*.

Abstract

Hollow fiber-based membrane filtration has emerged as the dominant technology for cell retention in perfusion processes yet significant challenges in alleviating filter fouling remain unsolved. In this work, the benefits of co-current filtrate flow applied to a tangential flow filtration (TFF) module to reduce or even completely remove Starling recirculation caused by the axial pressure drop within the module was studied by pressure characterization experiments and perfusion cell culture runs. Additionally, a novel concept to achieve alternating Starling flow within unidirectional TFF was investigated. Pressure profiles demonstrated that precise flow control can be achieved with both lab-scale and manufacturing scale filters. TFF systems with co-current flow showed up to 40% higher product sieving compared to standard TFF. The decoupling of transmembrane pressure from crossflow velocity and filter characteristics in co-current TFF alleviates common challenges for hollow-fiber based systems such as limited crossflow rates and relatively short filter module lengths, both of which are currently used to avoid extensive pressure drop along the filtration module. Therefore, co-current filtrate flow in unidirectional TFF systems represents an interesting and scalable alternative to standard TFF or alternating TFF operation with additional possibilities to control Starling recirculation flow.

Keywords: perfusion cell culture, tangential flow filtration (TFF), co-current filtrate flow, Starling recirculation, product sieving

Abbreviations: TFF, tangential flow filtration; ATF, alternating tangential flow filtration; TMP, transmembrane pressure; rTFF, reverse tangential flow filtration; HPTFF, high performance tangential flow filtration; scTFF, stepping co-current tangential flow filtration; PT_{R1-2} , pressure transmitter in retentate loop; PT_{F1-2} , pressure transmitter in filtrate loop; PT_{A1-5} , additional pressure transmitter on filtrate side of hollow fiber filter; PT_{AB1-5} , additional pressure transmitter on backside of filtrate side of hollow fiber filter; FS_R , flow sensor in retentate loop; FS_F , flow sensor in filtrate loop; CD_{R1-2} , centrifugal discharge pump in retentate loop; CD_F , centrifugal discharge pump in filtrate loop; PP_H , peristaltic pump in harvest line; VCV, viable cell volume; VCD, viable cell density.

1 Introduction

Hollow fiber-based tangential flow filtration has emerged as one of the most preferred cell retention technologies for mammalian perfusion processes with applications in main stage perfusion bioreactors and also in N-1 bioreactors improving existing fed-batch production units [1–3]. Despite significant advancements in pump technology, such as low-shear diaphragm pumps or levitated centrifugal pumps [4–7], to improve culture viability and thereby reduce the load of fouling-provoking particles on the filter membrane, filter clogging and product retention remain major challenges on the way to robust manufacturing processes.

Tangential flow filtration (TFF) in unidirectional crossflow mode (frequently driven by a levitated centrifugal pump) and alternating tangential flow (ATF, driven by a diaphragm pump) are the most commonly reported systems in perfusion processes [8–10]. Most studies revealed that ATF showed superior product sieving compared to TFF at lab-scale and suggested ATF as a more suitable technology for long-term perfusion operation [5, 7, 11]. However, ATF systems driven by diaphragm pumps were associated with operational instability at manufacturing scale [2, 12–14]. Furthermore, multiple parallel ATF system were required to operate 2,000 L perfusion bioreactors, requiring considerably more floor space compared to similar TFF systems [2, 15]. Therefore, TFF systems were claimed to be the preferred choice within the industry at large scale due to smaller facility footprint and higher robustness, whereas ATF systems showed improved product sieving and reduced development time for pilot-scale operations [2].

In TFF, concentration polarization and fouling can both affect product retention [16–20]. Compared to industrial TFF applications that have short operating times and high filtrate flux [21–23], TFF systems used as cell retention devices in perfusion processes must be operational for as much as several months (without cleaning) and are operated at comparably very low filtrate fluxes of around $2 \text{ L m}^{-2} \text{ h}^{-1}$ [24]. Due to the low filtrate fluxes and high axial pressure drops, a reverse flow of filtrate back into the fiber lumen occurs at the filter exit. This so-called Starling recirculation [25] was modelled and shown to be significantly larger than the actual harvest rate during typical perfusion processes [24]. As a consequence, only slightly more than 50% of the actual hollow fiber membrane surface area is used for filtration [24].

More recently, alternating TFF systems have been described either with one levitated centrifugal pump and valves to switch crossflow direction [26], or with two alternating, inversely positioned centrifugal pumps in the retentate loop called reverse TFF (rTFF) [27, 28]. Both setups showed reduced product retention compared

to unidirectional TFF systems. While each individual phase of alternating crossflow filtration (ATF, rTFF or alternating crossflow by valve switching) can be compared to the situation in a TFF system, the distinguishing factor lies in the alternating direction of the crossflow and therefore the change in the location of the filter inlet. When working with cell lines prone to aggregation, switching the filter inlet can prevent fiber blocking [26, 29]. Improved product sieving with alternating crossflow systems compared to TFF was further attributed to the short period of zero net flow between phases resulting in a very low TMP across the entire filter length, possibly leading to deposit layer relaxation [23, 26]. It was also suggested that the Starling recirculation, which switches between the two ends of the hollow fiber, could remove deposited material and thereby minimize fouling [11, 24]. Additionally, alternating crossflow filtration makes use of the entire filter length, harnessing the full membrane surface of the module [24]. The increased performance of alternating TFF is likely due to a combination of these factors.

Although there are several advantages associated with alternating crossflow filtration, it is important to note that the backflush of filtrate at the filter exit must be counterbalanced by an increased filtrate flux near the filter inlet to maintain the same overall level of filtration. This causes an increase in the drag forces that push particles into the membrane [30], which can lead to a denser deposit and greater particle penetration into the membrane, both detectable as an increase of irreversible fouling resistance [28]. Sundar et al. [31] demonstrated that the greatest fouling in ATF systems occurs at the ends of the hollow fiber module, i.e., where the filtrate flux is greatest. This might explain studies observing significant product sieving losses despite using properly sized ATF modules [7, 32].

These phenomena provide notable constraints in hollow fiber designs and determining optimal operating conditions for perfusion systems. Crossflow velocities, for example, must be kept low to decrease the pressure drop along the filter length and thereby reduce the Starling recirculation. However, reducing crossflow increases the residence time of the cells within the recirculation loop, risking oxygen depletion [33]. In addition, low crossflow leads to greater concentration polarization, i.e., greater accumulation of cells at the membrane surface. The increasing axial pressure drop with increasing length of the hollow fiber modules favors the use of relatively short filtration modules, requiring multiple filters in parallel to meet the needs for larger filtration area. Increasing the inner diameter of the hollow fibers would also reduce the pressure drop along the fiber length, but at a cost of much greater hold-up volume within the module.

Although all these strategies to improve filtration performance try to reduce the

impact of the pressure drop and Starling flow, none of them solve the fundamental problem that the local TMP is coupled to the magnitude of the crossflow (which determines the axial pressure drop) and the filter characteristics. In order to achieve a nearly uniform TMP throughout the module, a similar pressure drop must be generated on the filtrate side of the module as on the retentate side. This concept for the biopharmaceutical industry was originally called High Performance TFF (HPTFF) and was successfully demonstrated to control concentration polarization along the filter length to enable high resolution protein-protein separations in downstream operations [34, 35]. It has also improved purification of viral vectors using ultrafiltration [36]. The concept is further known in the dairy industry for microfiltration [37–39]. The ability to control the filtrate flux and Starling flow independently of the crossflow and length of the filtration module offers a promising tool to overcome challenges in current TFF and ATF systems in perfusion processes. To the authors knowledge, HPTFF to alleviate product retention in perfusion processes has not been evaluated in the literature.

The aim of this study was to develop a co-current filtration flow system for perfusion processes based on single use low-shear centrifugal pumps in combination with pressure sensors with the ultimate goal to reduce product retention. This so-called HPTFF system was characterized for a wide range of operating conditions by measuring the TMP along the length of the filter module. Steady-state perfusion cell culture runs demonstrated superior performance during HPTFF compared to standard TFF. Further, a new concept of stepping co-current TFF (scTFF) was introduced, allowing us to generate alternating Starling recirculation within a unidirectional TFF system. Subsequently, scalability of HPTFF and scTFF were successfully evaluated by recording pressure profiles along a modified large-scale hollow fiber module.

2 Materials and Methods

2.1 Lab-scale system setup for pressure characterization

An experimental setup capable of operating TFF, rTFF, HPTFF and scTFF was built to characterize the different filtration systems at lab-scale (Figure A.41A). Pressure transmitters (PREPS-N-038, PendoTECH, Princeton, USA) were installed in the retentate loop at the inlet (PT_{R1}) and outlet of the filter (PT_{R2}). Further pressure transmitters were positioned in the filtrate loop at the inlet (PT_{F1}) and outlet (PT_{F2}) of the module. A PES hollow fiber-module with a total module length

of 70 cm, an effective fiber length of 65 cm, an inner fiber diameter of 1 mm, a pore size of $0.2\ \mu\text{m}$ and a membrane surface area of $0.15\ \text{m}^2$ was used (S06-P20U-10-N, Repligen, Waltham, Massachusetts, USA). For the pressure tests, the hollow fiber module was modified by drilling holes and gluing additional pressure transmitters (PT_{A1-5}) into the filtrate side to monitor the filtrate pressures along the filter length. Considering the total length of the hollow fiber module, the additional pressure transmitters (PT_{A1-5}) were placed at 5.5 cm, 20 cm, 35 cm, 50 cm and 64.5 cm measured from the start of the module. Flow sensors (LFSC-i10X-001, Levitronix GmbH, Zurich, Switzerland) were installed in the retentate loop (FS_R) and in the filtrate loop (FS_F). Three levitated centrifugal pumps (PuraLev i30SU, Levitronix GmbH, Zurich, Switzerland) were integrated into the experimental setup. Two pumps were integrated into the retentate loop, of which one was directed towards the filter inlet (CD_{R1}) and the other towards the filter outlet (CD_{R2}). The third centrifugal pump (CD_F) was inserted into the filtrate loop directed towards the filter inlet side. A peristaltic pump (PP_H) was inserted into the harvest stream. Data was recorded by connecting 3 process control units (LCO-i100, Levitronix GmbH, Zurich, Switzerland).

2.2 Large-scale system setup for pressure characterization

For large-scale pressure characterization, a similar experimental setup as described for lab-scale experiments was built to achieve TFF, HPTFF and scTFF operation (Figure A.47A and B). A PES hollow fiber-module with a total module length of 78 cm, an effective fiber length of 68 cm, an inner fiber diameter of 1 mm, a pore size of $0.2\ \mu\text{m}$ and a membrane surface of $7.15\ \text{m}^2$ was used (X06-P20U-10-N, Repligen, Waltham, Massachusetts, USA). Pressure transmitters (PREPS-N-1-1, PendoTECH, Princeton, USA) were installed in the retentate loop (PT_{R1} and PT_{R2}) and in the filtrate loop (PT_{F1} and PT_{F2}). To measure pressures as closely as possible to the inlet and outlet of the hollow fibers, holes were drilled to place pressure transmitters (PREPS-N-038, PendoTECH, Princeton, USA) into the adapter piece of the filter module (PT_{RC1} and PT_{RC2}). Further pressure transmitters (PREPS-N-038, PendoTECH, Princeton, USA) on the filtrate side were attached along the filter length at 15.5 cm, 27.5 cm, 38.5 cm, 50 cm and 62.5 cm measured from the start of the module (PT_{A1-5}). Additionally, pressure transmitters at the same filter length but in the back were attached (PT_{AB1-5}). Flow sensors (LFSC-i35X, Levitronix GmbH, Zurich, Switzerland) were installed in the retentate (FS_R) and filtrate loops (FS_F). One levitated centrifugal pump (PuraLev-2000SU, Levitronix GmbH, Zurich, Switzerland) was inserted into the retentate loop (CD_{R1}) and a second lev-

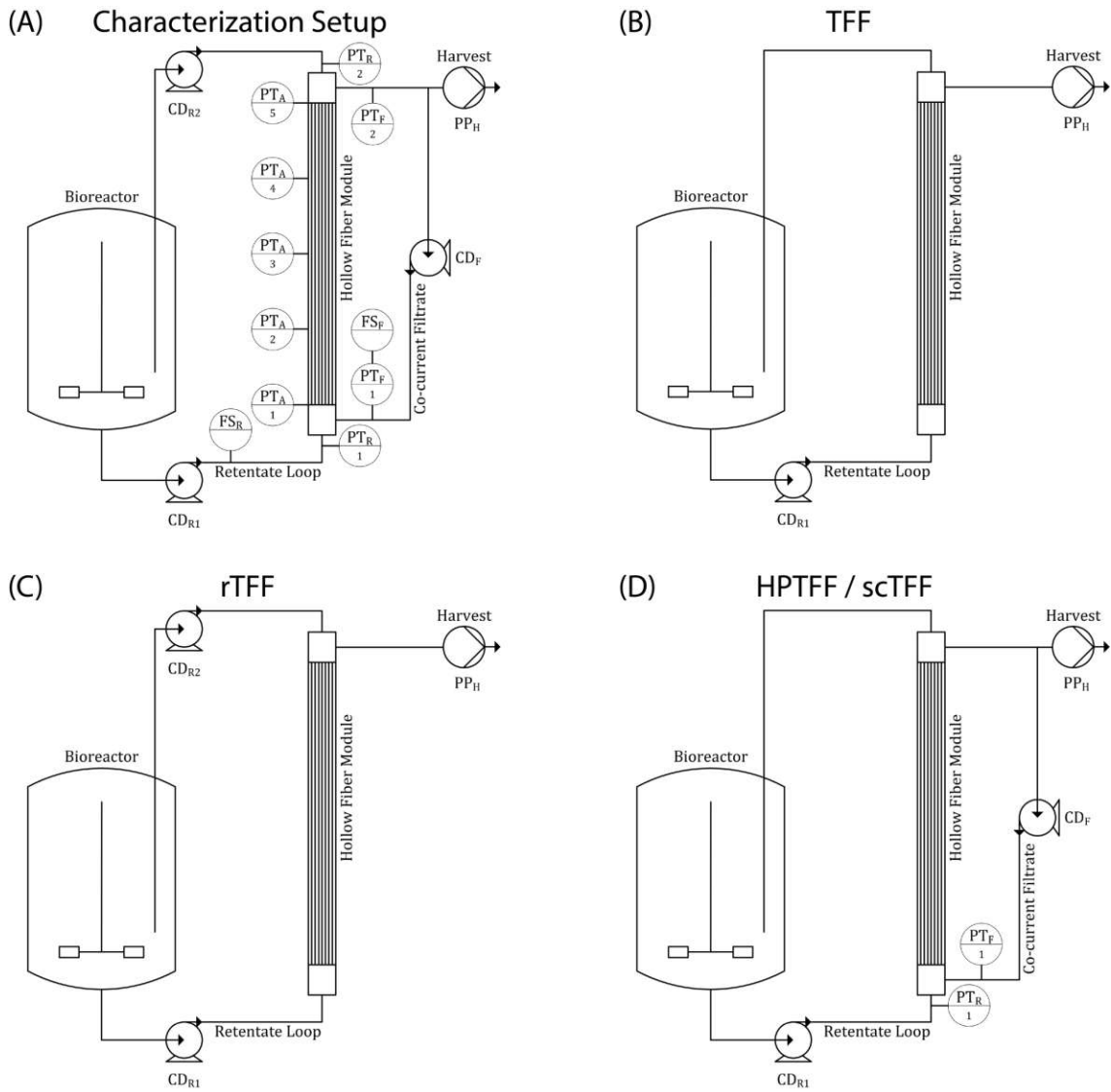


Figure A.41: Detailed schematic representation of the experimental setup for the pressure characterization in water (A). Pressure transmitters (PT), flow sensors (FS), centrifugal pumps (CD) and peristaltic pumps (PP) are specified with subscripted letters according to their position (R: Retentate; F: Filtrate; A: Additional sensors on filtrate side; H: Harvest). Minimal required setups for TFF (B), rTFF (C) and HPTFF or scTFF (D) operation used for cell culture runs are further shown.

itated centrifugal pump (PuraLev-600SU, Levitronix GmbH, Zurich, Switzerland) was placed in the filtrate loop (CD_F). A peristaltic pump (PP_H) was inserted into the harvest stream. Data recording was achieved by coupling 6 process control units (5x LCO-i100 and 1x LCO-600, Levitronix GmbH, Zurich, Switzerland).

2.3 Experimental procedure for pressure characterization

Pressure characterization studies were performed with water as a medium. To characterize the TFF system, only pump CD_{R1} was operational. To realize the HPTFF

and scTFF systems, pump CD_{R1} in the retentate loop and pump CD_F in the filtrate loop were active simultaneously. For the rTFF systems, pump CD_{R1} was used for the first phase and pump CD_{R2} was used for the second phase with reversed crossflow. For all lab-scale setups, crossflow was kept at 650 mL min^{-1} , except for ramping experiments where the crossflow was ramped from $0 - 1,500 \text{ mL min}^{-1}$. For crossflow ramping in HPTFF, a delta pressure PI control (P-term: $2 \text{ rpm } \Delta\text{mbar}^{-1}$; I-term: $5 \text{ rpm } \Delta\text{mbar}^{-1} \text{ s}^{-1}$) was used with a setpoint of 0 mbar, meaning that the pump speed of pump (CD_F) was controlled such that pressure PT_{F1} matched PT_{R1} . For scTFF characterization, the co-current filtrate flow rate was set at 870 mL min^{-1} (scTFF phase 1) and $1,890 \text{ mL min}^{-1}$ (scTFF phase 2) to achieve a delta pressure control of $\pm 10 \text{ mbar}$. To characterize large-scale TFF operation, the crossflow was ramped from $0 - 45 \text{ L min}^{-1}$. For HPTFF pressure characterization, additional filtrate flow was applied by a delta pressure PI control (P-term: $2 \text{ rpm } \Delta\text{mbar}^{-1}$; I-term: $5 \text{ rpm } \Delta\text{mbar}^{-1} \text{ s}^{-1}$) such that PT_{F1} was kept 6 mbar higher than PT_{R1} . Filtrate flow ramping to assess scTFF operation was achieved by maintaining a crossflow of 14.5 L min^{-1} and ramping the co-current filtrate flow from $0 - 70 \text{ L min}^{-1}$. To compare filtration conditions between filtration module scales, shear rates provided by the manufacturers lookup tool were considered (Repligen, Waltham, Massachusetts, USA).

2.4 Perfusion culture process

A proprietary CHO-K1 cell line producing a bispecific mAb was expanded in an incubator (Multitron, Infors HT, Bottmingen, Switzerland) for 21 days using a proprietary chemically defined perfusion platform medium and an on-demand proprietary feed (Merck KGaA, Corsier-sur-Vevey, Switzerland). Perfusion bioreactors (Labfors 5 Cell, Infors HT, Bottmingen, Switzerland) were inoculated at a seeding density of 0.6×10^6 viable cells mL^{-1} . Culture conditions were maintained at $36.5 \text{ }^\circ\text{C}$ with a dissolved oxygen setpoint at 50% (VisiFerm DO Arc, Hamilton, Bonaduz, Switzerland). The pH was controlled at 7.07 ± 0.17 (EasyFerm Plus Arc probe Hamilton, Bonaduz, Switzerland) by sparging CO_2 and using a $1.1 \text{ M Na}_2\text{CO}_3$ solution. Bioreactors were operated at 2 L working volume. After an initial growth phase, an online capacitance probe (Incyte Arc, Hamilton, Bonaduz, Switzerland) was used to keep the viable cell volume (VCV) constant at 12%. Perfusion started on day 0 and was kept constant at 1.3 reactor volumes per day until the end of the process.

2.5 Cell retention devices in perfusion cell culture

Bioreactor harvests were gravimetrically controlled to maintain the bioreactor weight constant using the same hollow fiber module. Cell retention devices were either operated as TFF (Figure A.41B), rTFF (Figure A.41C), HPTFF or scTFF systems (Figure A.41D). In all setups, the crossflow was generated by levitated centrifugal pumps (PuraLev i30SU, Levitronix GmbH, Zurich, Switzerland) to ensure comparability of sieving studies. Pump speeds in the retentate loop were set to 3,500 rpm, initially corresponding to a crossflow velocity of 650 mL min⁻¹. For TFF, HPTFF and scTFF operations, the retentate loop pump CD_{R1} was stopped every 3 min for 3 s to release accumulated air bubbles within the centrifugal pump head. For HPTFF operations, a delta pressure PI control (P-term: 2 rpm Δ mbar⁻¹; I-term: 5 rpm Δ mbar⁻¹ s⁻¹) between pressure PT_{R1} and pressure PT_{F1} was used with a setpoint of 0 mbar to control the speed of the filtrate pump CD_F . As such, filtrate pressures were matched with retentate pressures along the filter length. scTFF operation was achieved by delta pressure control of -5 mbar during scTFF phase 1 and +5 mbar during scTFF phase 2 between pressure PT_{R1} and pressure PT_{F1} . rTFF operation consisted of two phases. In the first phase, the first retentate pump CD_{R1} was operational and the second retentate pump CD_{R2} was stopped. During the second phase, pump CD_{R2} was operational and the pump CD_{R1} was stopped. Phase times were 20 s.

2.6 Reference analytics

Cell density, viability, cell diameter, and pH were measured using a BioProfile FLEX2 (Nova Biomedical, Waltham, USA). Bioreactors were automatically sampled by the FLEX2 On-Line Autosampler (Nova Biomedical, Waltham, USA) and samples were fractionated using a Teledyne Cetac ASX-7200 (Teledyne CETAC Technologies, Omaha, Nebraska, USA). Viable cell volume was calculated as follows [40]:

$$\text{VCV} = \frac{\frac{4}{3} \cdot \pi \cdot \left(\frac{D}{2}\right)^3 \cdot \text{VCD}}{V} \cdot 100 \quad (\text{A.18})$$

where D is the average cell diameter, VCD is the viable cell density, and V is the cell culture volume, assuming a spherical shape of the cells. Bioreactor titer samples were prepared by centrifugation (3,200 g for 10 min) and 0.22 μ m filtered. Harvest titer samples were directly analyzed without further sample preparation.

Process titers were determined using a protein A affinity high performance liquid chromatography device (PA-HPLC, Waters, Milford, Massachusetts, USA). Cell debris was measured using an optical density (OD) measurement (Spectronic Genesys 10 Bio, Thermo Electron Corporation, Waltham, Massachusetts, USA). Therefore, bioreactor samples were centrifuged (3,200 g for 10 min) and measured at 600 nm against a 0.22 μm filtered reference sample.

3 Results

3.1 Pressure characterization of TFF, rTFF and HPTFF

Measurement of pressure gradients within the hollow fiber and on the filtrate side along the filter length for the TFF, rTFF and HPTFF system was performed with a special characterization setup enabling the operation of all three systems (Figure A.41A). This setup not only allowed us to measure the retentate loop and filtrate pressures at the inlet of the filter module (PT_{R1} and PT_{F1}) and at the outlet of the filter module (PT_{R2} and PT_{F2}), but enabled us to get additional measurements of the filtrate pressure along the filter module length (PT_{A1-5}). A crossflow ramping from 0 – 1,500 mL min^{-1} to simulate the TFF system or one of the rTFF phases demonstrated that the axial pressure drop within the retentate loop increased with increasing crossflow as seen in the diverging retentate inlet pressure PT_{R1} and retentate outlet pressure PT_{R2} (Figure A.42A). All remaining pressure sensors on the filtrate side, irrespective of the crossflow, indicated the average pressure of PT_{R1} and PT_{R2} . Aligning the pressures at a crossflow of 650 mL min^{-1} according to their position revealed positive TMP at the filter inlet and negative TMP at the filter outlet. The TMP was zero in the middle of the filtration module (Figure A.42C). A similar crossflow ramping was performed to characterize pressures for the HPTFF system with activated delta pressure control to match the filtrate inlet pressure PT_{F1} with the retentate inlet pressure PT_{R1} (Figure A.42B). In contrast to the TFF and rTFF, filtrate pressures along the filter were not identical anymore but matched the retentate pressure gradient along the entire filter length (Figure A.42D). The only filtrate pressure sensor with a discrepancy to the respective retentate pressure was PT_{F2} . This discrepancy was negligible for crossflows below 400 mL min^{-1} but increased slightly with larger crossflow (Figure A.42B). Required co-current filtrate flows for varying crossflows using the lab-scale filter are provided in the Supporting Information (Figure A.48A).

Time resolved pressure recordings for the operation of a TFF and rTFF system

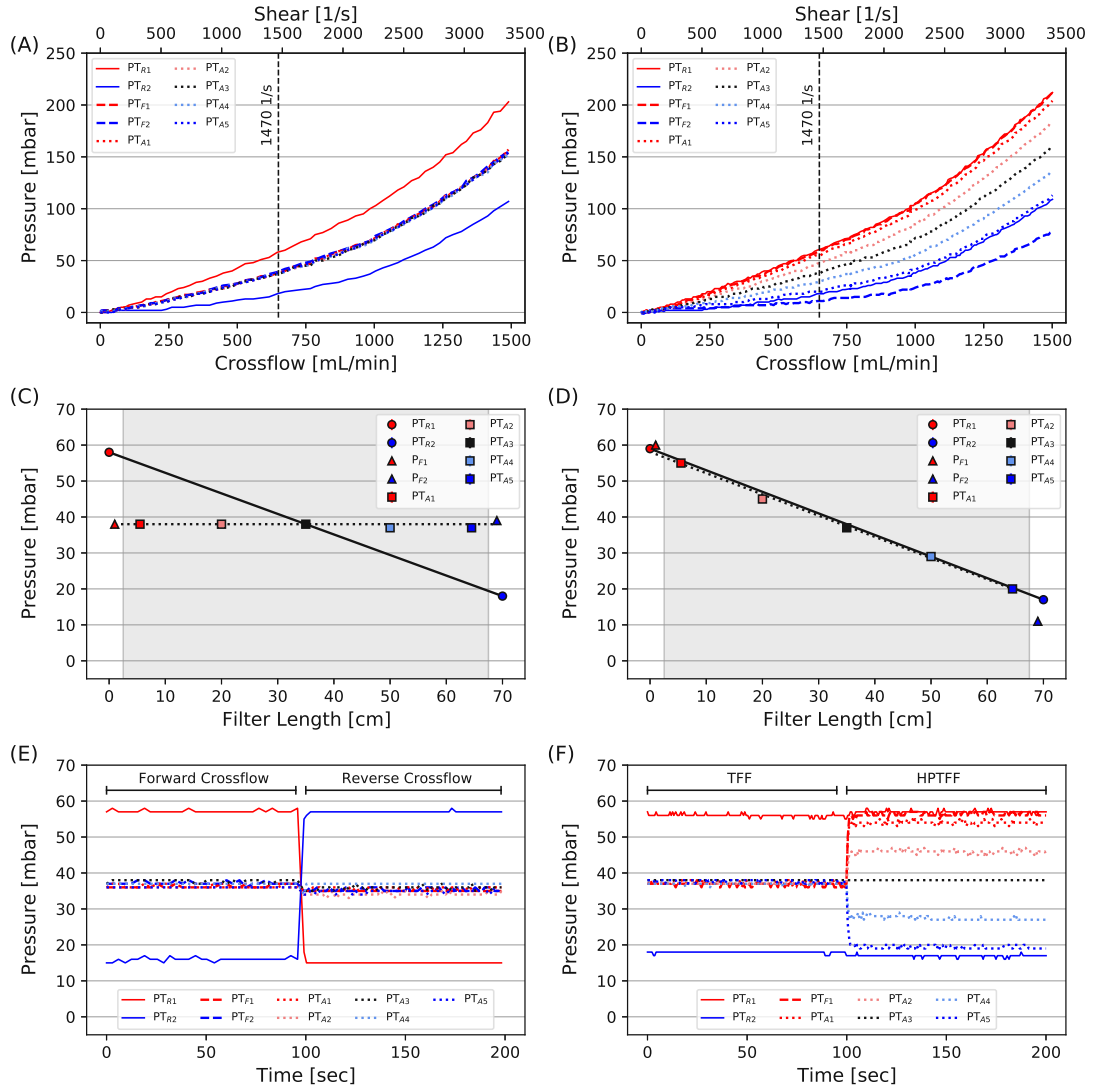


Figure A.42: Pressure characterization results for TFF, rTFF and HPTFF operation. Crossflow ramping in TFF and rTFF operation (A) and crossflow ramping with delta pressure control in HPTFF operation (B). Dashed lines represent the standard operating region of $1,470 \text{ s}^{-1}$ shear resulting in approximately 650 mL min^{-1} crossflow. Pressure measurements according to their position along the filter length are provided for TFF and the forward crossflow phase of rTFF (C), and for HPTFF (D), grey areas represent absolute fiber length. Pressure distributions at 650 mL min^{-1} crossflow versus time are shown for TFF and rTFF (E), where the forward crossflow phase corresponds to TFF operation, and rTFF is defined by alternation between forward and reverse crossflow. HPTFF pressure distribution versus time upon co-current filtrate flow activation was further measured at 650 mL min^{-1} crossflow (F).

at a crossflow of 650 mL min^{-1} are provided in Figure A.42E. TFF is represented by only considering the forward crossflow phase. The rTFF is described by adding a reverse crossflow phase, and thereby alternating the crossflow. The only changing pressures upon crossflow reversal were the retentate pressures, with PT_{R1} taking the

previous value of PT_{R2} and vice-versa. HPTFF operation at 650 mL min^{-1} crossflow was achieved upon delta pressure control activation with a co-current filtrate flow of approximately $1,400 \text{ mL min}^{-1}$ (Figure A.42F). Immediately, filtrate pressures align with the retentate pressure gradient and are stably maintained at the target values.

A schematic representation of the pressure characterization experiments summarizes the findings for the TFF system (Figure A.43A), rTFF system (Figure A.43B) and for the HPTFF system (Figure A.43C). The schematic pressure plots demonstrate the TMP differences along the fiber length for the TFF and the rTFF system. A zoomed view into a hollow fiber at the beginning, in the middle and at the end of the filter module further highlights the Starling recirculation indicated by arrows. Compared to the TFF and rTFF system, the filtrate pressures in the HPTFF system are well aligned with the retentate pressure thereby generating a uniform TMP of only slightly above zero along the length of the filtration module. Small arrows from retentate to filtrate indicate that the entire filtration area is utilized for filtration by avoiding Starling recirculation.

3.2 Pressure characterization of scTFF

Whereas HPTFF operation focused on matching filtrate pressures with the retentate pressure gradient and thereby removing Starling recirculation completely, we also examined a novel operating mode for unidirectional TFF defined as stepping co-current TFF (scTFF). The scTFF consists of two phases, a first phase with lower co-current filtrate flow than required for HPTFF, and a second phase with higher co-current filtrate flow, resulting in a step profile for the co-current filtrate flow (Figure A.44A). To demonstrate the impact of co-current filtrate flow on the pressure profiles, a co-current filtrate flow ramping was performed by fixing the crossflow to 650 mL min^{-1} (Figure A.44B). At 0 mL min^{-1} co-current filtrate flow, the system basically corresponded to a standard TFF operation. With increasing co-current filtrate flow, the pressure aligned more and more to the retentate pressure gradient and matched it at about $1,400 \text{ mL min}^{-1}$, corresponding to the situation in HPTFF operation. Further increasing the co-current filtrate flow led to higher filtrate pressures in the first half of the filter and lower filtrate pressures in the second half of the filter compared to the retentate pressure gradient. The filtrate pressure at the outlet PT_{F2} was not plotted as similar discrepancies to the retentate pressure gradient as seen in Figure A.42B were observed. Selecting a co-current filtrate flow of 870 mL min^{-1} for phase 1 (blue vertical dashed line) and $1,890 \text{ mL min}^{-1}$ for phase 2 (red vertical dashed line) of the scTFF operation, a delta pressure between PT_{R1} and

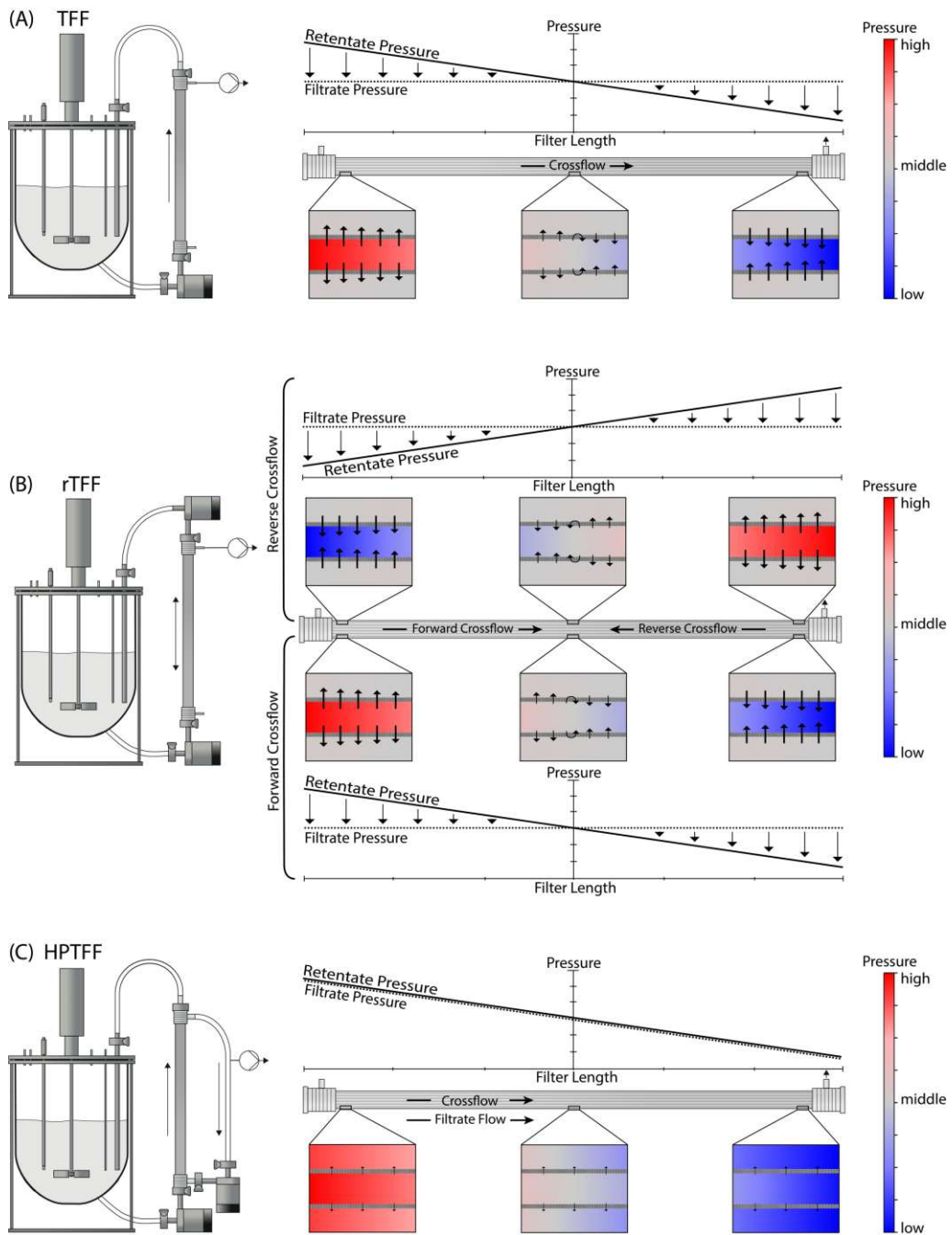


Figure A.43: Schematic representation for TFF (A), rTFF (B) and HPTFF (C) systems with centrifugal pumps based on pressure characterization. Pressure curves along the filter length for each system are given and arrows indicate filtrate flux, longer arrows represent larger fluxes. Additionally, a zoom into a fiber at the beginning, middle and at the end of the filter is provided and colored from red (high pressure) to blue (low pressure). As rTFF consist of two phases, the situation for forward crossflow and reverse crossflow are depicted.

PT_{F1} of -10 mbar and +10 mbar, respectively, was achieved. Pressures recorded for the two phases of scTFF were then plotted according to their position along the filter (Figure A.44C). The black line represents the retentate pressure gradient, the blue dashed line represents the pressure drop on the filtrate side for scTFF phase 1 and the red line represents the pressure drop on the filtrate side for scTFF phase 2. A common intersection of all three lines was located in the middle of the filter length, meaning the absolute TMP is zero in the middle of the filter and gets larger the closer to one of two filter ends.

By switching between scTFF phase 1 and scTFF phase 2 with defined phase times, a scTFF system with unidirectional crossflow but reversing Starling recirculation was obtained (Figure A.44C). Red areas represent the flux of filtrate back into the retentate due to higher filtrate pressures compared to the retentate pressures, whereas blue areas represent flux from retentate to filtrate due to higher retentate pressures compared to filtrate pressures. As such, filtrate pressure PT_{A1} positioned at 5.5 cm from the filter inlet was lower than the corresponding retentate pressure at 5.5 cm filter length (black dashed line) during scTFF phase 1 and got larger than the corresponding retentate pressure during scTFF phase 2. Similar, but reversed, behaviour was observed for pressure PT_{A5} positioned on the second half of the filter at 64.5 cm filter length. In this case, PT_{A5} was larger than the retentate pressure during scTFF phase 1 and smaller than the retentate pressure during scTFF phase 2. A combined HPTFF-scTFF operation is also possible by integrating a sweeping into the HPTFF operation. The sweeping was achieved by lowering the co-current filtrate flow (scTFF phase 1) and subsequently increasing the co-current filtrate flow (scTFF phase 2). After the sweep, the system was again operated at HPTFF conditions (Figure A.44D).

3.3 Characterization of performance in perfusion cell culture processes

Cell culture parameters and product retention were compared for TFF, rTFF, HPTFF and scTFF operation in steady-state perfusion processes. For all four cell retention setups (Figure A.41B to D), steady-state operation was achieved after approximately 5 days and culture viability was not impacted by the cell retention operating mode (Figure A.45A). Target process run time of 30 days was achieved for all runs except TFF_1 and HPTFF_2. These runs were terminated at day 19 (TFF_1) and day 21 (HPTFF_2) due to a sudden decrease in crossflow caused by inlet blocking of the fibers. Cell diameter increased slightly with runtime for all of

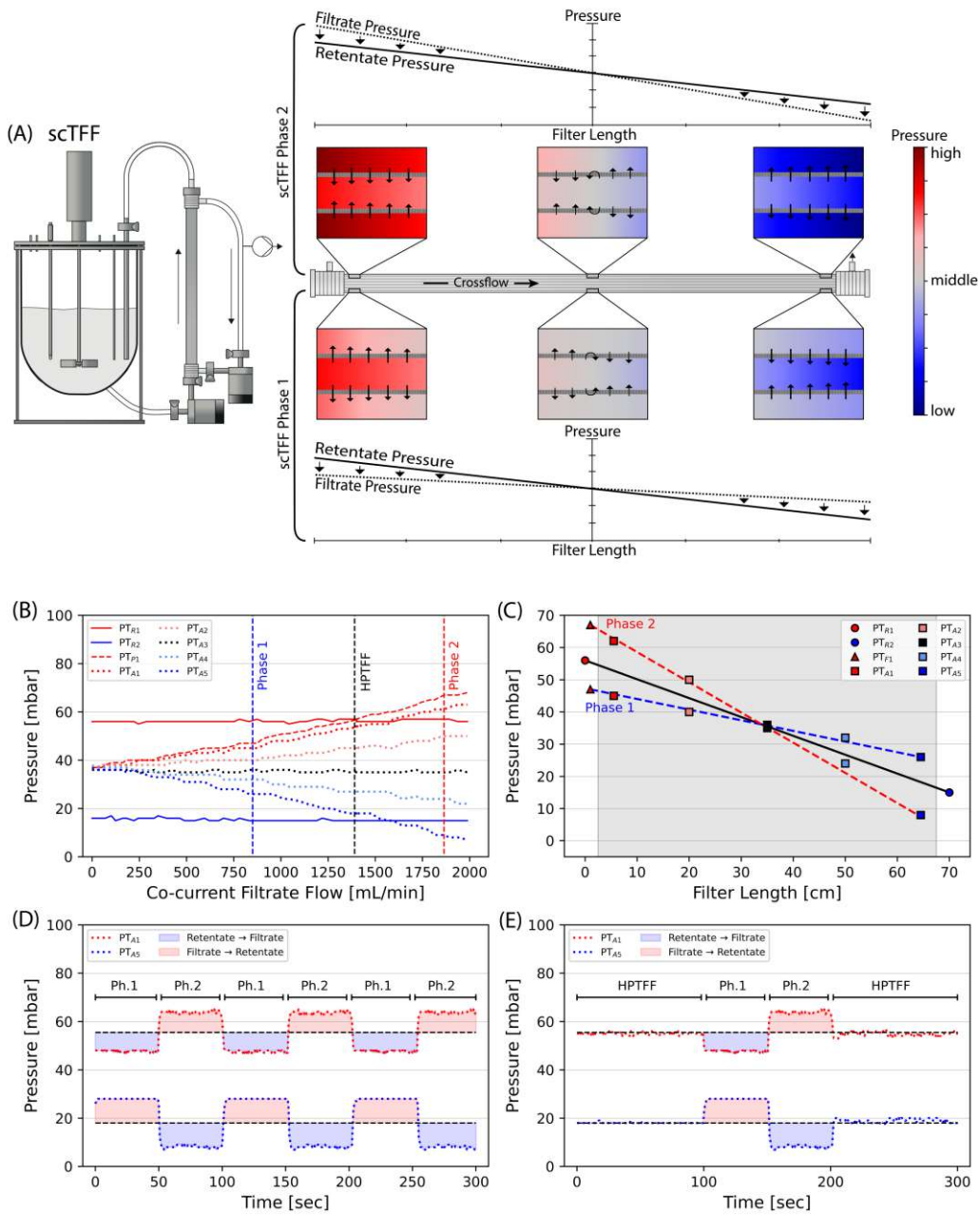


Figure A.44: Concept of stepping co-current TFF (scTFF) by schematic representation of pressure gradient along filter length (A). Co-current flow ramping at 650 mL min^{-1} crossflow (B). Vertical dashed lines represent operating conditions for HPTFF (black), scTFF phase 1 with -10 mbar pressure difference (blue) and scTFF phase 2 with $+10 \text{ mbar}$ pressure difference (red) on filter inlet. Pressure measurements according to their position along the filter length are provided for all three dashed lines (C), grey areas represent absolute fiber length. Operation of scTFF with two alternating phases ($\pm 10 \text{ mbar}$ pressure difference) is demonstrated by time resolved pressure distribution plots (D). Alternative operating mode of HPTFF with alternating membrane sweeps by scPTFF phases of $\pm 10 \text{ mbar}$ in between HPTFF phases (E). Red areas represent flux of filtrate back into the retentate, blue areas represent flux from retentate to filtrate.

the cell retention systems (Figure A.45B) and pH stayed within the defined range of 7.07 ± 0.17 for all runs (Figure A.45C). Cell debris increased for most runs until day 25, after which a slight decrease in cell debris was observed. In general, TFF and rTFF runs showed slightly higher debris levels compared to HPTFF and scTFF runs especially after day 13 (Figure A.45D). The harvest titer plot (Figure A.45E) and the product sieving plot (Figure A.45F) revealed significantly reduced product sieving of around 80% for the TFF operation after only a few first days of steady-state operation. Product sieving further decreased down to 60% or lower for TFF. Product sieving for rTFF stayed above 90% for the entire experiment for run rTFF_1 and remained above 80% for run rTFF_2. HPTFF operation resulted in similar or even higher product sieving with yields above 95% for the entire run.

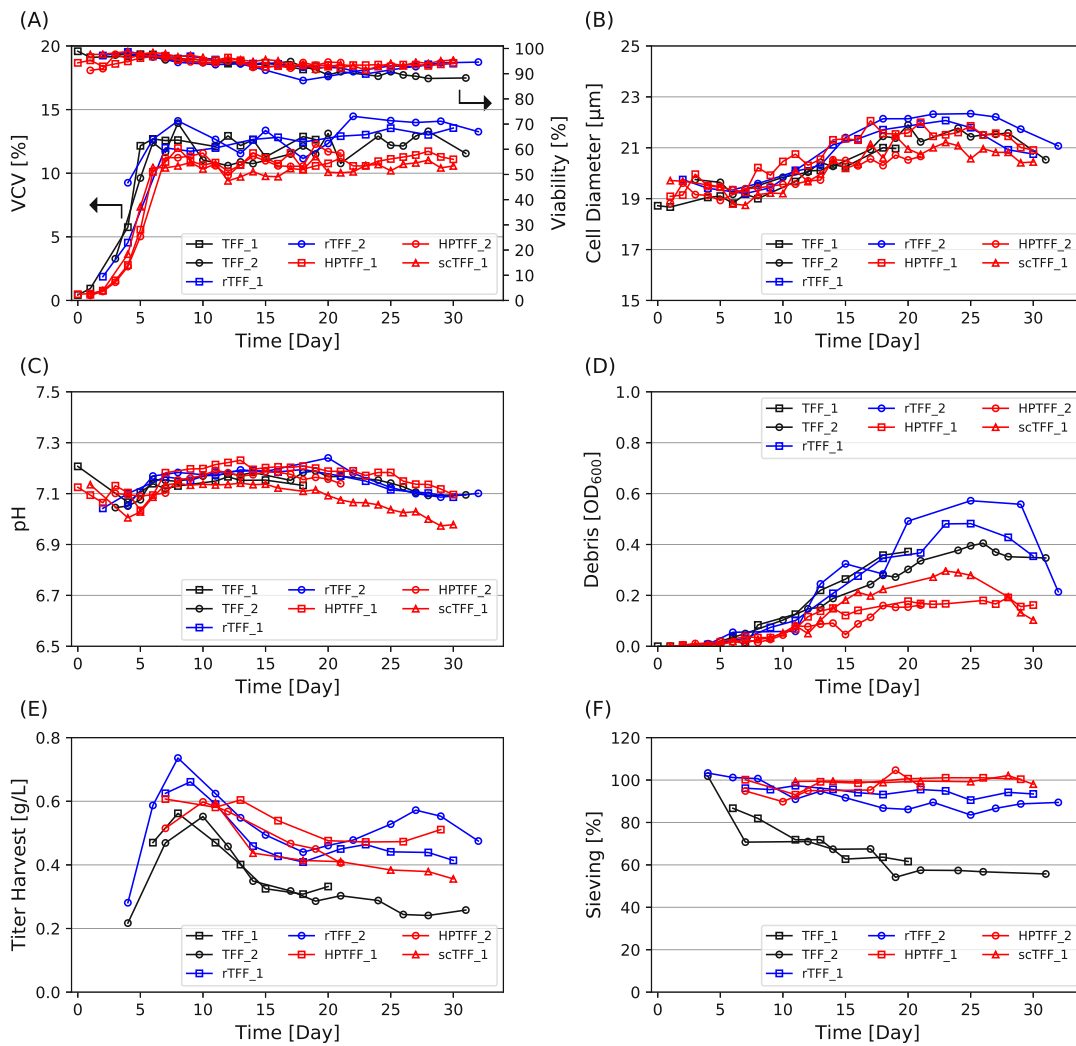


Figure A.45: Perfusion cell culture runs with TFF (black), rTTF (blue), HPTFF or scTFF (red) as cell retention devices. VCV and viability (A), cell diameter (B), pH (C), cell culture debris (D), harvest titer (E) and product sieving (F).

Cell culture bioreactors must be oxygenated to support cell growth by sparging air or oxygen. Centrifugal pumps in unidirectional crossflow operations (TFF, HPTFF and scTFF) tend to accumulate gas bubbles coming into the cell recirculation loop. This problem was solved by stopping the pumps for 3 s every 3 min to release the air from the pump head. With activated delta pressure control during HPTFF operation controlling delta pressure to 0 mbar, stopping the crossflow for 3 s caused a sharp change in the pressure profile along the filter length (Figure A.46A). Due to some delay of the PI controlled co-current filtrate flow regulation, the filtrate pressure PT_{F1} was higher than the retentate pressure PT_{R1} immediately after crossflow stopping, which resulted in a negative delta pressure up to -14 mbar (Figure A.46B red area). After reactivation of the crossflow, the co-current filtrate flow was reduced and the PI control required some more time to establish HPTFF conditions. During that time interval, a positive delta pressure of up to 5 mbar was seen at the filter inlet (Figure A.46B blue area). Taken together, stopping the crossflow during HPTFF operation resulted in a slight membrane sweeping. In rTFF operation, gas bubble trapping was alleviated by positioning the pumps such that they are pointing towards each other, with air removed from the pump head by alternating activation of the retentate pumps.

3.4 Large-scale filter pressure characterization

Large-scale experiments using TFF, HPTFF and scTFF operation confirmed results from the lab-scale experiments. Crossflow ramping from 0 – 45 L min⁻¹ showed a continued increase in the pressure gradient along the filter length in TFF operation while the permeate pressures were independent of position (Figure A.47C). Considering similar crossflow conditions with 29 L min⁻¹ corresponding to a shear rate of 1,470 s⁻¹ as applied during lab-scale perfusion cell culture runs resulted in a fiber inlet pressure of 71 mbar PT_{RC1} , a fiber outlet pressure of 31 mbar (PT_{RC2}) and an average filtrate pressure (PT_{A1-5}) of 51 mbar (Figure A.47E). Filtrate pressures on the filtrate inlet and outlet (PT_{A1-5}) showed similar values as the filtrate pressure sensors on the backside of the filter module (PT_{AB1-5}).

HPTFF operation could be achieved by controlling pressure PT_{F1} so that it was 6 mbar above the pressure PT_{R1} for all evaluated crossflows up to 45 L min⁻¹ (Figure A.47D). Filtrate pressures on the filtrate inlet and outlet (PT_{A1-5}) were aligned with the corresponding filtrate pressures on the backside (PT_{AB1-5}) (Figure A.47F). In contrast to TFF operation, filtrate pressures matched the pressure gradient of the retentate loop, with pressure sensors PT_{A1} and PT_{AB1} slightly lower than the corresponding retentate pressures. The filtrate outlet pressure PT_{F2} was significantly

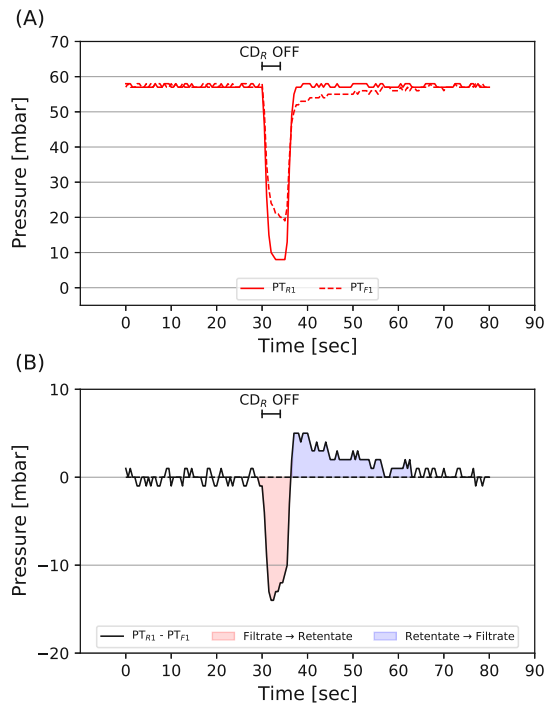


Figure A.46: Membrane sweep in HPTFF operation upon crossflow stop. Inlet pressure of the retentate (PT_{R1}) and inlet pressure on filtrate side (PT_{F1}) were recorded upon a 3 s stop of the levitated centrifugal pump (CD_{R1}) to release air bubbles (A). The delta pressure ($PT_{R1} - PT_{F1}$) was calculated and the blue area represents a negative delta pressure during which a backflush is happening in the first half of the filter, whereas the red area represents a positive delta pressure resulting in a backflush at the second half of the filter (B).

lower compared to the other pressure sensor readings. Co-current filtrate flows to achieve HPTFF at varying crossflows are provided in the Supporting Information section (Figure A.48B).

scTFF operation to generate controlled Starling recirculation was further demonstrated with a large-scale filter module and the data are provided in the Supporting Information section (Figure A.49). As such, a filtrate loop ramping at constant crossflow (Figure A.49A) and pressure distribution along the filter length for scTFF phase 1 (Figure A.49B) and for scTFF phase 2 (Figure A.49C) are provided. In addition to changing the filtrate flow, a crossflow stop whilst keeping the filtrate PI control active was able to achieve effective membrane sweeping (Figure A.49D).

4 Discussion

Applying co-current filtrate flow represents a promising tool to alleviate product retention in mammalian perfusion processes by achieving uniform TMP conditions

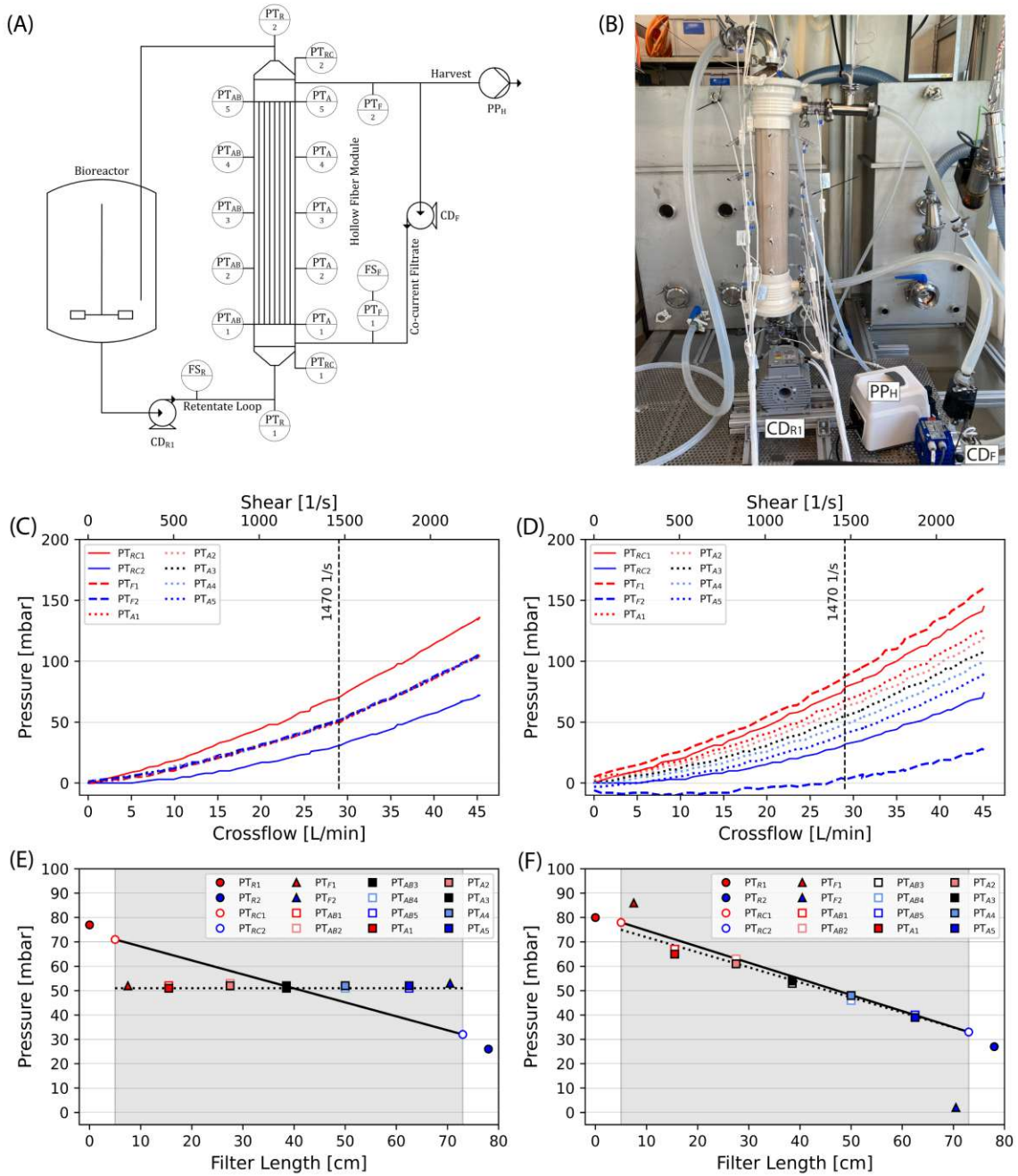


Figure A.47: Large-scale pressure characterization results. Schematic representation of the experimental setup for the large-scale pressure characterization in water (A). Pressure transmitters (PT), flow sensors (FS), centrifugal pumps (CD) and peristaltic pumps (PP) are specified with subscripted letters according to their position (R: Retentate; F: Filtrate; A and AB: Additional sensors on filtrate side; H: Harvest). Picture of experimental setup (B). Large-scale crossflow ramping in TFF operation (C) and crossflow ramping with delta pressure control in HPTFF operation (D). Pressure measurements according to their position along the filter length are provided for TFF (E) and for HPTFF (F) at standard operation of $1,470 \text{ s}^{-1}$ shear, grey areas represent absolute fiber length.

along the filter length. This decreases (or eliminates) the Starling recirculation flow, reducing the filter load by using the entire membrane surface [24]. In this study, pressure characterization experiments demonstrated that HPTFF operation is possible for a wide range of perfusion relevant crossflows using levitated centrifugal pumps that provide uniform (non-pulsatile) flow (Figure A.42B). By matching the inlet retentate pressure PT_{R1} and the inlet filtrate pressure PT_{F1} with a simple delta pressure control to 0 mbar, a uniform TMP was achieved along the lab-scale filter (Figure A.42C). Interestingly, the outlet filtrate pressure PT_{F2} showed increasing discrepancy from the retentate outlet pressure PT_{R2} with increasing co-current filtrate flow. This discrepancy may come from increasing turbulence at the filtrate outlet, although it had no effect on the filtrate pressure profile PT_{A1-5} . A reduced setup consisting of two pressure sensors (PT_{R1} and PT_{F1}), a retentate centrifugal pump CD_{R1} and a filtrate centrifugal pump CD_F are therefore sufficient to operate the HPTFF system (Figure A.41D).

Large-scale pressure characterization revealed that HPTFF can also be achieved with manufacturing scale filters (Figure A.47). With the filtration module used in this study, the inlet filtrate pressure PT_{F1} had to be increased by 6 mbar compared to the inlet retentate pressure PT_{R1} to match the filtrate pressures PT_{A1-5} with the retentate pressure drop. A pressure decrease from PT_{R1} positioned in the inlet retentate tubing compared to the pressure sensor located in the adapter piece connecting tube was observed (Figure A.47E and F). This offset might be due to the change in tube diameter from the inlet tubing to the much wider adapter piece connecting to the hollow fiber module. Further, pressure PT_{F1} had to be controlled higher than expected to achieve HPTFF. As already observed in lab-scale, the outlet pressure sensor in the filtrate loop PT_{F2} was lower than anticipated. These findings might be explained by a combination of a relatively smaller filtrate inlet adapter diameter than in the lab-scale and perturbation of the flow pattern at elevated co-current filtrate flows in the large-scale module. Nevertheless, determination of the offset by pressure characterization allowed us to achieve HPTFF operation across the entire tested crossflow range from 0 – 45 L min⁻¹ by only measuring pressures PT_{R1} and PT_{F1} .

In perfusion cell culture, a uniform TMP, as per definition in HPTFF, is not necessarily the highest priority as in protein separations [34, 35]. The main objective in perfusion processes is to avoid filter clogging and reduce product retention. Therefore, a membrane sweep from time to time in the form of a backflush can be beneficial to remove some deposited material, but avoiding intense backflushing as attributed to irreversible fouling [28]. A novel operating mode was designed in

this study named stepping co-current TFF (scTFF). scTFF can be operated with the same hardware setup as described for the HPTFF (Figure A.41D). By lowering and subsequently increasing the co-current filtrate flow rate compared to HPTFF operation, a TMP gradient was achieved along the filter length resulting in a Starling recirculation (Figure A.44A). The Starling recirculation changed direction upon switching from scTFF phase 1 to phase 2, generating a backflush on the first half of the filter and then on the second half of the filter similar to what occurs in ATF or rTFF operation [24, 27, 28]. However, in contrast to ATF and rTFF, where the strength of the Starling recirculation is a function of crossflow velocity and filter length, the strength of the Starling recirculation in scTFF can be tuned independently of both crossflow velocity and fiber length. For demonstration, a TMP of ± 10 mbar was targeted (Figure A.44C), but any other TMP larger or smaller can be achieved just by varying the co-current filtrate flow rates (Figure A.44B). Furthermore, scTFF can either be operated by switching between scTFF phase 1 and phase 2 (Figure A.44D), or by operating at HPTFF conditions and integrating a membrane sweeping from time to time by lowering or increasing the co-current filtrate flow (Figure A.44E). The duration of each phase can thereby freely be chosen, giving even more operational flexibility. scTFF operation was demonstrated at lab-scale, and pressure characterization experiments revealed applicability at manufacturing scale without changing the system setup (Figure A.49).

Perfusion cell culture runs revealed significantly reduced product sieving below 60% for TFF operation (Figure A.45F). This agrees with the literature, where similarly reduced product sieving was reported [7, 11, 27]. It is worth mentioning that the average filtrate fluxes in this study were particularly low with $0.6 \text{ L m}^{-2} \text{ h}^{-1}$ compared to commonly reported filtrate fluxes of $2\text{-}3 \text{ L m}^{-2} \text{ h}^{-1}$ [15, 24].

Despite similar pressure drop and therefore comparable absolute Starling recirculation flow of rTFF compared to TFF, rTFF showed significantly improved product sieving above 90%, which is comparable to what has been observed in ATF systems [27]. This confirms that with an identical pump system, rTFF clearly outperformed TFF. However, this study does not allow us to distinguish between the beneficial contributions of backflushing at both the inlet and outlet, utilization of the entire membrane surface, and/or relaxation of the fouling deposit when the crossflow direction changes. The rTFF_2 run with higher amount of cell culture debris showed lower product sieving than rTFF_1 (Figure A.45D), highlighting that rTFF is still prone to product retention which can likely be attributed to pronounced fouling at the inlet or exit of the hollow fiber modules at elevated debris levels [31].

HPTFF operation entirely removing Starling recirculation due to a uniform TMP

along the filtration module showed similar or even higher product sieving than rTFF operation. The HPTFF operation was interrupted every 3 min for 3 s by stopping the crossflow to release potentially trapped gas bubbles from the centrifugal pump head, which might even have had a beneficial impact on product sieving. The slightly delayed PI-response controlling the co-current filtrate flow resulted in a quick sweep of the membrane, initially backflushing the membrane on the first filter half, followed by backflushing of the second filter half upon crossflow re-activation (Figure A.46). Whereas bubble trapping in the centrifugal pump head plays a minor role at larger scales, intentional pump stopping from time to time to generate a membrane sweep in HPTFF operation might still be an attractive option (Figure A.49D). It must be mentioned that a similar effect can be achieved by shortly increasing the crossflow by maintaining the co-current filtrate flow PI control active.

Similar but more controlled sweeping of the membrane was alternatively achieved by increasing or lowering the co-current filtrate flow at constant crossflow (Figure A.44A). Intensity and location of the backflush can be adjusted by changing the magnitude of the co-current filtrate flow (Figure A.44B), offering a wide range of possibilities not available in ATF or rTFF operation. scTFF allows the Starling recirculation flow to be adjusted independently of filtration module specifications or crossflow velocities without changing the hardware setup. This novel approach enables further research to evaluate the benefits of membrane sweeping in a controlled but flexible manner to define best operating conditions depending on process requirements.

A critical aspect of unidirectional crossflow systems remains filter inlet blocking [26, 29]. Cell clumps or aggregates getting into the cell recirculation loop can be trapped at the filter inlet blocking entire hollow fibers. In two unidirectional crossflow runs (TFF_1 and HPTFF_2) filter inlet blocking led to premature run termination. When working with cell lines prone to aggregation, rTFF should be the chosen cell retention operation mode to prevent inlet blocking by crossflow reversal. When aggregation is not an issue and unidirectional crossflow represents no risk to premature run termination, HPTFF or scTFF clearly outperform conventional TFF operation. Further, HPTFF and scTFF offer greater flexibility compared to ATF or rTFF systems by alleviating previously described restrictions on filter characteristics and operation parameters:

1. Crossflow velocity: No restriction to low crossflows as strategy to avoid extensive Starling recirculation.
2. Filtration module length: Enabling longer filtration modules due to TMP control and thereby reducing system complexity with multiple parallel modules.

3. Inner fiber diameter: No need for increased inner fiber diameters to reduce pressure gradient at the cost of membrane surface area or greater hold-up volume.
4. Pore size: Possibility to utilize larger pores sizes without increasing Starling recirculation caused by lower membrane resistance.

Ultimately, the combination of alternating crossflow to prevent inlet blocking and co-current filtrate flow to allow Starling flow control would combine the best attributes of both systems. With the ability to prolong each crossflow phase in rTFF, co-current filtrate flow could equally be alternated to reach HPTFF conditions for both crossflow directions. Given the unidirectional flow generation by the centrifugal pumps in this study would however result in an even more complex system setup with two pumps in the retentate loop and two pumps in the filtrate loop, unless low-shear bidirectional pumps become available. Whether the gained filtration performance outweighs the additional system complexity must be assessed case by case and the ideal cell retention strategy might vary depending on the process characteristics. Further, co-current filtrate flow might find application in other domains of upstream or downstream processing and might be combined with other setups such as flat sheet filters.

5 Conclusion and Outlook

This study evaluated the impact of co-current filtrate flow on product retention during steady-state perfusion processes using hollow fiber modules as cell retention devices. Whereas Starling recirculation in TFF and alternating crossflow TFF is dependent on crossflow velocity and filter module characteristics, co-current filtrate flow enabled independent control of Starling recirculation. Pressure characterization studies performed by inserting additional pressure sensors along the filter module length revealed detailed insights into the filtrate pressure gradient and confirmed the theoretical concept of altering TMP by co-current filtrate flow. Further, control of Starling flow was not only demonstrated at lab-scale, but also successfully applied to a manufacturing scale filtration module. The benefits of HPTFF operation or precisely controlling the direction and intensity of Starling recirculation in scTFF operation was further demonstrated in steady-state perfusion cell culture processes which showed much higher product sieving compared to standard TFF operation. Starling flow control enabled by co-current filtrate flow operation represents an effective tool not only to study filter fouling, but also to reduce product retention in

steady-perfusion cell culture processes as well as other operations such as dynamic perfusion or N-1 perfusion.

Acknowledgements

The authors would like to thank Pavel Dagorov and his workshop team (FHNW) for hollow fiber filter modification and Sebastian Schneider and Silvia Pavone (FHNW) for supporting experimental work on perfusion processes. The authors also thank the entire Levitronix team for support, especially Philipp Campos, Lorenz Schüssler and Knut Kuss for valuable inputs and support. Dominik Schieman, Paul Niepold and David Garcia Munzer (Novartis) kindly sponsored the manufacturing scale filter module. Moreover, the authors would like to acknowledge specifically the Bioprocess Sciences (BPS) team of Merck Serono SA (an affiliate of Merck KGaA) for material and analytical support and for valuable discussions and support throughout the project, especially Alexandre Châtelin and the analytical team.

Conflict of interest

Antony Sibilis is an employee of Levitronix GmbH, a company which produces and markets centrifugal pumps and flow sensors used in the present study. He was not involved in the interpretation of data or statistical analysis. All other authors declare that they have no known competing financial interests or personal relationships that could have appeared to influence the work reported in this paper.

Data availability statement

The data that support the findings of this study are available from the corresponding author upon reasonable request.

Supporting Information

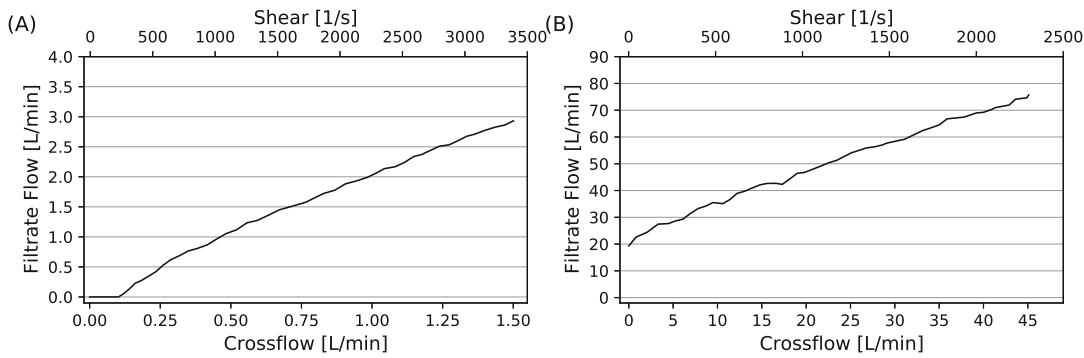


Figure A.48: Required co-current filtrate flow to generate HPTFF operation at respective crossflows for lab-scale filter (A) and large-scale filter (B).

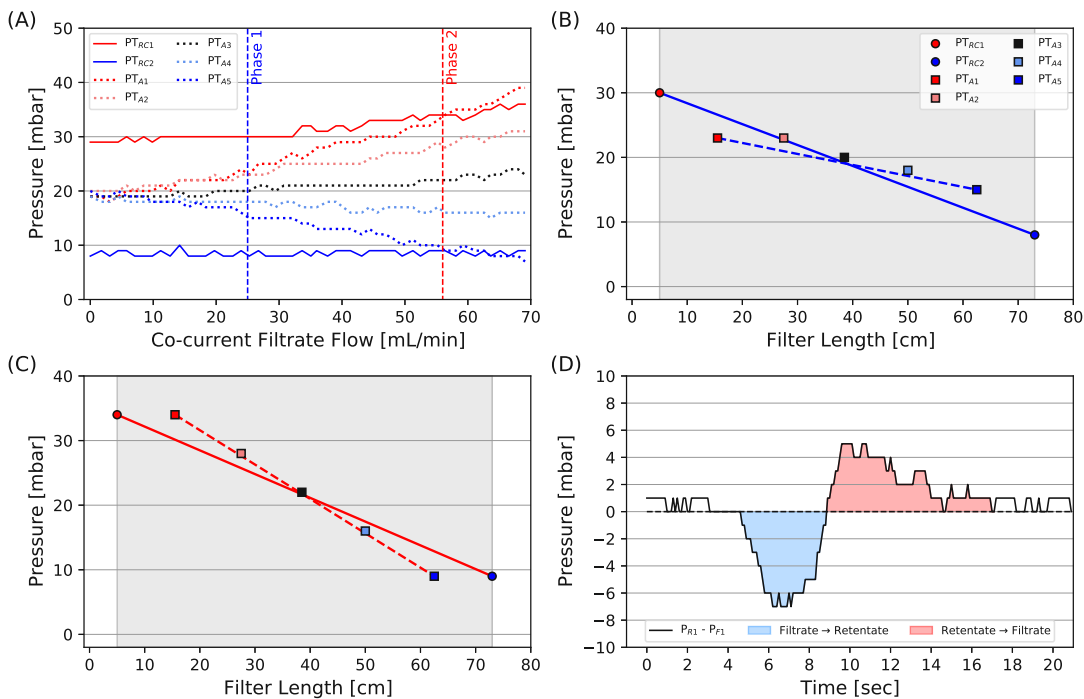


Figure A.49: Pressure characterization for scTFF operation with large-scale filter. Co-current flow ramping at 14.5 L min^{-1} crossflow (A). Vertical dashed lines represent operating conditions for scTFF phase 1 (blue) and scTFF phase 2 (red). Pressure measurements according to their position along the filter length are provided for scTFF phase 1 (B) and scTFF phase 2 (C), grey areas represent absolute fiber length. Membrane sweeping could further be demonstrated upon crossflow stop keeping the co-current filtrate flow control active (D). The delta pressure ($PT_{R1} - PT_{F1}$) leads to a backflush in the first half of the filter (blue area), whereas the red area represents a positive delta pressure resulting in a backflush at the second half of the filter.

References

- [1] Jean-Marc Bielser et al. “Perfusion mammalian cell culture for recombinant protein manufacturing – A critical review”. In: *Biotechnology Advances* 36.4 (2018), pp. 1328–1340. ISSN: 07349750. DOI: 10.1016/j.biotechadv.2018.04.011.
- [2] Jonathan Coffman et al. “A common framework for integrated and continuous biomanufacturing”. In: *Biotechnology and Bioengineering* 118.4 (2021), pp. 1721–1735. ISSN: 10970290. DOI: 10.1002/bit.27690.
- [3] Moritz Wolf, Jean-Marc Bielser, and Massimo Morbidelli. *Perfusion cell culture processes for biopharmaceuticals*. Cambridge University Press, 2020.
- [4] Katharina Blaschczok et al. “Investigations on Mechanical Stress Caused to CHO Suspension Cells by Standard and Single-Use Pumps”. In: *Chemie Ingenieur Technik* 85.1-2 (2013), pp. 144–152. ISSN: 0009286X. DOI: 10.1002/cite.201200135.
- [5] Marie-Françoise Clincke et al. “Very high density of Chinese hamster ovary cells in perfusion by alternating tangential flow or tangential flow filtration in WAVE bioreactor™—part II: Applications for antibody production and cryopreservation”. In: *Biotechnology Progress* 29.3 (2013), pp. 768–777. ISSN: 8756-7938. DOI: 10.1002/btpr.1703.
- [6] William Kelly et al. “Understanding and modeling alternating tangential flow filtration for perfusion cell culture”. In: *Biotechnology Progress* 30.6 (2014), pp. 1291–1300. ISSN: 87567938. DOI: 10.1002/btpr.1953.
- [7] Samantha Wang et al. “Shear contributions to cell culture performance and product recovery in ATF and TFF perfusion systems”. In: *Journal of Biotechnology* 246 (2017), pp. 52–60. ISSN: 18734863. DOI: 10.1016/j.jbiotec.2017.01.020.
- [8] Adam C. Fisher et al. “The Current Scientific and Regulatory Landscape in Advancing Integrated Continuous Biopharmaceutical Manufacturing”. In: *Trends in Biotechnology* 37.3 (2019), pp. 253–267. ISSN: 01677799. DOI: 10.1016/j.tibtech.2018.08.008.
- [9] Michael A. MacDonald et al. “Perfusion culture of Chinese Hamster Ovary cells for bioprocessing applications”. In: *Critical Reviews in Biotechnology* 42.7 (2022), pp. 1099–1115. ISSN: 0738-8551. DOI: 10.1080/07388551.2021.1998821.

- [10] Cary Matanguihan and Paul Wu. “Upstream continuous processing: recent advances in production of biopharmaceuticals and challenges in manufacturing”. In: *Current Opinion in Biotechnology* 78 (2022), p. 102828. ISSN: 09581669. DOI: 10.1016/j.copbio.2022.102828.
- [11] Daniel J. Karst et al. “Characterization and comparison of ATF and TFF in stirred bioreactors for continuous mammalian cell culture processes”. In: *Biochemical Engineering Journal* 110 (2016), pp. 17–26. ISSN: 1369703X. DOI: 10.1016/j.bej.2016.02.003.
- [12] R. Pavlik. *United States Patent, US 2018/0236407 A1*. 2017.
- [13] R. Pavlik. *Australian Patent, W O 2019/133487 A1*. 2019.
- [14] J. Shevitz. *United States Patent, US 2019/0201820 A1*. 2018.
- [15] Patrick Romann et al. “Maximizing yield of perfusion cell culture processes: Evaluation and scale-up of continuous bleed recycling”. In: *Biochemical Engineering Journal* 193 (2023), p. 108873. ISSN: 1369703X. DOI: 10.1016/j.bej.2023.108873.
- [16] Georges Belfort, Robert H. Davis, and Andrew L. Zydney. “The behavior of suspensions and macromolecular solutions in crossflow microfiltration”. In: *Journal of Membrane Science* 96 (1994), pp. 1–58.
- [17] Jia Wei Chew, James Kilduff, and Georges Belfort. “The behavior of suspensions and macromolecular solutions in crossflow microfiltration: An update”. In: *Journal of Membrane Science* 601.October 2019 (2020), p. 117865. ISSN: 18733123. DOI: 10.1016/j.memsci.2020.117865.
- [18] Robert Field. “Fundamentals of Fouling”. In: *Membrane Technology*. Vol. 44. Wiley-VCH Verlag GmbH & Co. KGaA, 2010, pp. 1–23. DOI: 10.1002/9783527631407.ch1.
- [19] Christine Taddei et al. “Yeast cell harvesting from cider using microfiltration”. In: *Journal of Chemical Technology & Biotechnology* 47.4 (1990), pp. 365–376. ISSN: 10974660. DOI: 10.1002/jctb.280470407.
- [20] Robert van Reis and Andrew Zydney. “Bioprocess membrane technology”. In: *Journal of Membrane Science* 297.1-2 (2007), pp. 16–50. ISSN: 03767388. DOI: 10.1016/j.memsci.2007.02.045.
- [21] Sanjeev G. Redkar and Robert H. Davis. “Crossflow Microfiltration of Yeast Suspensions in Tubular Filters”. In: *Biotechnology Progress* 9.6 (1993), pp. 625–634. ISSN: 15206033. DOI: 10.1021/bp00024a009.

- [22] Takaaki Tanaka et al. “Characteristics in Crossflow Filtration Using Different Yeast Suspensions”. In: *Separation Science and Technology* 32.11 (1997), pp. 1885–1898. ISSN: 01496395. DOI: 10.1080/01496399708000743.
- [23] Maria E. Weinberger and Ulrich Kulozik. “Pulsatile crossflow improves microfiltration fractionation of cells and proteins”. In: *Journal of Membrane Science* 629 (2021). ISSN: 18733123. DOI: 10.1016/j.memsci.2021.119295.
- [24] Flaka Radoniqi et al. “Computational fluid dynamic modeling of alternating tangential flow filtration for perfusion cell culture”. In: *Biotechnology and Bioengineering* 115.11 (2018), pp. 2751–2759. ISSN: 10970290. DOI: 10.1002/bit.26813.
- [25] Ernest Henry Starling. “On the Absorption of Fluids from the Connective Tissue Spaces”. In: *The Journal of Physiology* 19.4 (1896), pp. 312–326. ISSN: 00223751. DOI: 10.1113/jphysiol.1896.sp000596.
- [26] Maria E. Weinberger and Ulrich Kulozik. “On the effect of flow reversal during crossflow microfiltration of a cell and protein mixture”. In: *Food and Bioproducts Processing* 129 (2021), pp. 24–33. ISSN: 09603085. DOI: 10.1016/j.fbp.2021.07.001.
- [27] Magdalena Pappenreiter et al. “Product Sieving of mAb and its High Molecular Weight Species in different modes of ATF and TFF Perfusion Cell Cultures”. In: *Journal of Chemical Technology & Biotechnology* (2023). DOI: 10.1002/jctb.7386.
- [28] Maria E. Weinberger and Ulrich Kulozik. “Understanding the fouling mitigation mechanisms of alternating crossflow during cell-protein fractionation by microfiltration”. In: *Food and Bioproducts Processing* 131 (2022), pp. 136–143. ISSN: 09603085. DOI: 10.1016/j.fbp.2021.11.003.
- [29] Andrew L. Zydney. “Continuous downstream processing for high value biological products: A Review”. In: *Biotechnology and Bioengineering* 113.3 (2016), pp. 465–475. ISSN: 10970290. DOI: 10.1002/bit.25695.
- [30] Siegfried Ripperger and Justus Altmann. “Crossflow microfiltration – state of the art”. In: *Separation and Purification Technology* 26.1 (2002), pp. 19–31. ISSN: 13835866. DOI: 10.1016/S1383-5866(01)00113-7.
- [31] Vikram Sundar et al. “Use of scanning electron microscopy and energy dispersive X-ray spectroscopy to identify key fouling species during alternating tangential filtration”. In: November 2022 (2023), pp. 1–6. DOI: 10.1002/btpr.3336.

- [32] Seung Chul Kim et al. “Effect of transmembrane pressure on Factor VIII yield in ATF perfusion culture for the production of recombinant human Factor VIII co-expressed with von Willebrand factor”. In: *Cytotechnology* 68.5 (2016), pp. 168–1696. ISSN: 15730778. DOI: 10.1007/s10616-015-9918-1.
- [33] Jason Walther, Jean McLarty, and Timothy Johnson. “The effects of alternating tangential flow (ATF) residence time, hydrodynamic stress, and filtration flux on high-density perfusion cell culture”. In: *Biotechnology and Bioengineering* 116.2 (2019), pp. 320–332. ISSN: 10970290. DOI: 10.1002/bit.26811.
- [34] Robert van Reis. *United States Patent, 5,256,294*. 1993.
- [35] Robert van Reis et al. “High performance tangential flow filtration”. In: *Biotechnology and Bioengineering* 56.1 (1997), pp. 71–82. ISSN: 00063592. DOI: 10.1002/(SICI)1097-0290(19971005)56:1<71::AID-BIT8>3.0.CO;2-S.
- [36] David L. Grzenia, Jonathan O. Carlson, and S. Ranil Wickramasinghe. “Tangential flow filtration for virus purification”. In: *Journal of Membrane Science* 321.2 (2008), pp. 373–380. ISSN: 03767388. DOI: 10.1016/j.memsci.2008.05.020.
- [37] U. Merin and G. Daufin. “Crossflow microfiltration in the dairy industry: state-of-the-art”. In: *Le Lait* 70.4 (1990), pp. 281–291. ISSN: 0023-7302. DOI: 10.1051/lait:1990421.
- [38] R. M. Sandblom. *United States Patent, 4,105,547*. 1978.
- [39] P.K Vadi and S.S.H Rizvi. “Experimental evaluation of a uniform transmembrane pressure crossflow microfiltration unit for the concentration of micellar casein from skim milk”. In: *Journal of Membrane Science* 189.1 (2001), pp. 69–82. ISSN: 03767388. DOI: 10.1016/S0376-7388(01)00396-9.
- [40] S. Metze et al. “Monitoring online biomass with a capacitance sensor during scale-up of industrially relevant CHO cell culture fed-batch processes in single-use bioreactors”. In: *Bioprocess and Biosystems Engineering* 43.2 (2020), pp. 193–205. ISSN: 1615-7591. DOI: 10.1007/s00449-019-02216-4.

B Curriculum Vitae

Patrick Romann

Email: patrick.romann@sunrise.ch

Nationality: Swiss

Date of Birth: 11th October 1993

Education

9/2020-10/2023	Doctor of Science in Bioprocess Technology , TU Wien. PhD Thesis: Advancing continuous biomanufacturing: Quality control and process intensification strategies for perfusion cell culture.
9/2018-8/2020	Master of Science in Biotechnology , University of Strasbourg. Master Thesis: Characterization of carbon dioxide mass transfer in stirred tank bioreactors for mammalian cell culture.
8/2015-8/2018	Bachelor of Science in Biochemistry , University of Zurich. Bachelor Thesis: Structural study of the Staphylococcus Aureus Csm6 ribonuclease.

Working Experience

8/2020-10/2023	Merck Serono S.A. , Corsier-sur-Vevey (CH), Visiting PhD Student, Upstream Process Development
1/2020-8/2020	Lonza Biologics , Slough (UK), Scientist, Upstream Processing.
7/2017-9/2017	Lonza Biologics , Basel (CH), Intern, Drug Product Services.
6/2015-8/2015	Galderma Spirig , Egerkingen (CH), Intern, Preclinical Development.

Awards

2022	Winner of the ACTIP Fellowship , for excellent research in the field of animal cell culture technology from the Animal Cell Technology Industrial Platform.
------	--------------------------------------------------------------------------------------------------------------------------------------------------------------------

Publications

- 2021 | **Development of a unique rapid test to detect antibodies directed against an extended RBD of SARS-CoV-2 spike protein**, L. Brosi, E. Kübler, A. Weston, P. Romann, S. Panikulam, L. Dirscherl, M. Gerspach, C. Giegelmann, D. Dolce, M. Ueberschlag, A. Melone, F. Bantleon, T. K. Villiger, and C. B. Gerhold, *Chimia*, 75, 446-452
- 2022 | **Advancing Raman model calibration for perfusion bioprocesses using spiked harvest libraries**, P. Romann, J. Kolar, D. Tobler, C. Herwig, J. Bielser, and T. K. Villiger, *Biotechnology Journal*, 17, 2200184
- 2023 | **Maximizing yield of perfusion cell culture processes: Evaluation and scale-up of continuous bleed recycling**, P. Romann, J. Kolar, L. Chappuis, C. Herwig, T. K. Villiger, and J.-M. Bielser, *Biochem. Eng. J.*, 193, 108873
- 2023 | **Raman-controlled pyruvate feeding to control metabolic activity and product quality in continuous biomanufacturing**, P. Romann, S. Schneider, D. Tobler, M. Jordan, A. Perilleux, J. Souquet, C. Herwig, J.-M. Bielser, and T. K. Villiger, under review
- 2023 | **Maduramycin, a novel glycosylation modulator for mammalian fed-batch and steady-state perfusion processes**, P. Romann, T. Vuillemin, S. Pavone, M. Jordan, A. Perilleux, J. Souquet, J.-M. Bielser, C. Herwig, and T. K. Villiger, under review
- 2023 | **Co-current filtrate flow in TFF perfusion processes: Decoupling transmembrane pressure from crossflow to improve product sieving**, P. Romann, P. Giller, A. Sibilia, C. Herwig, A. Zydney, A. Perilleux, J. Souquet, J.-M. Bielser, and T. K. Villiger, under review
- 2023 | **Characterization of hydrodynamic stress in Erbi Breeze perfusion bioreactors**, P. Romann, D. Trunov, H. Lee, K. Lee, J.-M. Bielser, M. Soos, and T. K. Villiger, in preparation

